Designed Ultra-microporous Metal Organic Frameworks for Selective CO_2 Capture

A Thesis

Submitted in Partial Fulfilment of the Requirements

for the Degree of

Doctor of Philosophy

by

Shyamapada Nandi

ID: 20123207

Indian Institute of Science Education and Research (IISER), Pune

2018

Dedicated to

My parents and wife

Certificate:

This is to certify that the work incorporated in the thesis entitled "**Designed Ultra-microporous Metal Organic Frameworks for Selective CO_2 Capture**" submitted by **Shyamapada Nandi** carried out by the candidate at the Indian Institute of Science Education and Research (IISER), Pune, under my supervision. The work presented here or any part of it has not been included in any other thesis submitted previously for the award of any degree or diploma from any other University or Institution.

Date:

Dr. R. Vaidhyanathan

(Research Supervisor)

Associate Professor, IISER-Pune

Pune-411008, India

Declaration:

I hereby declare that the thesis entitled "**Designed Ultra-microporous Metal Organic Frameworks for Selective CO_2 Capture**" submitted for the degree of Doctor of Philosophy in Chemistry at Indian Institute of Science Education and Research (IISER), Pune has not been submitted by me to any other University or Institution. This work was carried out at Indian Institute of Science Education and Research (IISER), Pune, India under the supervision of Dr. R. Vaidhyanathan.

Date:

Shyamapada Nandi

Acknowledgments:

First of all, I would like express my sincere thanks to my research supervisor Dr. R. Vaidhyanathan for his continuous encouragement and support throughout last five and half years. I have learnt a lot from him in each step of my journey especially how to design a scientific project and complete the work in a constructive manner. One of the most important achievement, I have accomplished is how to setup a brand new lab from the scratch. I also would like to express my sincere appreciation for his dedication to any work.

I would like to express my sincere gratitude to Indian Institute of Science Education and Research (IISER), Pune and our former Director Prof. K. N. Ganesh for providing state-of-the-art research facilities, funding and an excellent research atmosphere. Also I would like to acknowledge our current director Prof. Jayant B. Udgaonkar for taking over the responsibility and continuing with same pace.

I am very much thankful to my Research Advisory Committee (RAC) members Dr. R. Boomi Shanker (IISER Pune) and Dr. Rajesh G. Gonnade (NCL Pune) for their valuable suggestions during my PhD which indeed help me to shape my projects. I am also thankful to Prof. Tom Woo (university of Ottawa), Prof. Praveen Thallapally (PNNL, USA), Dr. Jens Rother (Rubo lab, Germany), Dr. Sreekumar Kurungot (NCL pune), Dr. Vinod C. Prabhakaran (NCL Pune) and Prof. Ulrike Werner-Zwanziger (university of Dalhousie) for their collaborative research inputs. Special thanks to prof. Tom Woo for helping us with his computational knowledge. I am extremely thankful to all faculty members at IISER Pune and Prof. M. Jayakanan (chair chemistry) for their kind cooperation.

I would like to thank my lab mates Dinesh, Debanjan, Rahul, Shalini, Sattwick, Kingshuk, Aparna and Rinku for their help and support during last five and half years. I also would like to acknowledge the former group members Harpeet, Satya, Neha, and the summer project fellow Hemkalyan, Shuvangi, Suchit, Nidhi, Bhabin and Yogesh.

I am thankful to the students of our collaborators Dr. Sean Collins and Phil De-Luna (from University of Ottawa), Dr. Vishal M. Dhavale, Dr. Santosh K. Singh and Rajith (NCL Pune), Dr. Debasis Banerjee (PNNL, USA) who has executed some of our collaborative work.

I also would like to express my sincere gratitude to my BSc and MSc teachers who taught me lot of things whether it is academic or non-academic. Special thanks to prof. Ranjit Pathak for his enormous support and encouragement during my B.Sc. study. I sincerely acknowledge the efforts of my M.Sc. thesis supervisor Prof. B. K. Patel (IIT Guwahati) and all other faculties of Chemistry department (IIT Guwahati).

Now it's time for my friends from IISER and outside. I am thankful to all my friends and seniors Biplab Da, Manna Da, Avishek Da, Avigyan Da, Partha Da, Kaushik Da, Barun Da, Arunava Da, Soumya Da, Tanmoy Da, Sudeb Da, Avik, supratik, Arindam Da, Sunil, Maidul Da, Bijay Da, Reja, Amit, Partha, Arunava, Rahi, Chandramouli, Plawan, Soumendu, Sushil, Sudeshna, Sanjit and many more. I am also thankful to my school, college and Masters friends Sandip, Mahadev, Shilaj, Amit, Arup, soumendu, Rameswar, Debashis and more. Special thanks to one of my best friends, Rajkumar who has always supported me during my tough time.

I would like to thank Dr. Umeshareddy Kacherki (deputy librarian) and Anuradha for library support and all other instrument operators (Mr. Parveen Nasa, Mrs. Archana, Mr. Nilesh Dumbre, Ms. Swati, Ms. Nayana, Mr. Anil, Mr. Mahesh, Mr. Yatish, Mr. Nitin, Mrs. Megha to name a few), as well as all the IISER Pune non-teaching staff members, especially Mr. Mayuresh, Mr. Tushar, Ms. Vrushali, Mr. Prabhas, Mr. Suresh, Mr. Sandeep, Ms. Mariamma for their support during last five years.

I am extremely thankful to my parents for their unconditional support and trust throughout my whole academic career. I also thank the other family members for their continuous support. Without their support, it was impossible for me to be here.

I would also like to acknowledge American Chemical Society (ACS), American Association for the Advancement of Science (AAAS) Royal Society of Chemistry (RSC), John Wiley & Sons (Wiley-VCH), Nature Publishing Group (NPG) and Springer for publishing a number of my research articles produced during my PhD tenure at IISER Pune. Also I am extremely thankful to DST, SERB, CII and Enovex for supporting me for 2 years through PM fellowship. I also would like to thank IISER Pune for rest of the financial support during my doctoral studies.

Finally I would like to sign off thanking my dearest and nearest one, my wife, Mrs. Mou Roy, who has sacrificed so many things just for encouraging and supporting me throughout my whole Ph.D.

Shyamapada Nandi

Table of Contents:

Abstract:

Carbon dioxide (CO_2) is a major heat-trapping gas responsible for global warming through the greenhouse effect. Anthropogenic activities such as deforestation and burning fossil fuels account for large-scale CO_2 emissions, along with some natural processes such as respiration and volcanic eruptions. According to the recent report (2017) from NASA, the atmospheric CO_2 concentration is already reaching alarming levels. In fact, the Mid-Tropospheric CO_2 concentration has gone up by 110 ppm (from 365ppm to 475ppm) since last one and half decade. So, there is a need for developing technologies to reduce the atmospheric CO_2 concentration. Also, this can bring some economic benefits in coal-based power production. Carbon Capture and Storage (CCS) is the most promising technique for this purpose. Though the present industrial CO_2 capture technology uses liquid amine-based sorbents, adsorptive separation methods employing solid sorbents are realized to be the most energy efficient and thereby cost-effective. The large-scale adsorptive separation of CO_2 from industrial gas mixtures is achieved using zeolites, activated carbons, silica gels as sorbents. With an ever-growing demand for more energy-saving and thereby cost-effective, and environmentally friendly procedures for gas separation, new-generation sorbents with better efficiency are required. Metal Organic Frameworks (MOFs), made up of metal ions/metal-oxo clusters connected via organic linkers, have been recognized as well-suited materials for the application mentioned above. During last decade several reports on gas separation using both Micro/Ultra-micro porous MOFs have appeared. However, MOFs with ultra-micropores (< 6 Å) seems to be the most potential candidate for the gas separation applications, especially for carbon capture. In this context, we have developed few ultra-microporous MOFs (Um-MOFs) which display very interesting CO_2 capture characteristics. For example, a Um-MOF, $Ni_9(\mu\text{-}H_2O)_4(H_2O)_2(4\text{-}PyC)_{18}(H_2O)_{17}(CH_3OH)_4(C_4H_8O)_4$, IISERP-MOF1, displays the best properties suitable for pre-combustion CO_2 capture and H_2 purification. While, another MOF, $Ni(4\text{-}PyC)_2$.DMF, IISERP-MOF2, exhibits lowest parasitic energy (655 KJ/kg CO_2) when applied for post-combustion CO_2 capture. Following this, we have developed few more 4-PyC based MOFs utilizing Mg, Mn and Cu metal ions. However, these MOFs are dense as ascertained from the crystal structure. In one of the chapters in my thesis, we show how porosity can be introduced into such non-porous frameworks by utilizing coordination flexibility. In another study, we have incorporated different basic functional moieties (triazolyl, imidazolyl and benzimidazole) to form Um-MOFs and have investigated the atomic-level details about their adsorption sites using a combined

experimental-computational approach. Our investigations include (i) the triazolyl and imidazolyl functionalized MOFs with hydrophobic methyl group-lined pores for humid CO_2 capture; (ii) understanding the adsorption characteristics of MOF simultaneously lined with strong adsorptions sites of different chemistry.

List of Acronyms:

Å	Angstrom
AcOH	Acetic acid
ACN	Acetonitrile
BET	Brunauer–Emmett–Teller
BTA	1,2,3- benzenetriazole
CCS	Carbon Capture and Storage
CMS	Carbon Molecular Sieve
COF	Covalent Organic Framework
DCM	Dichloromethane
DFT	Density Finctional Theory
DMA	Dimethylacetamide
DMF	Dimethylformamide
DMSO	Dimethyl sulfoxide
DOBDC	2,5-dihydroxybenzene-1,4-dicarboxylic acid
DSC	Differential Scanning Calorimetry
DSL	Dual Site Langmuir
EtOH	Ethanol
g	Gram
HCl	Hydrochloric Acid
HOA	Heat of Adsorption
IAST	Ideal Adsorption Solution Theory
INA / INT	Isonicotinic acid
IR	Infrared
MeOH	Methanol
mg	Miligram
min	Minutes
ml	Mililiter
µl	Micro liter
mmol	Mili moles
MOF	Metal Organic Framework
MSD	Mean Square Displacement
NLDFT	Non-local Density Functional Theory
NMP	N-Methyl-2-Pyrrolidone
NMR	Nuclear Magnetic Resonance
OMS	Open Metal Sites
PALS	Positron Annihilation Lifetime Spectroscopy
PE	Parasitic Energy
PSA	Pressure Swing Adsorption
PXRD	Powder X-Ray Diffraction
4-PyC	4-Pyridinecarboxylic Acid/ Isonicotinic acid

RT	Room temperature
S	Selectivity
SCXRD	Single Crystal X-ray Diffraction
SSL	Single Site Langmuir
TDA	Thiophene-2,5-dicarboxylic acid
TGA	Thermo Gravimetric Analysis
THF	Tetrahydrofuran
TSA	Temperature Swing Adsorption
Um-MOF	Ultra-microporous Metal Organic Framework
WC	Working Capacity
ZIF	Zeolitic Imidazolate Framework

Research Publications:

Included in Thesis

1. **Shyamapada Nandi**, Phil De Luna, Thomas D. Daff, Jens Rother, Ming Liu, William Buchanan, Ayman I. Hawari, Tom K. Woo and Ramanathan Vaidhyanathan, Single Ligand Ultra-microporous MOF for Pre-combustion CO_2 Capture and Hydrogen Purification, *Sci. Adv*., 1:e1500421, (**2015**).
2. **Shyamapada Nandi**, Sean P. Collins, Debanjan Chakraborty, Debasis Banerjee, Praveen K. Thallapally, Tom K. Woo, & Ramanathan Vaidhyanathan, Ultra-low parasitic energy for post-combustion CO_2 capture realized in a nickel isonicotinate MOF with excellent moisture stability, *J. Am. Chem. Soc*., 139, 1734-1737 (**2017**).
3. **Shyamapada Nandi**, Sattwick Haldar, Debanjan Chakraborty and Ramanathan Vaidhyanathan, Strategically designed azolyl-carboxylate MOFs for potential humid CO_2 capture, *J. Mater. Chem. A*, 5, 535-543, (**2016**).
4. **Shyamapada Nandi**, Rahul Maity, Debanjan Chakraborty, Hemkalyan Ballav, and Ramanathan Vaidhyanathan, CO_2 Adsorption Characteristics of an Ultra-microporous MOF with Cavities Lined by Basic Groups and Open-metal Sites, (**2017**) submitted.
5. **Shyamapada Nandi**, Phil De Luna, Rahul Maity, Debanjan Chakraborty, Tom K. Woo and Ramanathan Vaidhyanathan, Gas and pressure dependent porosity into a non-porous solid via coordination flexibility, (**2018**) submitted.

Not Included in Thesis

6. **Shyamapada Nandi**, Debanjan Chakraborty & Ramanathan Vaidhyanathan, Permanantly Porous Single Molecule H-bonded Organic Framework for Selective CO_2 capture, *Chem. Commun*., 52, 7249, (**2016**).

7. **Shyamapada Nandi** and Ramanathan Vaidhyanathan, Tuning Porosity via Control of Interpenetration in a Zinc Isonicotinate Metal Organic Framework, *J. Chem. Sci*., 126, 1393–1398, (**2014**).
8. Aparna Banerjee, **Shyamapada Nandi**, Parveen Nasa and Ramanathan Vaidhyanathan, Enhancing Carbon Capture Capacities of a Rigid Ultra-microporous MOF Through Gate-opening at Low CO_2 Pressures Assisted by Swiveling Oxalate Pillars, *Chem Commun*., 52, 1851, (**2016**).
9. Arvind K. Gupta, Ashok Yadav, Anant Kumar Srivastava, Kormathmadam Raghupathy Ramya, Harshad Paithankar, **Shyamapada Nandi**, Jeetender Chugh, and Ramamoorthy Boomishankar, A Neutral Cluster Cage with a Tetrahedral $[Pd_{12}IIL_6]$ Framework: Crystal Structures and Host–Guest Studies, *Inorg. Chem*., 54, 3196–3202, (**2015**).
10. **Shyamapada Nandi**, Ulrike Werner-Zwanziger and Ramanathan Vaidhyanathan, A Triazine-Resorcinol Based Porous Polymer with Polar Pores and Exceptional Surface Hydrophobicity Showing CO_2 Uptake at Under Humid Conditions, *J. Mater. Chem. A*, 3, 21116-21122, (**2015**).
11. **Shyamapada Nandi**, Vishal M. Dhavale, Sorout Shalini, Ulrike Werner-Zwanziger, Harpreet Singh, Sreekumar Kurungot and Ramanathan Vaidhyanathan, Lithium Assisted Proton Conduction at 150◦C in a Microporous Triazine-Phenol Polymer, *Adv. Mater. Interf.*, 2, 1500301, (**2015**).
12. Sandeep K. Gupta, Dhananjayan Kaleeswaran, **Shyamapada Nandi**, Ramanathan Vaidhyanathan, and Ramaswamy Murugavel, Bulky Isopropyl Group Loaded Tetraaryl Pyrene Based Azo-Linked Covalent Organic Polymer for Nitroaromatics Sensing and CO_2 Adsorption, *ACS Omega*, 2, 3572–3582, (**2017**).
13. **Shyamapada Nandi**, Santosh Kumar Singh, Dinesh Mullangi, Rajith Illathvalappil, Leena George, Chathakudath P. Vinod, Sreekumar Kurungot and Ramanathan Vaidhyanathan, Low Band Gap Benzimidazole COF Supported Ni_3N as Highly Active OER Catalyst, *Adv. Energy Mater*., 6, 1601189, (**2016**).
14. Dinesh Mullangi, Vishal Dhavale, Sorout Shalini, **Shyamapada Nandi**, Sean Collins, Tom Woo, Sreekumar Kurungot and Ramanathan Vaidhyanathan, Low-overpotential Electrocatalytic Water Splitting with Noble-Metal-Free Nanoparticles Supported in a sp3 N-rich Flexible COF, *Adv. Energy Mater*., 6, 1600110, (**2016**).
15. Dinesh Mullangi, **Shyamapada Nandi**, Sorout Shalini, Sheshadri Sreedhala, Chathakudath P. Vinod and Ramanathan Vaidhyanathan, Pd Loaded Amphiphilic COF as Catalyst for Multi-fold Heck Reactions, C-C Couplings and CO oxidation, *Sci. Rep*., 2, 10876, (**2015**).
16. Sattwick Haldar, Kingshuk Roy, **Shyamapada Nandi**, Debanjan Chakraborty, P. Dhanya, Yogesh Gawli, Satishchandra Ogale and Ramanathan Vaidhyanathan, High and reversible

lithium ion storage in a self-exfoliated triazole-triformyl phloroglucinol based Covalent Organic Nanosheets, *Adv. Energy Mater*., 1702170, (**2017**)

17. Dinesh Mullangi, Sorout Shalini, **Shyamapada Nandi**, Bhavin Choksi, and Ramanathan Vaidhyanathan, Super-hydrophobic Covalent Organic Frameworks for Chemical Resistant Coatings, Hydrophobic Paper and Textile Composites, *J. Mater. Chem. A*, 5, 8376-8384, (**2017**).
18. Aniruddha Basu, Kingshuk Roy, Neha Sharma, **Shyamapada Nandi**, Ramanathan Vaidhyanathan, Sunit Rane, Chandrashekhar Rode, and Satishchandra Ogale, CO_2 Laser Direct Written MOF-Based Metal-Decorated and Heteroatom-Doped Porous Graphene for Flexible All-Solid-State Microsupercapacitor with Extremely High Cycling Stability, *ACS Appl. Mater. Interf.*, 8, 31841–31848 (**2016**).
19. Maidul Islam, Nishanth D. Tirukoti, **Shyamapada Nandi**, and Srinivas Hotha, Hypervalent Iodine Mediated Synthesis of C-2 Deoxy Glycosides and Amino Acid Glycoconjugates, *J. Org. Chem.*, 79, 4470–4476, (**2014**).
20. Ketan Patel, Satej S. Deshmukh, Dnyaneshwar Bodkhe, Manoj Mane, Kumar Vanka, Dinesh Shinde, Pattuparambil R. Rajamohanan, **Shyamapada Nandi**, Ramanathan Vaidhyanathan, and Samir H. Chikkali, Secondary Interactions Arrest the Hemiaminal Intermediate To Invert the Modus Operandi of Schiff Base Reaction: A Route to Benzoxazinones, *J. Org. Chem*., 82, 4342–4351, (**2017**).

Patents:

1. Vaidhyanathan Ramanathan, **Shyamapada Nandi**, Aparna Banerjee, Adsorption Based Air Separation Using Porous Coordination Polymers, Publication number: 20150158012.
2. Vaidhyanathan Ramanathan, Dinesh Mullangi, **Shyamapada Nandi**, Covalent Organic Frameworks as Porous Supports for Non-Noble Metal Based Water Splitting Electrocatalysts, Publication number: 20170130349.

Chapter 1

Introduction to Carbon Capture, Metal Organic Frameworks and the Challenges in CO_2 Capture

1.1. Why Do We Need to Capture CO_2?

Carbon dioxide (CO_2) is the major component of the greenhouse gases responsible for global warming. In addition to the natural processes such as respiration and volcanic eruptions, anthropogenic activities such as deforestation and direct burning fossil fuels for power generation are responsible for generating substantial proportions of CO_2.[1,2] According to the recent report (2017) from NASA; the worldwide atmospheric CO_2 concentration is already reaching alarming levels. In fact, the Mid-Tropospheric CO_2 concentration has gone up by 110ppm (365ppm to 475ppm) in the last 10-15 years.[1] Therefore, capturing CO_2 from industrial sources will have marked impact on the global CO_2 concentration.[3] Carbon Capture and Storage (CCS) has attracted meaningful attention and become the best technology for mitigating worldwide CO_2 emissions.[4-5] During last 15 years, several reports have appeared based on carbon capture technologies which involve capturing CO_2 from different sources.[6-14] CO_2 capture can be classified into three distinct classes depending on the source from where the capture process happens. For example,

1) Post-combustion CO_2 capture; the source is industrial effluent with major component of 80-85% N_2, 10-15% CO_2, small amount of moisture, ppm level of SO_x and NO_x.
2) Pre-combustion CO_2 capture; the source is the mixture of 40% CO_2 and 60% H_2 generated via coal gasification.
3) Direct air capture; the origin is environmental air with low CO_2 (~400 ppm) concentration.

1.1.1. Post-combustion CO_2 Capture:

In post-combustion CO_2 capture, the CO_2 is separated from a mixture of 10-15% CO_2, 80-85% N_2, a small amount of moisture and ppm level of SO_x and NO_x; this mixture is commonly referred to as the flue gas, emitted from the tail pipe of industrial power plants.[4, 15,16] This is the most investigated topic in the area of carbon capture. In this process, the industrial effluent containing 80-85% N_2, 10-15% CO_2, small amount of moisture, ppm level of SO_x and NO_x is passed through an environmental air pollution control system to strip off the acidic vapours. The resulted gas stream is passed through a drier unit to strip off the moisture which results in a clean stream of 85% N_2 and 15% CO_2. This dry stream of 15% CO_2 and 85% N_2 is then passed through the adsorber unit where the sorbent selectively adsorbs CO_2 leaving out a clean stream of N_2. After the complete adsorption, the adsorbed CO_2 has to be regenerated and geo sequestered. A schematic diagram for post-combustion CO_2 capture is presented below (Fig. 1.1). Although aqueous amine-based post-combustion

CO_2 capture is the most used technology in industries, this is not energy efficient or cost-effective because of the high regeneration cost.[17-19] Alternatively, in porous solid sorbent based CO_2 capture, the combustion gas is passed through a solid sorbent bed which selectively adsorbs CO_2. Since it operates on much weaker interactions between the sorbent and the sorbate, less regeneration energy is required thus makes it energy efficient and thereby cost-effective. When the bed achieves full capacity, the captured CO_2 is regenerated, discharging a near pure CO_2 for compression followed by geosequestration. Zeolites, such as 13X, are currently being involved in large scale PSA systems as CO_2 scrubber of natural gas and landfill gases.[20] However, they do not perform well in humid conditions.

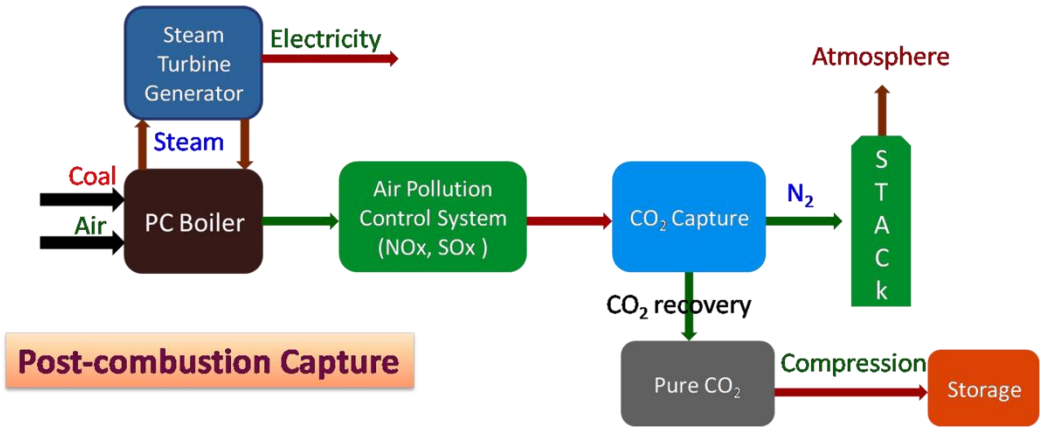

Figure 1.1. Schematic representation of the post-combustion CO_2 capture unit.

1.1.2. Pre-combustion CO_2 Capture:

Pre-combustion capture is a process that involves capturing the CO_2 from coal or fossil fuel even before it is fully combusted for electricity production. This process has a substantial advantage over post-combustion CO_2 capture. Nevertheless, this is much less investigated compared to post-combustion CO_2 capture. Although post-combustion carbon capture[11, 21] technologies have attracted a lot of attention, alternatives to straight burning coal and scrubbing of CO_2, will be more energy efficient and low cost technologies[22, 23] is still desirable.

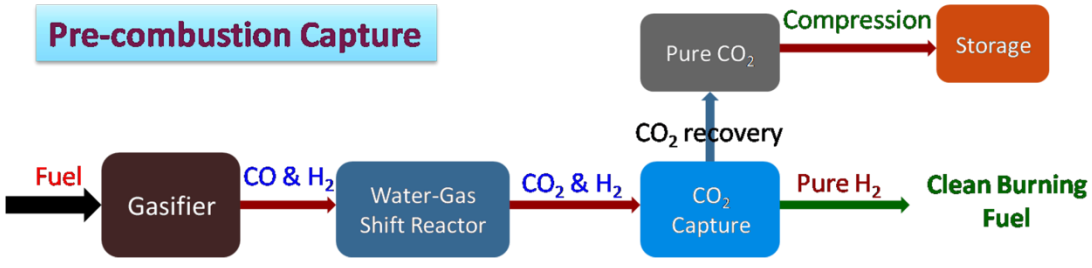

Figure 1.2. Schematic representation of the pre-combustion CO_2 capture unit.

In this direction, pre-combustion CO_2 capture can be the promising technology. Here, unlike in post-combustion capture, CO_2 is separated from a mixture of CO_2 and H_2, which normally exist at high pressure generated from coal gasification.[23-25] Coal gasification is used to produce > 90% of the world's H_2.[26] Coal gasification is likely to be a key technology for future clean coal power and involves the catalytic steam reforming of the fuel to generate a high-pressure H_2/CO_2 ($60H_2$:$40CO_2$) gas mixture.[23-25] Upon selective removal of the CO_2 from the mixture results in a pure H_2 stream, *a clean-burning fuel*. In this industrial CO_2/H_2 separation, pressure swing adsorption (PSA) systems with solid sorbents, such as zeolite 13X or activated carbon, is the preferred method.[27-29] A schematic representation shows the pathway involved in pre-combustion processes (Fig. 1.2).

1.1.3. Direct Air Capture:

Recently, direct CO_2 adsorption from the ambient air also known as direct air capture (DAC), is becoming important as a complementary technique for carbon capture.[30,31] Pre-combustion and post-combustion capture where CO_2 is captured from more concentrated sources such as flue gas (CO_2 + N_2) or water gas shift (CO_2 + H_2) are more common compared to direct air capture. The concept of DAC was first proposed by Lackner.[32] DAC has its own benefit in terms of location flexibility as well as the input gas stream which indirectly means this can be installed anywhere in the world without much of a complicacy. The input gas stream, in this case, is the ambient air which is having less concentration of acidic vapours such as NO_x and SO_x. This makes the input gas stream relatively cleaner compared to post-combustion and pre-combustion gas stream.[33,34] However, an extremely low concentration of CO_2 (~ 400 ppm) in the environmental air makes the input gas stream highly dilute which is a prime concern or challenge for DAC.[35] That is why a high capacity sorbent having reversible CO_2 capture ability at very low partial pressure will be highly advantageous. Mostly, Oxide-supported amines are the promising materials for CO_2 capture from this dilute source.[36]

1.2. Metal Organic Frameworks: Brief Introduction:

In recent times, Metal Organic Frameworks (MOFs), built from a combination of metal ions/clusters and organic linkers, have emerged as a new class of promising functional solid materials (Fig. 1.3).[37-39]

These are class of materials with high surface area and ordered crystallinity.[40-45] High degree of structural flexibility as well as diversity, tuneable pore size and the ability to

functionalizing the pore surface makes them find use in gas storage,[46-61] separation,[62-76] catalysis,[77-88] photoluminescence,[89-95] sensing,[96-100] proton conductivity,[101-109] electrical conductivity[110-114] and energy storage & conversion (Fig. 1.4).[115-121]

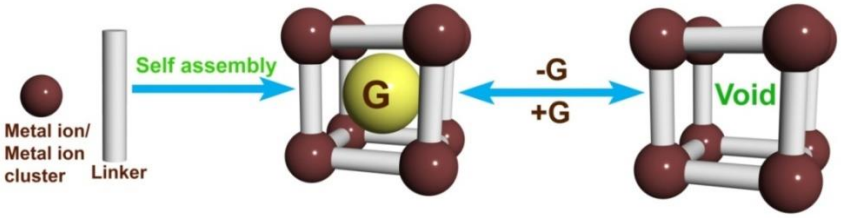

Figure 1.3. Schematic representation of MOF, a self assembled product of metal ion / metal ion cluster and linker.

Although these materials find use in diverse applications, the gas storage, separation and catalysis emerge to be the most promising.

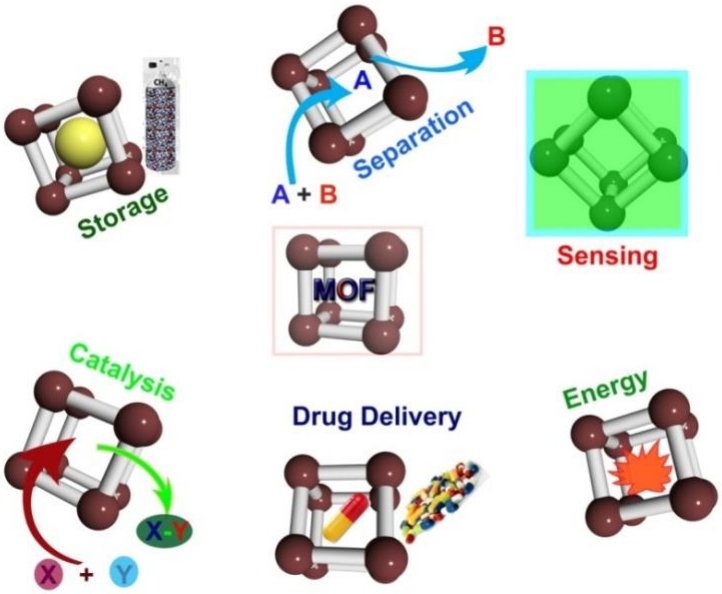

Figure 1.4. Schematic representation for the use or applications of MOF.

Over last 15 years many MOFs have been synthesized with pore size ranging from 4 to 25 Å.[46-88,122-127] Depending on the pore size these materials can be classified into three different regimes:

1. Ultra-microporous: pore size < 6 Å
2. Microporous: pore size 6-20 Å
3. Mesoporous: pore size > 20 Å

Among these three classes of MOFs, the small pore ones (Ultra-microporous and microporous) are more suitable for gas separation applications. On the other hand, the mesoporous MOFs are suitable for storage application.

1.3. Ultra-microporous Metal Organic Frameworks for CO_2 Capture: a Brief Account:

Generally, Ultra-microporous Metal Organic Frameworks (Um-MOFs) (pore size < 6 Å) are built from small rigid linkers.[63, 70, 76, 128-132] As the pore size is petite, it provides intrinsic molecular sieving capability as well as the cooperative interaction between guests molecules confined in such small pores.[76] This facilitates the stronger framework-guest and guest-guest interactions which makes the ultra-microporous MOFs best-suited candidate for CO_2 capture. In the last ten years, several Um-MOFs have been synthesized and investigated for CO_2 capture applications.[63, 70, 71, 75, 76, 129] Some of the best performing Um-MOFs along with some microporous MOFs have been discussed below.

1.3.1. Zinc Aminotriazolate Oxalate Derived Um-MOF:

Recently Vaidhyanathan *et al.*[76] reported a Zn-Atz-ox Based Um-MOF. Its structure is constructed from a layer-pillar convention where the Zn-Atz layers (Fig. 1.5A) are pillared by oxalic acid. The three-dimensional structure is a 6-connected cubic net (Fig. 1.5B).

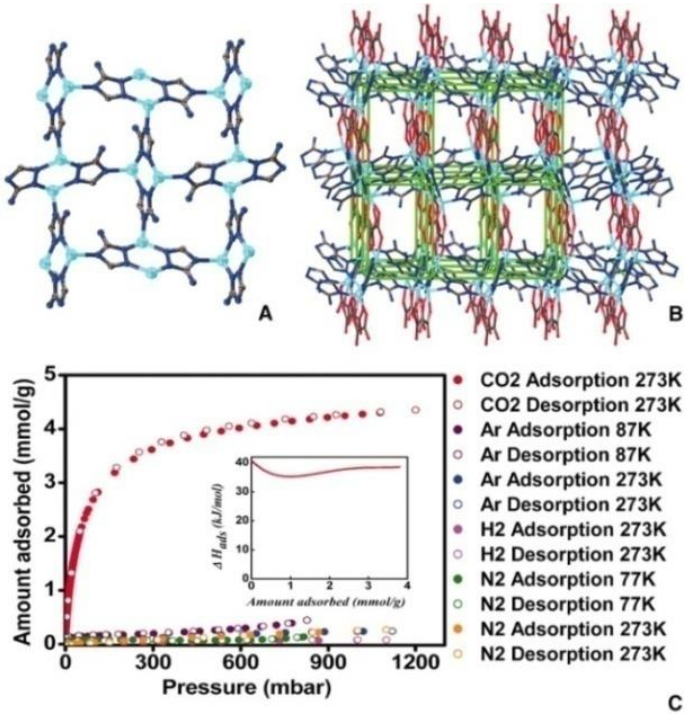

Figure 1.5. (A) Structure of the Zn-Atz layer in the MOF (Zn-cyan; C-black; N-blue). (B) Three dimensional structure of the MOF; the Zn-Atz layers are pillared by oxalate linkers (O-red) to form a six-connected cubic net as shown in green sticks. (C) Adsorption isotherms for different gases. The inset shows heat-of-adsorption calculated from the CO_2 isotherms at 273 and 293 K. The zero-loading heat of adsorption was estimated to be 40.8 kJ/mol (*Adopted from ref. 76 with permission from The American Association for the Advancement of Science*).

This MOF does not show any appreciable N_2 adsorption at 77 K. Interestingly, it shows very sharp CO_2 uptake at low partial pressure with a saturation capacity of 4.2 mmol/g at 273 K (Fig. 1.5C). At room temperature, the CO_2 capacity of this MOF was 3.8 mmol/g, which is among the highest reported CO_2 uptakes for Um-MOFs. However, it does not adsorb any other gases such as H_2, N_2 or Ar at room temperature. This makes the material as a suitable sorbent for selective CO_2 capture. The Heat of Adsorption (HOA) for this MOF was reported as 40 kJ/mol which is quite high, which could substantially increase the regeneration cost. However, the HOA trend was quite unusual. Contrary to the expected trend of decreasing δH_{ads} with increasing CO_2 loading, the MOF showed a subsequent increase in δH_{ads}, which was stabilized to a value of > 35 kJ/mol for the entire range of CO_2 loading (Inset of Fig. 1.5C). Such high HOA was explained by invoking a strong framework-CO_2 interaction (-NH_2-CO_2 interaction) and the abnormal HOA trend was attributed to a strong co-operative CO_2-CO_2 interaction between two distinct adsorption sites. Further, the authors have quantified the electrostatic and co-operative interaction energy which agrees well with the experimental observations. The crystallographic structure analysis of the CO_2 loaded MOF indicates the amine-CO_2 and CO_2-CO_2 interactions.

Followed by the previous literature, Banerjee *et al.*[133] reported the synthesis, characterization, thermal analysis and adsorption studies for a family of topologically related Zn-Atz-ox frameworks. Similar to the previous report, a series of layered-pillared ZnAtzOx MOFs were developed by varying the solvent combinations. In all the cases, the observed basic framework topology (6 connected cubic net) was very similar to the previous one (Fig. 1.6A).[76] However, the adsorption characteristics were very different from the parent phase (the water-methonol phase).[76] In one of the cases, where the MOF was synthesized in a mixture of water and butanol, it showed interesting CO_2 adsorption characteristics. The CO_2 adsorption isotherm of the Water-Butanol phase exhibited unusual gate opening phenomenon. The gate opening increases the CO_2 capacity of this material even more than the parent one (Fig. 1.6B). The authors had explained this gate opening behaviour via a 'molecular swiveling' of one weakly coordinated O atom from the oxalate linker.

Very similar to the parent material, this MOF also exhibited high selectivity towards CO_2 over other gases. Another important observation is the initial slope of the CO_2 isotherms. The CO_2 isotherms are much steeper at low partial pressure than that was observed in case of the parent phase. This indicated very strong framework-CO_2 interactions, which was further

demonstrated from the HOA calculation. A dual site Langmuir-Freundlich model was used to determine the energetics associated with the CO_2-framework interactions.

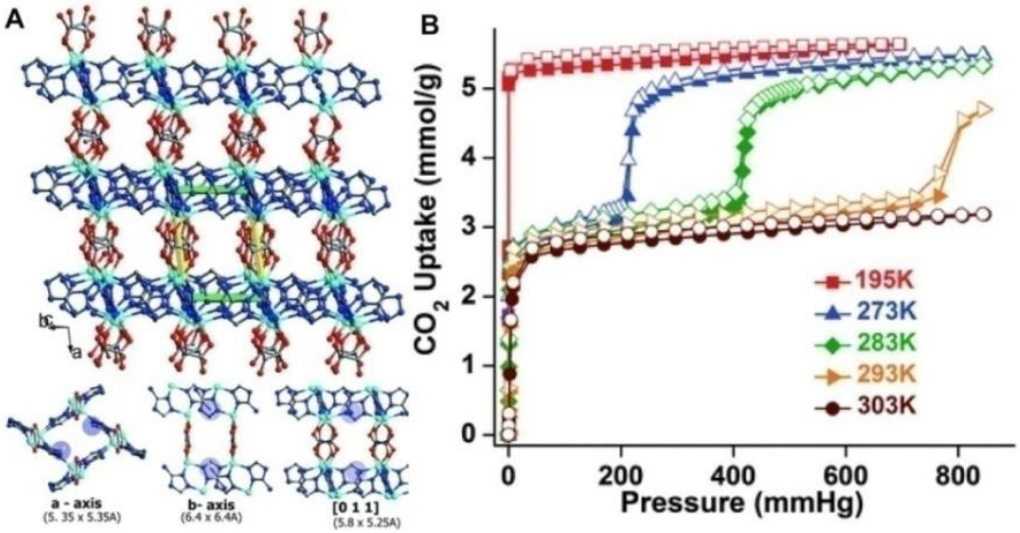

Figure 1.6. (A) Three-dimensional structure of ZnAtzOx, grown from the water/butanol solvent. The ZnAtz layers upon pilaring by the oxalate units resulted in ultra-micropores along three different axes. The dimensions do not factor in the van der Waals radii. Colour code: Zn-cyan; O-red; N-blue; C-grey. (B) CO_2 adsorption isotherms at different temperatures (*Adopted from ref. 133 with permission from Royal Society of Chemistry*).

Dual site calculations resulted in a very high HOA of 46 kJ/mol for one site, while the other site exhibited a HOA value of 32 kJ/mol. This result indicated the occurrence of two different adsorption sites which is in agreement with the earlier report.[76] A comparison of these values against the HOA values observed for parent phase convey some brilliant observations. The parent material[76] had a site with relatively high HOA (40 kJ/mol) which was dominated by the amine-CO_2 interactions, and the second site with a HOA of 32 kJ/mol mostly dominated by the CO_2-CO_2 interactions. Which would mean the site with interaction strength of 46 kJ/mol could have even stronger NH_2...CO_2 interactions. However, this cannot be confirmed without obtaining the locations for the CO_2 within the pores of this new Zn-Atz-Ox MOF.

1.3.2. Cobalt Adeninate derived Um-MOF:

Rosi and co-workers reported a cobalt adeninate based Um-MOF functionalized with basic amine and pyrimidine nitrogens which showed very interesting CO_2 adsorption behaviour.[134] $Co_2(ad)_2(CO_2CH_3)_2 \cdot 2DMF \cdot 0.5H_2O$ (bio-MOF-11) was successfully synthesised in pure form via a solvothermal reaction of adenine and cobalt acetate in DMF medium. The structure is constructed from a cobalt-adenine-acetate paddle-wheel cluster as presented in figure 1.7A. In these clusters, two $Co^{(II)}$ are bridged by two adeninates nitrogens and two

acetate moieties. Now these clusters are connected among themselves via apical coordination of the N atom of the adeninate to $Co^{(II)}$ of the next cluster creating a 3D framework (Fig. 1.7B). Although, adenine contains imidazole type moieties, it does not form ZIF like structure in this case. The 3D structure of bio-MOF-11 consists of porous channel (cavity aperture of 5.2 Å) along a and b axes.

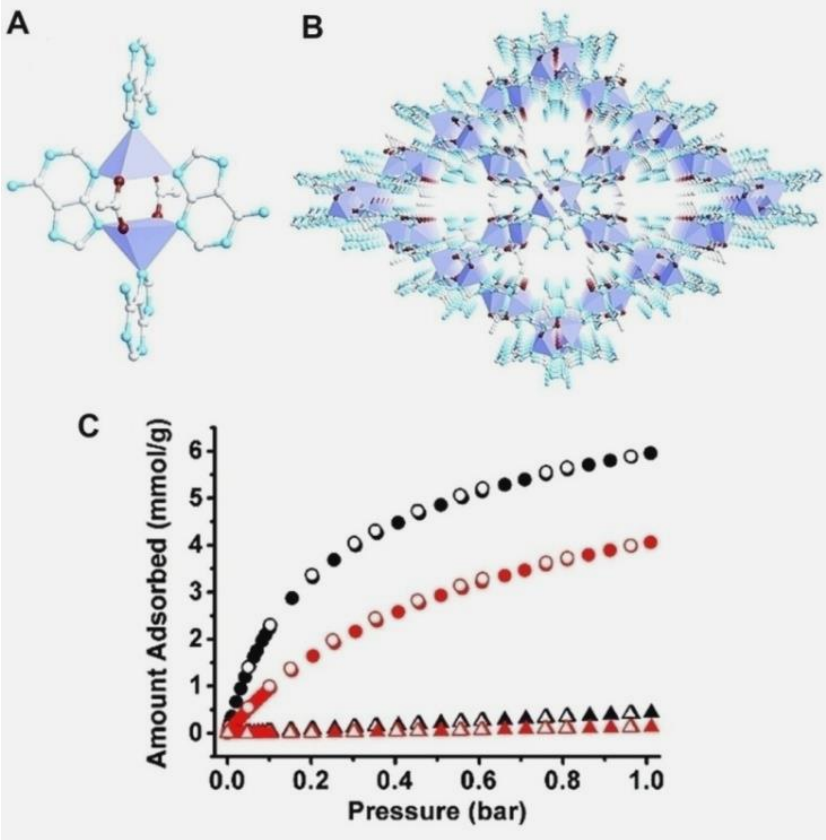

Figure 1.7. (A) $Co^{(II)}$-adeninate-acetate paddle wheel clusters as secondary building unit. (B) Three dimensional view of bio-MOF-11, each cluster has been presented as a square (dark-blue). (C) CO_2 (circles) and N_2 (triangle) Sorption isotherms at 273 (black) and 298 K (red) (*Adopted from ref. 134 with permission from American Chemical Society*).

The CO_2 isotherms at 273 K and 298 K displayed a maximum uptake of 6 and 4.1 mmol/g (Fig. 1.7C). Advantageously, the N_2 uptake at these temperatures was very low (0.4 mmol/g at 273 K and 0.1 mmol/g at 298 K). The rapid increase in CO_2 uptake compared to N_2 uptake at low partial pressure found this to be used as a selective (CO_2/ N_2 selectivity of 80:1 and 75:1 at 273 and 298 K; calculated from initial slope method) CO_2 capture material. The authors attributed this high CO_2 uptake to the presence of porous channel densely lined with lewis basic amino and pyrimidine groups. However, there was no direct evidence for the CO_2....N interactions.

1.3.3. SiF_6 Based Anion-pillared Um-MOF:

Another series of ultra-microporous MOFs which have been investigated for their CO_2 capture ability both in humid and dry conditions are built from bridging anionic SiF_6 units. Recently, Zaworotko and co-workers reported three such MOFs (SIFSIX-2-Cu, SIFSIX-2-Cu-i and SIFSIX-3-Zn) for their excellent CO_2 capture ability.[63] These materials were generally synthesized via a room temperature diffusion of a solution containing the neutral pillaring ligands (such as 4, 4′-dipyridylacetylene / Pyrazene) into a solution of $MSiF_6$ (where, M=Cu/Zn). Reaction of 4, 4′-dipyridylacetylene, dpa, with $CuSiF_6$ afforded purple coloured rod-shaped crystals of $[Cu(dpa)_2(SiF_6)]_n$, which the authors referred to as SIFSIX-2-Cu. SIFSIX-2-Cu exists in a primitive-cubic net with square channels (pore dimension 13.05 Å, Fig 1.8A). They reported also the 2-fold interpenetrated framework of the same $[Cu(dpa)_2(SiF_6)]_n$, SIFSIX-2-Cu-i, which was prepared via a similar protocol but with different solvents. In this structure the independent nets are in staggered form, yielding 5.15 Å pores (Fig. 1.8B). SIFSIX-3-Zn was synthesized via room temperature diffusion of a methanol solution of pyrazine into a methanol solution of $ZnSiF_6$. Similar to the other two MOFs this also crystallized in a primitive cubic cell which create a cubic channel (pore dimension = 3.84 Å; Fig. 1.8C).

The 77 K N_2 adsorption isotherms of SIFSIX-2-Cu and SIFSIX-2-Cu-i yielded BET surface areas of 3,140 and 735 m^2/g, respectively. SIFSIX-3-Zn showed negligible N_2 uptake at 77 K and thus a satisfactory BET fit could not be achieved with this data. The CO_2 isotherms at low partial pressure of SIFSIX-2-Cu showed a saturation capacity of 1.84 mmol/g at 298 K and 1 bar.

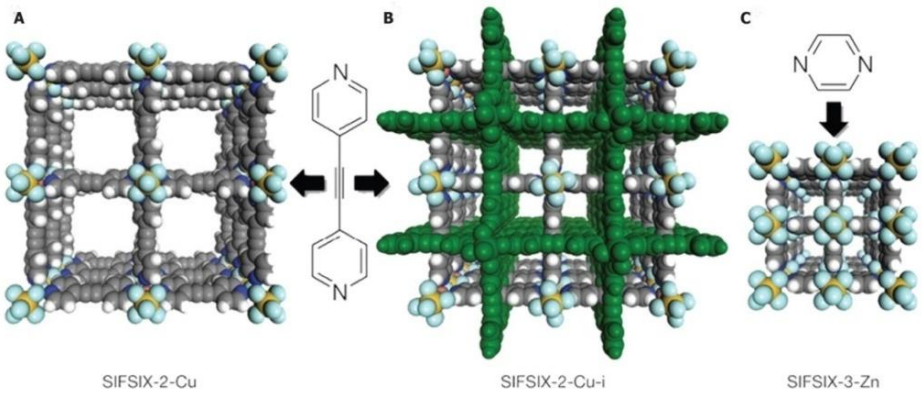

Figure 1.8. Three Dimensional structure of (A) SIFSIX-2-Cu; pore size 13.05 Å (B) SIFSIX-2-Cu-i; pore size 5.15 Å, (C) SIFSIX-3-Zn; pore size 3.84 Å. Colour code: C-grey; N-blue; Si-yellow; F-light blue; H-white (*Adopted from ref. 63 with permission from Nature Publishing Group*).

However, the interpenetrated form of the same, SIFSIX-2-Cu-i exhibited an exceptionally high CO_2 capacity of 5.41 mmol/g at similar conditions (Fig. 1.9A). The CO_2 uptake of SIFSIX-2-Cu-i at 298 K and 1 bar is among the highest reported till date for the metal organic materials (for example, MgMOF-74, ZnMOF-74, MIL-101, Cu-TDPAT, UTSA-20a, ZIF-78, $Zn_5(BTA)_6(TDA)_2$, Zn(bdc)(dabco), MOF-177 and HKUST-1).[75] The *IAST* calculations using binary gas compositions ($10CO_2$:$90N_2$; $50CO_2$:$50CH_4$) led to a drastic increase of selectivity of CO_2 over other gases when moving to the interpenetrated form of the SIFSIX-2-Cu. For example the CO_2/N_2 selectivity jumps from 13.7 to 140 and the CO_2/CH_4 selectivity jumps from 5.3 to 33 upon moving from non-interpenetrated to interpenetrated form. Contraction of the pores led to a remarkable increase in CO_2 uptake at low partial pressure. For instance, SIFSIX-3-Zn showed CO_2 uptake of 11 wt% at 0.1 bar whereas SIFSIX-2-Cu-i showed a CO_2 uptake of 4.4 wt% at 0.1 bar. SIFSIX-3-Zn exhibited very high CO_2 uptake which is close to that observed for Mg-dobdc and UTSA-16 at 0.15 bar of CO_2 pressure, relevant to post-combustion CO_2 capture (Fig.1.9B).

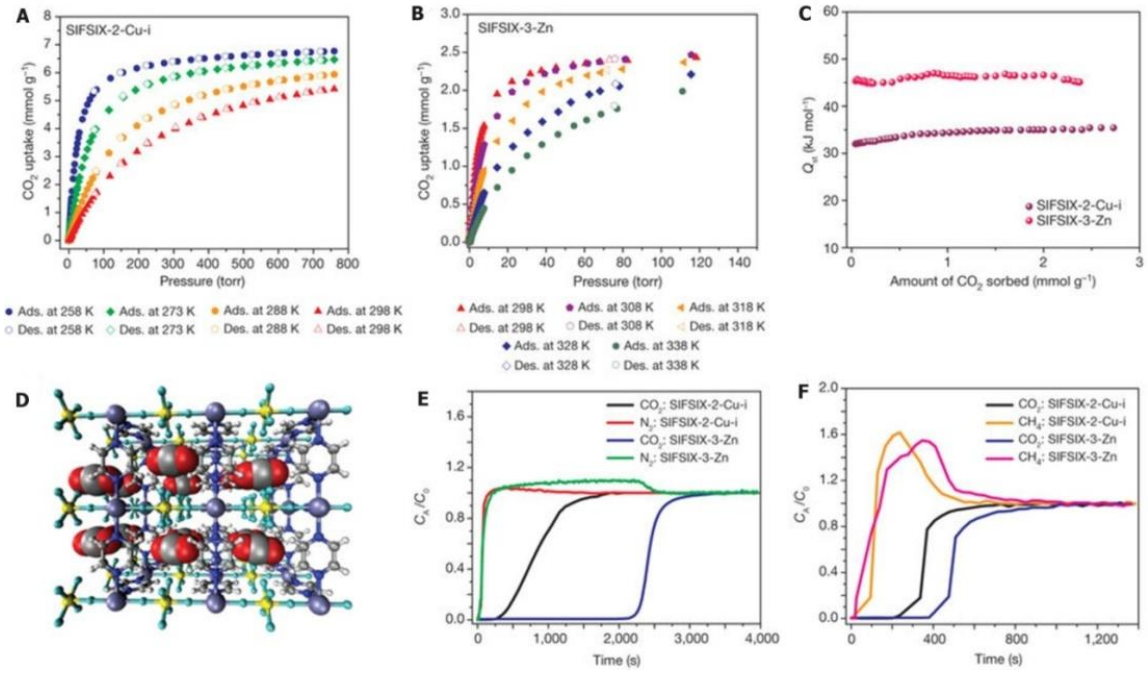

Figure 1.9. CO_2 sorption isotherms for SIFSIX-2-Cu-i (A) and SIFSIX-3-Zn (B). (C) HOA plots for SIFSIX-2-Cu-i and SIFSIX-3-Zn. (D) The most probable CO_2 positions in a $3 \times 3 \times 3$ super cell of SIFSIX-3-Zn shows the interactions between the δ^{+ve} C atoms of CO_2 and F atoms of SIFSIX anions. Colour code: C-grey; H-white; N-blue; O-red; Si-yellow; F-green; Zn-purple. Mixed-gas analysis breakthrough experiments for a (E) CO_2/N_2:10/90 gas mixture (298 K, 1 bar) and (F) CO_2/CH_4:50/50 gas mixture (298 K, 1 bar) carried out on SIFSIX-2-Cu-i and SIFSIX-3-Zn (*Adopted from ref. 63 with permission from Nature Publishing Group*).

However, the CO_2 uptake of SIFSIX-2-Cu-i at 0.15 bar was less than Mg-dobdc. This indicated strong framework-CO_2 interaction for SIFSIX-3-Zn compared to SIFSIX-2-Cu-i, which was further confirmed from heat of adsorption for CO_2 as shown in figure 1.9C (45 kJ/mol for SIFSIX-3-Zn vs. 33 kJ/mol for SIFSIX-2-Cu-i). Although these HOA values are in the higher regime still the adsorption desorption happened reversibly in these materials and was further confirmed from molecular simulation studies (Fig. 1.9D). The CO_2/N_2 (72 for SIFSIX-2Cu-i; 495 for SIFSIX-3-Zn) and CO_2/CH_4 (51 for SIFSIX-2-Cu-i; 109 for SIFSIX-3-Zn) selectivity calculated from column breakthrough technique (Figs. 1.9E and 1.9F) agrees well with the values obtained from *IAST* calculation employing pure component equilibrium adsorption isotherms.

Later on, Eddaoudi and co-workers had successfully synthesized SIFSIX-3-Cu,[128] the same analogue of SIFSIX-3-Zn. As expected the structure of SIFSIX-3-Cu (primitive cubic net) was same as observed in case of the Zn-analogue (Fig. 1.10A). However the CO_2 adsorption characteristics were different from SIFSIX-3-Zn. Here, the CO_2 isotherms for the Cu MOF were much steeper than that was observed for SIFSIX-3-Zn (Fig. 1.10B) at very low partial pressure which indirectly indicated relatively stronger CO_2-framework interactions than the Zn analogue.

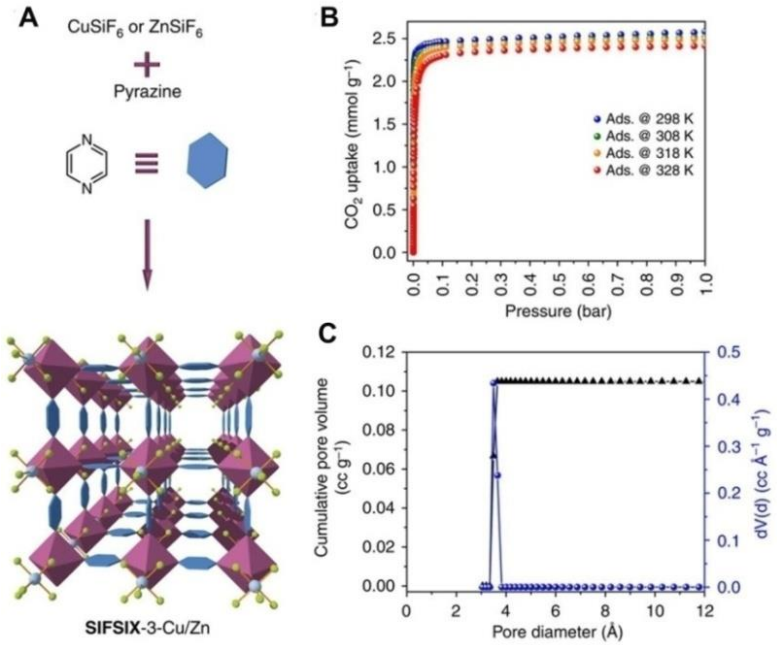

Figure 1.10. (A) Three dimensional structure of SIFSIX-3-Zn and/or SIFSIX-3-Cu. Colour code: pyrazine (pyz-blue polygon); Zn/Cu=purple polyhedral; Si-light blue spheres; F-light green spheres. (B) CO_2 adsorption isotherms at different temperatures for SIFSIX-3-Cu. (c) pore size distribution (PSD) obtained from the CO_2 sorption isotherm (CO_2 at 273 K NLDFT) for SIFSIX-3-Cu *(Adopted from ref. 128 with permission from Nature Publishing Group)*.

This stronger interaction is due to the confinement of the CO_2 molecules in a very small pore with pore diameter of 3.85 Å as observed from the NLDFT fit to the 273 K CO_2 isotherm (Fig. 1.10C). This was further confirmed from high HOA (53 kJ/mol) for CO_2. Because of the strong interaction, this material is capable of capturing CO_2 even from input stream with very low concentration of CO_2. Further the authors have exploited this material for direct air capture where the CO_2 has to be captured from extremely low concentration of CO_2 (400 ppm).

1.3.4. Cobalt-citrate Um-MOF:

Chen and co-workers reported a citrate built Um-MOF (UTSA-16) which is among the best-performing ones for post-combustion CO_2 capture.[75] The open framework structure consists of a basic secondary building unit, Co_4O_4 cubic cluster. Each citrate linker chelates with one such cluster, two Co tetrahedral and two K-ion. K-ion is again coordinated to two water molecules (Fig. 1.11A).

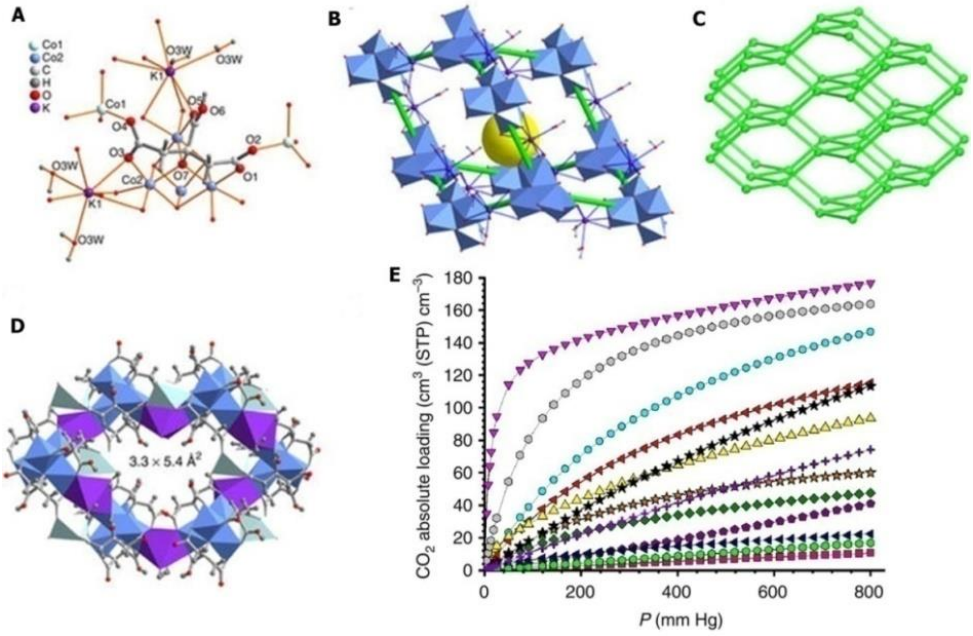

Figure 1.11. (A) The coordination environment of the citrate linker. (B) Each cubic (Co_4O_4) cluster node is linked by four K polyhedral linkers to give a diamondoid cage, the citrate ligands are presented as green sticks (C) The resulting diamondoid network. (D) The diamondoid cage with small window with the dimensions of 3.3×5.4 $Å^2$. (E) CO_2 adsorption isotherms for MgMOF-74 (magenta down triangle), UTSA-16 (grey hexagon), ZnMOF-74 (cyan circle), bio-MOF-11 (red left triangle), CuBTC (black star), Cu-TDPAT (yellow up triangle), UTSA-20a (violet cross), ZIF-78 (orange star), $Zn_5(BTA)_6(TDA)_2$ (olive diamond), Zn(bdc)(dabco) (purple pentagon), MIL-101 (navy left triangle), Yb(BPT) (green hexagon) and MOF-177 (pink square) at 296 K and 1 bar (*Adopted from ref. 75 with permission from Nature Publishing Group*).

Each cubic Co_4O_4 cluster is now linked to four K polyhedral linkers to generate a diamondoid cage (Fig. 1.11B and 1.11C). Four crystallographically independent water molecules are coordinated to these four K ion. The resulting diamondoid cage has a small entry (3.3 Å x 5.4 Å) as shown in figure 1.11.D. UTSA takes up quiet large amount of CO_2 (160 cc/cc) at 296 K and 1 bar (Fig. 1.11E). The authors had compared this uptake with some of the best performing materials reported in literature for post-combustion CO_2 capture. As shown in figure 1.11E the only material that marginally beats UTSA-16 is the MgMOF-74 in terms of capacity. Although MgMOF-74 has higher CO_2/CH_4 selectivity compared to UTSA-16, The CO_2/N_2 selectivity of both the materials are very much comparable.

1.3.5. Copper Silicate with Ultra-microporous Framework:

From a long time microporous aluminosilicate, the zeolite, was known for their use in CO_2 capture applications. However, transition metal silicates had not been investigated for these applications. A very recent report from Datta *et al.*[135] has describes the CO_2 adsorption behaviour of a microporous copper silicate under dry and humid conditions.

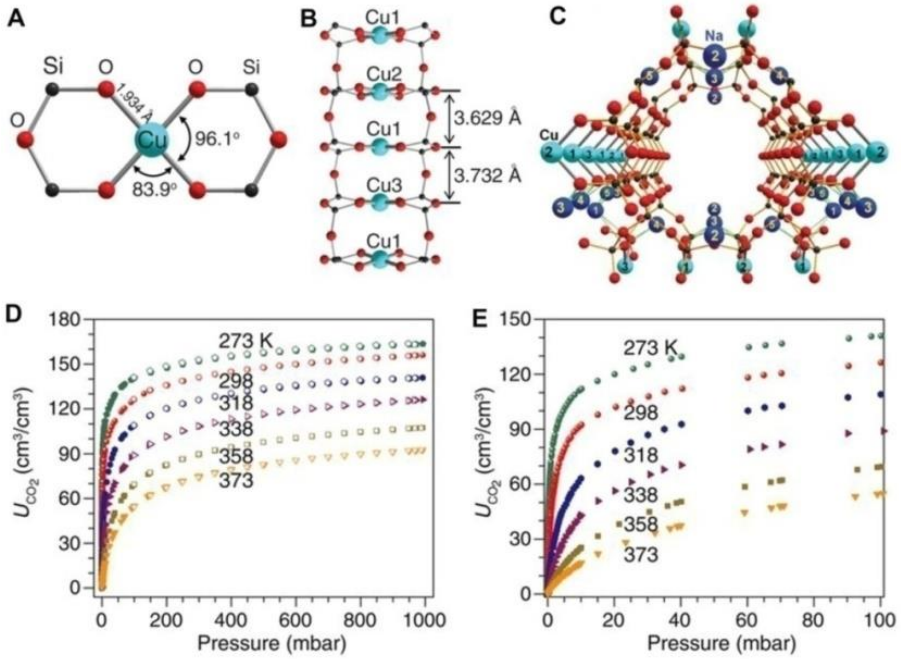

Figure 1.12. (A) The fundamental secondary building unit, $[CuO_4]$ in square planar geometry (B). $[CuO_4]$ columnar stack in side view. (C) Five different Na ions in the channel. (D) CO_2 adsorption isotherms of SGU-29 up to 1000 mbar. (E) CO_2 adsorption isotherms of SGU-29 up to 100 mbar *(Adopted from ref. 135 with permission from The American Association for the Advancement of Science).*

This material, SGU-29 with the composition $Na_2CuSi_5O_{12}$ forms as a pure phase in bulk quantities. The structure consists of $Cu^{(II)}$ ions which exist in a square planar geometry (Fig.

1.12A). Each CuO_4 square plane is linked to four surrounding SiO_4 tetrahedra (Fig. 1.12B). These CuO_4 square planar units are arranged in a near parallel fashion to each other with the typical distances of 3.629 and 3.732 Å (Fig. 1.12B). Five crystallographically distinct Na^+ ions are present in this structure; the positions are shown in figure 1.12C. Na2 is positioned at the cross section of two channels, and Na3 is connected to four different O atoms which are bound to $Cu^{(II)}$ ions from the side of the channel. Now both Na2 and Na3 will be able to interact with guest molecules incorporated into the channels. The channel present in SGU-29 has an effective window size of 4.5 × 7.3 Å.

This material showed some interesting CO_2 capture characteristics. It exhibited very high CO_2 uptake at low partial pressures relevant to post-combustion capture. The CO_2 adsorption isotherms of SGU-29 in the pressure range of 0 to 1 bar and 0 to 0.1 bar at different temperatures (between 273 and 373 K) are presented in figure 1.12D and 1.12.E, respectively. When the CO_2 uptake at 0.1 bar was compared with some of the best performing materials, SGU-29 beats even the best performing materials MgMOF-74. The CO_2 heat of adsorption (~ 50 kJ/mol) for SJU-29 was very much similar to the NaX, the best performing zeolite till date. This material exhibited remarkable thermal stability (up to 550^{o}C in open air). This remarkable stability and exceptionally high CO_2 uptake makes this material a superior candidate for post combustion CO_2 capture or even for air capture.

1.3.6. Magnesium-4,4′-Bipyridine-N,N′-dioxide-Terephthalate Based Um-MOF:

Cheap and less toxic porous MOFs that can adsorb large quantities of CO_2 with high selectivity are highly desirable for carbon capture applications. In this context, utilization of Group II ($Mg^{(II)}$ and $Ca^{(II)}$) ions as building blocks can offer inexpensive materials that further add to biocompatibility. However, example of $Mg^{(II)}$ and $Ca^{(II)}$ MOFs are extremely narrow as compared to the transition metals. This is most likely due to unavailability of neutral bridging linkers for these metal ions. Recently, Nakamura and co-workers have reported a neutral and charge polarized bridging linker, 4,4′-bipyridine-N,N′-dioxide (bpdo), as a promising partner for $Mg^{(II)}$ and $Ca^{(II)}$ ions.[136] They have successfully synthesized and characterized three-dimensional $Mg^{(II)}$ and $Ca^{(II)}$ MOFs. These MOFs, $\{[Mg_2(1,4\text{-bdc})_2(bpdo)]\cdot 2DMF\}_n$ and $\{[Ca(1,4\text{-bdc})(bpdo)]\cdot 0.5DMF\}_n$ were synthesized as phase pure compounds via a solvothermal reaction of $MgCl_2\cdot 6H_2O$ or $Ca(NO_3)_2\cdot 4H_2O$ with 1,4-benzenedicarboxylic acid (1,4-H_2bdc) and bpdo in N,N-dimethylformamide (DMF).

In case of the Mg-MOF, the $Mg^{(II)}$ is octahedrally coordinated with four O atoms from 1,4-bdc and another two O atoms from the bpdo linker (Fig. 1.13A). These corner-shared MgO_6 units are connected with each other by both the organic moieties and thereby form infinite chains. These chains are then linked by both bpdo and 1,4-bdc linkers, giving rise to a three-dimensional porous network having one-dimensional channels (Fig. 1.13B), channel size: 4.5 × 4.1 $Å^2$).

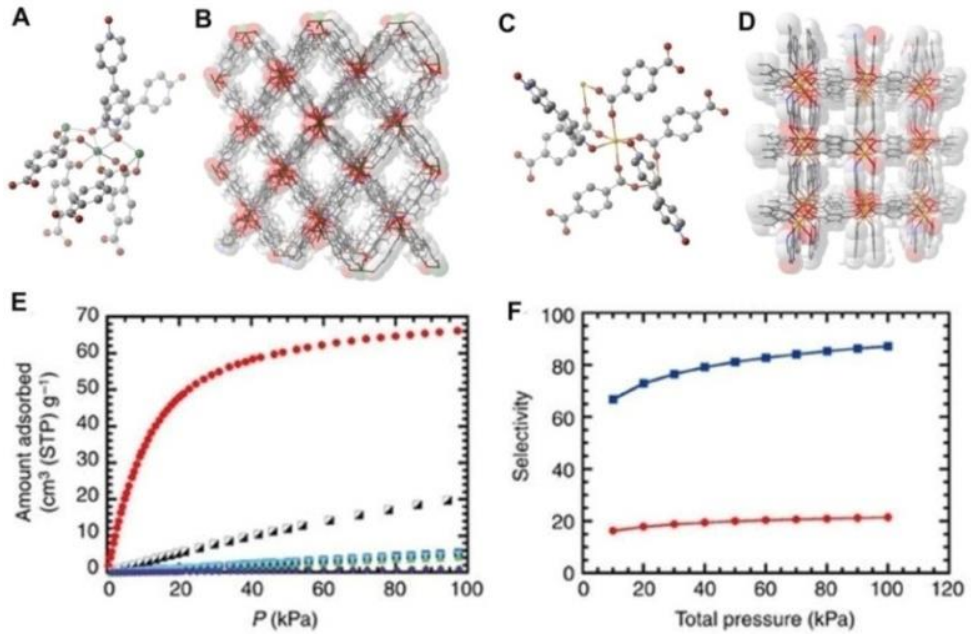

Figure 1.13. (A) Coordination environment around the $Mg^{(II)}$ ions present in {[Mg_2(1,4-bdc)$_2$(bpdo)]·2DMF}$_n$. (B) Three-dimensional view of {[Mg_2(1,4-bdc)$_2$(bpdo)]·2DMF}$_n$ showing one dimensional channel. (C) Coordination environment around the Ca(II) ion present in {[Ca(1,4-bdc)(bpdo)]·0.5DMF}$_n$. (D) Three-dimensional view of {[Ca(1,4-bdc)(bpdo)]·0.5DMF}$_n$. Colour code: Green-Mg; orange-Ca; red-O; blue-N; grey-C; and white-H. (E) CO_2 (red circle), CH_4 (black half-filled square), N_2 (blue square), O_2 (green triangle), Ar (sky-blue inverted triangle) and H_2 (purple rhombus) isotherms for [Mg_2(1,4-bdc)$_2$(bpdo)]$_n$ at 298 K. (F) CO_2/CH_4 and CO_2/N_2 selectivity calculated using Ideal adsorbed solution theory (*IAST*) in [Mg_2(1,4-bdc)$_2$(bpdo)]$_n$ (gas composition used; CO_2:CH_4=40:60 and CO_2:N_2=10:90 *(Adopted from ref. 136 with permission from Nature Publishing Group).*

In case of the Ca-MOF, the $Ca^{(II)}$ ions are octahedrally coordinated with four O atoms of 1,4-bdc and two O atoms from bpdo linker very similar to Mg MOF but arranged in a cis fashion (Fig. 1.13C). The CaO_6 octahedral building units are further connected with each other via two carboxylate units thereby forming one-dimensional $Ca^{(II)}$ chains. These chains are linked by 1,4-bdc linkers, generating a 2D layered network which are further linked by bpdo linkers, giving rise to a 3D framework having one-dimensional channels (Fig. 1.13D, channel size: 3.4 × 3.2 $Å^2$). Thus the Mg and Ca MOFs are slightly different in their construction, but both yield a framework with one-dimensional ultra-microporous channels.

Among these two Um-MOFs only the Mg-MOF showed interesting low pressure CO_2 capture ability. Mg-MOF exhibited 3.0 mmol/g of CO_2 uptake at ambient condition (298 K and 1 bar) as presented in figure 1.13E. Although it adsorbed reasonable amount of CH_4, the uptake for N_2, O_2 and H_2 was negligible (Fig. 1.13E). This resulted in appreciable CO_2/N_2 (90 calculated from *IAST*) and CO_2/CH_4 (20 calculated from *IAST*) selectivities at ambient conditions (Fig. 1.13F). Further the ability of this Um-MOF to separate CO_2 from CH_4 or N_2 was established by dynamic breakthrough analysis. Mg-MOF has slightly larger ultra-micro pore, while Ca-MOF due to slight decrement in pore dimension becomes less porous compared to Mg-MOF.

1.3.7. Zinc-terephthalate bpNDI Based Um-MOF:

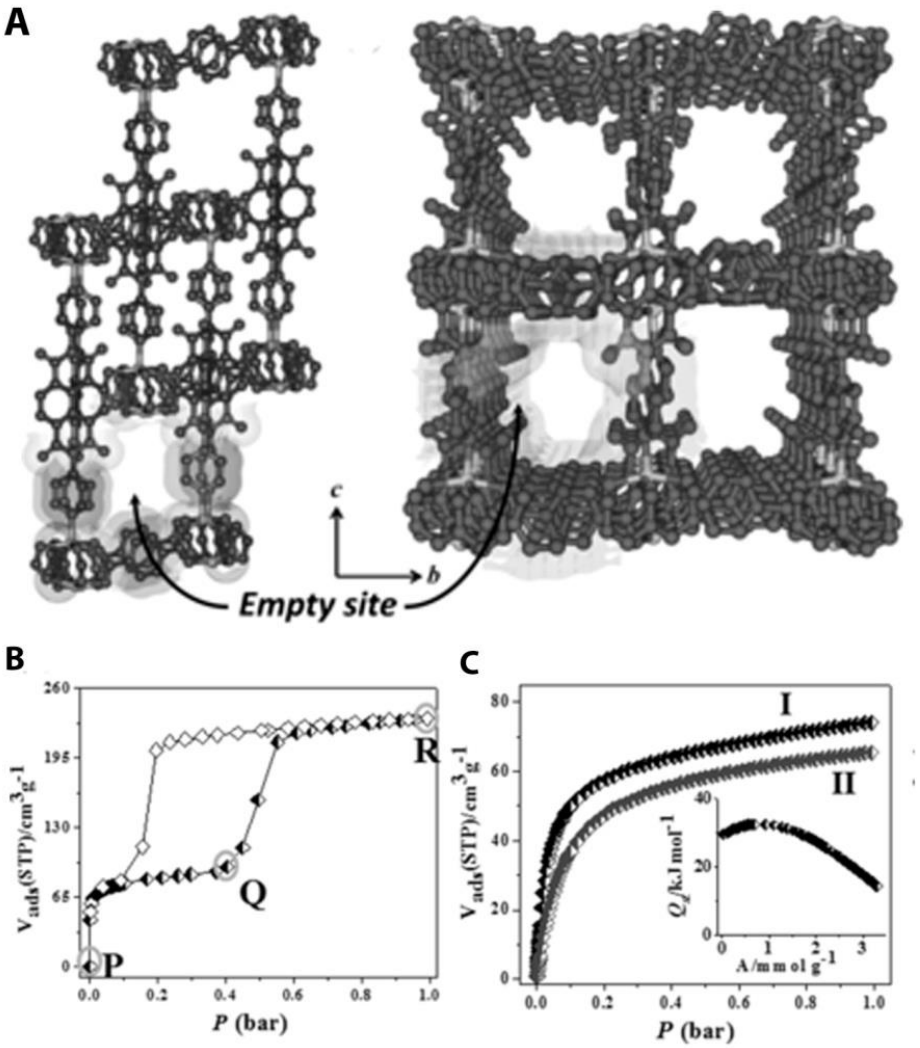

Figure 1.14. Structural details of compound 1: (A) two-fold entangled nets and pore view along the a direction. CO_2 adsorption isotherms: (B) at 195 K (C) at 273 (I) and 298 K (II). Inset: isosteric heat of adsorption plot *(Adopted from ref. 137 with permission from John Wiley and Sons).*

Sikder *et al.* reported a two-fold entangled dynamic framework $\{[Zn_2(bdc)_2(bpNDI)]\cdot 4DMF\}_n$ (1; where bdc = 1,4-benzenedicarboxylate, bpNDI = N,N'-bis-(4-pyridyl)-1,4,5,8-naphthalenediimide) with pore surface carved with polar functional groups and aromatic π clouds.[137] These properties in the MOF have been exploited for selective capture of CO_2 at ambient condition. This compound was synthesized via a typical solvothermal reaction of $Zn(NO_3)_2\cdot 6H_2O$, H_2bdc and bpNDI in DMF at 95°C for 3 days. Single crystal structure analysis revealed that it is a two-fold entangled 3D pillared-layer framework with α-polonium type topology. The structure is built from a $\{Zn_2(COO)_4\}$ paddle wheel secondary building units (SBUs). These SBUs are connected via bdc linkers to generate a 2D square grid along bc plane (Fig. 1.14A). The pillaring of the 2D network by bpNDI results in an extended 3D network.

It showed very interesting gas adsorption properties. The framework displayed stepwise CO_2 and C_2H_2 uptake at 195 K. However, at 298K, both the gases showed type I behaviour (Figs. 1.14B and C). The framework did not show appreciable CH_4 uptake at room temperature which gave rise to a huge selectivity of CO_2 over CH_4 (598 at 298 K) as predicted from *IAST*. This selectivity is the highest reported to date among all the MOFs without open metal sites.

1.3.8. Aminoclay Supported Um-MOF:

Chakraborty *et al.* reported a 2D F-MOF, {[Cu(pyrdc)(bpp)](5H_2O)}n (Flexible MOF; F-MOF1, where pyrdc= pyridine-2,3-dicarboxylate; bpp=1,3-bis(4-pyridyl)-propane) with a pillared-bilayer structure.[138] Single crystal structure revealed that it is a 2D pillared-bilayer type of framework where a 2D honeycomb layer is extended by the bpp linker (Fig. 1.15A). The bpp linker shows conformational flexibility along the –(CH_2)– chains. Also, F-MOF1 showed structural contraction upon removal of the guest water molecules (Fig. 1.15A). F-MOF1 displayed gate-opening behaviour at 298 K and 273 K in the presence of CO_2 (Figs. 1.15C and D). Also, the authors demonstrated a new and facile method to stabilize F-MOF nanocrystals on an aminoclay (AC) support and studied their tuneable, enhanced gas adsorption and separation properties (Fig. 1.15). Interestingly the gas uptake of this flexible MOF was found to be increased upon stabilizing the framework on aminoclay support (Figs. 1.15C and D). Such studies involving composites with hierarchal porosities provide significant contributions to developing superior sorbents.

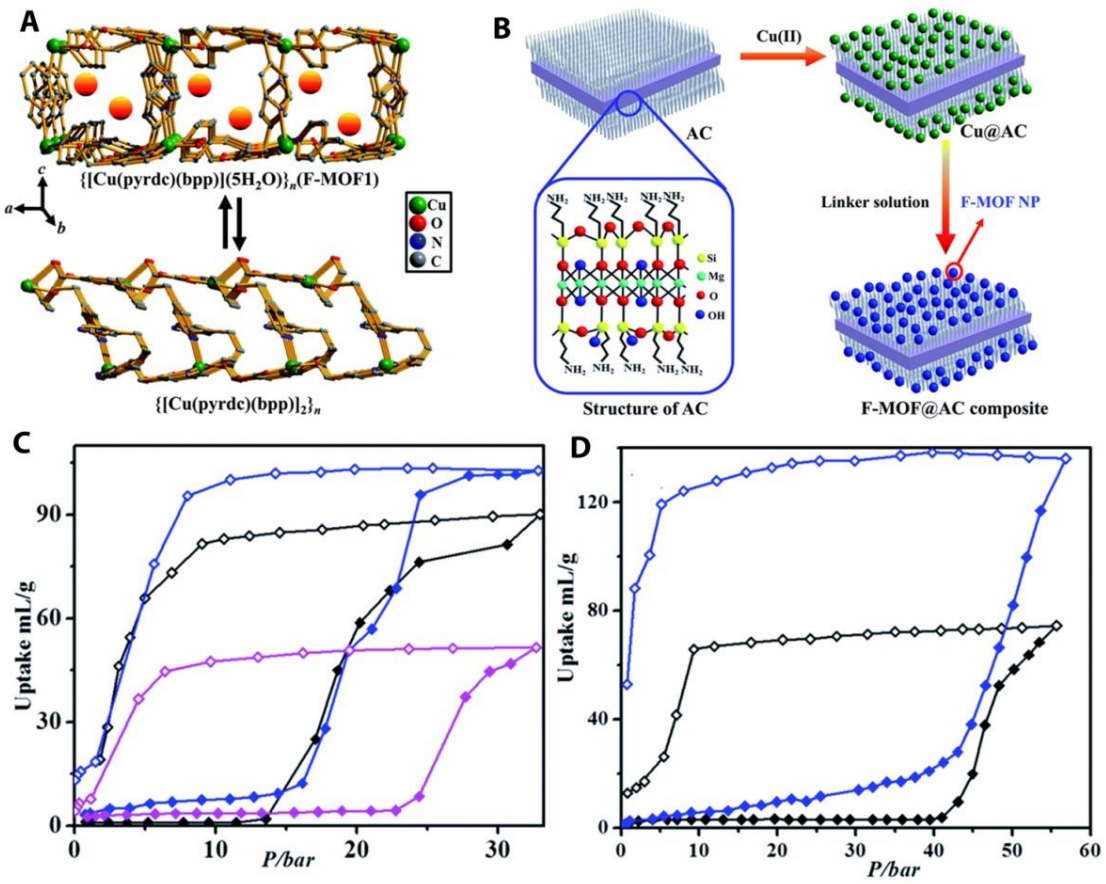

Figure 1.15. (A) Guest-induced structural transformation in F-MOF1. (B) The structure of AC and the schematic of the stepwise formation of F-MOF@AC composites. High pressure CO_2 adsorption isotherms at (C) 273 K and (D) 298 K. Color code: F-MOF1: black, AC: red, F-MOF1@AC-1: blue *(Adopted from ref. 138 with permission from Royal Society of Chemistry).*

1.3.9. Zinc-aminoterephthalate-bpmh Based Um-MOF:

Parshamoni *et al.* reported a new $Zn^{(II)}$-based metal organic frameworks (MOFs), namely, $[Zn(2\text{-}NH_2BDC)(4\text{-bpmh})]_n \cdot n(EtOH)$ (2) (2-NH_2BDC = 2-aminoterephthalic acid, 4-bpmh = N,N-bis-pyridine-4-ylmethylene-hydrazine).[139] This material was synthesized via the slow diffusion technique employing 4-bpmh and 2-aminoterephthalic acid as the linker at room temperature. Structural analysis revealed that compounds have 3D networks with diamondoid (dia) topologies and exhibit 6-fold interpenetration (Fig. 1.16). Gas adsorption studies disclosed that it adsorbs good amount of CO_2 at 273 K and 298 K. However the CH_4 uptakes at these temperatures are very less (Fig. 1.16E). This indirectly indicated that the material is capable of selectively adsorbing CO_2 over CH_4. However, true selectivity was not calculated using *IAST* model.

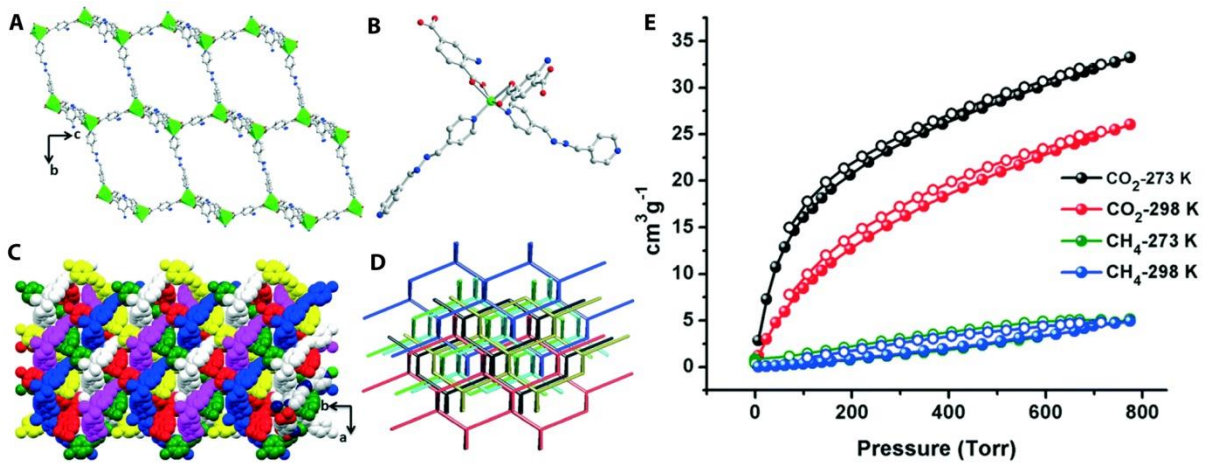

Figure 1.16. (A) Illustration of 3D porous framework found in 2. Color code: oxygen (red), nitrogen (blue), carbon (light gray) and zinc (green). (B) A view of SBU found in compound 2. (C) Illustration of the 6-fold interpenetrated 3D network. (D) A view of the diamondoid (dia) net topology with the Schläfli point symbol $\{6^6\}$. (E) Gas adsorption isotherms of compound 2 at 273 K and 298 K *(Adopted from ref. 139 with permission from Royal Society of Chemistry)*.

1.3.10. Amine Functionalized Cu Based MOF:

Sharma *et al.* reported a porous $Cu^{(II)}$-MOF that showed very high (60 wt%) CO_2 uptake at 298 K and 32 bar.[140] This MOF $\{[Cu_6(L)_3(H_2O)_6]\cdot(14DMF)(9H_2O)\}n$ (1) was synthesized as a pure phase via a solvothermal reaction of copper nitrate and amine functionalized tetra carboxylic acid ligand. The single crystal structure revealed that the framework is built from a typical paddle-wheel $Cu_2(COO)_4$ SBUs where each Cu(II) ion adopted a distorted square-pyramidal geometry. The framework contains large near-spherical of diameter ~11 Å (Fig. 1.17A). The amine groups in the linkers were free as anticipated. The three dimensional structure consists of porous channels along the a-axis (Fig. 1.17B).

This material shows typical type-I N_2 isotherm at 77 K which yielded a BET surface area of 1480 m^2/g. Also, the material showed interesting CO_2 adsorption behaviour both at low as well as high pressure. It showed a CO_2 uptake of 90 cc/g at 298K and 1 bar. However, it displayed much higher CO_2 uptake (290 cc/g) at 298K and 32 bar (Figs. 1.17C and D). This high CO_2 capacity of this MOF could be effective for separation of gas mixtures which normally exist at high pressure. However, such high uptake at ambient pressure is not so beneficial when considered for a pressure swing adsorption application. For example, to achieve a high working capacity for a 10 to 1 bar PSA, the material needs to have low capacity at 1 bar and very high capacity at 10 bar.

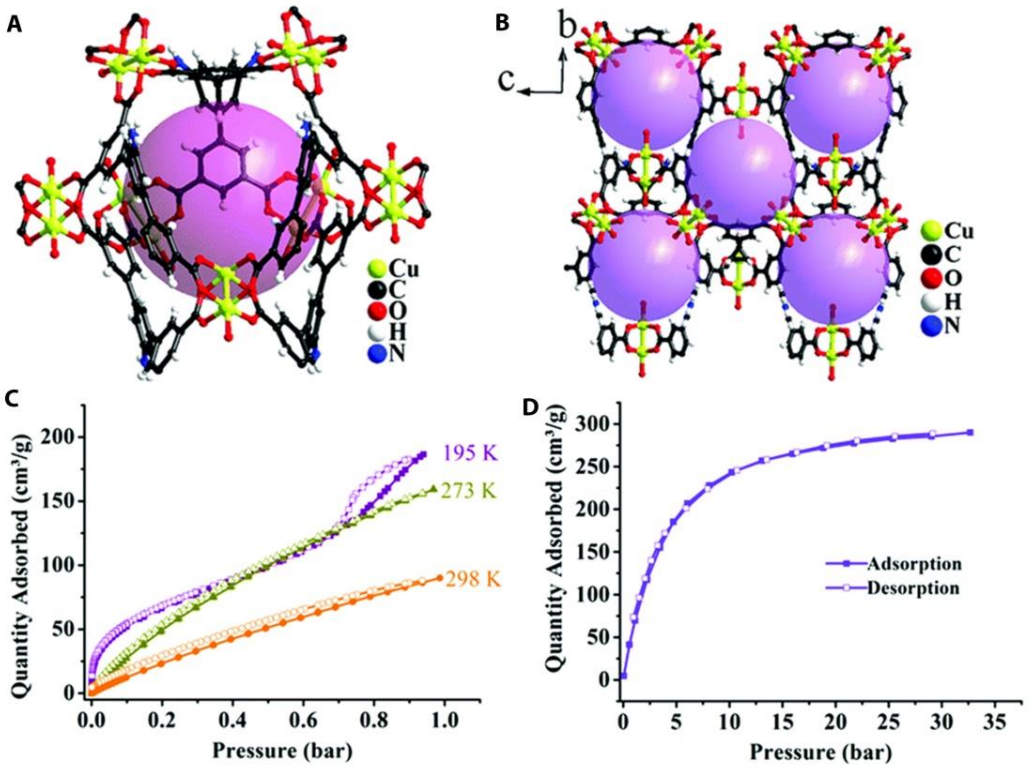

Figure 1.17. (A) Spherical cage in $\{[Cu_6(L)_3(H_2O)_6]\cdot(14DMF)(9H_2O)\}n$ (B) view along the a-axis showing porous channels. (C) CO_2 physisorption isotherms at 195, 273 and 298 K up to 1 bar pressure. (D) CO_2 physisorption isotherms at 298 K up to 32 bar pressure *(Adopted from ref. 140 with permission from Royal Society of Chemistry)*.

1.3.11. Co-SDB Based Water Stable Um-MOF:

Pal *et al.* reported a 2-fold interpenetrated water stable microporous MOF for selective CO_2 capture.[141] A cobalt based MOF $\{[Co_2(SDB)_2(L)]\cdot(H_2O)_4\cdot(DMF)\}_n$, (IITKGP-6) was successfully synthesized from the combination of a bent dicarboxylate linker 4,4′-sulfonyldibenzoic acid (H_2SDB), flexible N,N-donor spacer 1,4-bis(4-pyridyl)-2,3-diaza-1,3-butadiene (L) and $Co(NO_3)_2\cdot6H_2O$ via a solvothermal reaction. The structure of the MOF is built from a di-nuclear paddlewheel type SBU (Fig. 1.18A). When these SBUs get connected via the spacer, it generates the layered framework. In actual structure these layers are present with 2 fold interpenetration. However, IITKGP-6 still showed lozenge-shaped channels (3.4 × 5.0 $Å^2$) along [1 1 0] direction (Fig. 1.18B). This framework displayed high thermal and hydrolytic stability. The desolvated phase of IITKGP-6 exhibited modest CO_2 uptake (50.6 and 37.4 cc/g at 273 and 295 K respectively) as shown in figure 1.18C and D. However, it displayed low N_2 and CH_4 uptake at similar condition which resulted in a high CO_2/N_2 and CO_2/CH_4 selectivity.

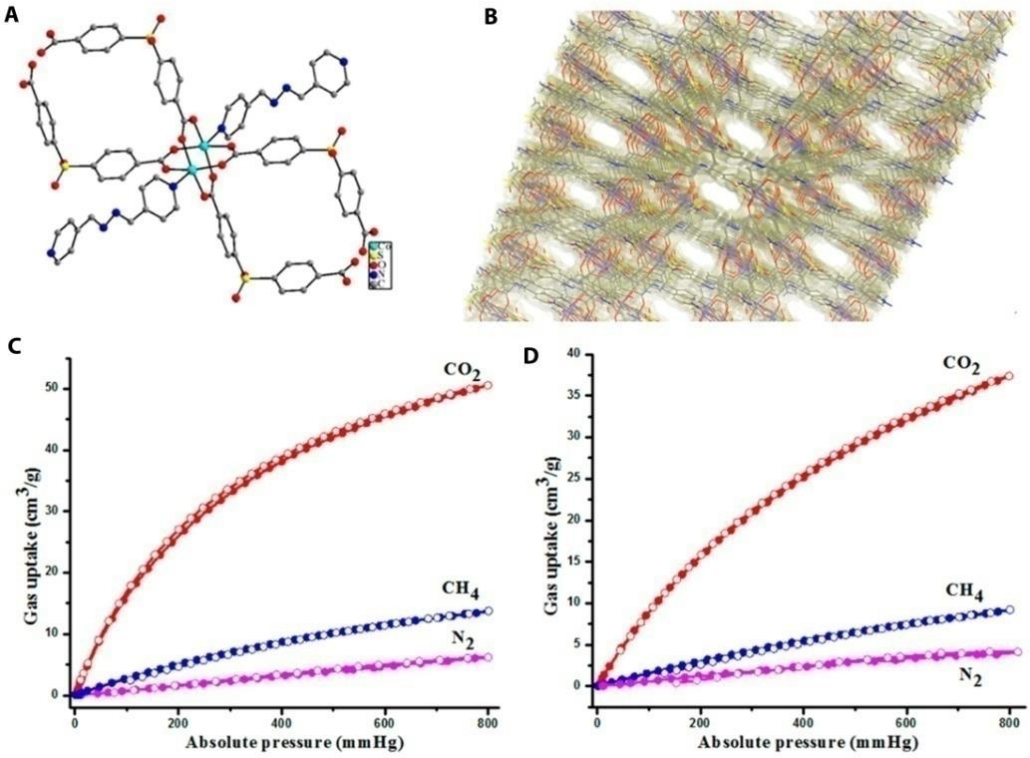

Figure 1.18. (A) View of paddle-wheel unit and surrounding environment in IITKGP-6. (B) Packing diagram showing pore surfaces decorated with SO_2 functionality along [1 1 0] direction.CO_2, CH_4, and N_2 sorption isotherms of IITKGP-6a (C) at 273 K and (D) at 295 K (CO_2: red, CH_4: blue, N_2: magenta) *(Adopted from ref. 141 with permission from American Chemical Society)*.

1.3.12. 4-Pyridine Carboxylate (4-PyC) or Isonicotinate Based MOFs:

As mentioned earlier, we are looking for a rigid ultra-microporous MOFs build up from short linkers. There are several short linkers such as oxalate, aminotriazolate, triazolate, imidazolate, pyrazine, isonicotinate etc. for construction of MOFs. However, most of the linkers are well explored in the construction of different structural motifs. But, a thorough literature survey revealed that relatively fewer reports are found for isonicotinate based Um-MOFs of which very few have been investigated for their CO_2 capture applications.

The above examples bring out the fact that the tight binding pockets provided by the ultra-micropores are very effective for selective CO_2 capture. The dimensions of isonicotinate units are quite comparable to many of the above mentioned ligands and they have a mildly basic character which should favour optimal interactions with CO_2 and they are readily available and cheap. Considering these facts, we chose isonicotinate as a linker for the construction of rigid Um-MOFs. In the following sections, some of the isonicotinate based MOFs which had been applied for CO_2 capture applications are presented.

1.3.12.1. Cobalt-isonicotinate MOF:

Moushi *et al.*[142] have reported a Co isonicotinate based MOF where they investigated CO_2 capacity and the separation ability from a CO_2/CH_4 mixture. They have successfully synthesized a pure phase of the MOF with the molecular formula $\{[Co_9(INA)_{18}(H_2O)_6]\cdot 11DMF\cdot 15H_2O\}$, where INA = isonicotinate. The repeating unit consists of four $[Co^{II}_2(\mu\text{-}O_2CR)_2(\mu\text{-}H_2O)]$ subunits which are linked via bridging isonicotinates coordinated to another isolated Co octehedra as depicted from the assymmetric unit presented in figure 1.19A.

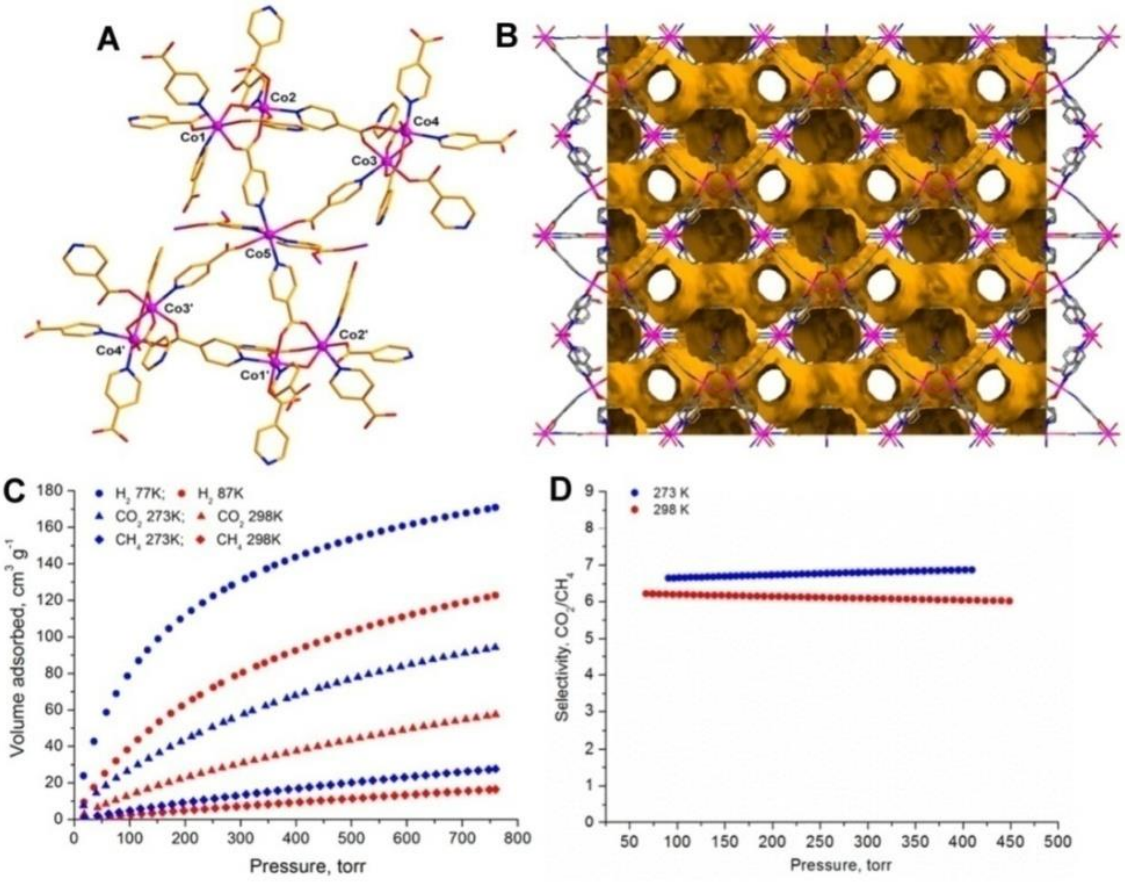

Figure 1.19. (A) The repeating unit showing the water molecule bridging between two Co. (B) Connoly surface diagramme of the MOF showing 1D channel. (C) Gas adsorption isotherms at different temperatures. (D) CO_2/CH_4 selectivities at 273 K and 298 K *(Adopted from ref. 142 with permission from American Chemical Society)*.

Thus it forms a rigid 3D porous structure as presented in figure 1.19B. The Ar adsorption at 77 K confirmed its permanent porosity with a BET surface area of 910 m^2/g. It displayed moderate CO_2 capacities of 4.2 mmol/g and 2.6 mmol/g at 273 and 298 K, respectively (Fig. 1.19C). However, low CH_4 uptake (1.2 mmol/g at 273 K, 0.7 mmol/g at 298 K) at similar conditions suggests this to be a potential candidate for CO_2/CH_4 separation. The *IAST*

calculation predicted the CO_2/CH_4 selectivity to be ~7 at both temperatures (Fig. 1.19D). These selectivity values are quiet moderate.

Cobalt is also well known to form clusters with μ^3-OH. One of such clustuer based MOF, $\{[Co_6(\mu^3\text{-}OH)_4(INA)_8](H_2O)_{10}(DMA)_2\}_n$, involving isonicotinic acid has been reported by Du and co-workers.[143] In this article, they studied selective adsorption of C_2H_2 over CO_2 and CH_4. The structure consists of hexanuclear Co clusters formed by 3 crystallographically independent Co centres (Fig. 1.20A). The assymetric unit contains three crystallographically independent $Co^{(II)}$ ions, four isonicotinate units and two μ^3-OH cluster. Co1 and Co2 are coordinated by three carboxylate O atoms and two pyridyl nitrogenatoms from five different isonicotinates. The sixth coordination is filled by bridging hydroxyl.

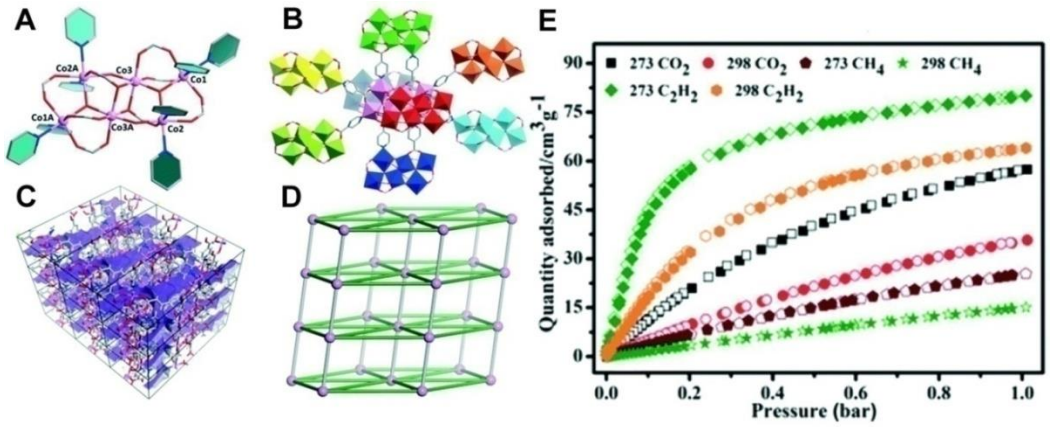

Figure 1.20. (A) The Co_6 cluster present in the MOF (B) Eight-connected Co_6 cluster (c) A side view of the 2D honeycomb channels (D) Hex topological representation generated by converting the clusters to a nodes. (E) Sorption isotherms at different temperatures *(Adopted from ref. 143 with permission from Royal Society of Chemistry)*.

Where as Co3 is surrounded by three carboxylates from isonicotinate and three μ^3-OH units. Co_6 clusters are now connected to six adjacent clusters with six different isonicotinate (Fig. 1.20B) forming a triangle-tessellated layer which created trigonal window along the ab plane. This layers are then pillared by four isonicotinate along c axis thereby generating a 3D network (Figs. 1.20C and 1.20D). Permanent porosity was confirmed by N_2 adsorption at 77 K which showed a type I isotherm with BET surface area of 631 m^2/g. Pore size distribution based on the Horvath–Kawazoe method revealed a distribution of micropores at 4.6 to 5.8 Å. Although, this small pore MOF displayed preferential C_2H_2 uptake (64 cc/g) over CO_2 (34 cc/g) at 298 K and 1 bar, the selectivity (3.4 at 298 K) is poor (Fig. 1.20E).

Recently, Pachfule *et al.* reported the gas adsorption properties of metal organic frameworks (MOFs) derived from the isonicotinic acid (INA) and the fluorinated INA.[144]

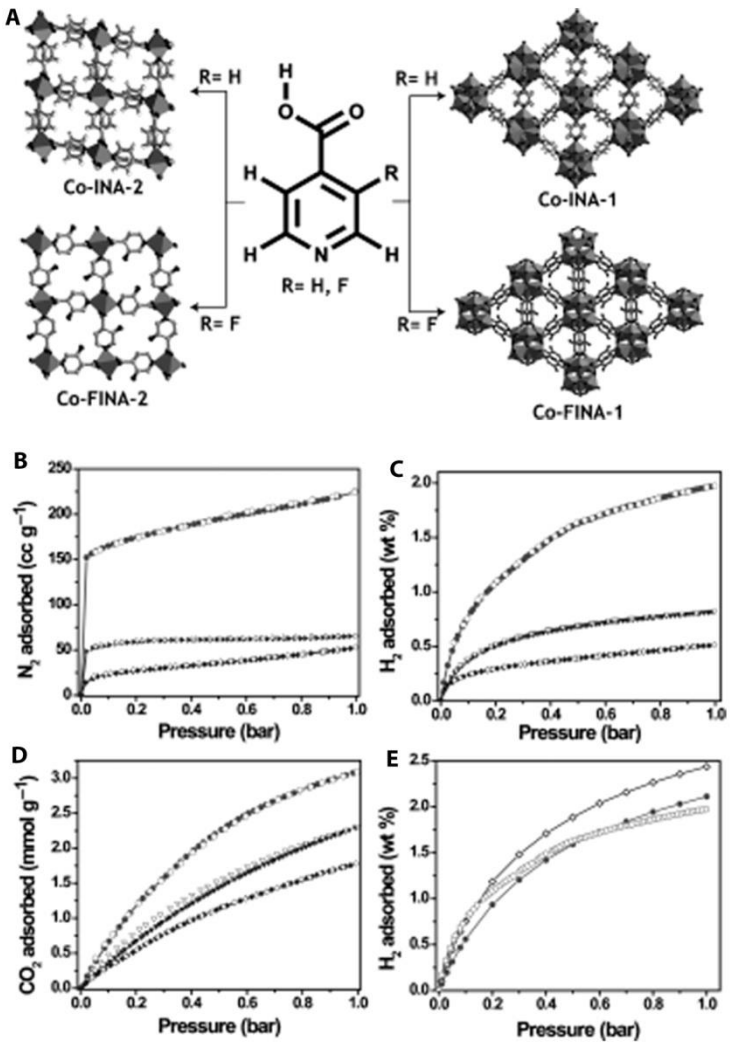

Figure 1.21. (A) Structures of fluorinated and non fluorinated MOFs derived from 3-fluoroisonicotinic acid (FINA) and isonicotinic (INA) acid along with Co^{II} as a metal center. Guest and coordinated solvent molecules are omitted for clarity. Gas adsorption isotherms of Co-FINA-1, Co-FINA-2, and Co-INA-2: (B) N_2 (•=Co-FINA-1; ▸=Co-FINA-2; ♦=Co-INA-2), (C) H_2 (•=Co-FINA-1; ▾=Co-FINA-2; ♦=Co-INA-2), and (D) CO_2 (•=Co-FINA-1; ▾=Co-FINA-2; ♦=Co-INA-2) adsorption isotherms. Filled and open branches represent adsorption and desorption, respectively. (E) Simulated and experimental adsorption isotherms of H_2 in Co-FINA-1 (•; ○) and Co-INA-1 (◊) at 77 K. The open symbols are from experimental results and the filled symbols are from simulation data *(Adopted from ref. 144 with permission from John Wiley and Sons).*

In this work they have successfully synthesized 4 new Co based MOFs using INA and fluorinated INA. Co-INA-1, ($[Co_3(INA)_4(O)(C_2H_5OH)_3][NO_3]\cdot C_2H_5OH\cdot 3\,H_2O$;) and Co-INA-2, ($[Co(INA)_2]\cdot$DMF) are structural isomers (Fig. 1.21A). Similarly, Co-FINA-1 ($[Co_3(FINA)_4(O)(C_2H_5OH)_2]\cdot H_2O$; FINA = 3-fluoroisonicotinic acid) and Co-FINA-2 ($[Co(FINA)_2]\cdot H_2O$) are structural isomers. Furthermore, Co-INA-1 and Co-FINA-1 are isostructural as are Co-INA-2 and Co-FINA-2 (Fig. 1.21A). The structure of Co-INA-2 and

Co-FINA-2 is composed of doubly-bridged infinite $Co^{(II)}$ carboxylate chains. The pyridyl groups of the INA and FINA linkers point outwards from the chains and the resulting chain is cross-linked by N-Co coordination to create the 3D frameworks having square channel along c axis. However, the structure of Co-INA-1 and Co-FINA-1 is composed of the trinuclear-oxo cluster and each $[Co_3(O)]$ metal cluster is connected to eight INA/FINA linkers through four bridging μ^2-carboxylates, four pyridyl N, two coordinated EtOH, and one coordinated water. These clusters are connected to the eight neighbouring SBUs resulting in a 3D framework with a channel of dimension 4.2 Å along the a axis and a square-shaped channel (3.2×2.8 $Å^2$) along c axis (Fig. 1.21A).

The gas adsorption behaviour of these MOFs displayed some interesting observation. It has been observed that for Co-FINA-1 and -2, fluorine insertion has increased the surface area compared to the non fluorinated analogues (Fig. 1.21B). All these MOFs showed reversible CO_2 and H_2 uptake at 298 K and 77 K respectively (Figs. 1.21C, D and E). Among all the 4 MOFs Co-FINA1 exhibited high CO_2 uptake (3.1 mmol/g) at room temperature. However, the stability of this fluorinated MOFs was not investigated. Usually fluorinated ligands because of the withdrawn electron density by the F atoms coordinate with metal weakly compared to non fluorinated ligands.

1.3.13. 4-PyC Containing Mixed Ligand MOFs and Their CO_2 Capture Characteristics:

1.3.13.1. Zinc-Adenine-Isonicotinate MOF:

Zeolite Imidazolium Frameworks (ZIFs) which mimics the structure of zeolites is one of the most investigated MOFs for different purposes. ZIFs are structurally constructed by tetrahedrally coordinated di-valent metal ions and imidazolate linkers. However, the choice of frameworks with just imidazolate linker is limited. To expand the library, attempts have been made to replace imidazolate ligand with mono-negatively charged ligands. For example, adenine, which offers similar coordination atmosphere, is one of the potential candidates.

Wang *et al.*[145] first reported adenate and isonicotinate based mixed ligand MOF, TIF-A1 with a molecular formula [Zn(ad)(int)](DMF) and studied its CO_2 adsorption behaviour. Similar to ZIFs, in this MOF, $Zn^{(II)}$ is tetrahedrally coordinated by two adenine ligands and two isonicotinate ligands (Fig. 1.22A). Nitrogens from two five membered rings bridge between two $Zn^{(II)}$ resulting in infinite 2_1 helices along c- axis (Fig.1.22B). Both right handed and left handed helices coexist in the crystal structure. These helices are now connected via

isonicotinate to generate the 3D framework which possesses large rhombic channels with dimensions of 8.0 x 7.0 $Å^2$ along the c-axis as displayed in figure 1.22C and 1.22D.

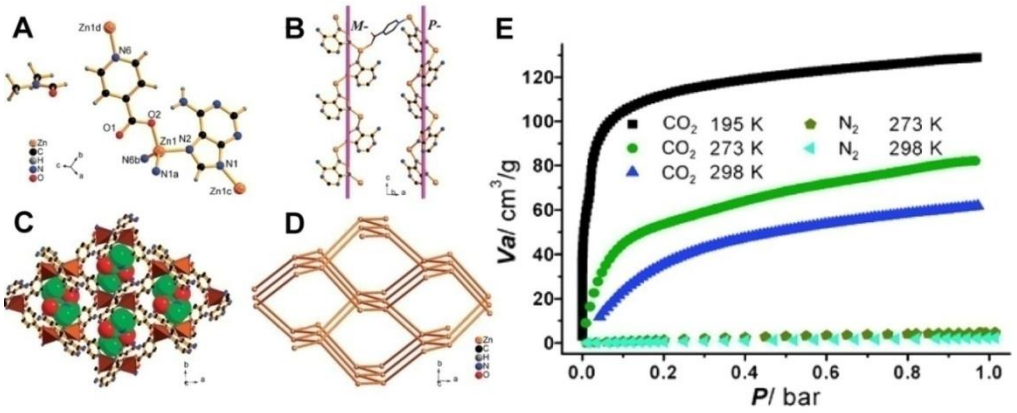

Figure 1.22. (A) Coordination environment around $Zn^{(II)}$ (B) The zigzag Zn-adenine helices (C) 3D framework with DMF inside the pore (D) dmp topology present in the MOF. (E) CO_2 and N_2 adsorption isotherms at different temperatures *(Adopted from ref. 145 with permission from Royal Society of Chemistry)*.

The CO_2 adsorption isotherms at different temperatures revealed high capacity of 82.2 cc/g (3.67 mmol/g) at 273 K and 61.7 cc/g (2.75 mmol/g) at 298 K (Fig. 1.22E). In comparison, ZIF-69 possesses the maximum CO_2 capacity of 70 cc/g at 1 bar at 273 K.[146] The authors attributed the high CO_2 uptake mainly to three factors, (1) Isonicotinate as a rigid aromatic molecule provides stable and permanent porous framework, (2) Adenine can provide imidazolate coordination environment as ZIFs, (3) Uncoordinated amino and pyrimidine groups provide Lewis basic sites for adenine-guest interactions. These observations have provided some key insights for the design and synthesis of newer MOFs with varied compositions.

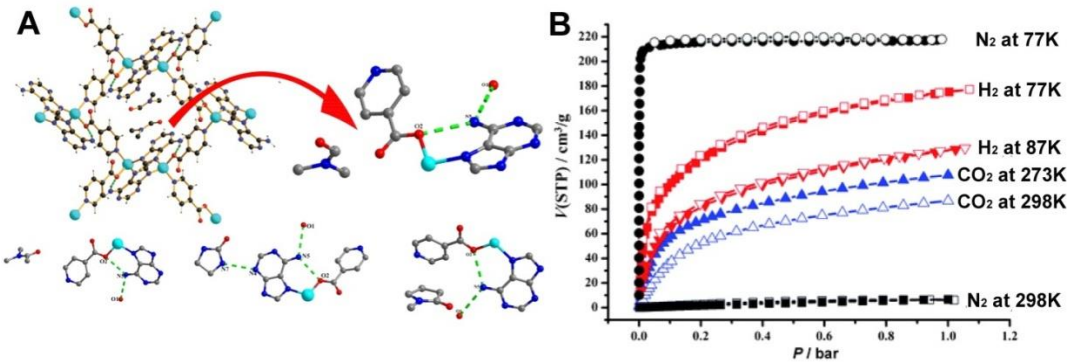

Figure 1.23. (A) Crystal stucture of the MOF showing H-bonding interaction between the guest molecules and the framework. (B) Gas adsorption isotherms at different temperatures *(Adopted from ref. 147 with permission from Royal Society of Chemistry)*.

Wang *et al.*[147] reported guest selectivity during the crystallization of the Zn- adenine-isonicotinate MOF. The order of the guest selctivity is DMF > e-urea > NMP > DMA. The guest is hydrogen bonded with the uncoordinated amine group of the adenine moiety as shown in figure 1.23A. The guests seem to play both structure directing as well as templating role. However, the guest could be post-synthetically exchanged with low boiling solvents such as methanol, DCM etc. The methanol exchanged phase exhibited high H_2 and CO_2 adsorption capacity (4.81 mmol/g at 273 K and 3.87 mmol/g at 298 K) and remarkable selectivity towards CO_2 over N_2 as observed from figure 1.23B. Isosteric heat of adsorption for CO_2 obtained for this methanol exchanged phase was 31.0 kJ/mol which is optimal for facile regeneration.[148] The high CO_2/N_2 selectivity (90 obtained from *IAST* model) makes this material a potential solid sorbent for post-combustion CO_2 capture.

1.3.13.2. Cobalt-Isonicotinate-Tetrazolyl Benzoate Based Um-MOF:

In continuation with their previous work as discussed earlier, Du and coworkers[149] reported a Cobalt-TZB-INT (TZB = 4-Tetrazolyl benzoate and INT = Isonicotinate) based MOF, $\{[Co_5(\mu_3\text{-}OH)(INT)_3\text{-}(H_2O)_2(TZB)_3](DMA)_8\}_n$, for selective CO_2 capture. The structure consists of $Co_3(\mu^3\text{-}OH)$ clusters linked by TZB ligands forming a hexagonal honycomb channel along c axis. Each $Co^{(II)}$ ion is six-coordinated with two carboxylate O-atoms from the TZB ligands, two N-donors from the tetrazole rings of other TZB ligands, one N atom from INT, and one μ^3 bridging OH (Fig. 1.24A). Each $Co_3(\mu^3\text{-}OH)$ core is connected with six TZB linkers to construct a 3D porous framework with large hexagonal honeycomb channels running along the c axis, with an aperture size of approximately 14 Å. The INT connected to the trimeric clusters are running through the middle of the hexagonal channel. The other end of the INT connects to a six coordinated Co ion which is having two water molecules. This $CO(INT)_4(H_2O)_2$ sits exactly at the centroid of the larger hexagonal channel partioning the larger channel to six smaller trigonal channel (dimension ~5 Å) as shown in figure 1.24B. Figure 1.24C displayed the side view of the nano channel present in the crystal structure. Figure 1.24D showed the $\{[Co_2(H_2O)_2]_3[Co_3(OH)]_5(INT)_6(TZB)_6\}$ cages present in it. The entry of the cages are blocked by the isolated Co octahedra present in the structure. The CO_2 uptake at 195 K (367 cc/g)) was remarkably high for this material. However, the CO_2 uptake at 273 K (90 cc/g) and 298 K (46 cc/g) was relatively lower (Fig. 1.24E). Importantly, The C_2H_2 adsorption shows better uptakes (135 cc/g at 273 K and 86 cc/g at 298 K). This preferential C_2H_2 uptake over CO_2 was further reflected in the high C_2H_2/CO_2 selectivity (28 at 298 K and 1 bar; Fig. 1.24F) which identifed this MOF as potential

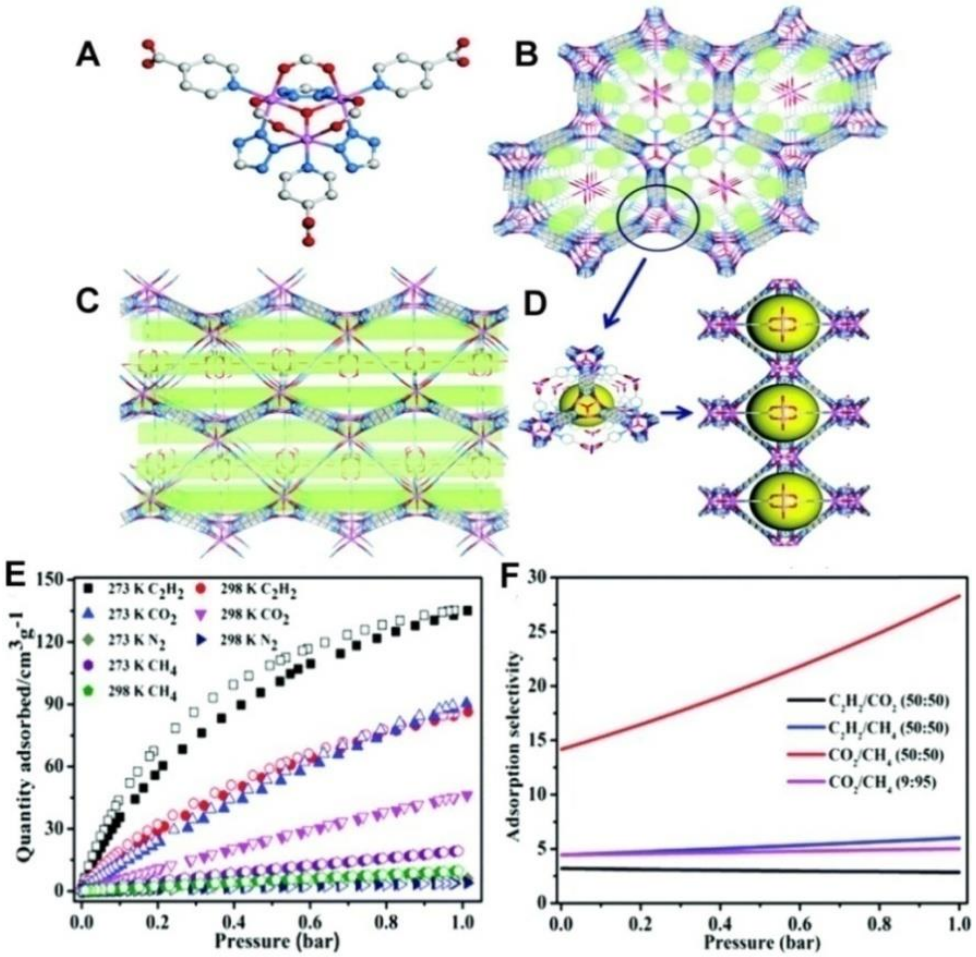

Figure 1.24. (A) The trinuclear Co(II) cluster present inthe MOF (B) 1D nano channels along the c axis (C) Side view of the nano channels (D) The $\{[Co_2(H_2O)_2]_3[Co_3(OH)]_5(INT)_6(TZB)_6\}$ cages present in it. (E) Sorption isotherms for the MOF at different temperatures. (F) *IAST* selectivity for different gas mixtures at 298 K *(Adopted from ref. 149 with permission from Royal Society of Chemistry).*

candidate for separation of C_2H_2 from mixture of C_2H_2 and CO_2. However, the drastic drop in CO_2 uptake when going from 195 K to 298 K (367 to 46 cc/g) is unusual and merits further investigation.

1.3.13.3. A Cobalt-Indium-Isonicotinate-Terephthalate MOF:

Along with mixed ligand MOFs, mixed metal MOFs are also considered as promising candidates to achieve framework rigidity and high gas uptake. One such example based on isonicotinic acid ligand has been reported by Zeng *et al.*[150] They synthesized a library of MOFs by combining indium with s, d and f block elements. In this perticular work they have used a mixed metal (In and Co) mixed ligand (INA = isonicotinate and BDC = 1,4-benzenedicarboxylate) concept and successfully isolated $[InCo_2(OH)(INA)_3(1,4\text{-}BDC)_{3}\text{-}]\cdot$solvent.

The structure is composed of trinuclear $[InCo_2(OH)]^{6+}$ clusters which are cross-linked by six BDC ligands and three isonicotinates generating a 3D framework (Fig. 1.25A), a nine-connected net (ncb topology). This MOF contains two types of polyhedral cages namely $\{[InCo_2(OH)]_4(1,4\text{-}BDC)_6\}$ which is tetrahedral and $\{[InCo_2(OH)]_8(INA)_{12}(1,4\text{-}BDC)_2\}$ having square antiprismatic geometry.

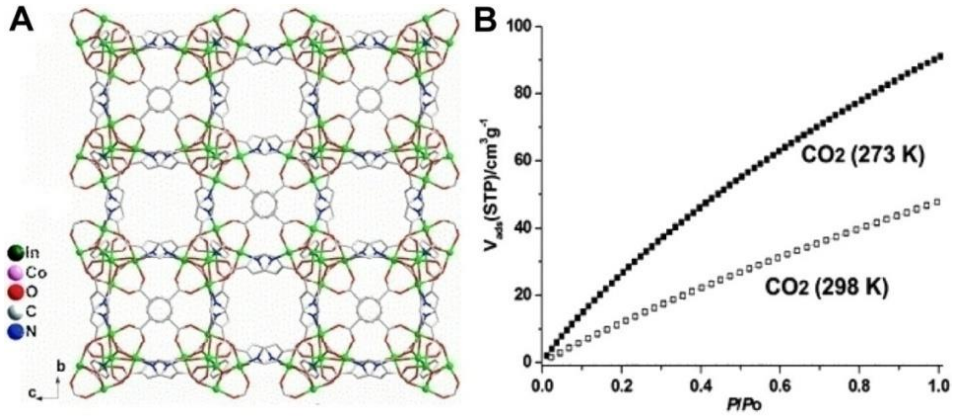

Figure 1.25. (A) 3D framework of the MOF. (B) CO_2 adsorption isotherms at different temperatures *(Adopted from ref. 150 with permission from American Chemical Society)*.

This framework exhibited interesting gas adsorption behaviour. It showed a type-I N_2 isotherm at 77 K. The high surface areas (1134 m^2/g), CO_2 uptakes (91.2 cc/g at 273 K and 47.7 cc/g at 298 K at 1 atm; Fig. 1.25B) and CO_2/N_2 selectivity (40:1 at 1 atm) makes this MOF as a potential candidate for post-combustion CO_2 capture.

1.3.13.4. Nickel-Pyridinecarboxylate-L2 (L2= linear di-topic carboxylate linkers) Based MOFs:

A family of MOFs involving isonicotinic acid along with other ditopic dicarboxylate linkers has been reported by Chen and co-workers. Their detailed structural analysis revealed the presence of unprecedented, uninodal, nine-connected ncb topology in these analogous frameworks.[151] Generally, trinuclear $M_3(\mu^3\text{-}O)(O_2CR)6(L1)_3$ clusters (D_3h) is the suitable candidate for nine-coordinated ncb framework, where L1 is a ditopic ligand functioning as two monodentate ligands. On the basis of these strategies, the authors synthesized 13 isoreticular MOFs $[Ni(II)_2Ni(III)\ (\mu^3\text{-}OH)(LP)_3(L2)_{1.5}]$ (LP = linear Pyridine carboxylate, L2= linear di-carboxylate) involving different pyridine carboxylate ligands and studied their adsorption properties. All the frameworks have a similar coordination environment (Fig. 1.26A) and thereby similar topology. These isoreticular MOFs are thermally stable (350°C) and posses surface areas in excess of 2000 m^2/g (determined from N_2 adsorption isotherm at 77 K temperature) (Fig. 1.26B).

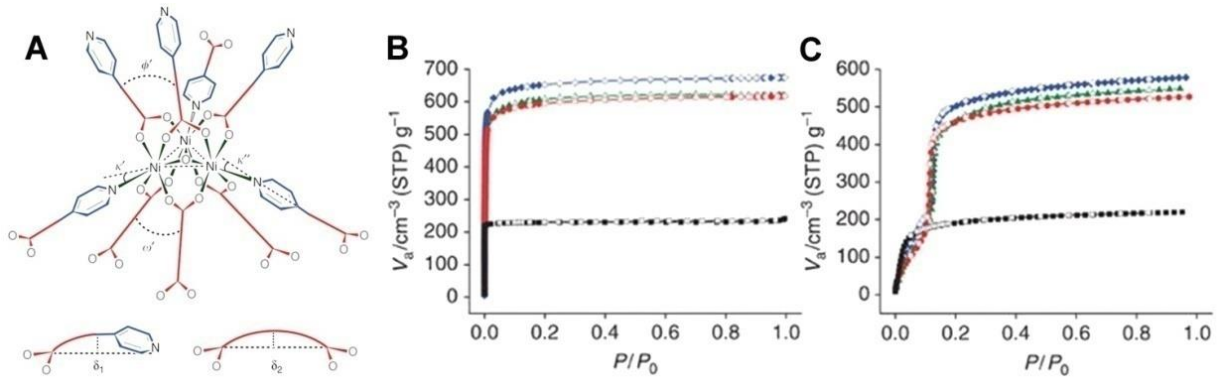

Figure 1.26. (A) Coordination environment of Ni and schematic representation of the distortion present in the framework. (B) N_2 adsorption at 77 K. (Black for isonicotinate-terephthalate combination) (C) CO_2 capacity at 195 K (Black for isonicotinate-terephthalate combination). *(Adopted from ref. 151 with permission from Nature Publishing Group).*

CO_2 adsorption isotherms at 195 K temperature exhibited very high capacity (Fig. 1.26C) which indirectly means these materials could be used as CO_2 capture material at high pressure. As these materials are containing large pores, the only problem could be with the compromised selectivities.

1.4. Design Principle of Scalable MOFs for Carbon Capture:

From the above discussions, we see that Metal Organic Frameworks (MOFs) especially the Ultra-microporous MOFs (Um-MOFs) have attracted significant attention due to their

1) High structural tunability
2) High CO_2 capacity
3) High CO_2 selectivity over the other gases

So, the first design principle should be the material to be ultra-microporous. Next consideration should be the choosing of linkers. Usually, small rigid linkers have been used for generating Um-MOFs.[70, 71, 75, 76, 128] However, large linkers also can provide Um-MOFs via interpenetrated networking.[63] As the Um-MOFs provide intrinsic molecular sieving along with co-operative guest-guest interactions; they are capable of capturing CO_2 selectively from a mixture of gases. In case of CO_2 separation by solid sorbents, once the saturation capacity is reached the adsorbed CO_2 has to be regenerated. This regeneration requires some amount of energy. Lower the regeneration energy higher will be the efficiency of those materials. This regeneration energy primarily relies on the HOA which again is decided by the strength of framework-CO_2 interaction. So a proper choice of linker is required so that the CO_2 molecules interact nominally with the framework and thereby the HOA will be optimal for a facile regeneration of the adsorbed CO_2.[148] Usually, the use of mildly basic groups can

provide such optimal interaction with the weakly acidic CO_2 molecule. Another decisive parameter for a superior sorbent is the smooth CO_2 kinetics within the nano-confinements of the pores. For a practical large-scale industrial CO_2 capture process, the sorbents are required in tonnes. Hence, even on a laboratory scale, it becomes imperative to demonstrate the MOF synthesis in grams. In this regard, making MOFs using a *single metal and a single ligand* precursor can be advantageous. In fact most of the commercially available MOFs have such compositions.[152] However, this does not rule out the multi-ligand MOFs, just that their synthesis and scale-up might be more challenging and require more optimizations. To sum up, a CO_2 capture MOF have to be Um-MOFs build from small rigid linker having proper functionality to optimally interact with CO_2 molecules and should have the following, generally contrasting features.

a) High CO_2 capacity
b) High selectivity for CO_2 over other gases
c) Faster kinetics
d) Optimal HOA for CO_2 (Low regeneration/parasitic energy).

1.5. Scopes of Work in the Current Context:

Coal-fired power plants which generate ~ 42% of the world's electricity form one of the largest sources of anthropogenic CO_2 emission.[153,154] This directly increases the environmental CO_2 concentration. Therefore, there is a strong need for mitigating the green house gas emissions from power generation. Although post-combustion CO_2 capture technologies have attracted significant attention[11, 21] there is scope to explore. For example, the gas separation process is still too energy demanding. This requires further optimization of the purification process. Although tuning of the process can play a key role, a massive reward lies in the development of efficient solid sorbents. When it comes to developing superior sorbents, defining a single parameter which can point out the superiority of one sorbent over the other is very important. Recently, Smit and co-workers[17] have come up with a metric, parasitic energy, which measures the energy needed to purify and compress unit Kg of CO_2 using a particular sorbent. This points out the superiority of one sorbent over other in totality. However, this metric is not well explored for many of the reported sorbents. Another critical point to be noted is the development of solid sorbents capable of meeting the multiple demands of CO_2 capture is always advantageous.

Although post-combustion CO_2 capture is one of the well-investigated technologies to mitigate CO_2 emissions from power plants, alternatives to straight firing coal and scrubbing CO_2 from the combustion gas exist, which can be more energy efficient and ultimately inexpensive.[22,23] Coal gasification, which is a key technology for future clean coal power involves catalytic steam reforming of the fuel that produces a high-pressure H_2/CO_2 gas mixture.[23-25] CO_2 is then removed from the mixture, resulting in a near-pure H_2 stream which can be used as a clean-burning fuel. Pressure Swing Adsorption (PSA) systems employing solid sorbents is one of the key technology for this large-scale CO_2 capture. Although these processes are energy demanding, the tuning of the process/technologies along with the development of better solid sorbents having high CO_2 capacity and selectivity at higher pressure will bring down the energy and thereby the cost associated.

Our target is to develop scalable Um-MOFs (from a combination of *single metal and single small rigid linkers*) with a modest surface area, high CO_2 capacity, selectivity towards CO_2 over other gases, good stability, smooth kinetics and optimal HOA for facile regeneration. Most importantly to develop MOFs that can provide low parasitic load to the power plant. A solid sorbent with these properties can bring down the cost associated with the purification process.

1.6. Overview of the Thesis Work:

Herein, our target is to develop new scalable, stable Um-MOFs from readily available & cheap components and investigating them for different carbon capture applications. We have mostly focused on the two major technologies of carbon capture. Firstly, the post-combustion CO_2 capture both in dry and humid conditions and the second one is the pre-combustion CO_2 capture.

In our design strategy, we always restrict ourselves to small pore MOFs those are synthesized from *single metal single ligand precursor*. This approach mostly eliminates the possibilities of multiple phases precipitating during the synthesis. In fact, most of the commercially available MOFs are made up of a single metal and single ligand, but this aspect has never been explicitly emphasized. In the development of high-performance CO_2 capturing Um-MOFs, it is always of beneficial to have some basic functionality in the linker which can interact with the gas molecules. In all the works enclosed in this thesis, we have chosen few linkers with basic character (considering the weakly acidic nature of CO_2), shown in figure 1.27.

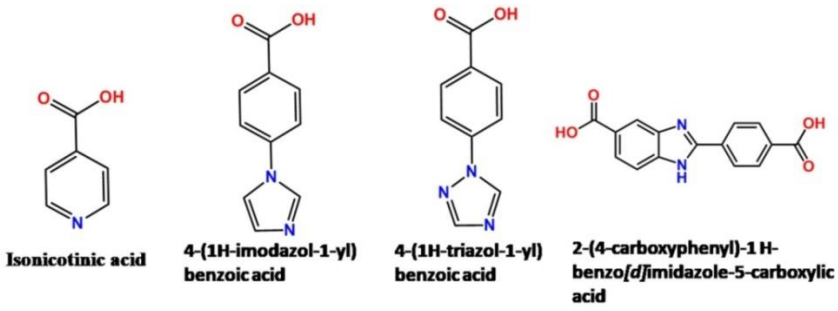

Figure 1.27. Different linkers used for developing Um-MOFs for CO_2 capture applications presented in this thesis work.

The whole thesis presented here contains a total of five chapters. The first chapter presents a brief account of CO_2 capture technologies and literature on some of the best-performing Um-MOFs as carbon capture materials. Whereas, the other chapters deal with the work that has been done by the authors from Advanced Porous Materials lab, Department of Chemistry, at IISER Pune (in some cases via collaboration with researchers from other institute). Chapter 2 deals with the pre-combustion CO_2 capture performance of a nickel-isonicotinate based 2D porous Um-MOF and chapter 3 deals with the post-combustion CO_2 capture performance of another 1D porous Um-MOF built from $Ni^{(II)}$ and isonicotinate as the linker. Chapter 4 is divided into two parts: The first part, chapter 4-I, describes a series of triazolyl/imidazolyl carboxylate functionalized MOFs for potential humid CO_2 capture and the second part, chapter 4-II, explains a benzimidazole functionalized Um-MOF and its CO_2 capture characteristics. Chapter 5, is a little bit different; it describes how the fundamental concept of hard-soft Lewis acid can be used in the design of Um-MOF with gas-specific coordination flexibility. Here, we have shown how coordination flexibility introduces gas specific porosity into an otherwise non-porous solid.

1.7. References:

1. https://climate.nasa.gov/vital-signs/carbon-dioxide/.
2. Inventory of U.S. Greenhouse Gas Emissions and Sinks: 1990–2015. (c) Keith, D. W.; *Science* **2009**, *325*, 1654.
3. Rochelle, G. T.; *Science* **2009**, *325*, 1652.
4. Boot-Handford, M. E.; Abanades, J. C.; Anthony, E. J.; Blunt, M. J.; Brandani, S.; Mac Dowell, N.; Fernandez, J. R.; Ferrari, M.-C.; Gross, R.; Hallett, J. P.; Haszeldine, R. S.; Heptonstall, P.; Lyngfelt, A.; Makuch, Z.; Mangano, E.; Porter, R.

T. J.; Pourkashanian, M.; Rochelle, G. T.; Shah, N.; Yao, J. G.; Fennell, P. S. *Energy Environ. Sci.* **2014**, *7*, 130.

5. MacDowell, N.; Florin, N.; Buchard, A.; Hallett, J.; Galindo, A.; Jackson, G.; Adjiman, C. S.; Williams, C. K.; Shah, N.; Fennell, P. *Energy Environ. Sci.* **2010**, *3*, 1645–1669.
6. Yan, J. Carbon Capture and Storage (CCS), *Applied Energy*, virtual issue.
7. Park, S. K.; Ahn, J. H.; Kim, T. S. *Applied Energy* **2011**. *88*, 2976-2987.
8. Jansen, D.; Gazzani, M.; Manzolini, G.; Dijk, E.-v.; Carbo, M. *International Journal of Greenhouse Gas Control* **2015**, *40*, 167-187
9. Dai, Z.; Ansaloni, L.; Deng, L. *Ind. Eng. Chem. Res.* **2016**, *55*, 5983–5992
10. Pardemann, R.; Meyer, B. *Pre-Combustion Carbon Capture*, 2015 DOI: 10.1002/9781118991978.hces061.
11. Samanta, A.; Zhao, A.; Shimizu, G. K. H.; Sarkar, P.; Gupta, R. *Ind. Eng. Chem. Res.* **2012**, *51*, 1438–1463.
12. Zhao, G.; Aziz, B.; Hedin, N. *Applied Energy* **2010**. *87*, 2907-2913.
13. Herzog, H. J. *Environ. Sci. Technol.* **2001**, *35*, 148A–153A
14. Yang, H.; Xu, Z.; Fan, M.; Gupta, R.; Slimane, R. B.; Bland, A. E. *J. Environ. Sci*. **2008**, *20*, 14–27.
15. Wang, Q.; Luo, J.; Zhong, Z.; Borgna, A. *Energy Environ. Sci*. **2011**, *4*, 42.
16. Markewitz, P.; Kuckshinrichs, W.; Leitner, W.; Linssen, J.; Zapp, P.; Bongartz, R.; Schreibera A.; Muller, T. E.; *Energy Environ. Sci.* **2012**, *5*, 7281.
17. Huck, J. M.; Lin, L. -C.; Berger, A. H.; Shahrak, M. N.; Martin, R. L.; Bhown, A. S.; Haranczyk, M.; Reuterb, K.; Smit, B. *Energy Environ. Sci*. **2014**, *7*, 4132.
18. Lin, L. -C.; Berger, A. H.; Martin, R. L.; Kim, J.; Swisher, J. A.; Jariwala, K.; Rycroft, C. H.; Bhown, A. S.; Deem, M. W.; Haranczyk, M.; Smit, B. *Nat. Mater.* **2012**, *11*, 633.
19. CO_2 Capture from Existing Coal-Fired Power Plants (US DOE): South Park Township, **2007**.
20. Ko, D.; Siriwardane, R.; Biegler, L. T. *Ind. Eng. Chem. Res*. **2003**, *42*, 339.
21. D'Alessandro, D. M.; Smit, B.; Long, J. R. *Angew. Chem. Int. Ed.* **2010**, *49*, 6058–6082.
22. Liu, K.; Song, C.; Subramani, V.; *Hydrogen and Syngas Production and Purification Technologies* (Wiley-AIChE, Hoboken, NJ, **2010**), 414–450.

23. Rand, D. A. J.; Dell, R. M. *Hydrogen Energy: Challenges and Prospects* (RSC Energy Series, the Royal Society of Chemistry, Cambridge, **2008**).
24. Mukherjee, S.; Kumar, P.; Hosseini, A.; Yang, A.; Fennell, P. *Energy Fuels* **2014**, *28*, 1028–1040.
25. Agarwal, A.; Biegler, L. T.; Zitney, S. E. *Ind. Eng. Chem. Res.* **2010**, *49*, 5066–5079.
26. Wang, Q. Hydrogen production, in Handbook of Climate Change Mitigation, W.-Y. Chen, J. Seiner, T. Suzuki, M. Lackner, Eds. (Springer-Verlag, New York, **2012**), 1091–1130.
27. Akten, E. D.; Siriwardane, R.; Sholl, D. S. *Energy Fuels* **2003**, *17*, 977.
28. Cao, D.; Wu, J. *Carbon* **2005**, *43*, 1364–1370.
29. Sircar, S.; Golden, T. C. *Sep. Sci. Technol*. **2000**, *35*, 667–687.
30. Sanz-Pérez, E. S.; Murdock, C. R.; Didas, S. A.; Jones, C. W. *Chem. Rev*. **2016**, *116*, 11840−11876.
31. Darunte, L. A.; Oetomo, A. D.; Walton, K. S.; Sholl, D. S.; Jones, C. W. *ACS Sustainable Chem. Eng.* **2016**, *4*, 5761−5768
32. Lackner, K. S.; Brennan, S.; Matter, J. M.; Park, A. H.; Wright, A.; van der Zwaan, B. *Proc. Natl. Acad. Sci. U. S. A.* **2012**, *109*, 13156.
33. Jones, C. W. *Annu. Rev. Chem. Biomol.Eng*. **2011**, *2*, 31−52.
34. Goeppert, A.; Czaun, M.; Prakash, G. S.; Olah, G. A. *Energy Environ. Sci*. **2012**, *5*, 7833−7853.
35. Trends in Atmospheric Carbon Dioxide; National Oceanic & Atmospheric Administration, **2015**.
36. Bollini, P.; Didas, S. A.; Jones, C. W. *J. Mater. Chem.* **2011**, *21*, 15100−15120.
37. Meek, S. T.; Greathouse, J. A.; Allendorf, M. D., *Adv. Mater.* **2011**, *23*, 249-267.
38. Batten, S. R.; Champness, N. R.; Chen, X.-M.; Garcia-Martinez, J.; Kitagawa, S.; Ohrstrom, L.; O'Keeffe, M.; Suh, M. P.; Reedijk, J. *CrystEngComm* **2012**, *14*, 3001-3004.
39. Tanaka, D.; Kitagawa, S., *Chem. Mater*. **2008**, *20*, 922-931.
40. Farha, O. K.; Eryazici, I.; Jeong, N. C.; Hauser, B. G.; Wilmer, C. E.; Sarjeant, A. A.; Snurr, R. Q.; Nguyen, S. T.; Yazaydın, A. Ö.; Hupp, J. T. *J. Am. Chem. Soc*. **2012**, *134*, 15016–15021.
41. Yun, R.; Lu, Z.; Pan, Y.; You, X.; Bai, J. *Angew. Chem. Int. Ed*. **2013**, *52*, 11282 – 11285.

42. Gru¨nker, R.; Bon, V.; Mu¨ller, P.; Stoeck, U; Krause, S.; Mueller, U.; Senkovska, I.; Kaskel, S. *Chem. Commun*. **2014**, *50*, 3450.
43. Furukawa, H.; Cordova, K. E.; O'Keeffe, M.; Yaghi, O. M. *Science* **2014**, *341*, 974.
44. Chae, H. K.; Siberio-Pe´rez, D. Y.; Kim, J.; Go, Y.-B.; Eddaoudi, M.; Matzger, A. J.; O'Keeffe, M.; Yaghi, O. M.; *Nature* **2004**, *425*, 523.
45. Banerjee, R.; Phan, A.; Wang, B.; Knobler, C.; Furukawa, H.; O'Keeffe, M.; Yaghi, O. M. *Science* **2008**, *319*, 939.
46. Li, H.; Eddaoudi, M.; O'Keeffe, M.; Yaghi, O. M. *Nature* **1999**, *402*, 276.
47. Rosi, N. L.; Eckert, J.; Eddaoudi, M.; Vodak, D. T.; Kim, J.; O'Keeffe, M.; Yaghi, O. M. *Science* **2003**, 300, 1127.
48. Millward, A. R.; Yaghi, O. M. *J. Am. Chem. Soc.* **2005**, *127*, 17998.
49. Rowsell, J. L. C.; Yaghi, O. M. *Angew. Chem. Int. Ed.* **2005**, 44, 4670.
50. Ma, S.; Zhou, H.-C. *Chem. Commun.* **2010**, *46*, 44.
51. Peng, Y.; Krungleviciute, V.; Eryazici, I.; Hupp, J. T.; Farha, O. K.; Yildirim, T. *J. Am. Chem. Soc*. **2013**, *135*, 11887.
52. He, Y.; Zhou, W.; Qian, G.; Chen, B. *Chem. Soc. Rev*. **2014**, 43, 5657.
53. Jayaramulu, K.; Datta, K. K. R.; Shiva, K.; Bhattacharyya, A. J.; Eswaramoorthy, M.; Maji, T. K. *Microporous Mesoporous Mater*. **2015**, *206*, 127.
54. Roy, S.; Chakraborty, A.; Maji, T. K. *Coord. Chem. Rev.* **2014**, *139*, 273–274.
55. Haldar, R.; Prasad, K.; Samanta, P. K.; Pati, S.; Maji, T. K. *Cryst. Growth Des*. **2016**, *16*, 82.
56. Li, B.; Chrzanowski, M.; Zhang, Y.; Ma, S. *Coord. Chem. Rev.* **2016**, *307*, 106.
57. Samai, S.; Biradha, K. *Chem Mater*. **2012**, *24*, 1165.
58. Dey, A.; Mandal, S. K.; Biradha, K. *CrystEngComm* **2013**, 15, 9769.
59. Liu, J.; Thallapally, P. K.; McGrail, B. P.; Brown, D. R.; Liu, J. *Chem. Soc. Rev.* **2012**, *41*, 2308.
60. Gygi, D.; Bloch, E. D.; Mason, J. A.; Hudson, M. R.; Gonzalez, M. I.; Siegelman, R. L.; Darwish, T. A.; Queen, W. L.; Brown, C. M.; Long, J. R. *Chem. Mater*. **2016**, *28*, 1128–1138.
61. Mason, J. A.; Veenstra, M.; Long, J. R. *Chem. Sci*. **2014**, *5*, 32-51.
62. Qiu, S.; Xue, M.; Zhu, G. *Chem. Soc. Rev.* **2014**, *43*, 6116.

63. Nugent, P.; Belmabkhout, Y.; Burd, S. D.; Cairns, A. J.; Luebke, R.; Forrest, K.; Pham, T.; Ma, S.; Space, B.; Wojtas, L.; Eddaoudi, M.; Zaworotko, M. J. *Nature* **2013**, *495*, 80.
64. Li, J.-R.; Sculley, J.; Zhou, H.-C. *Chem. Rev.* **2012**, *112*, 869.
65. Li, J.-R.; Kuppler, R. J.; Zhou, H.-C. *Chem. Soc. Rev.* **2009**, *38*, 1477.
66. Huang, A.; Chen, Y.; Wang, N.; Hu, Z.; Jiang, J.; Caro, J. *Chem. Commun*. **2012**, *48*, 10981.
67. Herm, Z. R.; Wiers, B. M.; Mason, J. A.; van Baten, J. M.; Hudson, M. R.; Zajdel, P.; Brown, C. M.; Masciocchi, N.; Krishna, R.; Long, J. R. *Science* **2013**, *340*, 960.
68. Biswal, B. P.; Bhaskar, A.; Banerjee, R.; Kharul, U. K. *Nanoscale* **2015**, *7*, 7291.
69. Thallapally, P. K.; Tian, J.; RadhaKishan, M.; Fernandez, C. A.; Dalgarno, S. J.; McGrail, P. B.; Warren, J. E.; Atwood, J. L. *J. Am. Chem. Soc.* **2008**, 130, 16842.
70. Bhatt, P. M.; Belmabkhout, Y.; Cadiau, A.; Adil, K.; Shekhah, O.; Shkurenko, A.; Barbour, L. J.; Eddaoudi, M. *J. Am. Chem. Soc.***2016**, *138*, 9301–9307.
71. Kumar, A.; Hua, C.; Madden, D. G.; O'Nolan, D.; Chen, K. –J.; Keane, L. –A. J.; Perry IV, J. J.; Zaworotko, M. J. *Chem. Commun*. **2017**, *53*, 5946.
72. Lin, J. B.; Zhang J.-P.; Chen, X. M. *J. Am. Chem. Soc.* **2010**, *132*, 6654.
73. Mason, J. A.; Sumida, K.; Herm, Z. R.; Krishna, R.; Long, J. R. *Energy Environ. Sci*. **2011**, *4*, 3030.
74. Zhang, Z.; Yao, Z. -Z.; Xiang, S.; Chen, B. *Energy Environ. Sci*. **2014**, *7*, 2868.
75. Xiang, S.; He, Y.; Zhang, Z.; Wu, H.; Zhou, W.; Krishna, R.; Chen, B. *Nat. Commun*. **2012**, *3*, 954.
76. Vaidhyanathan, R.; Iremonger, S. S.; Shimizu, G. K. H.; Boyd, P. G.; Alavi, S.; Woo, T. K. *Science* **2010**, *330*, 650.
77. Lee, J.; Farha, O. K.; Roberts, J.; Scheidt, K. A.; Nguyen, S. T.; Hupp, J. T. *Chem. Soc. Rev*. **2009**, *38*, 1450.
78. Liu, J.; Chen, L.; Cui, H.; Zhang, J.; Zhang, L.; Su, C.-Y. *Chem. Soc. Rev.* **2014**, *43*, 6011.
79. Corma, A.; García, H.; Llabrés i Xamena, F. X. *Chem. Rev*. **2010**, *110*, 4606.
80. Yoon, M.; Srirambalaji, R.; Kim, K. *Chem. Rev*. **2012**, *112*, 1196.
81. Mueller, U.; Schubert, M.; Teich, F.; Puetter, H.; Schierle-Arndt, K.; Pastre, J. *J. Mater. Chem*. **2006**, *16*, 626.
82. Wu, C.-D.; Lin, W. *Angew. Chem., Int. Ed*. **2007**, *46*, 1075.

83. Dybtsev, D. N.; Nuzhdin, A. L.; Chun, H.; Bryliakov, K. P.; Talsi, E. P.; Fedin, V. P.; Kim, K. A. *Angew. Chem., Int. Ed.* **2006**, *45*, 916.
84. Gao, W.-Y.; Wu, H.; Leng, K.; Sun, Y.; Ma, S. *Angew. Chem., Int. Ed*. **2016**, *55*, 5472.
85. Li, B.; Leng, K.; Zhang, Y.; Dynes, J. J.; Wang, J.; Hu, Y.; Ma, D.; Shi, Z.; Zhu, L.; Zhang, D.; Sun, Y.; Chrzanowski, M.; Ma, S. *J. Am. Chem. Soc*. **2015**, *137*, 4243.
86. Gole, B.; Bar, A. K.; Mallick, A.; Banerjee, R.; Mukherjee, P. S. *Chem. Commun.* **2013**, *49*, 7439.
87. Liu, Y.; Moon, S.-Y.; Hupp, J. T.; Farha, O. K. *ACS Nano*, **2015**, *9*, 12358–12364
88. Fei, H.; Shin, J.; Meng, Y. S.; Adelhardt, M.; Sutter, J.; Meyer, K.; Cohen, S. M. *J. Am. Chem. Soc*. **2014**, *136*, 4965–4973.
89. Sutar, P.; Maji, T. K. *Chem. Commun*. **2016**, *52*, 8055.
90. Roy, S.; Katiyar, A. K.; Mondal, S. P.; Ray, S. K.; Biradha, K. *ACS Appl. Mater. Interfaces* **2014**, *6*, 11493.
91. Cui, Y.; Yue, Y.; Qian, G.; Chen, B. *Chem. Rev*. **2012**, *112*, 1126.
92. Kundu, T.; Mitra, S.; DíazDíaz, D.; Banerjee, R. *ChemPlusChem* **2016**, *81*, 728.
93. Banerjee, K.; Biradha, K. *New J. Chem.* **2016**, *40*, 1997.
94. Marshall, R. J.; Kalinovskyy, Y.; Griffin, S. L.; Wilson, C.; Blight, B. A.; Forgan, R. S. *J. Am. Chem. Soc.* **2017**, *139*, 6253−6260.
95. Yang, Q.-Y.; Pan, M.; Wei, S.-C.; Li, K.; Du, B.-B.; Su, C.-Y. *Inorg. Chem*. **2015**, *54*, 5707–5716.
96. Kreno, L. E.; Leong, K.; Farha, O. K.; Allendorf, M.; Van Duyne, R. P.; Hupp, J. T. *Chem. Rev*. **2012**, *112*, 1105.
97. Nagarkar, S. S.; Joarder, B.; Chaudhari, A. K.; Mukherjee, S.; Ghosh, S. K. *Angew. Chem., Int. Ed.* **2013**, *52*, 2881.
98. Chen, B.; Wang, L.; Xiao, Y.; Fronczek, F. R.; Xue, M.; Cui, Y.; Qian, G. *Angew. Chem., Int. Ed*. **2009**, *48*, 500.
99. Chen, B.; Xiang, S.; Qian, G. *Acc. Chem. Res.***2010**, *43*, 1115.
100. Lu, G.; Hupp, J. T. *J. Am. Chem. Soc*. **2010**, *132*, 7832.
101. Shimizu, G. K. H.; Taylor, J. M.; Kim, S. *Science***2013**, *341*, 354.
102. Nagarkar, S. S.; Unni, S. M.; Sharma, A.; Kurungot, S.; Ghosh, S. K. *Angew. Chem., Int. Ed*. **2014**, *53*, 2638.

103. Saha, S.; Schön, E.-M.; Cativiela, C.; DíazDíaz, D.; Banerjee, R. *Chem. - Eur. J.* **2013**, *19*, 9562.
104. Sikdar, N.; Dutta, D.; Haldar, R.; Ray, T.; Hazra, A.; Bhattacharyya, A. J.; Maji, T. K. *J. Phys. Chem. C* **2016**, *120*, 13622.
105. Aiyappa, H. B.; Saha, S.; Wadge, P.; Banerjee, R.; Kurungot, S. *Chem. Sci.* **2015**, *6*, 603.
106. Zhang, F.-M.; Dong, L.-Z.; Qin, J.-S.; Guan, W.; Liu, J.; Li, S.-L.; Lu, M.; Lan, Y.-Q.; Su, Z.-M.; Zhou, H.-C. *J. Am. Chem. Soc*. **2017**, *139*, 6183–6189.
107. Yoon, M.; Suh, K.; Natarajan, S.; Kim, K. *Angew. Chem. Int. Ed*. **2013**, *52*, 2688 – 2700.
108. Pili, S.; Argent, S. P.; Morris, C. G.; Rought, P.; García-Sakai, V.; Silverwood, I. P.; Easun, T. L.; Li, M.; Warren, M. R.; Murray, C. A.; Tang, C. C.; Yang, S.; Schröder, M. *J. Am. Chem. Soc*. **2016**, *138*, 6352–6355.
109. Shalini, S.; Dhavale, V. M.; Eldho, K. M.; Kurungot, S.; Ajithkumar, T. G.; Vaidhyanathan, R. *Sci. Rep.* **2016**, *6*, 32489.
110. Sun, L.; Campbell, M. G.; Dincă, M. *Angew. Chem, Int. Ed*. **2016**, *55*, 3566.
111. Wang, L.; Han, Y.; Feng, X.; Zhou, J.; Qi, P.; Wang, B. *Coord. Chem. Rev*. **2016**, *307*, Part II, 361.
112. Givaja, G.; Amo-Ochoa, P.; Gomez-Garcia, C. J.; Zamora, F. *Chem. Soc. Rev*. **2012**, *41*, 115.
113. Dhara, B.; Nagarkar, S. S.; Kumar, J.; Kumar, V.; Jha, P. K.; Ghosh, S. K.; Nair, S.; Ballav, N. *J. Phys. Chem. Lett.* **2016**, *7*, 2945–2950.
114. Sun, L.; Hendon, C. H.; Park, S. S.; Tulchinsky, Y.; Wan, R.; Wang, F.; Walsh, A.; Dinca, M.; *Chem. Sci.* **2017**, *8*, 4450.
115. Zhao, Y.; Song, Z.; Li, X.; Sun, Q.; Cheng, N.; Lawes, S.; Sun, X. *Energy Storage Materials* **2016**, *2*, 35–62.
116. Shao, M.; Chang, Q.; Dodelet, J.-P.; Chenitz, R. *Chem. Rev.* **2016**, *116*, 3594.
117. Mahmood, A.; Guo, W.; Tabassum, H.; Zou, R. *Adv. Energy Mater.* **2016**, *6*, 1600423.
118. Ma, S.; Goenaga, G. A.; Call, A. V.; Liu, D.-J. *Chem. - Eur. J.* **2011**, *17*, 2063.
119. Ke, F.-S.; Wu, Y.-S.; Deng, H. *Journal of Solid State Chemistry* **2015**, *223*, 109.
120. Lin, X.-M.; Ni, J.-L.; Lin, J.; Wei, L.-M.; Hu, L.; Zhang, G.; Cai, Y.-P. *Inorg. Chem*. **2016**, *55*, 8244–8247.

121. Peng, Z.; Yi, X.; Liu, Z.; Shang, J.; Wang, D. *ACS Appl. Mater. Interfaces* **2016**, *8*, 14578–14585.
122. Xuan, W.; Zhu, C.; Liu, Y.; Cui, Y. *Chem. Soc. Rev*. **2012**, *41*, 1677–1695
123. Wang, C.; Liu, C.; He, X.; Sun, Z.-M. *Chem. Commun*. **2017**, *53*, 11670
124. Peng, L.; Zhang, J.; Xue, Z.; Han, B.; Sang, X.; Liu, C.; Yang, G. *Nat. Commun*. **2014**, *5*, 4465.
125. Fang, Q.-R.; Yuan, D.-Q.; Sculley, J.; Lu, W.-G.; Zhou, H.-C. *Chem. Commun*. **2012**, *48*, 254–256
126. Reinares-Fisac, D.; Aguirre-Díaz, L. M.; Iglesias, M.; Snejko, N.; Gutierrez-Puebla, E.; Monge, M. Á.; Gandara, F. *J. Am. Chem. Soc*. **2016**, *138*, 9089−9092.
127. Wang, K.; Feng, D.; Liu, T.-F.; Su, J.; Yuan, S.; Chen, Y.-P.; Bosch, M.; Zou, X.; Zhou, H.-C. *J. Am. Chem. Soc*. **2014**, *136*, 13983–13986.
128. Shekhah, O.; Belmabkhout, Y.; Chen, Z.; Guillerm, V.; Cairns, A.; Adil, K.; Eddaoudi, M. *Nat. Commun.* **2014**, *5*, 4228.
129. Adil, K.; Belmabkhout, Y; Pillai, R. S.; Cadiau, A.; Bhatt, P. M.; Assen, A. H.; Maurin, G.; Eddaoudi, M. *Chem. Soc. Rev*. **2017**, *46*, 3402-3430.
130. Elsaidi, S. K.; Mohamed, M. H.; Schaef, H. T.; Kumar, A.; Lusi, M.; Pham, T.; Forrest, K. A.; Space, B.; Xu, W.; Halder, G. J.; Liu, J.; Zaworotko, M. J.; Thallapally, P. K. *Chem. Commun*. **2015**, *51*, 15530–15533.
131. Mohamed, M. H.; Elsaidi, S. K.; Wojtas, L.; Pham, T.; Forrest, K. A.; Tudor, B.; Space, B.; Zaworotko, M. J. *J. Am. Chem. Soc*. **2012**, *134*, 19556–19559.
132. Scott, H. S.; Ogiwara, N.; Chen, K.-J.; Madden, D. G.; Pham, T.; Forrest, K.; Space, B.; Horike, S.; Perry Iv, J. J.; Kitagawa, S.; Zaworotko, M. J. *Chem. Sci*. **2016**, *7*, 5470–5476.
133. Banerjee, A.; Nandi, S.; Nasa, P.; Vaidhyanathan, R. *Chem. Commun*. **2016**, *52*, 1851-1854.
134. An, J.; Geib, S. J.; Rosi, N. L. *J. Am. Chem. Soc.* **2010**, *132*, 38–39.
135. Datta, S. J.; Khumnoon, C.; Lee, Z. H.; Moon, W. K.; Docao, S.; Nguyen, T. H.; Hwang, I. C.; Moon, D.; Oleynikov, P.; Terasaki, O.; Yoon, K. B. *Science* **2015**, *350*, 302.
136. Noro, S.-i.; Mizutani, J.; Hijikata, Y.; Matsuda, R.; Sato, H.; Kitagawa, S.; Sugimoto, K.; Inubushi, Y.; Kubo, K.; Nakamura, T. *Nat. Commun*. **2015**, *6*, 5851.

137. Sikdar, N.; Bonakala,S.; Haldar, R.; Balasubramanian, S.; Maji, T. K. *Chem. Eur. J.* **2016**, *22*, 6059.
138. Chakraborty, A.; Roy, S.; Eswaramoorthy, M.; Maji, T. K. *J. Mater. Chem. A* **2017**, *5*, 8423.
139. Parshamoni, S.; Konar, S. *CrystEngComm* **2016**, *18*, 4395.
140. Sharma, V.; De, D.; Saha, R.; Das, R.; Chattaraj, P. K.; Bharadwaj, P. K. *Chem. Commun*. **2017**, *53*, 13371.
141. Pal, A.; Chand, S.; Das, M. C. *Inorg. Chem*. **2017**, *56*, 13991.
142. Moushi, E. E.; Kourtellaris, A.; Spanopoulos, I.; Manos, M. J.; Papaefstathiou, G. S.; Trikalitis, P. N.; Tasiopoulos, A. J. *Cryst. Growth Des*. **2015**, *15*, 185−193.
143. Chen, D.-M.; Tian, J.-Y.; Liu, C.-S.; Du, M.; *CrystEngComm* **2016**, *18*, 3760–3763.
144. Pachfule, P.; Chen, Y.; Jiang, J.; Banerjee, R. *Chem. Eur. J*. **2012**, *18*, 688.
145. Wang, F.; Tan, Y.-X.; Yang, H.; Zhang, H.-X.; Kang, Y.; Zhang, J. *Chem. Commun*. **2011**, *47*, 5828–5830.
146. Zou, R.; Abdel-Fattah, A. I.; Xu, H.; Zhao, Y.; Hickmott, D. D. *CrystEngComm* **2010**, *12*, 1337-1353.
147. Wang, F.; Yang, H.; Kang, Y.; Zhang, J. *J. Mater. Chem*. **2012**, *22*, 19732–19737
148. Simmons, J. M.; Wu, H.; Zhou, W.; Yildirim, T. *Energy Environ. Sci*. **2011**, *4*, 2177–2185.
149. Chen, D.-M.; Tian, J.-Y.; Liu, C.-S.; Du, M. *Chem. Commun*. **2016**, *52*, 8413-8416.
150. Zheng, S.-T.; Wu, T.; Chou, C.; Fuhr, A.; Feng, P.; Bu, X. *J. Am. Chem. Soc*. **2012**, *134*, 4517−4520.
151. Zhang, Y.-B.; Zhou, H.-L.; Lin, R.-B.; Zhang, C.; Lin, J.-B.; Zhang, J.-P.; Chen, X.-M. *Nat. Commun.* **2012**, *3*, 642.
152. Basosiv M050 (magnesium formate), Basolite Z1200 (Zn-methylimidazole, ZIF-8), Basolite C300/F300 (Cu or Fe trimesate, HKUST-1), and Basolite A100 (aluminum terephthalate, MIL-53) are all sold under Sigma-Aldrich trademark.
153. Longwell, J. P.; Rubin, E. S.; Wilson, J. *Prog. Energy Combust. Sci*. **1995**, *21*, 269–360.
154. Coal: Medium-Term Market Report (International Energy Agency, Paris, **2012** and **2014**).

Chapter 2

Efficient Pre-combustion CO_2 Capture and H_2 Purification Using Single-ligand Ultra-microporous MOF

2.1. Introduction:

Currently, ~ 40% of the world's electricity is being produced by Coal-fired power plants which are one of the largest sources of anthropogenic CO_2 emissions.[1,2] For mitigating the greenhouse gas emissions of power generation, post-combustion CO_2 capture techniques have attracted large attention.[3,4] However, alternatives to straight burning fossil fuel (coal) and scrubbing CO_2 from the combustion gas exist that may be more energy efficient and ultimately cost-effective.[5,6]

Coal gasification (Scheme 2.1) is expected to be a chief technology for future clean coal power. This process involves the catalytic steam reforming of the fuel to generate a high pressure H_2/CO_2 (60:40) gas mixture.[6-8] CO_2 is then removed from the mixture, discharging in a near pure H_2 stream, a clean burning fuel that produce water as the only combustion product.

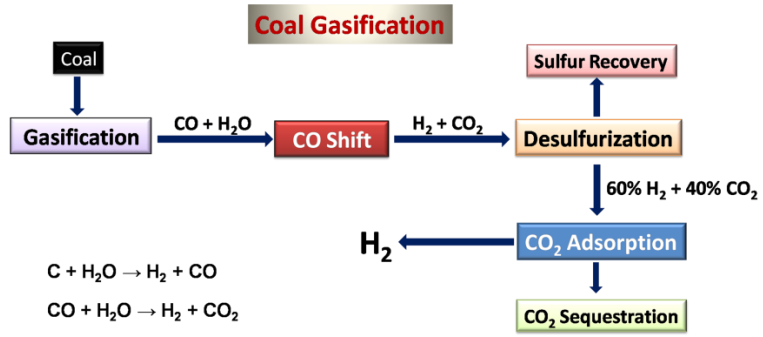

Scheme 2.1. A schematic representation of coal gasification.

Another important method for chemical hydrogen production is steam-hydrocarbon reforming (Scheme 2.2). This process involves catalytic steam reforming of hydrocarbon to produce a high pressure gas H_2/CO_2 ($80H_2$:$20CO_2$) gas mixture. Similar to coal gasification, here also CO_2 is removed from the gas mixture leaving a clean stream of pure H_2. At present, more than 90% of the world's hydrogen is produced from coal gasification.[9]

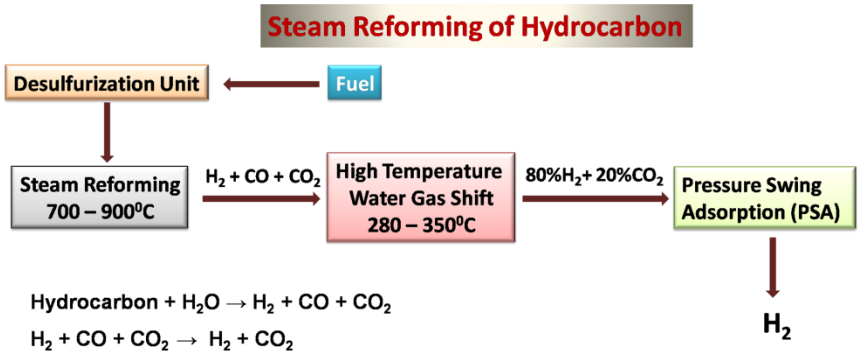

Scheme 2.2. A schematic representation of steam reforming of hydrocarbon.

These industrial processes involve pressure swing adsorption (PSA) systems which employ solid sorbents, such as zeolite 13X or activated carbon, for separating the CO_2 from the H_2/CO_2 mixture.[10-12] But, the process of separating CO_2 from H_2 is still too energy expensive for large scale coal gasification power plants to be commercially feasible. Therefore, further optimization of the purification process is necessary.[7, 10-12] Although process tuning will play a major role in this optimization process, the major opportunities lie in developing materials of the solid sorbents with better efficiency.

During last decade, Metal organic frameworks (MOFs) with high surface areas have attracted significant interest as solid sorbents for large-scale gas separation purposes.[13-16] For example, they have been rigorously studied for CO_2 capture from combustion flue gases where CO_2 is being separated from CO_2/N_2 gas mixture at low partial pressure.[3,4,16-22] Inspite of the potential application for coal gasification, literature on MOFs for high pressure CO_2/H_2 separations have been narrow.[23-27] Recently, Long and coworkers studied a wide variety of well-known MOFs, Zeolites, Carbon Molecular Seives (CMS) and acknowledged Mg_2(dobdc) and Cu-BTTri as the most promising candidates for CO_2/H_2 separations. Ihis was because they exhibited high CO_2/H_2 adsorption selectivities and huge CO_2 working capacities under PSA conditions relevant to coal gasification.[23] However, both the MOFs contains metal sites with unsaturated coordination or typically known as open metal sites. Although the open metal sites are of assistance to establish strong and preferential CO_2 binding, they could be challenging in terms of long term hydrolytic stability. Open metal sites, which are nornally strong Lewis acids, readily interact with even trace quantities of moisture resulting in either reduced adsorption properties or permanent degradation/transformation of the materials to some salt or nonporous material.[28-30] This is challenging for realistic gas separations as the complete elimination of water following the steam reforming during gasification is not possible.

Recently, ultra-microporous MOFs (pores size in the range of < 6.0 Å) with exceptional post-combustion CO_2 capture ability have been established.[21,31,32] Generally, ultra-microporous MOFs have some advantageous structural features which make them outstanding solid sorbents for gas separation applications. For example, in addition to the inherent molecular sieving abilities, the tiny pores can assist strong framework-gas (CO_2) interactions and can improve the cooperativity between the adsorbed gas molecules.[32] When it comes to the issue of stability, the short linkers generally tend give rise to rigid structures

with better shelf-life compared to the MOFs built from large organic linkers.[33-36] However, this does not rule out the possibility of a large pore MOF to be highly stable. In fact, some unusually stable large pore MOFs have been reported.[33,37-40] Ultra-microporous MOFs typically poses relatively low saturation limits at high pressure compared to large pore MOFs. This has made Ultra-microporous MOFs unattractive objective for PSA techniques. At high pressure, large pores present in the materials can permit the gas molecules to pack densely, leading to high saturation capacities which are imperative for gas separation processes. Thus achieving high CO_2 capacities at high pressures using ultra-microporous MOFs is apparently ironic and remains a challenge.

Herein we present a moisture stable Nickel-4-pyridylcarboxylate based ultra-microporous MOF (Ni-4PyC, $Ni_9(\mu\text{-}H_2O)_4(H_2O)_2(C_6NH_4O_2)_{18}$.solvent, IISERP-MOF1, with unusually high CO_2 saturation capacity (8.2 mmol/g) and outstanding CO_2/H_2 selectivity at high pressure. It also possesses favorable CO_2 diffusion coefficients and optimal heat of adsorption for low energy cycling under conditions relevant to PSA processes.[41] This was also straightforwardly synthesized in a one pot-synthesis employing a single *metal and single small, readily available linker*. This strategy in fact allow the easy scale-up for this MOF.[42] We have investigated the gas adsorption properties of IISERP-MOF1 for CO_2/H_2 separations and explore the origin of the unusually high CO_2 uptake by probing the adsorption sites via GCMC simulations.

2.2. Materials and Methods:

All the organic chemicals were purchased from Sigma Aldrich. The nickel salts were procured from Alfa Aesar. All reagents and solvents were used without any further purification.

2.2.1. Milligram Scale Synthesis:

A solvothermal reaction between Nickel carbonate (0.119 g; 1 mmol) and Pyridine-4-carboxylic acid (0.244 g; 2 mmol) in a solution containing 1.5 ml THF + 2.5 ml water + 2 ml MeOH was carried out at 150^{o}C for 72 hrs. A bright blue colored polycrystalline product was isolated by filtration and was washed with plenty of water and methanol. The air dried sample gave a yield of ~ 85% (based on Ni). The PXRD pattern indicated this to be a pure phase of IISERP-MOF1. We have also prepared 10-25 gms of this sample with an easy scale-up procedure. CHN analysis (calculated values within brackets: C: 43.45 (43.22); H: 3.62 (4.70); N: 7.02 (7.08)%. It was noted that the presence of THF was critical to the formation of this

phase. However, it could be exchanged in a post synthetic manner for methanol. Also, the use of nickel nitrate and other salts of nickel could not result in a pure phase of IISERP-MOF1. Initial pH: 4.0; Final pH: ~5.0.

2.2.2. Gram Scale Synthesis:

About 2.975 g of Nickel carbonate anhydrous was added to 6.1 g of 4-PyC in a solution containing 25 ml water + 20 ml MeOH + 10 ml THF, contents were stirred for 3 hours at room temperature. Contents were placed in a 123 ml teflon lined Parr stainless steel autoclave and heated at 150^{o}C for 72 hrs. A bright blue colored polycrystalline product identical in appearance to the smaller scale preparation was obtained. The air dried sample gave a yield of ~87% (based on Ni).

2.2.3. Single Crystal Structure Determination:

Single-crystal data was collected on a Bruker SMART APEX four-circle diffractometer equipped with a CMOS photon 100 detector (Bruker Systems Inc.) and with a Cu Kα radiation (1.5418 Å). The incident X-ray beam was focused and monochromated using Microfocus (IμS) system. Crystal of IISERP-MOF1 was mounted on nylon Cryo loops with Paratone-N oil. Data was collected at 173(2) K. Data was integrated using Bruker SAINT software and was corrected for absorption using SADABS. Structure was solved by Intrinsic Phasing module of the Direct methods and refined using the SHELXTL 97 software suite. All non-hydrogen atoms were located from iterative examination of difference F-maps following which the structure was refined using least-squares method. Hydrogen atoms were placed geometrically and placed in a riding model. Some of the 4-PyC units in the structure of IISERP-MOF1 were disordered over two sites and have been modeled satisfactorily using SIMU and DELU commands.

2.2.4. Analytical Characterizations:

Powder X-ray Diffraction

Powder XRDs were carried out using a Rigaku Miniflex-600 instrument and processed using PDXL software.

Thermogravimetric Analysis

Thermogravimetry was carried out on NETSZCH TGA-DSC system. The routine TGAs were done under N_2 gas flow (20 ml/min) (purge + protective) and samples were heated from RT to 550^{o}C at 2 K/min.

For the cycling experiments, no protective gas was used, and the gas flows were systematically switched between CO_2 and N_2 on the purge lines. The methanol exchanged sample of IISERP-MOF1 was loaded on to the Pt pans and evacuated for 16hrs prior to the runs. TGA and DSC calibration and corrections runs were done just prior to carrying out the cycling experiments. This seemed to be critical to obtain accurate data from these cycling experiments. Without these systematic preparations, the data were found to be highly over estimated.

IR Spectroscopy

IR spectra were obtained using a Nicolet ID5 attenuated total reflectance IR spectrometer operating at ambient temperature. The KBr pellets were used.

2.2.5. Adsorption Analysis:

All gas sorption isotherms were measured on a Micromeritics ASAP 2020HD or 3-FLEX instrument using ultra-high purity gases (≥ 4.8 grade). Samples were transferred to a glass tube for analysis, with dual stage activation: The as-made samples were solvent exchanged by soaking 200 mg in 7 ml methanol (reagent grade) for 72 hours, with the solvent being replenished every 24 hrs. Following this the 100 mg of the solvent exchanged sample was transferred to analysis glass vial and evacuated at 70°C on the degas port for 36 hrs (10^{-6} mbar), at which point the outgas rate was ≤ 2 μbar/min.

The rate of adsorption experiments were carried out on the Micromeritics ASAP2020HD instrument equipped with a ROA software capabilities. Numerous equilibrium points and associated kinetic data were recorded at 273 K, however for data analysis regularly spaced 10 CO_2 loading points were picked out in the interval of 0 to 1000 mbar.

Langmuir Fits

In most cases the isotherms were fit to the Single-Site Langmuir (SSL) equation. Modified Langmuir equations were utilized to account for significant errors in the Langmuir model. It is widely known that even small fitting errors will have a devastating impact on selectivity calculations. *Note:* 195 K CO_2 and N_2 isotherms were not used as the temperature is too close to the CO_2 phase change temperature.

The isotherms were fit by solving the Langmuir equation using the solver function in Microsoft Excel following a similar protocol to Keller *et al.*[43] Utilizing this routine circumvents some of the problems associated with favoring either high or low pressure

regions when linearizing the Langmuir equation as described by Richter *et al.*[44] and offers a balanced approach.

Single-Site Langmuir (SSL):

$$q_i = q_m \frac{K_i P}{1 + K_i P}$$

Dual-Site Langmuir (DSL):

$$q_i = q_{m,1} \frac{K_1 P}{1 + K_1 P} + q_{m,2} \frac{K_2 P}{1 + K_2 P}$$

Ideal Adsorbed Solution Theory (IAST)

IAST calculations were undertaken as described by Prausnitz *et al.*[45] The selectivity equation is provided below.

Selectivity:

$$S_{1,2} = \frac{q_1/q_2}{P_1/P_2}$$

Where, q_1 is the uptake of gas 1 at partial pressure of P_1 and q_2 is the uptake of gas 2 at partial pressure of P_2.

2.2.6. Positron Annihilation Lifetime Spectroscopy Experiment:

The Positron Annihilation Lifetime Spectroscopy (PALS) measurements were carried out at the positron facility of the NC State University. Ni-(4PyC), IISERP-MOF1, was characterized at RT before and after its thermal activation. Due to the small quantity of IISERP-MOF1, the aqueous ^{22}NaCl positron source was deposited and dried on a piece of Tungsten foil (4 mm in diameter), and the sample was directly placed on top of this one-sided source. In this configuration, half of the positrons from the source would be emitted towards the Tungsten foil. However, with the help of the high atomic number of Tungsten, approximately 40% of these positrons would be backscattered into the sample. Therefore, there would be ~70% of all the positrons implanted into the sample, while 30% into the Tungsten. The source and the sample were under vacuum throughout the process of heating and PALS measurement. The first time annealing of the sample was conducted at 90°C for 24 hrs. Another annealing at 100°C for 24 hrs was done after the sample cooled down to RT and the PALS spectrum was taken.

2.2.7. Column Breakthrough Test Set-up and Procedure:

About 10-12 gm of IISERP-MOF1 was loaded onto a stainless column fitted with mass flow controllers and pressure gauges to control the inlet and outlet pressures. IISERP-MOF1 was subjected to a pretreatment by heating at 70^{o}C under vacuum for 24 hours within the adsorption column. The CO_2/H_2 and CO_2/He breakthrough experiments were carried out using the RuboLab / Rubotherm VariPSA system. This instrument allows the measurement of breakthrough curves (BTC) on solid sorbent materials. Based on the sorbent the system settings were optimized. The adsorber column was designed to be approx. 8 ml in volume. To measure the sorption based temperature (adsorption front), three temperature sensors were integrated to measure the temperature at two different positions within the adsorber bed. (Thermocouple type K, 3 mm diameter of temperature sensor). The gas flow across the column was controlled using a micrometering valve. All measurements were performed by using a gas flow of 0.75 L/min. While the adsorption of CO_2 was indicated by its retention time on the column, the complete breakthrough of CO_2 was indicated by the downstream gas composition reaching that of the feed gas. Using the formula,

number of mole adsorbed $n = F * C_i * t$

where, F = molar flow, C_i = concentration of i^{th} component and t = retention time.

The CO_2 uptake was calculated to be 2.6 mmol/g for the $40CO_2/60He$ mixture and this uptake closely matched with the uptake obtained for the $40CO_2/60H_2$ mixture.

2.3. Results:

2.3.1. Single Crystal Structure Description:

The structure of IISERP-MOF1, shown in figure 2.1A, is built up from corner-sharing nickel dimers and isolated octahedral nickel centers (Figs. 2.A.1 and 2.A.2). There are two such nickel dimers, one built up from Ni(1) and Ni(2) atoms and the other from Ni(3), that are coordinated by PyC units and water molecules (terminal and bridging). The μ^2 water bridged Ni dimers[46,47] form the building unit of IISERP-MOF1 which are different from the μ^3 hydroxo bridged Ni clusters[48-50] reported in the literature. If the dimers are reduced to a node and the PyC moieties to linear linkers, the structure is a six-connected cubic network (Fig. 2.1). This three-dimensional framework consists of two types of channels and a cage system. Of the two channels, one is one-dimensionally aligned along the c-axis (~6.7 x 6.7 Å not accounting for the van der Waals radii). The other channel exhibits two-dimensional

accessibility along both a- and c- axes (7.8 x 7.8 Å and 7.5 x 7.5 Å), and four such channels surround the aforementioned one-dimensional channel.

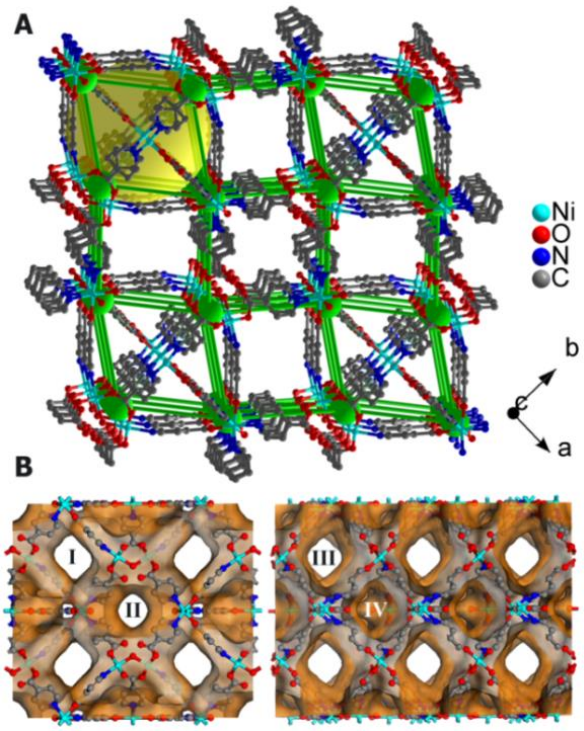

Figure 2.1. (A) Single crystal X-ray Structure of IISERP-MOF1 generated using OLEX, green balls-Ni dimers reduced to one node; Green sticks represent the PyC linker as lines. The green cones trace the six-connected distorted cubic arrangement; the yellow ball represents the cages. **(B)** The Connolly surface diagram of IISERP-MOF1 (probe radius = 1.4 Å). The channels labelled **I** and **III** are interconnected and run along the a- and c-axis respectively, while the channel labelled **II** is truly one-dimensional along the c-axis. **IV** represents the cages in IISERP-MOF1, which are lined with terminal water molecules in addition to the ligand groups.

The access to the one-dimensional channels from the a- and b-axes is blocked by the cages in the structure which are made up of the same nickel dimers which line the one-dimensional channels. These dimers are arranged into a square and are capped by two isolated nickel octahedra, Ni(5), on either side to generate the near-spherical cage (12 x 12 x 12 Å). Topologically, the channel system in IISERP-MOF1 is composed of alternating 2-D and the 1-D channels stacked long the b-axis (Fig. 2.1B). The carboxylate groups and bridging water molecules lining the channels impart a polar character to them. The ditopic PyC units were strongly disordered making the structure solution challenging; however, they could be modeled using a head-tail orientation. Obtaining the correct minimized geometry via disorder modeling was crucial to obtaining the correct chemical composition.

2.3.2. Porosity Analysis and CO_2 Adsorption Characteristics:

The N_2 adsorption isotherm at 77 K is given in Figure 2.2A confirms the permanent porosity and yields a BET surface area of 945 m^2/g. Despite the modest surface area, 195 K CO_2 uptake is markedly higher than that of most other ultra-microporous MOFs (Table 2.A.1). Figure 2.2B shows the CO_2 isotherms (up to 1 bar) over a range of temperatures which reveals a total uptake of 11mmol/g, 5.5mmol/g and 3.6mmol/g at 195 K, 273 K and 303 K respectively. The DFT model of the 195 K CO_2 adsorption branch resulted in a bimodal pore size distribution in the ultra-microporous regime with major pore sizes of 3.5 and 4.8 Å. (Fig. 2.A.11).

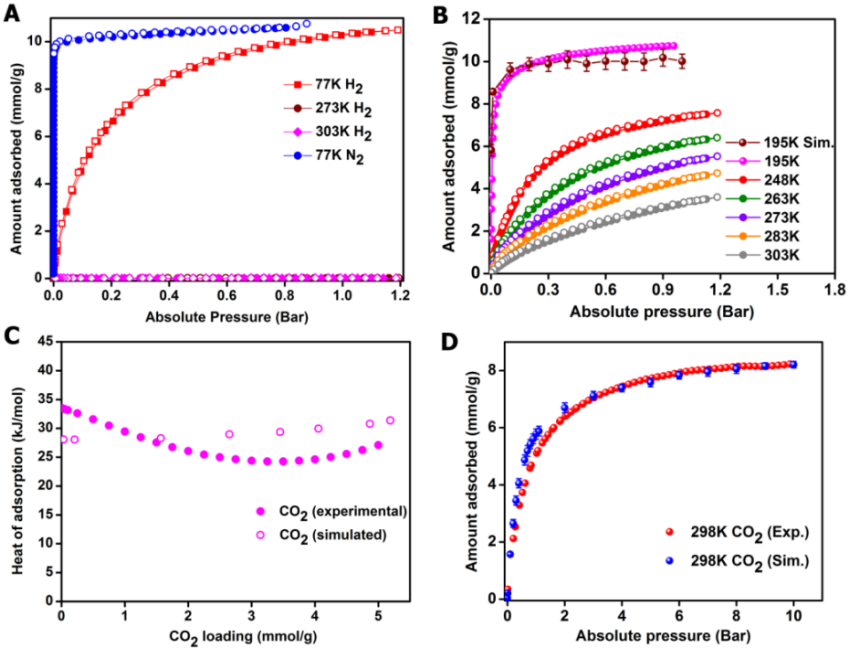

Figure 2.2. (A) Experimental H_2 and N_2 isotherms. **(B)** CO_2 sorption isotherms carried out at different temperatures (filled circles- adsorption; open circles- desorption). For CO_2 at 195 K, the simulated adsorption isotherm is shown. **(C)** Heat of adsorption for CO_2 obtained from a virial fit to isotherms at temperatures ranging from -25 °C to 30 °C. HOA determined from GCMC simulations at 25°C are also presented for a comparition. **(D)** Experimental and simulated high pressure CO_2 isotherms at 298 K.

A Positron Annihilation Lifetime Spectroscopy (PALS) measurement was also carried out to confirm the ultra-microporous character of IISERP-MOF1.[51] The PALS was recorded on a MeOH exchanged sample that was activated at 100°C for 24 hrs (See appendix section for more details). The spectra were least squares fit with the program POSFIT (Fig. 2.A.12),[52] using three lifetime components, as shown in Table 2.A.3. The fit to the 1.2-1.4 ns component of the o-Ps annihilation produced a spherical pore size of 3.9-4.4 Å, which is fairly consistent with the values obtained from the single crystal structure of IISERP-MOF1 as well as from the DFT fit to the 195 K CO_2 data. The CO_2 heat of adsorption in IISERP-

MOF1 was calculated via both virial and a DFT model using isotherms collected at -25°C, -10°C, 0°C, +10°C and +30°C. The virial fit presented in figure 2.2C shows that it has the zero-loading HOA value of 34 kJ/mol and this falls down to a value of 26 at ~2 mmol/g loading and settles down at a moderate 28 kJ/mol at higher loadings. Both the models showed a similar trend (Fig. 2.A.13).

2.3.3. Theoretical Calculations:

For an ultra-microporous material, IISERP-MOF1 exhibits exceptionally high CO_2 capacity of 11.0 mmol/g (at 195 K), which is indicative of that it might also poses a high CO_2 capacity at high pressure and high temperature, conditions pertinent to pre-combustion CO_2 capture and H_2 purification. The operatinal pressure of PSA systems used in pre-combustion CO_2 capture is typically 5-40 bar and happens at slightly elevated temperatures preferably at 40°C.[12,23] To explore this, we first carried out Grand canonical Monte Carlo Simulations (see Appendix section for details), which predicted a high CO_2 capacity of 8.2 mmol/g at 10 bar and 298 K. Since the simulated and experimental heats of adsorption and 195 K CO_2 adsorption isotherms were in good agreement with one another (Figs. 2.2B & C), this inspired us to measure the high pressure CO_2 adsorption. Figure 2.2D reveals that the simulated and experimental CO_2 adsorption between 1-10 bar and 298 K are in excellent agreement. In addition, the high pressure H_2 adsorption revealed that it did not show any appreciable H_2 uptake even at 35 bar (Fig. 2.A.16).

2.3.3.1. Adsorption Sites and Associated Energetic:

For an ultra-microporous material, the outstanding CO_2 capacity of IISERP-MOF1 near the saturation limits demands a molecular level investigation of the adsorption sites to realize how it is capable of accommodating such a large quantity of CO_2. To study this we examined the nature and location of the binding sites within Ni-4PyC via simulation. The GCMC simulations that are used to generate the adsorption isotherms also yield probability distributions of the guest molecules that can be used to locate the binding sites. We have performed a similar analysis on a ZnAtzOx MOF and found there to be excellent agreement between the computed CO_2 binding sites and those determined from crystallography.[32] The low temperature saturation limit of 11.0 mmol/g determined experimentally corresponds to approximately 28 CO_2 molecules per unit cell. Figure 2.3 shows the location of the strongest 30 binding sites, with binding energies ranging from -24.0 to -32.8 kJ/mol. These were calculated by geometry optimizing a single CO_2 molecule in the empty MOF starting from

the CO_2 position identified from the maxima of the probability distributions. Three main binding site regions were identified in this way that encompasses the main channels and cages previously described.

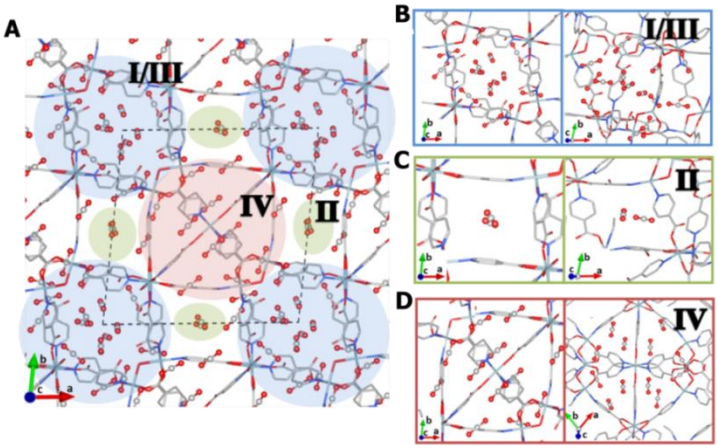

Figure 2.3. (A) A view looking down the c-axis of IISERP-MOF1 showing the top 30 CO_2 binding sites obtained from a GCMC simulation at 195 K, **1** bar. There are three distinct binding regions noted in blue-**I/III**, green-**II**, and red-**IV**. Binding region **I/III** corresponds to the 2-d channels depicted in figure 2.1B. Binding region **II** corresponds to the 1D channels labeled **II** in figure 2.1B. **IV** corresponds to the near-spherical cage. To the right are close ups and different views of binding regions **(B)** - **I/III**, **(C)** - **II** and (D) - **IV**.

The first region, labelled I/III in Figure 2.3, is contained within the intersection of channels I and III (Fig. 2.1). The second binding region labelled II is located within the 1D channel system first shown in figure 2.1. The third binding region contains the previously mentioned spherical cages, which are labelled region IV. Interestingly, the accessible surface area (calculated with a CO_2 probe radius) drops from 1194 m^2/g in the empty MOF, to < 1 m^2/g in the MOF with the 28 lowest energy CO_2 binding sites occupied demonstrating almost full saturation within IISERP-MOF1. Binding region IV possesses the strongest binding sites that are sandwiched between the aromatic planes of two PyC ligands, with binding energies ranging from -30.0 to -32.8 kJ/mol. The weakest binding sites are found in region II, which have binding energies of -24.0 to -27.2 kJ/mol. Interestingly, the binding in this region was found to have virtually no electrostatic component – in other words the binding was due almost entirely to dispersion interactions. This contrasts the binding sites in the other two regions (I/III and IV) whose binding energies were composed of up to 22% electrostatic interactions.

With a high density of binding sites, one might expect to see cooperative binding effects where bound guest molecules interact favorably with one another. By occupying the 28 most stable binding sites with CO_2, we find there is a significant cooperative binding

energy of 5.2 kJ/mol per guest molecule. In other words, with the 28 binding sites occupied there is a net stabilization of 146 kJ/mol due to favorable CO_2-CO_2 interactions. Interestingly, after 29 guest molecules (just beyond the low temperature saturation limit) the cooperative binding energy begins to diminish as additional CO_2 molecules interact unfavorably with existing guest molecules.[53] These results suggest that cooperative binding plays a significant role in the high CO_2 uptake capacities observed in Ni 4-PyC.

2.3.3.2. Selectivity and Working Capacity Calculation from Simulated Isotherms:

To more thoroughly examine the potential of this MOF for pre-combustion CO_2 capture, CO_2 and H_2 isotherms with binary mixtures of CO_2 and H_2 were simulated at 313 from 1-40 bar at two industrially relevant gas compositions - $80H_2$:$20CO_2$ and $60H_2$:$40CO_2$.

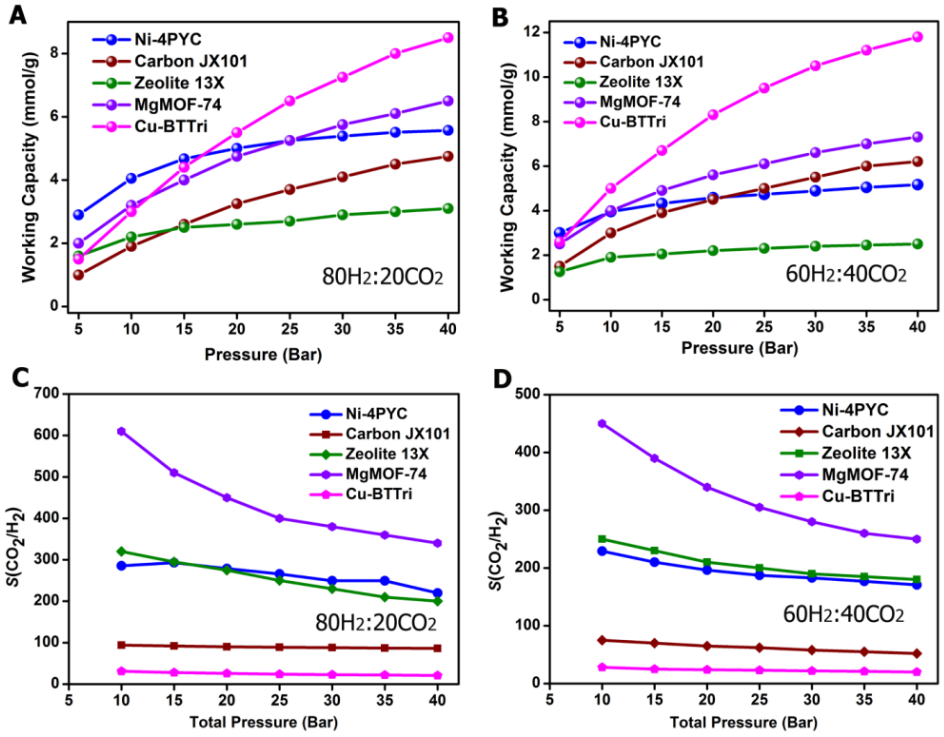

Figure 2.4. Working capacities and selectivity characteristics. **(A)** and **(B)** The working capacity of IISERP-MOF1 determined from simulation compared to that of several industrial sorbents and MOFs determined from (i) $80H_2$:$20CO_2$ and (ii) $60H_2$:$40CO_2$ gas mixtures at 313 K. The working capacities have been evaluated using a desorption pressure of 1 bar. **(C)** and **(D)** Comparison of the H_2/CO_2 selectivity of IISERP-MOF1 vs other known MOFs and industrial sorbents determined from (i) $80H_2$:$20CO_2$ and (ii) $60H_2$:$40CO_2$ gas mixtures at 313 K. Data for activated carbon JX101, zeolite 13X, Mg-MOF-74 and Cu-BTTri are taken from reference 23.

Figures 2.4A and 2.4B present the simulated PSA working capacities of this MOF (using a desorption pressure of 1 bar) against the working capacities of the recently reported industrial benchmarks zeolite 13X, activated carbon JX101, and two of the top performing MOFs, MgMOF-74 and CuBTTri.[23] A similar comparison of the CO_2/H_2 selectivities is presented in

Figures 2.4C and 2.4D at the two different H_2/CO_2 ratios. At low CO_2 concentrations (80% H_2, 20% CO_2), it exhibits the highest working capacity up to an adsorption pressure of 15 bar, but remains amongst the top performers in this respect throughout the whole pressure range. Only the MOF CuBTTri exhibits a significantly higher working capacity at pressures greater than 25 bar. Unfortunately, CuBTTri has a very poor H_2/CO_2 selectivity, the lowest of all the materials compared, making it not fitting for practical use [23]. However, at higher CO_2 concentrations (60% H_2, 40% CO_2), the working capacity of IISERP-MOF1 is less competitive. Nonetheless, when compared to zeolite 13X, which is used industrially for PSA based CO_2 scrubbing of natural gas, IISERP-MOF1 poses an almost identical CO_2/H_2 selectivity but nearly double the working capacity throughout the whole pressure range. When compared to the high performance activated carbon JX101, IISERP-MOF1 exhibits a higher working capacity for the 80:20 gas mixture, and a comparable working capacity for the 60:40 gas mixture throughout the whole pressure range. However, this MOF poses a CO_2/H_2 selectivity that is at least 2.5 times better than Carbon JX101 for both the gas compositions. Figure 2.4 shows that the MgMOF-74 has one of the largest working capacities at all pressures and both gas compositions. Moreover, in all cases MgMOF-74 exhibits the highest CO_2/H_2 selectivity, outperforming Ni4-PyC by at least 50% in this respect. Despite the favorable adsorption properties, MgMOF-74 is not hydrolytically stable due to the presence of open metal sites, which limits its practical use. We also note that IISERP-MOF1 poses one of the highest reported CO_2/H_2 selectivities of MOFs reported in the literature till date (See table 2.A.9. in the appendix section).

2.3.4. Stability Studies:

IISERP-MOF1 exhibits exceptional stability and recyclability properties, which are highly desirable for solid sorbents when employed in industrial PSA systems. A sample of IISERP-MOF1 upon exposure to steam for 160 hours retains the full crystallinity as observed from PXRD pattern (Fig. 2.5A). In another key experiment, it was maintained under a constant flow of humidified CO_2 (~ 30% relative humidity) for ~ 48 hrs. Figure 2.5B reveals that the CO_2 sorption isotherms are unaltered before and after this treatment. Also, a water vapor isotherm and a post adsorption PXRD further support its hydrolytic stability (Fig. 2.A.27). Even harsher humidity treatments did not seem to reduce its CO_2 capacity (Figs. 2.A.29 and 2.A.31). The exceptional hydrolytic stability of this MOF is accompanied by an excellent hydrostatic stability.[54] This MOF was found to retain its original porous structure after being subjected to 70 bar pressure for 24hrs as shown by the PXRD patterns presented

in figure 2.5A. In terms of shelf-life, we found that it retains > 90% of its porosity even upon exposing to ambient air for nearly 6 months (Fig. 2.A.33).

2.3.5. Cycling and Diffusion Kinetics Study:

IISERP-MOF1 displays smooth adsorption-desorption characteristics as depicted from TGA cycling experiments, shown in figure 2.5C. In this experiment the CO_2 uptake is cycled up to ~ 6.5% by weight at 35°C. During this experiment the CO_2 and N_2 were flowing in alternative cycles. It is clear from the figure 2.5C that a simple flow of N_2 is able to regenerate 100% of the adsorbed CO_2. This easy regeneration of CO_2 is attributable to the moderate interactions of CO_2 with the framework (HOA= 25-30 kJ/mol, optimal for a pressure swing).[41] This experiment fabricates the same results if He is used instead of N_2 as a sweep gas.

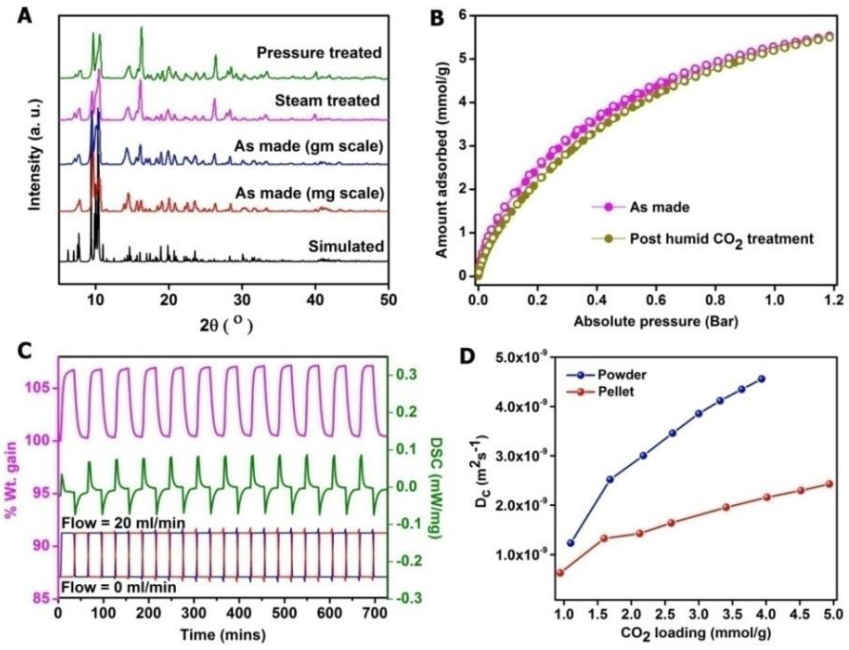

Figure 2.5. (A) PXRDs showing the hydrolytic, hydrostatic stabilities and the homogeneity of the mg and gm scale synthesis of IISERP-MOF1. **(B)** CO_2 adsorption isotherms of IISERP-MOF1 at 273 K for as made, and following exposure to humid (30% RH) CO_2 for 48 hrs. (filled circles- adsorption; open circles- desorption) **(C)** TGA cycling data on IISERP-MOF1 carried out at 308 K. Blue: CO_2 flow; Red: N_2 flow. **(D)** Diffusion coefficient as a function of CO_2 loading from eight loadings at 273 K for both the powder form and the pelletized forms of IISERP-MOF1.

When employed as solid sorbents in a PSA system, the tiny pores of ultra-microporous MOF may tremendously restrict the adsorption and desorption times in real operating conditions. This necessitates an examination of the kinetics associated with the CO_2 diffusion within the pores of IISERP-MOF1. For this a high resolution rate of adsorption

measurement was performed using the ASAP2020HD instrument at 273K in the pressure range of 0-1bar and 8 different pressure points were used to determine the diffusion coefficients by fitting them against a spherical pore model (Fig. 2.A.35).[55] From this, an average diffusion coefficient (Dc) of 3.03 x 10^{-9} m^2s^{-1} for CO_2 was calculated (Fig. 2.5D). On the other hand, the simulations yielded a Dc of 3.73 x 10^{-9} m^2s^{-1} at 298K under the flue gas compositions which matched well with the experimental Dc (Fig. 2.A.35). Importantly, this diffusivity is similar to those observed in some of the microporous MOFs, ZIF-8: 8 x 10^{-10}; MIL-53(Cr): ~5 x 10^{-8}; MOF-5: 1.17 x 10^{-9} and MOF-177: 2.3 x 10^{-9} m^2s^{-1} at 298 K.[56-60] The diffusion coefficient of IISERP-MOF1 is atleast two orders of magnitude higher than that observed for zeolite-13X which is currently being used in PSA scrubbers for natural gas purification.[58,60] Considering the practical application, when the CO_2 self-diffusion coefficient was measured using a pelletized form of IISERP-MOF1, only a minor drop in its value was observed (1.66 x 10^{-9} m^2s^{-1}, Fig. 2.5D).

2.3.6. Mixed Gas Analysis; Breakthrough Experiments:

To further validate the adsorption of CO_2 from a binary gas mixture, we Performed adsorption breakthrough measurements employing 60%H_2:40%CO_2 and 60%He:40%CO_2 mixtures on a Rubotherm VariPSA system fitted with a Non-dispersive Infrared (NDIR) sensor (see Appendix section for more details).

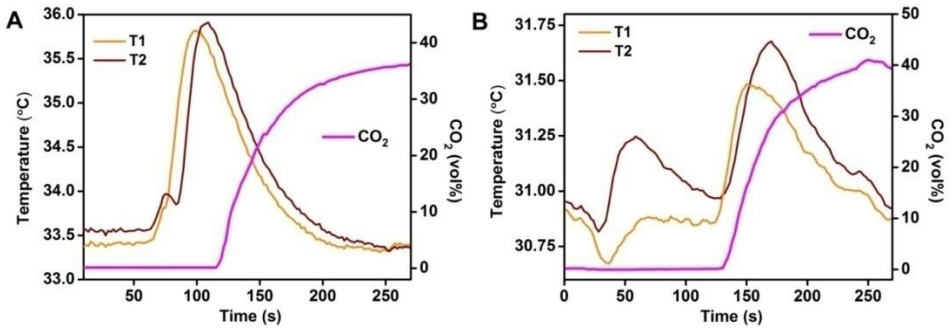

Figure 2.6. (A) Breakthrough curve for the 60%H_2:40%CO_2 binary component mixture measured at 298 K, 1bar. **(B)** Breakthrough curve for the 60%He:40%CO_2 binary component mixture measured at 298 K, 1bar. T1 and T2 represent the bed temperatures measured at two points along the column (adsorption front).

The temperature sensors positioned along the sample holder showed the noticeable increase in column temperature following the CO_2 adsorption. The complete breakthrough of CO_2 was pointed out by the downstream gas composition reaching that of the feed gas. The breakthrough profiles and CO_2 retention times for both gas mixtures were similar indicating good apparent selectivity for CO_2 over H_2 (Fig. 2.6). Also, when the column dimensions,

sample mass and the flow rates were normalized, the CO_2 retention times were similar to those observed for other ultra-microporous MOFs.[31] However, a quantitative measurements of CO_2/H_2 selectivity were not possible due to the lack of a direct method to determine the concentrations of H_2 adsorbed.

2.3.7. Scale-up Synthesis in Laboratory:

The laboratory gram scale synthesis is becoming a norm as a potential prerequisite for a future large scale synthesis.[42] The initial 150 mg solvothermal synthesis of IISERP-MOF1, could easily be scaled up to about 10-25 gms via a simple procedure (See Materials and Methods). This makes the single ligand MOF Ni 4-PyC an attractive candidate for the kg level scale ups necessary for actual PSA applications. In contrast, multi-ligand synthesis often leads to the challenge of competing phases precipitating from a one pot mixture, which is a serious impediment to large scale synthesis. In fact, some of the most widely researched and commercially sold MOFs such as HKUST-1, MOF-5, SNU, ZIF, MIL and PCN series and are made up of single ligand.[61]

2.4. Discussion:

Ni 4-PyC, serves as an excellent prototype for representing how an ultra-microporous MOF built from a small and readily available ligand, can have highly favorable adsorption/desorption characteristics for gas separation processes, despite having pores < 6 Å in size and a modest surface area (945 m^2/g). It exhibits working capacities and CO_2/H_2 selectivities for PSA based pre-combustion CO_2 capture that is competitive with the best known MOFs for that application. Simulations of the CO_2 adsorption in it, suggest that strong cooperative guest-guest interactions, in part, allow for the exceptional 8.2 mmol/g CO_2 uptake capacity of IISERP-MOF1 at 10 bar, 298 K. In addition to possessing favorable gas adsorption properties, Ni 4-PyC also exhibits excellent stability and recyclability properties that are critical for practical operation in gas separation processes. Following 160 hours of steam treatment and 24 hours of exposure to 70 bar pressure, Ni-4PyC structure remains unchanged. Moreover, it retains its CO_2 adsorption properties following exposure to water. The simple, single ligand synthesis and isolation to the gram scale suggests that potential industrial-level scale ups should also be straight forward. With all these features and considering it is built from inexpensive and readily available components, IISERP-MOF1 is an attractive candidate for a variety of hydrogen purification applications. Such comprehensive performance with clear synthetic advantages from IISERP-MOF1 should

prompt revisiting ultra-microporous MOFs using small ligands as a design target for solid sorbents for gas separation applications.

2.5. References:

1. Longwell, J. P.; Rubin, E. S.; Wilson, J.; *Prog. Energy Combust. Sci*. **1995**, *21*, 269-360.
2. International Energy Agency, Coal: Medium term market report. (9 rue de la Fédération, 75739 Paris Cedex 15, France. **2012** and **2014**)
3. Samanta, A.; Zhao, A; Shimizu, G. K. H.; Sarkar, P.; Gupta, R. *Ind. Eng. Chem. Res.* **2012**, *51*, 1438-1463.
4. D'Alessandro, D. M.; Smit, B.; Long, J. R. *Angew. Chem. Int. Ed*. **2010**, *49*, 6058-6082.
5. Liu, K.; Song, C.; Subramani, V. *Hydrogen and Syngas Production and Purification Technologies.* (Eds.; Wiley-AIChE: Hoboken, NJ, **2010**, 414-450).
6. Rand, D. A. J.; Dell, R. M.; *Hydrogen Energy : Challenges and Prospects*. (Copyright: 2008, eISBN: 978-1-84755-802-2, DOI:10.1039/9781847558022).
7. Mukherjee, S.; Kumar, P.; Hosseini, A.; Yang, A.; Fennell, P. *Energy Fuels* **2014**, *28*, 1028-1040 and references therein.
8. Agarwal, A.; Biegler, L. T.; Zitney, S. E. *Ind. Eng. Chem. Res*. **2010**, *49*, 5066.
9. Wang, Q.; Chen, W. -Y.; Seiner, J.; Suzuki, T.; Lackner, M. *Hydrogen Production.* (Handbook of Climate Change Mitigation, **2012**, 1091-1130, Springer).
10. Akten, E. D.; Siriwardane, R.; Sholl, D. S. *Energy Fuels* **2003**, *17*, 977.
11. Cao, D.; Wu, J. *Carbon* **2005**, *43*, 1364.
12. Sircar, S.; Golden, T. C. *Sep. Sci. Technol*. **2000**, *35*, 667-687.
13. Li, J. -R.; Ma, Y.; McCarthy, M. C.; Sculley, J.; Yu, J.; Jeong, H. -K.; Balbuena, P. B.; Zhou, H. -C. *Coordination Chemistry Reviews* **2011**, *255*, 1791-1823.
14. Furukawa, H.; Cordova, K. E.; O'Keeffe, M.; Yaghi, O. M. *Science* **2013**, *341*, 974.
15. Zhou, H.-C. J.; Kitagawa, S. *Chem. Soc. Rev*. **2014**, *43*, 5415-5418.
16. Liu, Q.; Ning, L.; Zheng, S.; Tao, M.; Shi, Y.; He, Y. *Sci. Rep.* 3, 2916.
17. Yang, S.; Lin, X.; Lewis, W.; Suyetin, M.; Bichoutskaia, E.; Parker, J. E.; Tang, C. C.; Allan, D. R.; Rizkallah, P. J.; Hubberstey, P.; Champness, N. R.; Thomas, K. M.; Blake, A. J.; Schröder, M. *Nat. Mater*. **2012**, *11*, 710-716.

18. Dzubak, A. L.; Lin, L.-C.; Kim, J.; Swisher, J. A.; Poloni, R.; Maximoff, S. N.; Smit, B.; Gagliardi, L. *Nat. Chem*. **2012**, *4*, 810-816.
19. Mason, J. A.; Sumida, K.; Herm, Z. R.; Krishna, R.; Long, J. R. *Energy Environ. Sci.* **2011**, *4*, 3030-3040.
20. Andersen, A.; Divekar, S.; Dasgupta, S.; Cavka,J. H.; Aarti, Nanoti, A.; Spjelkavik, A.; Goswami, A. N.; Garg, M. O.; Blom, R. *Energy Procedia* **2013**, *37*, 33-39.
21. Xiang, S.; He, Y.; Zhang, Z.; Wu, H.; Zhou, W.; Krishna, R.; Chen, B. *Nat. Commun*. **2012**, *3*, 954.
22. 5. Huck, J. M.; Lin, L. -C.; Berger, A. H.; Shahrak, M. N.; Martin, R. L.; Bhown, A. S.; Haranczyk, M.; Reuterb, K.; Smit, B. *Energy Environ. Sci*. **2014**, *7*, 4132.
23. Herm, Z. R.; Swisher, J. A.; Smit, B.; Krishna, R.; Long, J. R. *J. Am. Chem. Soc*. **2011**, *133*, 5664-5667.
24. He, Y.; Xiang, S.; Zhang, Z.; Xiong, S.; Wu, C.; Zhou, W.; Yildirim, T.; Krishna, R.; Chen, B. *J. Mater. Chem. A* **2013**, *1*, 2543-2551.
25. Reddy, S.; Vyas, S. *Energy Procedia* **2009**, *1*, 149-154.
26. Qingyuan, Y.; Qing, X.; Bei, L.; Chongli, Z.; Smit, B. *Chinese Journal of Chemical Engineering* **2009**, *17*, 781-790.
27. Chou, C. -T.; Chen, F. -H.; Huang, Y.-J.; Yang, H.-S. *Chemical Engineering Transactions* **2013**, *32*, 1855.
28. Kizzie, A. C.; Wong-Foy, A. G.; Matzger, A. J. *Langmuir* **2011**, *27*, 6368-6373.
29. Saha, D.; Deng, S. *J. Phys. Chem. Lett*. **2010**, *1*, 73-78.
30. Yu, J.; Balbuena, P. B. *J. Phys. Chem. C* **2013**, *117*, 3383-3388.
31. Nugent, P.; Belmabkhout, Y.; Burd, S. D.; Cairns, A. J.; Luebke, R.; Forrest, K.; Pham, T.; Ma, S.; Space, B.; Wojtas, L.; Eddaoudi, M.; Zaworotko, M. J. *Nature* **2013**, *495*, 80-84.
32. Vaidhyanathan, R.; Iremonger, S. S.; Shimizu, G. K. H.; Boyd, P. G.; Alavi, S.; Woo, T. K. *Science* **2010**, *330*, 650-653.
33. Bosch, M.; Zhang, M.; Zhou, H.- C. *Advances in Chemistry* **2014**, *2014*, Article ID 182327, doi.org/10.1155/2014/182327.
34. Dinca, M.; Yu, A. F.; Long, J. R. *J. Am. Chem. Soc*. **2006**, *128*, 8904-8913.
35. Taylor, J. M.; Mahmoudkhani, A. H.; Shimizu, G. K. H. *Angew. Chem. Int. Ed*. **2007**, *46*, 795-798.

36. Bae, Y. -S.; Dubbeldam, D.; Nelson, A.; Walton, K. S.; Hupp, J. T.; Snurr, R. Q. *Chem. Mater*. **2009**, *21*, 4768-4777.
37. J. H. Cavka, Jakobsen, S.; Olsbye, U.; Guillou, N.; Lamberti, C.; Bordiga, S.; Lillerud, K. P. *J. Am. Chem. Soc*. **2008**, *130*, 13850-13851.
38. Kalidindi, S. B.; Nayak, S.; Briggs, M. E.; Jansat, S.; Katsoulidis, A. P.; Miller, G. J.; Warren, J. E.; Antypov, D.; Cor, F.; Slater, B.; Prestly, M. R.; Marti-Gastaldo, C.; Rosseinsky, M. J. *Angew. Chem. Int. Ed*. **2015**, *54*, 221-226.
39. Feng, D.; Wang, K.; Su, J.; Liu, T. -F.; Park, J.; Wei, Z.; Bosch, M.; Yakovenko, A.; Zou, X.; Zhou, H. -C. *Angew. Chem. Int. Ed*. **2015**, *54*, 149 -154.
40. Zhao, D.; Yuan, D.; Sun, D.; Zhou, H. -C. *J. Am. Chem. Soc*. **2009**, *131*, 9186-9188.
41. Simmons, J. M.; Wu, H.; Zhou, W.; Yildirim, T.; *Energy Environ. Sci*. **2011**, *4*, 2177–2185.
42. Yang, Q.; Vaesen, S.; Ragon, F.; Wiersum, A. D.; Wu, D.; Lago, A.; Devic, T.; Martineau, C; Taulelle, F.; Llewellyn, P. L.; Jobic, H.; Zhong, C.; Serre, C.; Weireld, G. D.; Maurin, G. *Angew. Chem. Int. Ed*. **2013**, *52*, 10316-10320.
43. Kemmer, G.; Keller, S. *Nat. Protoc*. **2010**, *5*, 267–281.
44. Richter, E.; Schuetz, W.; Myers, A. L. *Chem. Eng. Sci*. **1989**, *44*, 1609–1616.
45. Myers, A. L.; Prausnitz, J. M. *AIChE J*. **1965**, *11*, 121–127.
46. Yang, G. -S.; Lan, Y. -Q.; Zang, H. -Y.; Shao, K. -Z.; Wang, X. -L.; Su, Z. -M.; Jiang, C. –J. *CrystEngComm* **2009**, *11*, 274-277.
47. Kumalah, S. A.; Holman, K. T. *Inorg. Chem*. **2009**, *48*, 6860-6872.
48. Zhang, Y.-B.; Zhou, H.-L.; Lin, R.-B.; Zhang, C.; Lin, J.-B.; Zhang, J.-P.; Chen, X.-M. *Nat. Commun*. **2012**, *3*, 642. And references therein.
49. Jiang, G.; Wu, T.; Zheng, S. -T.; Zhao, X.; Lin, Q.; Bu, X.; Feng, P. Cryst.*Growth Des*. **2011**, *11*, 3713-3716.
50. Cortijo, M.; Herrero, S.; Jimenez-Aparicio, R.; Perles, J.; Priego, J. L.; Torralvo, M. J.; Torroba, J. *Eur. J. Inorg. Chem*. **2013**, 2580-2590.
51. Liu, M.; Wong-Foy, A. G.; Vallery, R. S.; Frieze, W. E.; Schnobrich, J. K.; Gidley, D. W.; Matzger, A. J. *Adv. Mater*. **2010**, *22*, 1598-1601.
52. Kirkegaard, P.; Eldrup, M.; Comp. Phy. Commun. **1974**, *7*, 401.
53. Vaidhyanathan, R.; Iremonger, S. S.; Shimizu, G. K. H.; Boyd, P. G.; Alavi, S.; Woo, *Angew. Chem. Int. Ed*. **2012**, *51*, 1826-1829.

54. Chapman, K. W.; Halder, G. J.; Chupas, P. J. *J. Am. Chem. Soc*. **2009**, *131*, 17546-17547.

55. Malek, K; Coppensa, M.-O. *J. Chem. Phys*. **2003**, *119*, 2801.

56. Zhang, L; Wu, G.; Jiang, J. *J. Phys. Chem. C* **2014**, *118*, 8788-8794.

57. Salles, F.; Jobic, H.; Ghoufi, A.; Llewellyn, P. L.; Serre, C.; Bourrelly, S.; Frey, G.; Maurin, G. *Angew. Chem. Int. Ed*. **2009**, *48*, 8335-8339.

58. Zhao, Z.; Li, Z; Lin, Y. S. *Ind. Eng. Chem. Res*. **2009**, *48*, 10015-10020.

59. Saha, D.; Bao, Z.; Jia, F.; Deng, S. *Environ. Sci. Technol*. **2010**, *44*, 1820-1826.

60. Silva, J. A.C.; Schumann, K; Rodrigues, A. E. *Micro. Meso. Mater*. **2012**, *158*, 219-228 .

61. Basosiv™ M050 (Magnesium formate), Basolite® Z1200 (Zn-methylimidazole, ZIF-8), Basolite® C300/F300 (Cu or Fe trimesate, HKUST-1), Basolite® A100 (Aluminum terephthalate, MIL-53) all sold under Sigma-Aldrich trademark.

2.A. Appendix for Chapter 2:

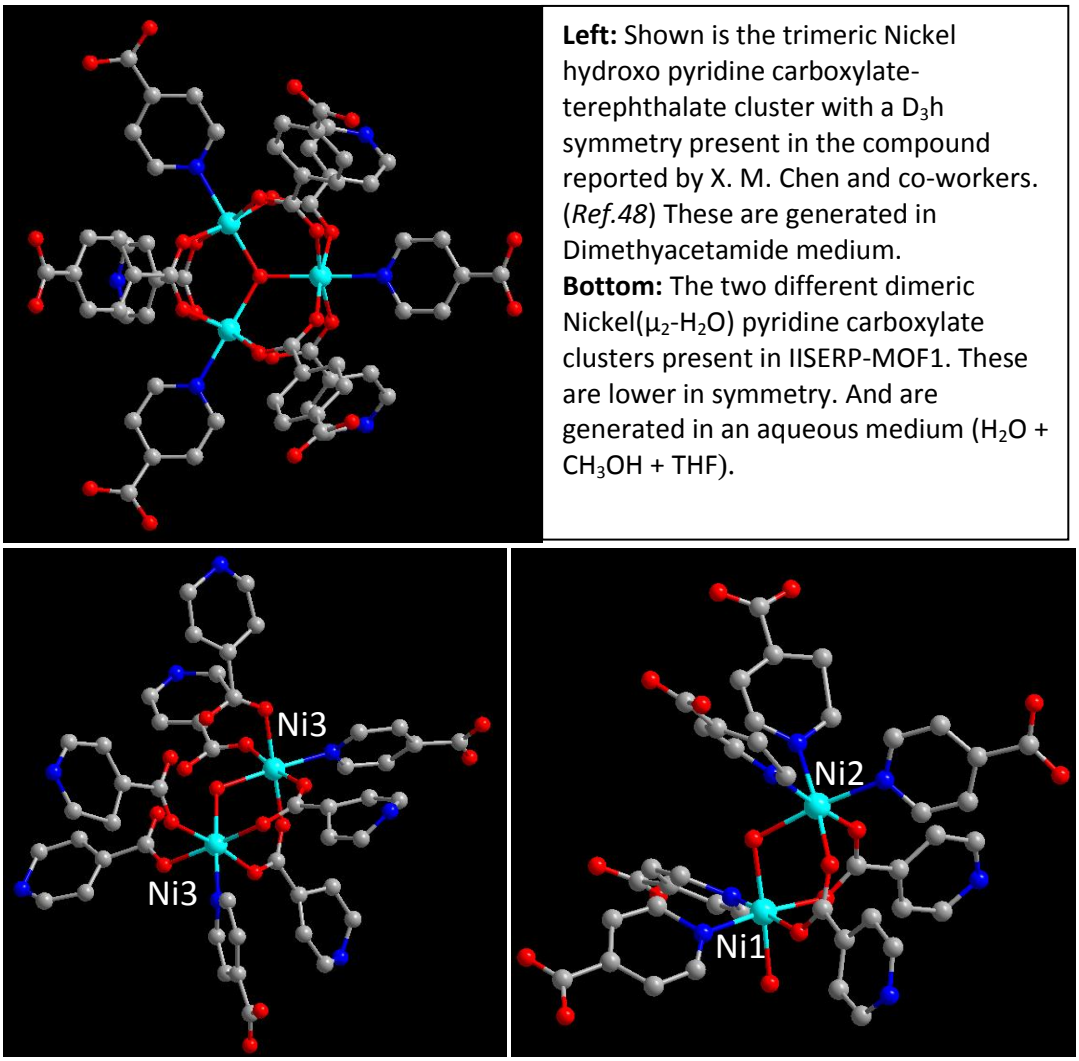

Left: Shown is the trimeric Nickel hydroxo pyridine carboxylate-terephthalate cluster with a D_3h symmetry present in the compound reported by X. M. Chen and co-workers. (*Ref.48*) These are generated in Dimethyacetamide medium.
Bottom: The two different dimeric Nickel(μ_2-H_2O) pyridine carboxylate clusters present in IISERP-MOF1. These are lower in symmetry. And are generated in an aqueous medium (H_2O + CH_3OH + THF).

Figure 2.A.1. Comparison of the Nickel clusters present in IISERP-MOF1, with the recently reported nickel clusters in a pyridine carboxylate based MOF. Note that these hydroxo and water based clusters have much better stability toward hydrolysis in air as compared to the oxo-type clusters present in many widely studied MOFs synthesized in DMF or DMA medium. These molecular level features could play a critical role in the hydrolytic stability of the material. The dimers formed of Ni3 atoms connects to the other dimers (Ni1, Ni2) and also to the isolated nickel octahedra formed by Ni4, not shown here.

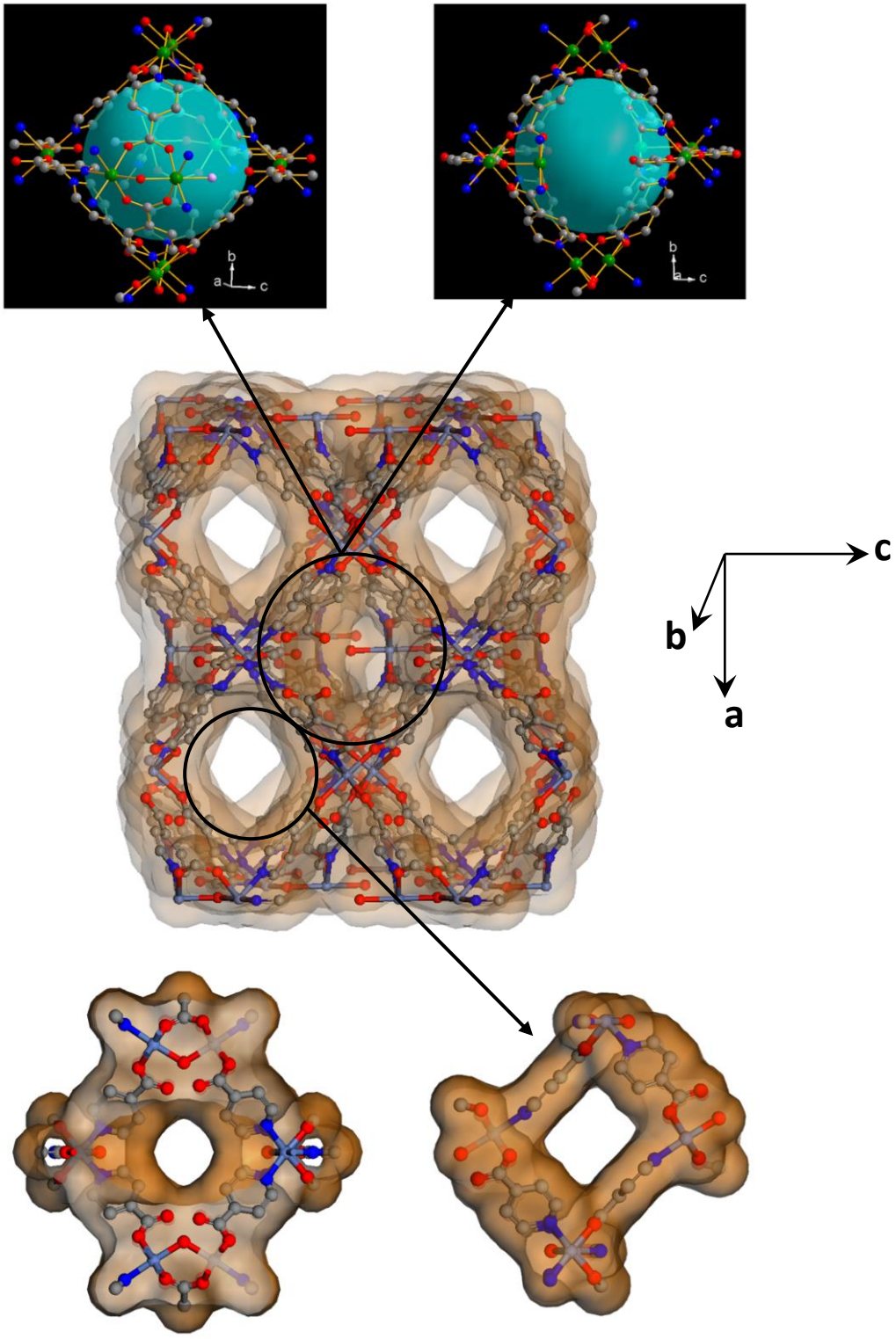

Figure 2.A.2. Top: The water lined cavities in IISERP-MOF1, these are not accessible even upon the removal of cooridnated water (Top right) and do not contribute to overall porosity. Shown are the two accessible channels in IISERP-MOF1, the circular one is along the c-axis, while the square shaped one is along the b-axis. Notice that the former is polar.

Table 2.A.1. CO_2 uptakes at 195 K and 273 K for selected ultra- and microporous MOFs.

MOF	Pore dia. (Å)	CO_2 uptake (mmol/g)		HOA (kJ/mol)	Reference
		195K	273K		
BioMOF-11	5.80(cavity) & 5.20x5.20 (window)a	------	6.56	33.1	Chem. Sci. 4, 1746 (2013)
BioMOF-12	5.70(cavity) & 5.20x5.00 (window)a	------	4.5	38.4	Chem. Sci. 4, 1746 (2013)
ZIF-78	7.10e	------	3.34	------	J Am Chem Soc. 131, 3875 (2009)
ZIF-69	7.80e	------	3.03	------	J Am Chem Soc. 131, 3875 (2009)
Cu-TDPAT	cub-Oh size-12a T-Td size-9.1a T-Oh size-17.2a	------	10.1	42.2	Angew. Chem. Int. Ed. 51, 1412 (2012)
SNU-M10	4.85 x 12.12 and 1.21x4.37a	5.4	3.2	------	Angew. Chem. Int. Ed. 48, 6865 (2009)
SNU-M11	1.16 x 6.29a	5.35	Very low		Angew. Chem. Int. Ed., 48, 6865 (2009)
Cu-BTTri	----------	19	3.9	22	J. Am. Chem. Soc. 131, 8784 (2009)
Ni 4-PyC	3.48, 4.80b	10.8	5.53	34	Present work
Mg(DOBDC)	10.81b	------	10.30	48	J. Am. Chem. Soc. 130, 10870 (2008)
IR MOF-11	9.03b	------	------	------	Energy Environ.Sci. 3,268 (2010)
IR MOF-12	13.02b	------	------	------	Energy Environ.Sci. 3, 268 (2010)
IR MOF-13	10.00 b	------	------	------	Energy Environ.Sci. 3, 268 (2010)
IR MOF-14	13.80b	------	------	------	Energy Environ.Sci. 3, 268, (2010)
PCN-61	12.00b	------	5.71	21.4	J.Am.Chem.Soc. 133,748 (2011)
NJU_Bai7	---------	------	2.95	40.5	J. Am. Chem. Soc. 135, 562 (2013)
SYSU	6.3 × 6.3a	------	4.5	28.2	J. Am. Chem. Soc. 135, 562 (2013)
[Ni3(μ3OH)(ina)3(bdc) 1.5]·2.5DMA·CH3OH	7.80a 7.40a 5.20a	9.35	------	------	Nature Comm.3, 1 (2011)
ZTF-1	4.50a	------	5.35	22.5	Chem. Commun. 47, 2011 (2011)
ZnAtzOx	4.7 & 5.15b	4.30	4.25	40	Science, 650, 330 (2010)
ZnAtzPO4	5.6 & 7.8b	4.85	3.2	32	Angew. Chem. Int. Ed. 51, 1826 (2012)
BioMOF-1	12.77x12.77a 9.97x9.97	------	3.41	21.9	J. Am. Chem. Soc. 132, 5578 (2010)
TMA@BioMOF-1	,,	------	4.46	23.9	J. Am. Chem. Soc. 132,

					5578 (2010)
TEA@BioMOF-1	,,	------	4.16	26.5	J. Am. Chem. Soc. 132, 5578 (2010)
TBA@BioMOF-1	,,	------	3.44	31.2	J. Am. Chem. Soc. 132, 5578 (2010)
SIFSIX-3-Cu	3.50e	------	2.54(298K)	54	DOI: 10.1038/ncomms. 5228 (2014)
SIFSIX-3-Zn	3.84e	------	2.40(298K)	45	DOI: 10.1038/ ncomms. 5228 (2014)

[a] Experimentally determined. [b] Calculated from Single crystal structure (do not factor in the Van Der waal radii). ------- = Data not available.

Analytical Characterizations:

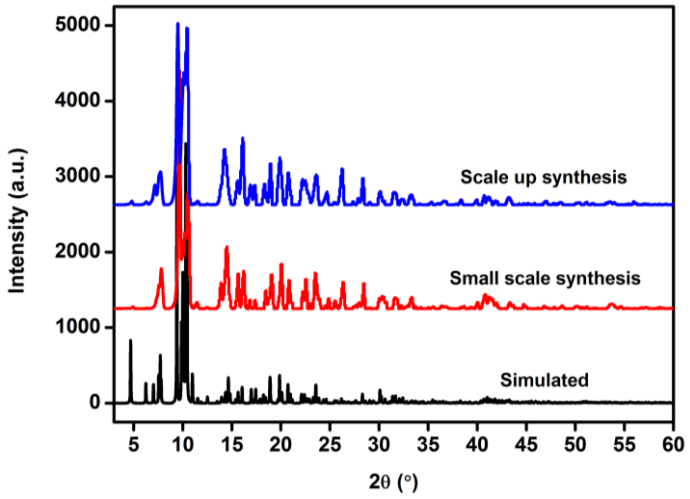

Figure 2.A.3. Comparison of the powder X-ray diffraction patterns of IISERP-MOF1 with the ones simulated from single crystal data.

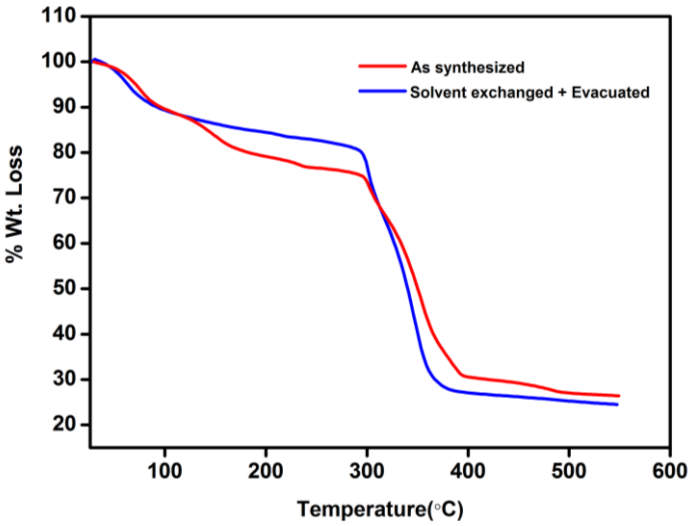

Figure 2.A.4. TGA plots of the as-made sample and the completely activated sample.

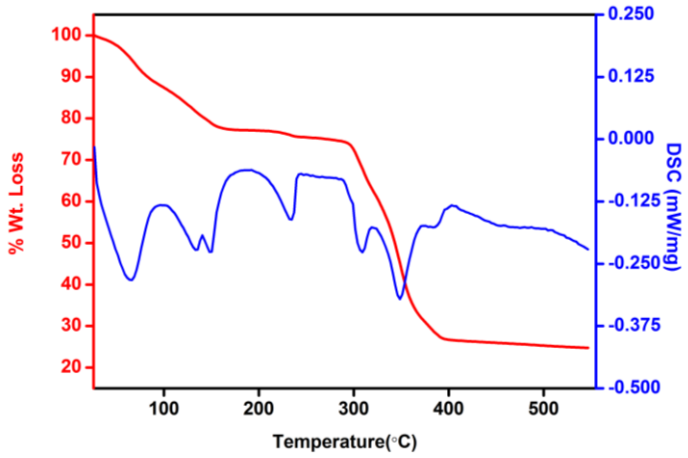

Figure 2.A.5. TGA carried out on the methanol exchanged sample of IISERP-MOF1. The weight loss have been calculated using the formula $Ni_9(\mu\text{-}H_2O)_4(H_2O)_2(C_6NH_4O_2)_{18}(H_2O)_{17}(CH_3OH)_4(C_4H_8O)_4$ (M. Wt. **3557.2**) . All the volatile solvent molecules are removed by 100°C (4 THF + 4 MeOH + 2 H_2O (surface adsorbed) loss, calc: 12.71%, obsd: 12.7), while most of the free solvent water and the coordinated water come off at 180°C (calc: 9.61%; obsd: 10.21). Some of the water molecules (2.02%) do not leave the structure even at 200°C. It is highly likely that this is some of the bridging water molecules (calc: 2.05%) that are crucial for holding the framework together. The loss of this 2% water triggers the collapse of the structure.

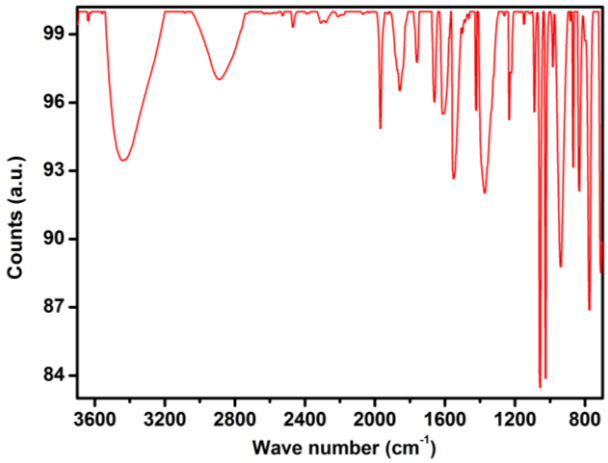

Figure 2.A.6. Infra red spectra of IISERP-MOF1, showing the various stretching and bending modes present . Selected peaks: IR (KBr pellet, cm-1): ν(O-H)solvent: 3460s; ν(C-H): 2989; ν(COO): 1656s and 1594vs, ν(COO)s 1423s, 1373 νs; ν (C=C): 1200 to 800.

Adsorption Studies:

Table 2.A.2. CO_2 adsorption and desorption data of IISERP-MOF1 at 195 K.

Adsorption		Desorption	
Absolute Pressure (mmHg)	Amount adsorbed (mmol/g)	Absolute Pressure (mmHg)	Amount adsorbed (mmol/g)
0.326985	0.994017	702.613	10.74472
0.995764	1.802344	666.5468	10.69284
1.664418	2.463762	635.6925	10.64847

2.810029	3.395624	604.3189	10.59939
4.665151	4.677797	574.3057	10.55156
9.078659	6.326634	542.7305	10.49995
12.98214	6.955803	512.0017	10.45088
17.32202	7.374822	482.4595	10.4034
21.54473	7.647347	450.4844	10.34625
35.99794	8.201156	419.851	10.28622
48.14801	8.476302	388.6154	10.21997
60.27357	8.679774	357.8197	10.15184
79.99664	8.918617	327.6313	10.08352
90.18822	9.016615	296.299	10.00777
100.3322	9.1075	265.7375	9.926239
129.4362	9.302295	235.2899	9.83405
143.3174	9.383777	204.7804	9.731097
157.9865	9.462093	173.999	9.609619
171.7103	9.526138	143.3287	9.457468
186.3498	9.589897	112.362	9.269522
201.0119	9.649938	81.5944	9.008897
214.5985	9.699312	50.62249	8.595077
229.3281	9.752921	35.36989	8.2579
243.5784	9.799399	19.97945	7.627915
272.3251	9.880699	12.14666	6.920757
300.1215	9.957195	4.473279	4.62628
328.6635	10.02957	1.00466	1.833463
344.4715	10.07298		
357.3972	10.1043		
385.7692	10.16378		
414.7627	10.22106		
443.475	10.27739		
473.2558	10.33604		
500.6811	10.38649		
529.3032	10.43835		
557.9955	10.49106		
586.8552	10.54366		
615.5965	10.59726		
645.4814	10.64686		
674.0063	10.69388		
702.613	10.74472		

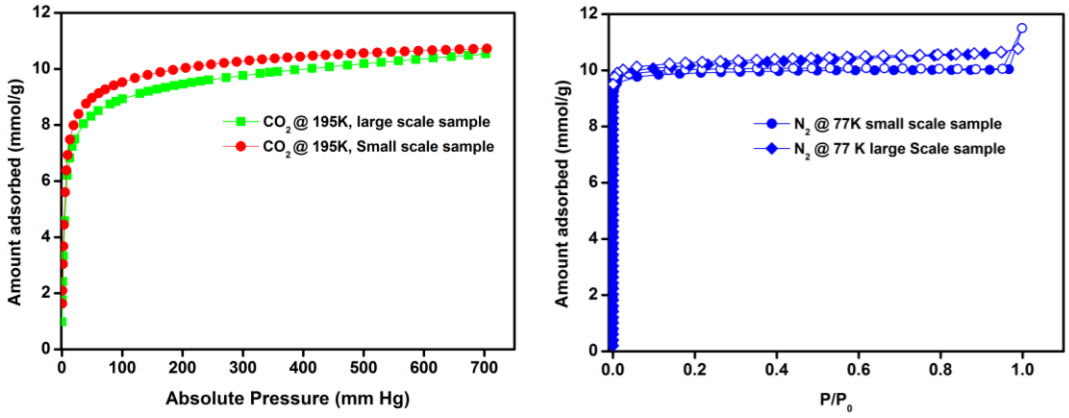

Figure 2.A.7. Comparison of the 195 K CO_2 and 77 K N_2 adsorption isotherms of the mg and gm scale syntheses, showing the laboratory scale scalability. The DFT done to the adsorption branch of the isotherm gives a pore size of 5.76 Å.

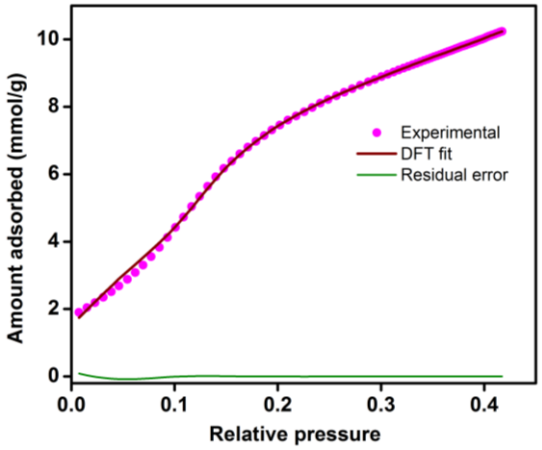

Figure 2.A.8. Shows the fitting comparison obtained for the NLDFT fit done to the adsorption branch of the 195 K CO_2 data.

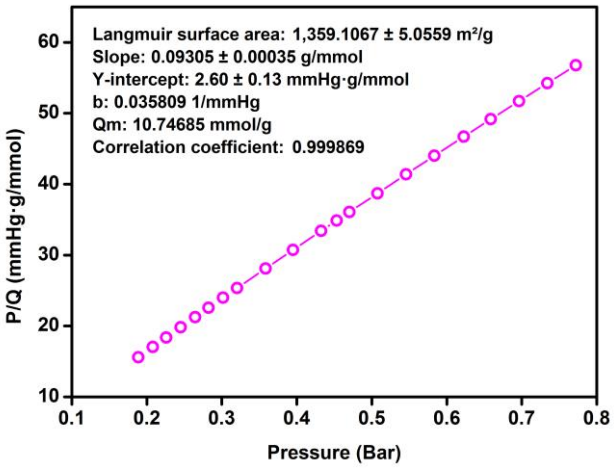

Figure 2.A.9. Shows the fitting comparison obtained for the Langmuir model done to the adsorption branch of the 195 K CO_2 data.

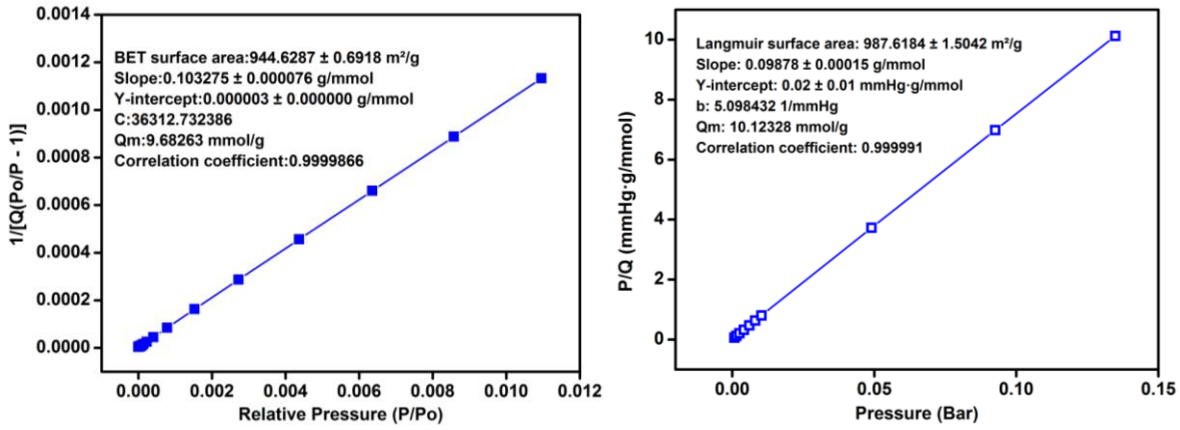

Figure 2.A.10. BET and Langmuir fits from the 77 K N_2 data.

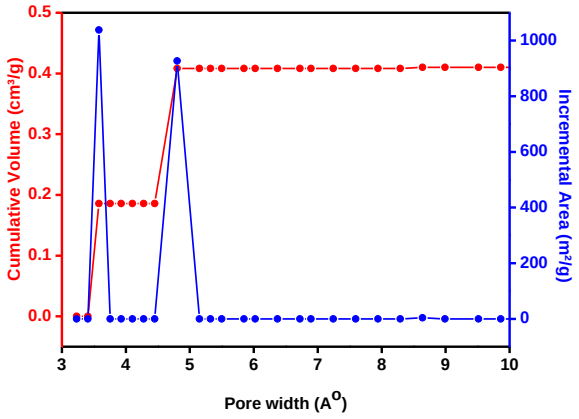

Figure 2.A.11. Pore size distribution in IISERP-MOF1 obtained by fitting the NLDFT model to the 195 K CO_2 adsorption branch. Note the presence of a bimodal distribution with pores of dimensions ~3.5 and ~4.8 Å.

Pore Size from Positron Annihilation Lifetime Spectroscopy (PALS):

The background subtracted and peak normalized PALS spectra of the as-received and the annealed sample are shown together in figure 2.A.12. There is a slight change in PALS spectrum after the annealing at 90°C, however, it is obvious that the most dramatic change occurs after the heating to 100°C. The spectra were best fitted, using a least-square fitting program, POSFIT, with three lifetime components, as shown in table 2.A.3. Here the third lifetime (τ3) and its intensity (I3) are due to the o-Ps annihilation that is most interesting to us. Based on the well-established Tao-Eldrup model (S. J. Tao, *J. Chem. Phys*. 56, 5499 (1972), M. Eldrup, *Chem. Phys.* 63, 51 (1981), this 1.2-1.4 ns component can be converted to a spherical pore size of 3.9-4.4 Å, which is fairly consistent with the chemical structure of **1** as well as the CO_2 adsorption result at 195 K. In the CO_2 adsorption data, however, the measured pore size distribution is bimodal, while the PALS results appear to be consistent

with the average of the sizes of these two pore populations. This is not surprising since the two pore sizes measured by CO_2 adsorption, ~ 3.6 Å and ~ 4.9 Å, are very close to each other, corresponding to o-Ps lifetimes of 1.1 ns and 1.6 ns and could not have been separated from the fitting program.

Table 2.A.3. Discrete fitting results of Ni-4PyC, IISERP-MOF1

Treatment	τ1 (ns)	I1 (%)	τ2 (ns)	I2 (%)	τ3 (ns)	I3† (%)
As Received	0.263±0.008*	72±2	0.620±0.031	24.8±1.7	1.44±0.07	3.54±0.64
90°C, 24 hrs	0.271±0.008	63±3	0.639±0.036	32.8±1.5	1.21±0.09	4.6±1.7
100°C, 24 hrs	0.228±0.011	51±3	0.494±0.019	34.6±2.6	1.24±0.01	14.1±0.4

*Errors are statistical errors of the fitting; †The o-Ps intensities are not corrected to account for the fact that 30% of the positrons are implanted into the Tungsten source; Note: SN322 refers to material Ni 4-PyC, IISERP-MOF1.

The o-Ps intensity (I3 in table 2.A.3.) increased noticeably after the first annealing at 90°C, and jumped drastically from 4.6% to 14.1% after heating to 100°C. Within the same chemical environment, this change of o-Ps intensity can be directly correlated to the change of porosity. Obviously, most of the activation of the SN-322 occurred after the second annealing when the porosity increased significantly.

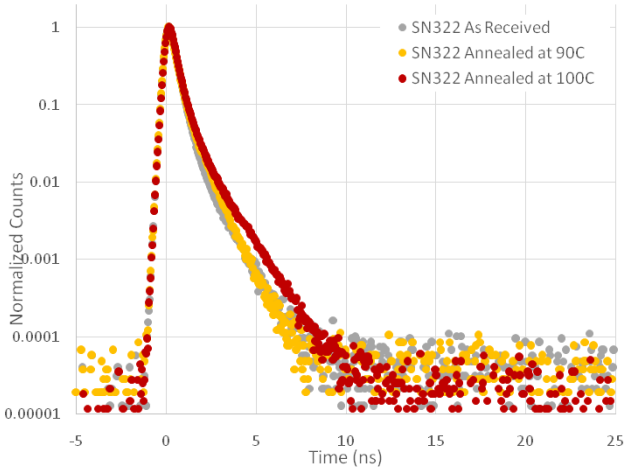

Figure 2.A.12. The background noise corrected and peak normalized PALS spectra of SN322 taken at RT before and after the thermal annealing. Note: SN322 refers to material Ni-4PyC, IISERP-MOF1.

Heat of Adsorption for CO_2 from Virial and NLDFT Models:

$$ln(P) = ln(Va)+(A0+A1*Va +A2*Va^2 \ldots + A6*Va^6)/T+(B0+B1*Va) \ldots\ldots\ldots (1)$$

Where P is pressure, Va is amount adsorbed, T is temperature, and A0, A1, A2 … , A4 and B0, B1are temperature independent empirical parameters.

Table 2.A.4: Summary of the fitted Virial parameters

A0	-4015.961213	B0	17.90621071
A1	769.7356334	B1	-2.117488599
A2	-169.8811741	B2	0.52322824
A3	7.424735813		
A4	0.247999083		

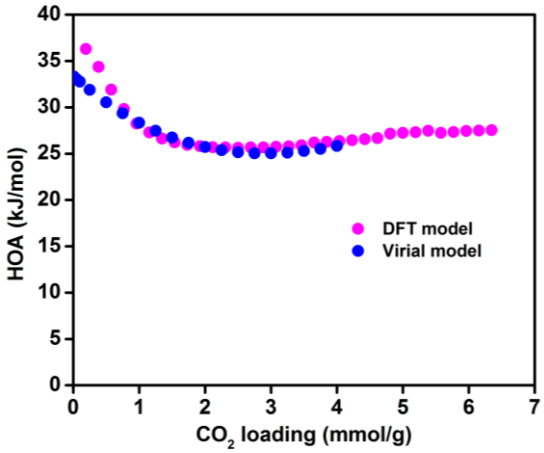

Figure 2.A.13. Comparison of the HOA trend obtained from the virial and DFT modeling done using the CO_2 isotherms carried out at -10°C, 0°C, +10°C and +30°C.

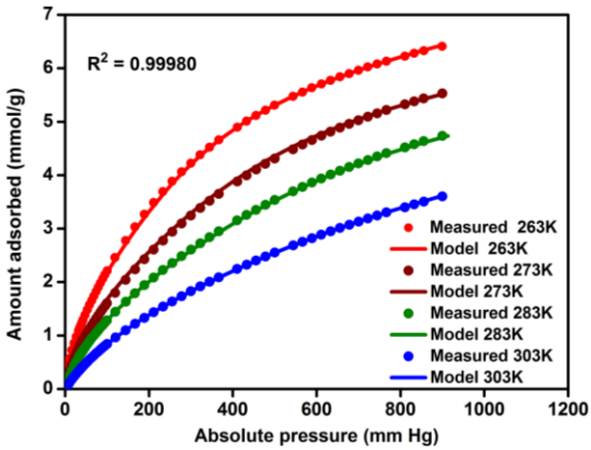

Figure 2.A.14. Comparison of experimental isotherms to the ones obtained from virial modeling carried out using CO_2 isotherms collected at -10°C, 0°C, +10°C and +30°C.

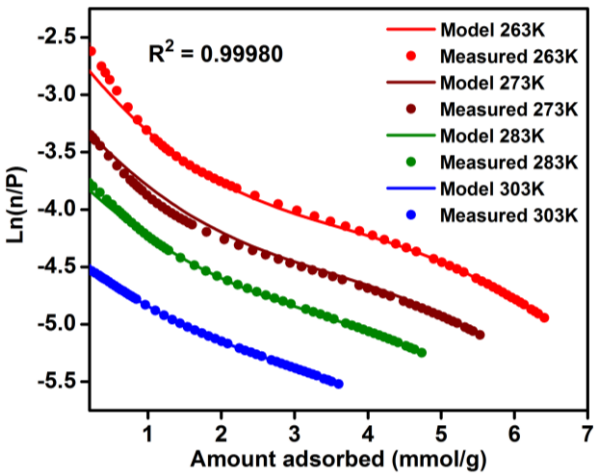

Figure 2.A.15. Virial plots carried out using CO_2 isotherms collected at -10°C, 0°C, +10°C and +30°C.

High Pressure H_2 Isotherm at 298 K

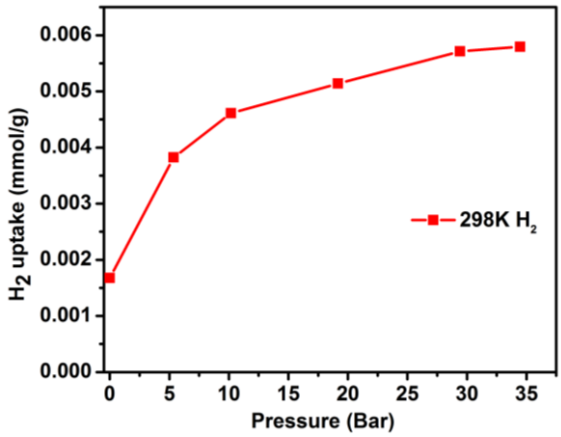

Figure 2.A.16. High pressure H_2 isotherm of IISERP-MOF1 measured at 298 K.

Computational and Molecular Modeling Details

The simulated uptake of Ni-4PyC was calculated using Grand Canonical Monte Carlo (GCMC) calculations. Both single component and binary mixtures of CO_2 and H_2 were performed. The initial experimental crystal structure of IISERP-MOF1 had disorder with respect to the orientation and direction of the organic SBU. The SBU could either bind the metal centre via the nitrogen of the pyridine ring or the oxygen of the carboxylic acid, which resulted in the observed disorder. Of all possible combinations of the organic SBU orientations, only three had no serious steric overlap. These three structures had almost identical isotherms with the greatest difference in uptake being only 0.1 mmol/g through the pressure range from 0-1 bar. The structure with the least symmetry was used. Before GCMC calculations could be performed, the MOF framework structure was optimized using periodic

density functional theory (DFT) (P. Hohenberg, *Phys. Rev.* 136, B864 (1964); W. Kohn, et al. *Phys. Rev.* 140, A1133 (1965)). Geometry optimizations were performed starting from high quality experimental X-ray structures with all atoms and unit cell parameters optimized. Periodic DFT calculations were performed with the VASP code (G. Kresse et al., *Phys. Rev.* B 47, 558 (1993); *Phys. Rev.* B 54, 11169 (1996)) using the PBE exchange-correlation functional (J. P. Perdew et al. *Phys. Rev. Lett.* 77, 3865 (1996)). PAW pseudopotentials (P. E. Blöchl, *Phys. Rev. B* 50, 17953 (1994); G. Kresse, *Phys. Rev. B* 59, 1758 (1999)) were used in a plane wave basis set with a kinetic energy cut-off of 520 eV. All calculations were spin polarized and only the Γ-point was sampled. Empirical dispersion corrections of Grimme (S. Grimme, *J. Comput. Chem.* 27, 1787 (2006)) were included in both energy and force calculations with the default scaling factor of 0.75, as parameterized by Grimme, for the PBE functional.

GCMC calculations were performed with the framework held fixed while the gas guest molecules were assumed to be rigid. The electrostatic energetic contributions were determined by partial atomic charges assigned to each atom calculated with the REPEAT method (C. Campañá et al. *J. Chem. Theory Comput.* 5, 2866 (2009)) using the DFT derived electrostatic potential. Dispersive and steric repulsive interactions were included by a 12-6 Lennard-Jones (L-J) potential for each atom. The ε and σ parameters for the framework were taken from the Universal Force Field (UFF) (A. K. Rappe *et al. J. Am. Chem. Soc.* 114, 10024 (1992)). H_2 Lennard-Jones parameters, the H-H bond length (0.742 Å), and point charges for the five-site H_2 model were taken from work by Belof *et al.* (*J. Chem. Theory Comput.* 4, 1332 (2008)) which is a hydrogen potential for condensed phase simulation. These parameters have been used in the simulation of H_2 in to study the adsorption of H_2 in ultra-microporous MOFs (K. A. Forrest, *J. Phys. Chem. C* 117, 17687 (2013)) and are shown below in table 2.A.5.

Table 2.A.5. Forcefield parameters for the 5-site H_2 model taken from by Belof *et al.* (2008). H2E corresponds to the true atomic positions of hydrogen atoms, H2G coincides with the center-of-mass site, and H2N contains the additional Lennard-Jones sites.

Atom	R / Å	Q / e	ε / kcal mol^{-1}	σ / Å
H2E	-0.371	0.3732	0.0000000	0.0000
H2N	-0.329	0.0000	0.0080798	2.3406
H2G	0.000	-0.7464	0.0175899	3.2293
H2N	0.329	0.0000	0.0080798	2.3406
H2E	0.371	0.3732	0.0000000	0.0000

The ε and σ parameters of CO_2 were taken from García-Sánchez *et al.* (*J. Phys. Chem. C* 113, 8814 (2009)) which were developed to fit experimental adsorption isotherm data in zeolite frameworks. The C-O bond length (1.149 Å) and partial charges on CO_2 atoms (C = +0.6512*e*, O = -0.3256*e*) were taken from the potential by Harris and Yung (*J. Phys. Chem.* 99, 12021 (1995)). Lennard-Jones parameters of all atom types are given in table 2.A.6.

Table 2.A.6. Lennard-Jones parameters for framework atoms from the UFF forcefield, CO_2 guest molecules.

Forcefield	Atom	ε / kcal mol^{-1}	σ / Å
UFF	C	0.1050	3.4309
UFF	O	0.0600	3.1181
UFF	N	0.0690	3.2607
UFF	Ni	0.0150	2.5248
García-Sánchez *et al.*	O (CO_2)	0.1702	3.0170
García-Sánchez *et al.*	C (CO_2)	0.0595	2.7450

GCMC simulations were performed with an in-house code. The number of production steps used was 10^7 after an initial equilibration stage of 10^6 steps for each gas pressure point on the isotherm. The Monte Carlo algorithm utilized equal probabilities for the moves of guest displacement, insertion, and deletion. A cut-off of 12.5 Å was used for long range interactions which were calculated using a Ewald summation. For pressures less than 1 bar, the ideal gas pressure was used in the Monte Carlo guest insertion and deletion criteria. Conversely, pressures greater than 1 bar was corrected for fugacity by evaluating the uptake based on pressures fitted to the Peng-Robinson Equation of State. (R. Stryjek *et al. Can. J. Chem. Eng.* 64, 323 (1986)). A 2x2x3 super-cell was used for the GCMC simulations. A similar approach has been used by us successfully to analyze CO_2 binding within an amine-functionalized MOF.

From the probability distributions generated via the GCMC simulations the most probable CO_2 binding sites were calculated. The in-house code uses a Gaussian filter to smooth the GCMC probabilities. From here the maxima in the smoothed probability is determined. A single atom is fitted to this maxima and then the molecule is built such that the orientation fits maxima in the probability distributions of the other atom types in the molecule. The geometry was then optimized using the DL_POLY package (T. R. Forrester et al. DL_POLY ver. 2.18 (C.L.R.C. Daresbury Laboratory, Daresbury, UK, 1995)) with 200 MD steps at zero Kelvin. The ranking of binding sites were based on interaction energy and the occupancy of the binding sites with respect to the probability distributions. For determination of the binding energies, single point calculations were performed with

interaction energies subdivided into dispersion and electrostatic contributions. The binding energy per CO_2 molecule is defined as,

$$E_{binding} = E(\mathrm{MOF} + n\mathrm{CO_2}) - E(\mathrm{MOF}) - nE(\mathrm{CO_2}) \qquad (2.A.1)$$

where the configurational energies for the MOF with the guest CO_2included in the simulations are used for $E(\mathrm{MOF} + n\mathrm{CO_2})$. $E(\mathrm{MOF})$ is the configurational energy of the MOF with no guests. $nE(\mathrm{CO_2})$is the configurational energy of one CO_2 molecule times *n* number of CO_2 molecules. The cooperative energy was calculated as,

$$E_{cooperative} = E(\mathrm{MOF} + n\mathrm{CO_2}) - E(\mathrm{MOF} + (n-1)\mathrm{CO_2}) \qquad (2.A.2)$$

where the configurational energy of the MOF with *n* number of CO_2 molecules in the unit cell is $E(\mathrm{MOF} + n\mathrm{CO_2})$. The term $E(\mathrm{MOF} + (n-1)\mathrm{CO_2})$ is the summation of the binding energies of *n-1* number of CO_2 molecules in the unit cell as such,

$$\sum_{i=1}^{n-1} E(\mathrm{MOF} + n\mathrm{CO_2}) - E(\mathrm{MOF}) - nE(\mathrm{CO_2}) \qquad (2.A.3)$$

A summary of cooperative binding energies of the 9 least ranked binding site CO_2 molecules is shown in table 2.A.7.

Table 2.A.7. Cooperative CO_2-CO_2 energies with respect to the number of molecules loaded.

n CO_2 per unit cell	Total Cooperative Energy (kJ/mol)	Cooperative Energy Per CO_2(kJ/mol)
22	-108.7	-4.9
23	-118.5	-5.1
24	-120.0	-5.0
25	-121.2	-4.8
26	-123.8	-4.8
27	-136.3	-5.0
28	-146.6	-5.2
29	-152.9	-5.3
30	-145.3	-4.8

Molecular dynamics simulations were performed with DL_POLY in order to calculate the diffusion coefficients. The diffusion coefficients were determined from a single time origin from the calculated mean-square displacement (MSD) over time. The MSD is calculated as an average property of all *N* CO_2 molecules as,

$$MSD(t) = \frac{1}{N}\langle\sum_{i=1}^{N}|\boldsymbol{r_i}(t) - \boldsymbol{r_i}(0)|^2\rangle = \langle|\boldsymbol{r}(t) - \boldsymbol{r}(0)|^2\rangle \qquad (2.A.5)$$

where $r_i(0)$ corresponds to a starting position at time t = 0 and $r_i(t)$ corresponds to a position at time t. The diffusion coefficient, D, is defined as the slope of MSD with respect to time,

$$\lim_{t\to\infty} \frac{d\langle|\boldsymbol{r}(t)-\boldsymbol{r}(0)|^2\rangle}{dt} = 6D \qquad (2.A.6)$$

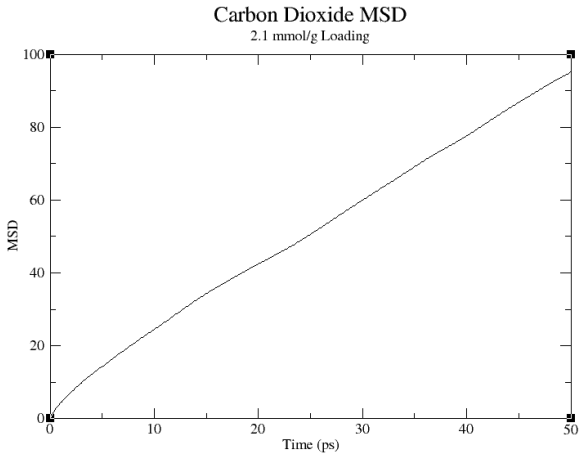

Figure 2.A.17. Plot of the Mean Square Displacement (MSD) as a function of time resulting from a molecular dynamics simulation of CO_2 in IISERP-MOF1 at 298.15 K and 1 bar with a loading of 2.1 mmol/g.

The MD simulation was done at 298.15 K and 1 bar with 0.2 ns of equilibration, 1 ns for the production run, and a time step of 0.001 ps with an NVT ensemble. This was done at flue gas conditions with a binary mixture of $15CO_2$:$85N_2$ in a 2x2x3 supercell with 69 CO_2 molecules which corresponds to a 2.10 mmol/g loading. A graph of the MSD with respect to time is shown in figure 2.A.17.

The void volume (0.0434 cm^3/g) and surface area (1193.16 m^2/g) were calculated using the Zeo++ code (T. F. Willems et al. *Microporous Mesoporous Mater.* 149, 134 (2012); R. L. Martin, *J. Chem. Inf. Model.* 52, 308 (2012)) with a probe radii (1.72 Å) corresponding to CO_2 gas molecules. The accessible volume as measured by a solvent probe radius of 1.72 Å shows the presence the 1D channels which running through the unit cell. The center pore was found to be accessible via the channels at 1.00 Å which was also found to contain the strongest binding sites as mentioned in the result section. Depending on the orientation of the CO_2 molecule, it should be able to access this pocket via the channels. A graphical representation of the accessible volume is shown in figure 2.A.18.

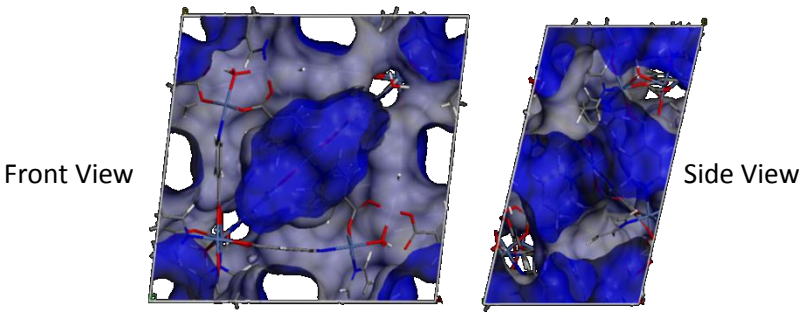

Figure 2.A.18. A graphical representation of the accessible volume of IISERP-MOF1 with a probe radii of 1.41 Å.

In order to validate whether the CO_2 molecules are accessible to the middle cage, molecular dynamics simulations were performed with DL_POLY. Two configurations were tested, one where the channels were saturated and the cage was empty and vice versa. This was done at 313 K and 10 bar to model high pressure adsorption with 0.2 ns of equilibration, 1 ns for the production run, and a time step of 0.001 ps with an NVT ensemble. In both simulations the CO_2 molecules diffuse into and out of the cages. It was found that cage to channel diffusion occurred throughout the simulation time length while channel to cage diffusion occurred almost instantaneously. Snapshots of the simulation are showed in figure 2.A.19.

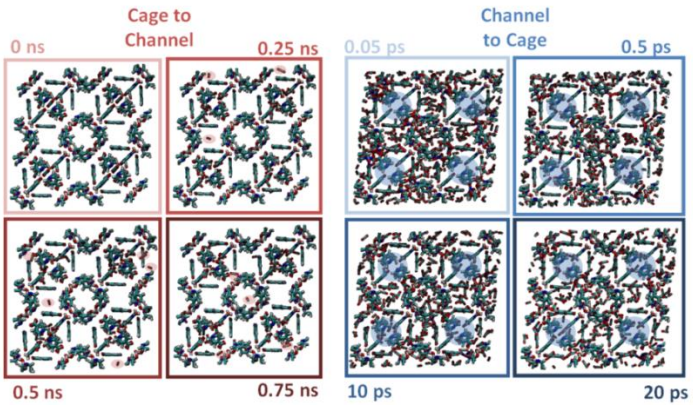

Figure 2.A.19. Snapshots from the MD simulation of CO_2 diffusing from the cage to the channel and vice versa. Highlighted in red are the CO_2 molecules which have diffused from the cage to the channel and highlighted in blue are the cages with CO_2 molecules inside.

Simulation of 195 K CO_2 isotherm and 298 K high pressure (40 bar) does not show significant no differences in adsorption sites. Figure 2.A.20 compares the probability distributions of the CO_2 molecules resulting from GCMC simulations at the two conditions.

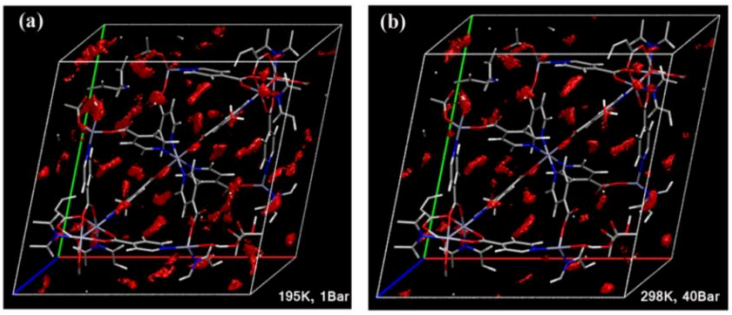

Figure 2.A.20. Probability densities of CO_2 center of mass as determined via GCMC calculations at a) 195 K and 1 bar and b) 298 K and 40 bar. The isosurface representation has an isovalue of 0.04 molecules/Å^3. The densities are very similar between low temperature, low pressure, and high temperature, high pressure.

The selectivity of CO_2 over H_2 was calculated from a binary GCMC simulation where both guest molecules were present within the GCMC simulation at the same time. This was done by specifying the partial pressures of each gas molecule with a ratio of 40:60 and 20:80 (CO_2: H_2) which is an industrially relevant mixture comparable to that found in flue gas (Ref. 23) and then evaluating the uptake with this mixture using the GCMC methods that were explained above. The selectivity was calculated using the following formula,

$$Selectivity_{1,2} = \frac{\frac{q_1}{P_1}}{\frac{q_2}{P_2}} \qquad \text{(S7)}$$

where q_1 is the calculated uptake of CO_2, P_1 is the partial pressure of CO_2 within the binary mixture, q_2 is the uptake of H_2, and P_2 is the partial pressure of H_2 within the binary mixture.

Isosteric heat of adsorptions (HOA) were calculated from the GCMC simulations via the Green – Kubo fluctuation theory expression,

$$q_{isosteric} = \frac{\langle UN\rangle - \langle U\rangle\langle N\rangle}{\langle N^2\rangle - \langle N\rangle\langle N\rangle} + RT \qquad \text{(2.A.8)}$$

where N is the number of CO_2 gas molecules in the GCMC simulation and U is the total configuration energy for the CO_2 molecules (T. Vuong et al. *Langmuir* 12, 5425 (1996)). The HOA is shown to match well with experiment as shown in figure 2.2C.

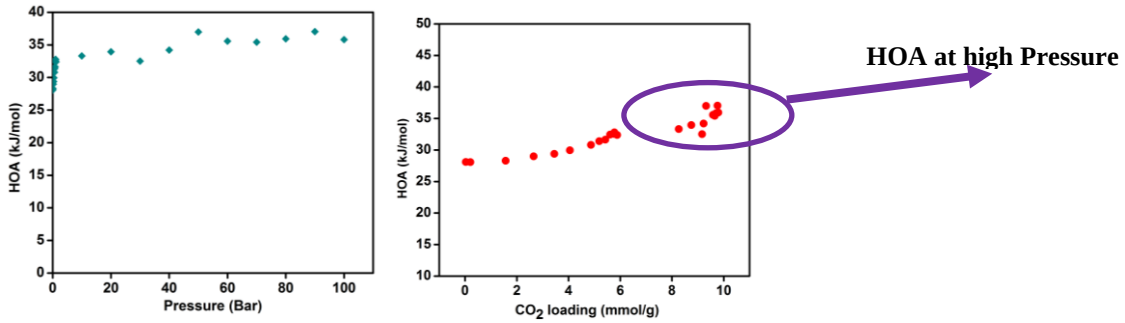

Figure 2.A.21. Simulated HOA plots. The HOA climbs up from 28 to 35 kJ/mol as we go from ambient to higher pressures. Importantly, the simulations indicate increased CO_2-CO_2 interactions at higher pressures or around the saturation limit. However, when the CO_2 per unit cell goes beyond the value of 28 molecules/unit cell, they start to interact unfavorably.

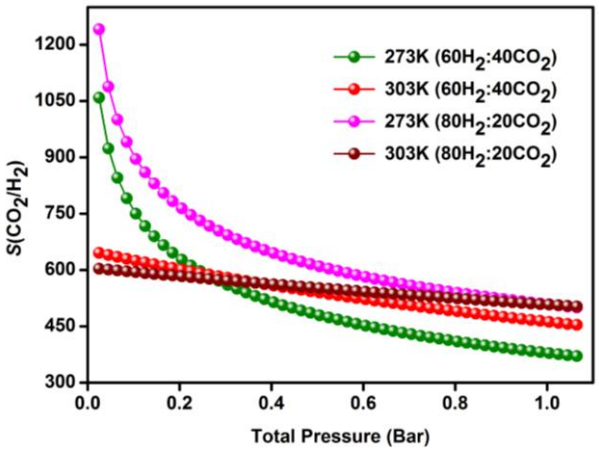

Figure 2.A.22. CO_2 selectivity over H_2 calculated using the 273 and 303 K pure component adsorption isotherms employing the *IAST* model with a nominal composition of $60H_2$:$40CO_2$ (pre-combustion mix) and $80H_2$:$20H_2$ (H_2 purification mix).

Table 2.A.8. Working capacities and selectivities for a PSA from 10 bar to 1 bar at 313 K at the relevant H_2/CO_2 gas mixtures for H_2 purification (80:20) and pre-combustion CO_2 capture (60:40) for integrated gasification and combined cycle (IGCC) systems.

Material	H_2 Purification Working Capacity (mol/kg)	H_2 Purification Selectivity	Precombustion CO_2 Capture Working Capacity (mol/kg)	Precombustion CO_2 Capture Selectivity
Ni-4PyC	4.05	285	3.95	229
Activated Carbon JX101	1.90	94	3.00	75
Zeolite 13x	2.20	320	1.90	250
Mg_2(dobdc)	3.20	610	4.00	450
Cu-BTTri	3.00	31	5.00	28

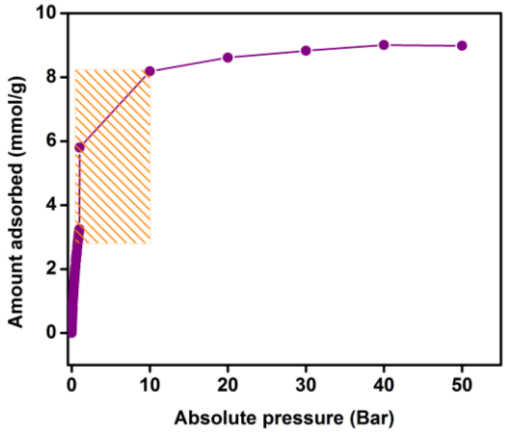

Figure 2.A.23 Working capacity 5.0 mmol/g for a PSA (10 bar to 1 bar) at 298 K for the pure component.

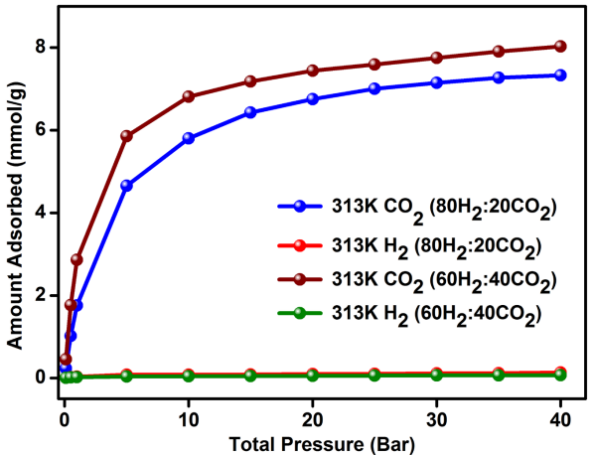

Figure 2.A.24. Isotherms simulated from a hydrogen purification ($80H_2$:$20CO_2$) and pre-combustion mixture ($60H_2$:$40CO_2$).

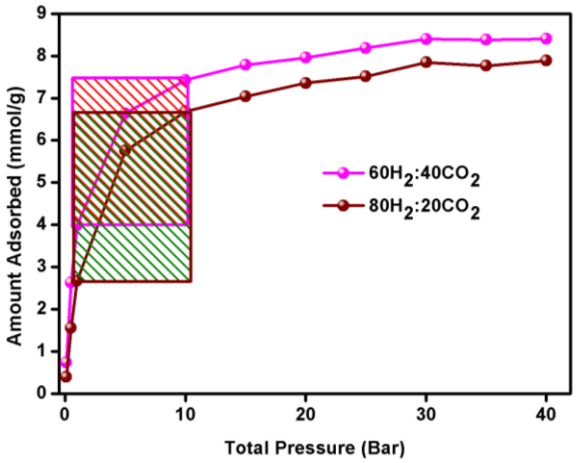

Figure 2.A.25. Working capacity for a PSA (10 bar to 1 bar) at 298 K for the gas mixture with $60H_2$:$40CO_2$ and $80H_2$:$20CO_2$.

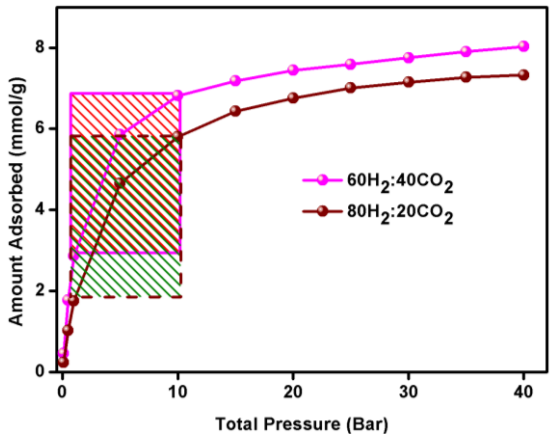

Figure 2.A.26. Working capacity for a PSA (10 bar to 1 bar) at 313 K for the flue gas mixture with $60H_2$:$40CO_2$ and $80H_2$:$20CO_2$.

Stability Study:

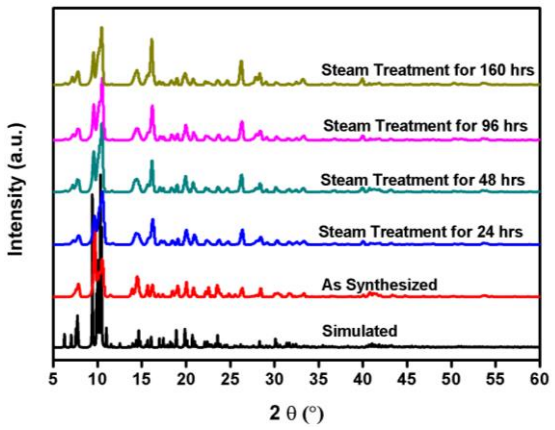

Figure 2.A.27 PXRD comparisons of the as-made sample with the simulated. Presented is also the PXRDs indicating the hydrolytic stability of IISERP-MOF1.

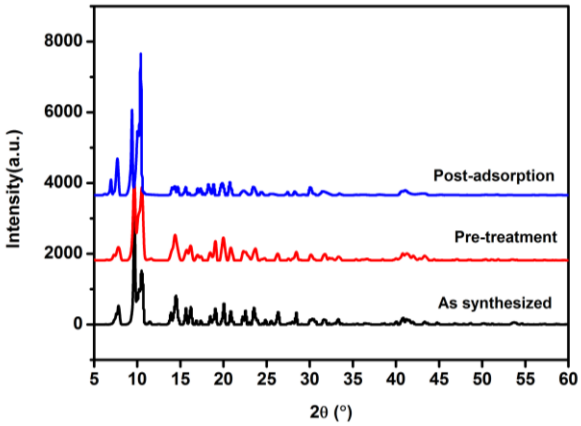

Figure 2.A.28. Comparison of PXRDs indicating the complete retention of crystallinity following repeated (~8-10 cycles) heating and cooling of IISERP-MOF1 during multiple gas adsorption studies.

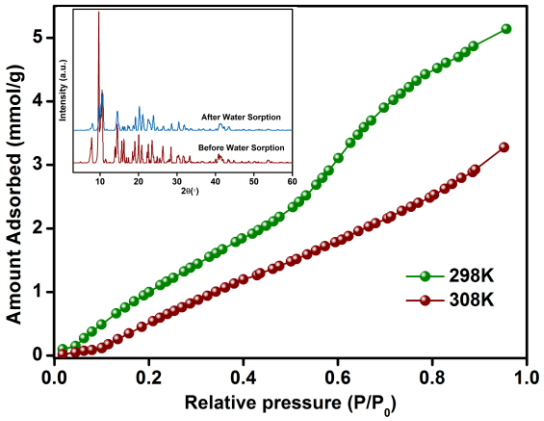

Figure 2.A.29. The water adsorption isotherm carried out on IISERP-MOF1 at 298 K. Inset showing the PXRD of the post adsorption phase. Both together represent the hydrolytic stability of IISERP-MOF1.

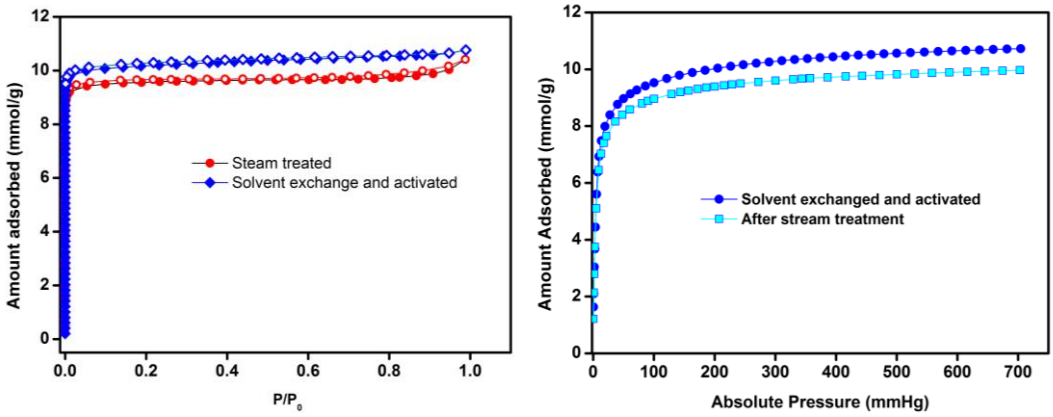

Figure 2.A.30. Hydrolytic stability of IISERP-MOF1. left: Comparison of the N_2 adsorption at 77 K for the freshly activated sample and the sample that was exposed to > 75% steam. Right: Comparison of the CO_2 adsorption at 195 K for the freshly activated sample and the sample that was exposed to >75% steam.

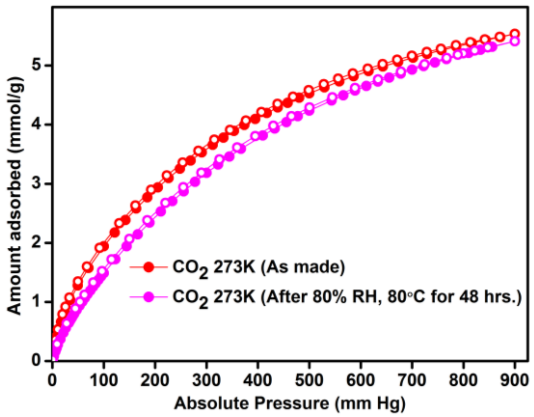

Figure 2.A.31. The comparison of the CO_2 adsorption isotherms of IISERP-MOF1, as made (red) vs sample exposed to 80%RH at 80°C for 48 hrs (magenta).

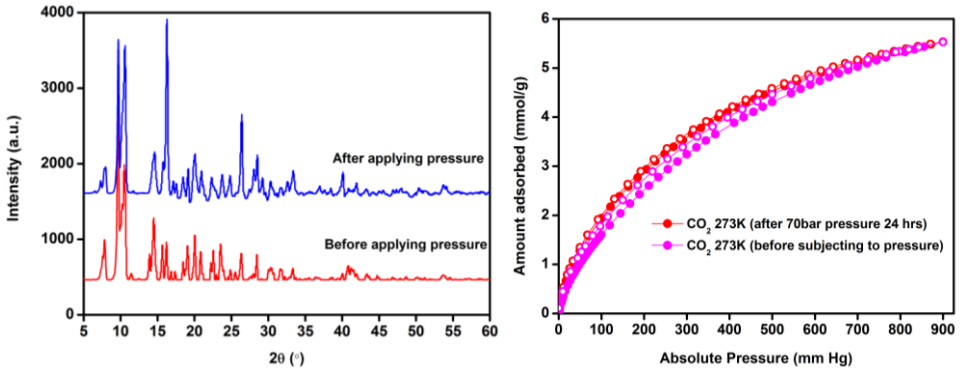

Figure 2.A.32. Pressure induced amorphization test for IISERP-MOF1. Note there is hardly any loss in crystallinity or gas uptake. Pressure of 70 bar is twice what is industrially used.

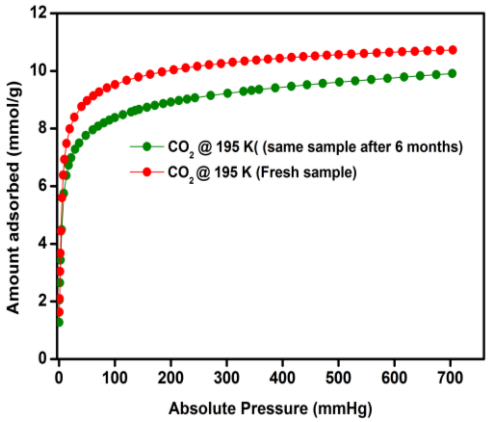

Figure 2.A.33. The comparison of the CO_2 adsorption in IISERP-MOF1 between a freshly prepared phase and one that has been sitting in a bottle for over 6 months.

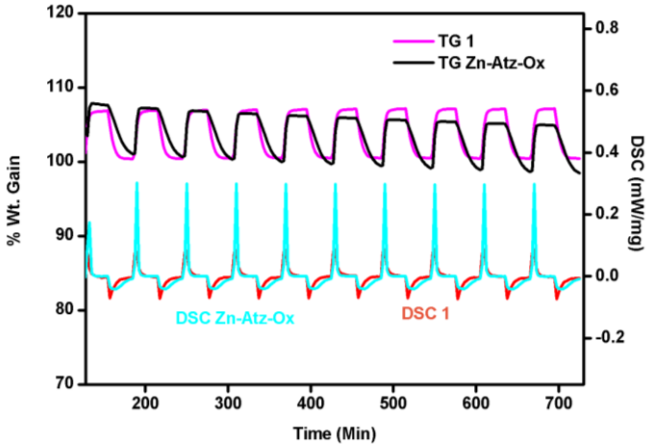

Figure 2.A.34. TGA cycling data for CO_2-N_2 cycling done on IISERP-MOF1 and ZnAtzOx at 35°C. N_2 and CO_2 were flowed at 20 ml/min and each cycle starts with a CO_2 (30 mins) followed by a N_2 (30 mins). Both IISERP-MOF1 and ZnAtzOx show ~6.5% Wt. gain. Comparison of the DSC trace indicates the higher heat of adsorption for the latter as would be expected (HOA: 28 kJ/mol for IISERP-MOF1 vs. 40 kJ/mol for ZnAtzOx). Also, a closer look at the profiles of the TG shows the facile removal of the CO_2 in IISERP-MOF1, as compared to ZnAtzOx as indicated by the sharper desorption for IISERP-MOF1. The drift in the TGA with time in the case of ZnAtzOx is entirely due to baseline issues, the weight gain remains unchanged between cycles.

Self-diffusion Coefficient CO_2 in IISERP-MOF1:

Diffusion coefficient determination from Rate of adsorption measurements: An extremely high resolution rate of adsorption measurement was carried out using the ASAP2020HD instrument at 273 K in the pressure range of 0-1 bar. The diffusion coefficient was calculated as a function of CO_2 loading. For this purpose, 8 different loading points (N = 1.09, 1.67, 2.17, 2.60, 2.99, 3.31, 3.63 and 3.93) were used and each of the ROA data was fitted to a spherical pore model (Kourosh et al. *J. Chem. Phys.*, 119, 2801 (*2003*); Adsorption analysis and equilibria and kinetics, D. D. Do, Imperial College Press, Ed. 2008):

$$F = 1 - \frac{6}{\pi^2} \sum_{n=1}^{\infty} \frac{1}{n^2} \text{Exp}(-n^2 \pi^2 \tau)$$

F = fractional uptake; τ = non-dimensional time given by $\tau = Dt/R^2$, where R= particle size; t= time (secs); D = apparent diffusivity.

The single-component diffusion coefficient was estimated to be 3.08 x 10^{-9} m^2s^{-1} taking the average of these eight points. Note: the kinetics of the low loadings (< 1 mmol/g) were extremely hard to model.

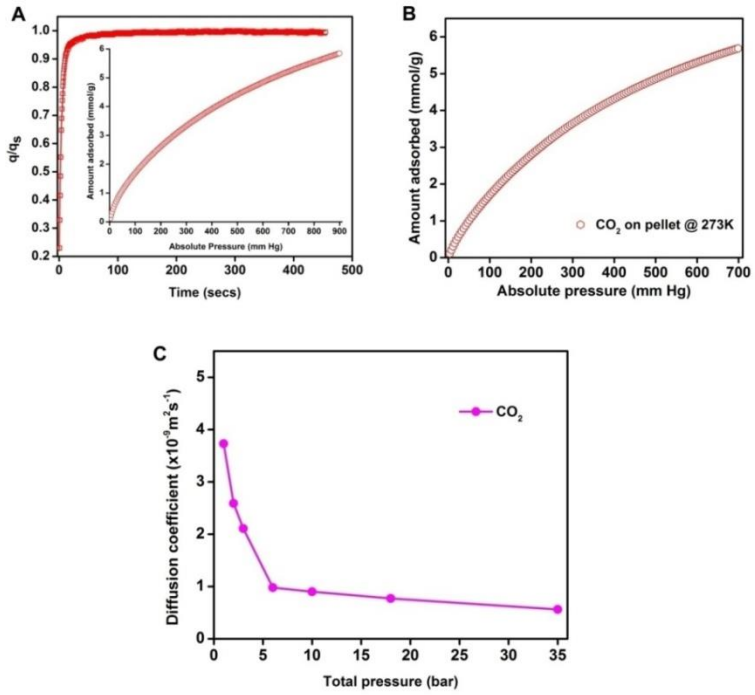

Figure 2.A.35. Top: Representative plot of the adsorbate fractional filling vs. time showing the fit between the spherical model (line) and the collected data (spheres) obtained from the single component CO_2 isotherm. Inset shows the high resolution 273 K adsorption isotherm used in this diffusion modeling. Note nine such fittings were considered to obtain the average diffusion coefficient. Bottom: Self-diffusion coefficient for CO_2 obtained from simulation studies.

Comparison of CO_2/H_2 Selectivities of MOFs Reported in the Literature:

Table 2.A.9. H_2/CO_2 Selectivities from literature

Material	Temperature (k)	Pressure (bar)	Selectivity	Composition (H_2/CO_2)	Source
Ni4PyC	313	10	229.29	60/40	This Work
		1	168.15	60/40	
		10	285.51	80/20	
		1	194.51	80/20	
CarbonJX	313	10	75	60/40	Long et al.[a]
		1	100	60/40	
		10	94	80/20	
		1	98	80/20	
Zeolite 13X 313		10	250	60/40	
		1	310	60/40	
		10	320	80/20	
		1	390	80/20	
Mg2(dobdc)	313	10	450	60/40	
		1	620	60/40	
		10	610	80/20	
		1	880	80/20	
Cu-BTTri	313	10	28	60/40	
		1	30	60/40	
		10	31	80/20	
		1	40	80/20	
MOF-177	313	10	9	60/40	
		1	9	60/40	
		10	10	80/20	
		1	10	80/20	
Co(BDP)	313	10	6	60/40	
		1	5	60/40	
		10	7	80/20	
		1	6	80/20	
Bio-MOF-11	298	10	475	10/90	Atci et al.[b] (simulated)
		1	400	10/90	
IRMOF-1	298	10	~10	10/90	Keskin et al.[c] (simulated)
		1	~10	10/90	
IRMOF-8	298	10	~10	10/90	
		1	~10	10/90	
IRMOF-10	298	10	~10	10/90	
		1	~10	10/90	
IRMOF-14	298	10	~10	10/90	
		1	~10	10/90	

COF-102	298	10	25	10/90	
		1	20	10/90	
IRMOF-9	298	10	50	10/90	
		1	90	10/90	
COF-6	298	10	75	50/50	Liu et al.[d] (simulated)
		1	60	50/50	
COF-8	298	10	<20	50/50	
		1	<20	50/50	
COF-10	298	10	<20	50/50	
		1	<20	50/50	
COF-102	298	10	<20	50/50	
		1	<20	50/50	
COF-103	298	10	<20	50/50	
		1	<20	50/50	
COF-105	298	10	<20	50/50	
		1	<20	50/50	
Cu-BTC	298	10	70	50/50	
		1	90	50/50	
IRMOF-1	298	10	<20	50/50	
		1	<20	50/50	
IRMOF-8	298	10	<20	50/50	
		1	<20	50/50	
IRMOF-10	298	10	<20	50/50	
		1	<20	50/50	
IRMOF-14	298	10	<20	50/50	
		1	<20	50/50	
IRMOF-16	298	10	<20	50/50	
		1	<20	50/50	
HKUST-1	298	1	4.52 - 6.84	50/50	Guo et al.[e]

[a]Herm, Z. R.; Swisher, J. A.; Smit, B.; Krishna, R.; Long, J. R. *J. Am. Chem. Soc.* **2011**, *133* (15), 5664. [b]Atci, E.; Erucar, I.; Keskin, S. *J. Phys. Chem. C* **2011**, *115* (14), 6833. [c]Keskin, S.; Sholl, D. S. *Langmuir* **2009**, *25* (19), 11786. [d]Liu, Y.; Liu, D.; Yang, Q.; Zhong, C.; Mi, J. *Ind. Eng. Chem. Res.* **2010**, *49* (6), 2902. [e]Guo, H.; Zhu, G.; Hewitt, I. J.; Qiu, S. *J. Am. Chem. Soc.* **2009**, *131* (5), 1646.

Chapter 3

Post-combustion CO_2 Capture in a Moisture stable Nickel Isonicotinate MOF with Ultra-low Parasitic Energy

3.1. Introduction:

Electrical power generation from the combustion of fossil fuels, such as coal, accounts for about 40% of the world's anthropogenic CO_2 emissions.[1] Scrubbing the CO_2 from these stationary sources is seen as a practical means of meaningfully reducing green house gas emissions in the near term since existing power plants can be retrofitted with post-combustion CO_2 capture systems. Although large scale scrubbing technologies based on aqueous amines exist, they are not energy efficient enough to enable widespread carbon capture. It has been estimated that aqueous amine CO_2 scrubbers in coal burning power plants would make electricity 60-80% more expensive.[2,3] These high energetic and associated monetary costs are the most significant technological challenges to large scale deployment of carbon capture and storage. Pressure and temperature swing adsorption (P/TSA) gas separation systems are considered amongst the most promising technologies to enable cost effective post-combustion CO_2 capture[4] where CO_2 must be separated from a humid flue gas composed of ~85% N_2,10-15% CO_2. In such systems, the combustion gas is passed through a solid sorbent bed, which selectively adsorbs and removes the CO_2 from the flue gas. When the bed reaches capacity, the captured CO_2 is desorbed releasing near pure CO_2 for subsequent storage. Zeolites, such as 13X, are currently used in large scale PSA systems for CO_2 scrubbing of natural gas and landfill gases.[5] Unfortunately, zeolites do not perform well in the humid gas streams of post-combustion CO_2 capture.[6] For this purpose, metal organic frameworks (MOFs) have attracted significant attention due to their high functional tunability.[7,8]

While MOFs with large CO_2 uptake capacities are often promoted as ideal materials for post-combustion CO_2 capture,[9] other adsorption properties are more important for low cost capture. In particular the CO_2/N_2 selectivity, the CO_2 working capacity (the difference between the uptake capacity at the adsorption and desorption conditions) and heat of adsorption are critical. Other physiochemical properties such as the thermal and hydrolytic stability are also critical.[10] In order to assess how energy efficient the CO_2 capture will be with a particular material, Smit and others have advocated using the parasitic energy (PE) as a single figure of merit to compare materials.[3] This is the energy required to regenerate the sorbent during the desorption process in addition to the subsequent energy cost to pressurize the CO_2 to 150 bar for transportation. The PE gives a pragmatic quantification of the efficiency of the solid sorbent used in these large scale separations. Recently, Huck *et al.*[3a] compared the PEs of MOFs and other solid sorbents such as zeolites. Mg-MOF-74 was found

to have the lowest PE (727 kJ/kg of CO_2) of all materials evaluated. For comparison, the PEs for state-of-the-art aqueous amine tech-nologies are estimated to be at least 1000 kJ/kg of CO_2.[3b,c] Although Mg-MOF-74 possesses a record low PE, it is known to irreversibly decompose in humid gas streams, making it impractical for post-combustion CO_2 capture. One material that was computed to have a relatively low PE[3a] that also exhibits significant moisture stability is the ultra-microporous SIFSIX-3-Zn.[11]

Herein we present a nickel isonicotinate based ultra-microporous MOF [Ni-(4Pyc)$_2$•DMF], IISERP-MOF2, with the lowest PE for post-combustion CO_2 capture reported to date. It also exhibits remarkable moisture stability with CO_2 adsorption properties that are essentially unchanged following steam treatment and long exposure to humidity. IISERP-MOF2 also poses a high CO_2 diffusion coefficient for favourable adsorption/desorption kinetics. Furthermore, breakthrough measurements on IISERP-MOF2 under both dry and 50% RH conditions show that IISERP-MOF2 retains most of its performance.

3.2. Materials and Methods:

All the organic chemicals were purchased from sigma aldrich. The nickel salts were procured from Alfa Aesar. Compounds and solvents were all used without any further purification.

3.2.1. Milligram Scale Synthesis of IISERP-MOF2:

IISERP-MOF2 was synthesized via a solvothermal method by reacting Nickel acetate and 4-pyridine carboxylic acid in a mixture of dimethyl formamide (DMF) and acetonitrile (ACN). In a typical reaction about 0.249 g of Nickel$^{(II)}$ acetate tetra hydrate was added to 0.244 g of 4-Pyc in a solution containing 6 ml of DMF and 4 ml of ACN. The mixture was stirred for 30 min at room temperature and then about 75 µl of triethylamine was added to it. The solution was homogenized by stirring for another 30 min at room temperature. Contents were placed in a 20 ml teflon lined Parr stainless steel autoclave and heated at 150°C for 72 hrs followed by slow cooling to room temperature (over 12 hrs). A bluish green colored polycrystalline product was isolated by filtration and was washed with water, methanol and acetone. The air dried sample gave yield of 83% (based on Ni). The PXRD pattern indicated this to be a pure phase of IISERP-MOF2. We have also prepared 10-25 gms of this sample with an easy scale-up procedure. CHN analysis (calculated values within brackets): C: 47.92 (48.05); H: 3.68 (3.76); N: 11.42 (11.21)%.

3.2.2. Gram Scale Synthesis of IISERP-MOF2:

About 7.5 g of Nickel acetate tetra hydrate was added to 7.35 g of 4-PyC in a solution containing 50 ml DMF and 25 ml of ACN. The reaction mixture was stirred at room temperature for about 1 hr followed by addition of 1 ml triethylamine. After that the mixture was further stirred for another 1 hr at room temperature. Contents were placed in a 123 ml teflon lined Parr stainless steel autoclave and heated at 150°C for 72 hrs. A bluish green colored polycrystalline product identical in appearance to the smaller scale preparation was obtained. The air dried sample gave a yield of ~85% (based on Ni).

3.2.3. Single Crystal Structure Determination:

Single-crystal data was collected on a Bruker SMART APEX four-circle diffractometer equipped with a CMOS photon 100 detector (Bruker Systems Inc.) and with a Cu Kα radiation (1.5418 Å). The incident X-ray beam was focused and monochromated using Microfocus (IμS). Crystal of IISERP-MOF2 was mounted on nylon Cryo loops with Paratone-N oil. Data was collected at 150 (2) K. Data was integrated using Bruker SAINT software and was corrected for absorption using SADABS. Structure was solved by Intrinsic Phasing module of the direct methods and refined using the SHELXTL 97 software suite. All non-hydrogen atoms were located from iterative examination of difference F-maps following which the structure was refined using least-squares method. Hydrogen atoms were placed geometrically and placed in a riding model.

3.2.4. Analytical Characterizations:

Powder X-ray Diffraction:

Powder XRDs were carried out using a Rigaku Miniflex-600 and Bruker instrument and processed using PDXL software.

Thermogravimetric Analysis:

Thermogravimetry was carried out on NETSZCH TGA-DSC system. The routine TGAs were done under N_2 gas flow (20 ml/min) (purge + protective) with heating rate of 2 K/min.

IR Spectroscopy:

IR spectra were obtained using a Nicolet ID5 attenuated total reflectance IR spectrometer operating at ambient temperature. The dry KBr pellets were used for measurement.

3.2.5. Adsorption Analysis:

All gas sorption isotherms were measured on a Micromeritics ASAP 2020HD or 3-FLEX instrument using ultra-high purity gases (≥ 4.8 grade). About 100 mg of IISERP-MOF2 was transferred to the analysis tube and then evacuated at 160ºC for 24 hrs (10^{-6} mbar) at which point the outgas rate was ≤ 2 μbar/min.

Rate of adsorption experiments were carried out on the Micromeritics ASAP2020HD instrument equipped with a ROA software capabilities. Numerous equilibrium points and associated kinetic data were recorded at 273 K, however for data analysis regularly spaced 10 CO_2 loading points were picked out in the interval of 0 to 1000 mbar.

Lagmuir Fits:

In all cases the isotherms were fit to the Single-Site Langmuir (SSL) equation. It is widely known that even small fitting errors will have a large impact on selectivity calculations. That's why, the isotherms were fit by solving the Langmuir equation using the solver function in Microsoft Excel following a similar protocol to Keller *et al.*[12] Utilizing this routine circumvents some of the problems associated with favoring either high or low pressure regions when linearizing the Langmuir equation[13] offers a balanced approach.

Single-Site Langmuir (SSL):

$$q_i = q_m \frac{K_i P}{1 + K_i P}$$

Dual-Site Langmuir (DSL):

$$q_i = q_{m,1} \frac{K_1 P}{1 + K_1 P} + q_{m,2} \frac{K_2 P}{1 + K_2 P}$$

Ideal Adsorbed Solution Theory (IAST):

IAST calculations were undertaken as described by Prausnitz *et al.*[14] The selectivity equation is provided below.

Selectivity:

$$S_{1,2} = \frac{q_1/q_2}{P_1/P_2}$$

Cycling Experiment Procedure:

Cycling experimets were done using ASAP 2020HD instrument associated with Iso-Cycling software. About 100 mg of samples were loaded in the sample cell and activated according to the proper activation conditions untill the outgas rate was ≤ 2 μbar/min. The isocycling program was created with 15 cycles, each cycle having 14 to 15 data points (equilibration time 100 Sec) at regular interval in between 0.02 bar to 1.18 bar.

Rate of adsorption studies- CO_2 self-diffusion coefficients calculations and analysis:

Diffusion coefficient determination from Rate of Adsorption (ROA) measurements: An extremely high resolution isotherm measurement was carried out using the ASAP2020HD instrument at 273 K in the pressure range of 0-1 bar. The diffusion coefficient was calculated as a function of CO_2 loading. For this purpose, 8 different loading points were used and each of the ROA data was fitted to a spherical pore model[15]

$$F = 1 - \frac{6}{\pi^2} \sum_{n=1}^{\infty} \frac{1}{n^2} \text{Exp}(-n^2 \pi^2 \tau)$$

F = fractional uptake; τ = non-dimensional time given by $\tau = Dt/R^2$, where R= particle size; t= time (secs); D = apparent diffusivity.

The single-component diffusion coefficient was estimated to be 3.03 x 10^{-9} m^2s^{-1} for IISERP-MOF1 and is 6.04 x 10^{-9} m^2s^{-1} for IISERP-MOF2 taking the average of these eight points. Note: the kinetics of the low loadings (< 1 mmol/g) were extremely hard to model.

3.2.6. Breakthrough Measurements:

For the breakthrough measurements, 0.295 g of pre-activated (160°C under 10^{-4} Torr vacuum) sample of IISERP-MOF2 was packed in a 6.35 cm long and 0.5-cm diameter column. This was further activated at 50°C under flowing helium overnight. Pressurization of the 0.25" (6.35 mm) diameter column packed with compound IISERP-MOF2 was accomplished with a syringe pump (Teledyne ISCO) directly connected to the system through a series of 0.07 mm (ID) segments of tubing (PEEK) and valves. System pressure was maintained by coordinated adjustments to the syringe pump flow rate and the needle metering valve (Tescom). An inline pressure transducer was used to verify column pressure. The column was cooled to room temperature and a premixed mixture of 85% N_2 and 15% CO_2

was introduced with a flow rate of 1 ml/min at a total pressure of 15 psi (1.02 atm). Effluent gas chemistry was tracked with a Stanford Research residual gas analyzer (RGA). Masses (a.m.u.) corresponding to N_2 (28), CO_2 (44) and He (4) were monitored throughout the experiments. The flow rate (1 ml/min) through the needle metering valve created a sampling pressure of 5×10^{-5} torr to 3.0×10^{-4} torr in the RGA and was maintained throughout the experiments. Indications of N_2 and CO_2 breaking through the column were indicated by an increase in the pressure for masses 28 and 44 respectively. For breakthrough experiment under humidity (~50% RH), the same experimental setup was used except an additional column (~12 cm long and 0.5 cm diameter, termed as humidity column) containing water soaked glass wool was added to the delivery system. Also, only 100 mg of the sample from the same batch was utilized. The mixed gas (N_2/CO_2 = 85/15) was passed through the humidity column for evaluation before performing the actual breakthrough experiment and a humidity meter was used to measure the humidity of the gas flow, which turns out to be 50% RH. The under humidity breakthrough experiment were carried out immediately thereafter. The CO_2 uptake capacity was calculated by assigning the N_2 breakthrough point as time '0'. This also remove any potential calculation error while comparing the two breakthrough data (dry and under humidity). Note: In all experiments, before the start of the measurements dry He is flown for about ~30 min He to remove any air.

While the adsorption of CO_2 was indicated by its retention time on the column, the complete breakthrough of CO_2 was indicated by the downstream gas composition reaching that of the feed gas. Using the formula,

Number of mole adsorbed n = F * Ci * t, where F = molar flow, Ci = concentration of ith component and t = retention time.

3.2.7. Parasitic Energy Calculations:

In this work we employed the parasitic energy originally developed for aqueous systems[16] but has been employed for MOF and other nanoporous materials by Smit and co-workers.[3b] The parasitic energy is a term to describe the amount of energy necessary to regenerate a scrubber after has adsorbed CO_2. The parasitic energy was calculated using the equation:

$$E_{parasitic} = (0.75 Q_{thermal} \eta_{carnot}) + W_{Comp}$$

This equation is used by Huck *et al.*[3a] and takes into account the energy needed to remove the gas from the material ($Q_{thermal}$) as well as the energy necessary to compress it to transport conditions (W_{comp}). This model assumes that steam produced by the heat source of the power plant can be used to reduce the thermal contribution, $Q_{thermal}$. As the steam is not converted into electricity with 100% efficiently, it is multiplied by the Carnot efficiency and the efficiency of the gas turbine (75%).[16] In this work we use a version of the Carnot efficiency presented by Freeman *et al.*, where T_h is set to the desorption temperature, and T_C was set to 283 K.[16]

$$\eta_{Carnot} = \frac{T_h + 10 - T_C}{T_h + 10}$$

The $Q_{thermal}$ portion was calculated by the equation shown below. $Q_{thermal}$ accounts for the energy necessary to heat the material, and break the interactions with the guest molecules. The first term of $Q_{thermal}$ determines the energy necessary to increase the temperature, using the change in temperature (ΔT), the heat capacity of the sorbent ($C_{sorbent}$) and the mass of the sorbent ($m_{sorbent}$). The summation term accounts for the energy necessary to break the interactions of the guest molecules and framework, which is calculated using the heat of adsorption, Δh_i, for each type of guest, *i*, multiplied by the amount removed from the framework, Δq_i^a. To standardize the energies, they are placed in terms of the total amount of CO_2 removed, Δq_{CO2}^T.

$$Q_{thermal} = \frac{(\Delta T C_{sorbent} m_{sorbent} + \sum_i^n \Delta h_i \Delta q_i^a)}{\Delta q_{CO_2}^T}$$

Δq_{CO2}^T differs from Δq_{CO2}^a by accounting for the gas in void space of the container caused by packing loss. In this work we assumed a 35% packing loss for each material, the same as the work done by Huck *et al.*[3a] To convert the volume in the canister into an amount of gas the ideal gas law was used to the mild temperatures (313-333 K) and pressures (0.01-1 bar) used in this work.

The W_{comp} term contained the energy necessary to compress the captured gas to the transportation pressure of 150 bar. W_{comp} uses the temperature when compression occurs, T_{comp}, as well as the pressure of the desorption condition, p_{des}, and the purity of the captured gas, purity. We do not account for the energy necessary to place the system under vacuum to the desorption condition, as we assume the compressor that brings one system to the

transportation pressure, can create low-pressure that is used to bring another system down to it's desorption pressure. We assume that the compressor works at 85% efficiency for gaseous CO_2, however when it becomes supercritical CO_2, we assumed it works at 90% efficiency. These assumptions are all in line with those used by Huck *et al.*[3a]

$$W_{comp} = \frac{RT_{comp}}{purity} * \left(\frac{\ln\left(\frac{72.9}{p_{des}}\right)}{0.85} + \frac{\ln\left(\frac{150}{72.9}\right)}{0.9} \right)$$

The purity was defined as the amount of CO_2 removed from the flue gas per total gas of flue gas removed. This was calculated using the equation

$$purity = \frac{\Delta q^T_{CO_2}}{\Delta q^T_{CO_2} + \Delta q^T_{N_2}}$$

To determine the parasitic energies, we need values such as the selectivity, heat of adsorption, and the working capacities of the gas mixture. To determine these values, we used Ideal Adsorbed Solution Theory (IAST)[17] For IAST calculations, the isotherms were fit to either a single (*N=1*) or dual site (*N=2*) Langmuir given by the equation:

$$\sigma_i = \sum_{j=1}^{N} \frac{\sigma_{sat,i,j} k_{H\,i,j} p_i}{1 + k_{H\,i,j} p_i}$$

Where σ_i is the loading at partial pressure p_i, $k_{H\,i,j}$ and $\sigma_{sat,i,j}$ are the Henry coefficient and saturation loading respectively for guest *i* at adsorption site *j*. All reference materials, besides IISERP-MOF2, used the values and isotherms presented by Huck. e*t al.*[3a] The saturation loading and heats of adsorption were assumed to be constant over the presented temperature and pressure ranges. The Henry coefficient was assumed to have only a temperature dependence which was calculated using the van't Hoft equation show below. The van't Hoft equation shows the dependence of the Henry coefficient temperature on the temperature, *T*, the heat of adsorption, $\Delta h_{i,j}$, gas constant, *R*, and a calculated constant, *A*. The Henry coefficient was calculated for each guest, *i*, at each adsorption site, *j*.

$$\ln\left(K_{H\,i,j}\right) = A - \frac{\Delta h_{i,j}}{RT}$$

For IISERP-MOF2, all parameters were fit to experimental isotherms. CO_2 data were fit to a dual-site Langmuir isotherm, while the N_2 data was fit to a single site Langmuir-Freundlich, also known as Sips, isotherm model. The single site Sips model as this was found to better describe the data then the Langmuir model. The Sips model used is described as

$$\sigma_i = \frac{\sigma_{sat,i}(k_{H_i}p_i)^{n_i}}{1 + (k_{H_i}p_i)^{n_i}}$$

Where σ_i is the loading at partial pressure p_i, with k_{H_i}, $\sigma_{sat,i}$, n_i are the Henry coefficient and saturation loading and heterogeneity factor respectively for guest i.

In this work we looked using the materials in pressure-swing adsorption (PSA) system. Adsorption conditions were set to be relevant for flue gas at 313 K and 1 bar of pressure, using a gas composition of 14% CO_2 and 86% N_2. The desorption condition was set to a temperature of 333 K to account for the increase in temperature due to the heat of adsorption, and the gas composition was set to 99% CO_2 and 1% N_2. The desorption pressure was chosen to minimize the parasitic energy. The parasitic energy was evaluated at 0.01 and from 0.1 to 1 bar in 0.1 bar increments, with the minimum parasitic energy chosen for the desorption condition. The adsorption and desorption conditions were chosen to be similar to those used by Huck *et al*.

3.3. Results and Discussion:

3.3.1. Single Crystal Structure Analysis:

IISERP-MOF2 has a relatively simple structure formed by linking isolated Ni octahedra by 4-pyridylcarboxylate ligands (Fig. 3.1a). The framework of IISERP-MOF2 comprises of a diamondoid net-work. Each Ni octahedra is coordinated by bidentate carboxylate groups and two pyridyl units. Reducing the PyC to linear linkers, the effective coordination around each Ni is tetrahedral and these nodes connect to form a classic adamantane unit of the diamondoid framework (Fig. 3.1b and 3.A.2). The two-fold interpenetration is shown in figure 3.1b. The interpenetration blocks most channels of the individual framework leaving only square shaped, 7 x 7 Å channels along the a-axis (excluding van der Waals radii) as shown in figure 3.1c. Using a DFT model the pore size (C, CO_2 @ 273 K) for IISERP-MOF2 was estimated to be 4.7 Å. This MOF is compositionally related to an another ultra-microporous nickel isonicotinate MOF, ($Ni_9(\mu\text{-}H_2O)_4(H_2O)_2(C_6NH_4O_2)_{18}$), IISERP-MOF1 that has been reported elsewhere.[10a]

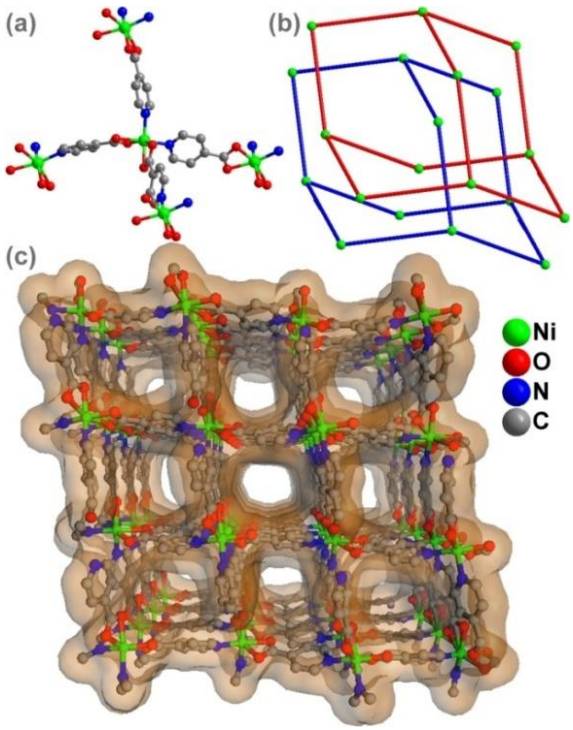

Figure 3.1. (a) Building unit of IISERP-MOF2, showing the coordination around the Ni center and the isonicotinate ligands. **(b)** 2-fold interpenetration present in the diamondoid structure of IISERP-MOF2 with only the Ni (green spheres) centers shown. **(c)** Structure of IISERP-MOF2 with the Connolly surface representation (probe radius = 1.4 Å) showing the ultra-microporous 1-D channels.

3.2.2. Porosity Analysis and CO_2 Adsorption Characteristics:

N_2 isotherms of IISERP-MOF2 at 77, 273 and 303 K are shown in figure 3.2a. A BET surface area of 470 m^2/g and a Langmuir surface area of 700 m^2/g have been determined for IISERP-MOF2. A surface area of 505 m^2/g is calculated using the crystal structure and a N_2 probe. These surface areas are on the high-end for an interpenetrated ultra-microporous MOF built from small linkers. Figure 3.2b shows the CO_2 adsorption isotherms of IISERP-MOF2 at 195, 303, 313 and 333 K. Interestingly, the 195 K isotherm shows that the material has a saturation uptake of about 7 mmol/g that is nearly the same as the saturation uptake it has for N_2 (cf. 77 K N_2 isotherm). This suggests that both gases are able to see the same accessible pores at low temperature. At 303 K and 0.15 bar the CO_2 uptake of IISERP-MOF2 is 1.6 mmol/g. This is 74% higher than that of IISERP-MOF1.[10a] The heat of adsorption (HOA) for CO_2 in IISERP-MOF2 was determined to be moderate (33 kJ/mol) via both virial fits and DFT model (See Appendix Section for more details). IISERP-MOF2 shows a fairly consistent HOA across all loadings, implying one unique binding site (Fig. 3.2c and 3.A.18). Grand canonical Monte Carlo simulations were performed to examine the CO_2-framework interactions. Four unique CO_2 binding sites were identified (see Appendix section). Analysis

of the CO_2-framework interactions in these binding sites reveals that the CO_2 molecules are primarily held by dispersion interactions with electrostatic interactions contributing less than 5% of the total binding energy in three of the four binding sites and 12% in the fourth site.

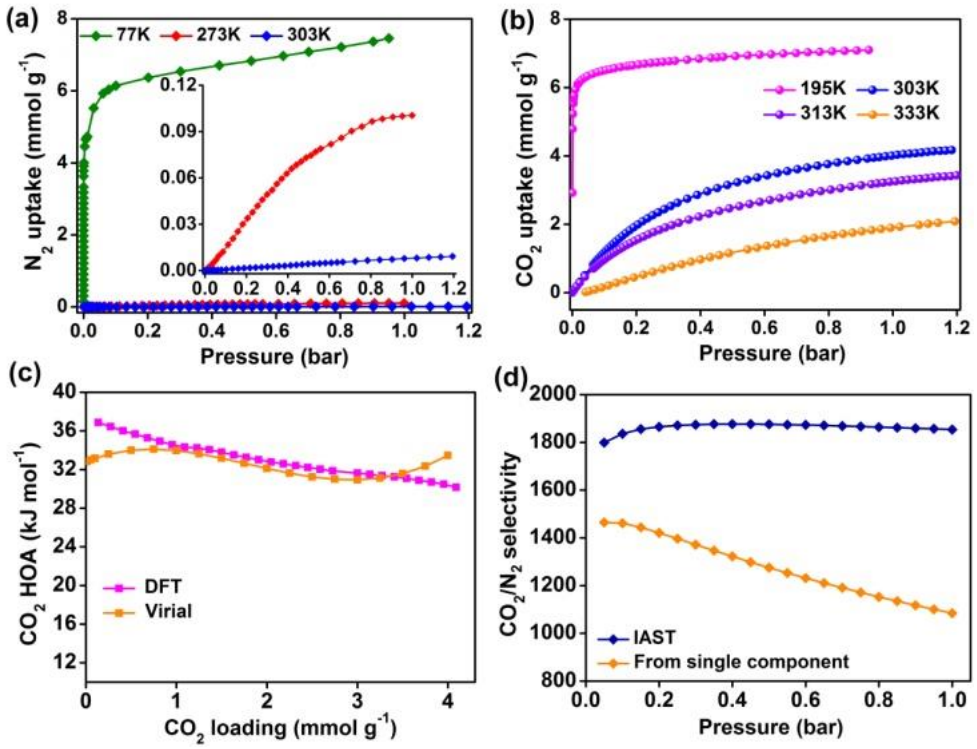

Figure 3.2. (a) N_2 adsorption isotherms of IISERP-MOF2. Inset: A zoom-in of the isotherms at 273 and 313 K. **(b)** CO_2 adsorption isotherms of IISERP-MOF2. **(c)** The HOA plots for CO_2 in IISERP-MOF2 determined using virial and DFT models. **(d)** CO_2/N_2 selectivity of IISERP-MOF2 calculated at 313 K using IAST (composition: $14CO_2$:$86N_2$). Single component selectivity calculated without considering competitive binding.

IISERP-MOF2 was found to adsorb unusually low amounts of N_2 at room temperature or higher, giving rise to exceptional CO_2/N_2 selectivities. Figure 3.2d shows the CO_2/N_2 selectivity of IISERP-MOF2 calculated using the experimental single component isotherms and ideal adsorbed solution theory (*IAST*) with a nominal composition of 14 CO_2:86 N_2. At 1 bar total pressure, and 313 K, conditions of relevance to post-combustion CO_2 capture, IISERP-MOF2 has an exceptional CO_2/N_2 selectivity of 1853. We note that this high selectivity is not an artifact of the competitive binding model used as simply taking the adsorption values from the single component isotherms to calculate the selectivity gives a value of 1084. The selectivity computed for IISERP-MOF2 compares very favorably to other MOFs promoted for post-combustion CO_2 capture, such as Mg-MOF-74 (148 at 1 bar and 323 K with 0.15 bar CO_2 and 0.75 bar N_2[9a] and SIFSIX-3-Zn (1818 at 1 bar and 298 K with 0.10 bar CO_2 and 0.9 bar N_2.[11a]

3.2.3. Parasitic Energy Calculation and Comparison with Top Performing MOFs:

To compare the potential post-combustion CO_2 capture performance of IISERP-MOF2 to other materials, the PEs were calculated following the methodology of Huck *et al.*[3a] using the adsorption data given in that work. While in the work of Huck *et al*. proprietary software was used to evaluate the compression terms of the PE, we used standard equations that are detailed in the materials and methods section. Nonetheless, comparing the PEs for 43 materials, our calculated results differed by only 4.5% on average compared to those reported by Huck *et al*. with a Spearman rank correlation coefficient of 0.998. Figure 3.3 compares the PE calculated for IISERP-MOF2 and a range of other reported materials where the total energy is broken down into the compression and thermal components. The PE for IISERP-MOF2 was calculated to be 655 kJ/kg CO_2, lower than all materials (both hypothetical and synthetically realized) reported by Huck *et al.* The adsorption properties of IISERP-MOF2 are compared to Mg-MOF-74 and SIFSIX-3-Zn in Table 2.A.4.

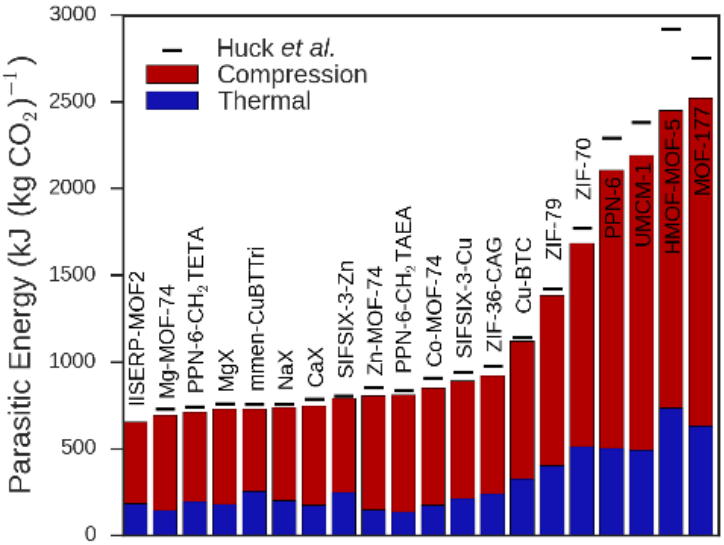

Figure 3.3. Optimized PEs of selected materials calculated with data taken from Huck et al. compared to that of IISERP-MOF2. The thermal (blue) and compression (red) components of the PE are shown. For comparison, values calculated by Huck et al. are shown as black lines.

Interestingly, although IISERP-MOF2 has the lowest reported PE of all materials, it is not the highest performing material in any one category. For example, materials such as Mg-MOF-74 have better CO_2 uptake and working capacities and SIFSIX-3-Cu has a higher CO_2/N_2 selectivity (5463). While it is not clear what the optimal HOA for carbon capture is, both UMCM-1 and MOF-177 have exceptionally low CO_2 HOAs (10.9 kJ/mol and 13.7 kJ/mol, respectively) while possessing very high PEs of greater than 2100 kJ/kg CO_2. One reason why IISERP-MOF2 has such a low PE, is that it optimized to a high desorption pressure of

0.2 bar, while most materials achieved their minimum PE at desorption pressures of between 0.1 to 0.01 bar. The mild desorption pressure for IISERP-MOF2 can, in part, be attributed to the strong response it has to the temperature increase from the adsorption to desorption conditions. It was found that the temperature increase from 313 K to 333 K resulted in a 75% decrease in CO_2 adsorption at 0.15 bar. The high desorption pressure in IISERP-MOF2 gives it the lowest energy of compression of all materials surveyed. If the energy required to place the system under vacuum is included in the total PE, IISERP-MOF2 not only remains the best material in this respect but the difference in the PE to the next closest material increases from 39 to 86 kJ/kg CO_2 (Fig. 3.A.27).

3.2.4. Stability Study:

Aside from having a record low PE for post-combustion CO_2 capture, IISERP-MOF2, possesses other favorable characteristics for post-combustion CO_2 capture. Unlike Mg-MOF-74, which has open metal sites and is known to decompose in humid conditions,[18] IISERP-MOF2 has no open metal sites and has exceptional hydrolytic stability. For example, following 7 days of steam treatment at > 85% RH, there was no loss of crystallinity or porosity in IISERP-MOF2 as confirmed by the PXRD patterns and CO_2 sorption measurements (Fig. 3.4a and 3.4b). The same sample sat on the shelf for 6 months exposed to the atmosphere with RH > 65%. Again there was no loss in crystallinity or porosity. The adsorption capacity at 0.15 bar CO_2 saw a decrease of only 1.7% after 7 days of steam treatment and a decrease of 2.4% following exposure to the atmosphere for 6 months. IISERP-MOF2 is also not susceptible to degradation by carbonic acid, which is known to form in humid CO_2 streams. This is evidenced by the fact that the CO_2 adsorption isotherm is also unchanged following exposure to a flow of humid CO_2 for 24 hours. CO_2 regeneration from the MOF, was evaluated from a cycling experiments on the ASAP2020HD ad-sorption instrument. During this, the sample was subjected to a pressure swing from 1.18 bar to 0.02 bar with each the sorption-desorption cycle lasting for 40 mins. As can be seen from figure 3.4c, the amount of CO_2 adsorbed remains constant. This parallels the large diffusion coefficients (Dc) for CO_2 within the pores of the MOF (Fig. 3.4d). The average Dc of IISERP-MOF2 over a range of CO_2 loadings was found to be 6.04 x 10^{-9} m^2s^{-1}, which is higher than that found in other MOFs with much larger pores such as MOF-5 (1.17 x 10^{-9} m^2s^{-1}) or MOF-177 (1.17 x 10^{-9} m^2s^{-1}).[19] The Dc is also higher than that of IISERP-MOF1 which is also ultra-microporous with a very similar pore chemistry.

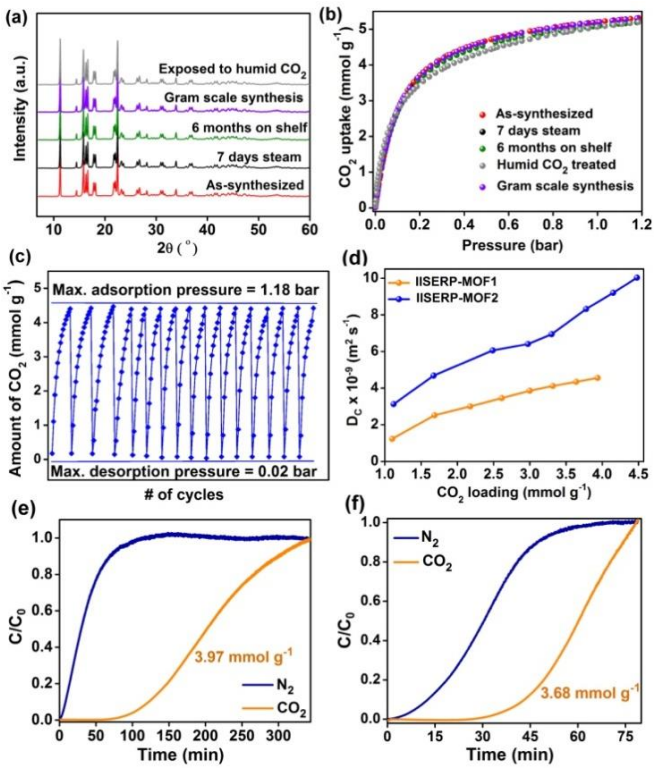

Figure 3.4. (a) PXRD pattern and **(b)** CO_2 adsorption isotherms of IISERP-MOF2: as-synthesized, after 7 days of steam treatment (> 85% RH), after 6 months exposure to atmosphere, after flowing humid CO_2 (74% RH) for 24hrs, and from a gram scale synthesis. **(c)** CO_2 adsorption-desorption cycles at 30°C. **(d)** CO_2 self-diffusion coefficients from kinetics measurement. Values for IISERP-MOF1 is taken from ref. 10. Breakthrough measurements under **(e)** Dry and **(f)** 50% RH conditions. Note: The amount of sample used in wet measurement was ~1/3rd of what was used in dry measurements.

Most notably, the Dc is more than two orders of magnitude higher than zeolite 13X, the currently used commercial PSA sorbent,[20] suggesting that ultra-microporous MOFs can have favorable sorption kinetics for gas separations.

3.2.5. Mixed Gas Analysis, Breakthrough Measurements:

To examine the adsorption kinetics in more real world condi-tions, breakthrough experiments were performed on IISERP-MOF2 under dry and wet (50% RH) conditions, which are shown in figure 3.4e and 3.4f. In both cases the N_2 comes off before the CO_2. Importantly, even under 50% RH IISERP-MOF2 loses only about 7% of its maximum CO_2 capacity. This compares closely to what was observed for the SIFSIX-2-Cu-i, which has been promoted for its optimal thermo-dynamics and kinetics.[11a] The CO_2 capacity of IISERP-MOF2 under dynamic conditions was found to be 3.97 mmol/g, which is lower than NiMOF-74 (4.5 mmol/g) but higher than the members of SIFSIX series, such as SIFSIX-3-Zn (1.9

mol/kg), SIFSIX-3-Cu (2.32 mol/kg), SIFSIX-3-Co (2.56 mol/kg), SIFSIX-3-Ni (2.54 mol/kg).[21] And is higher than those observed for the FJU series, whose breakthrough studies were carried out under a relatively higher flow rate (5 ml/min).[22]

3.3. Conclusions:

Since roughly 40% of our current anthropogenic CO_2 emissions are a result of burning fossil fuels to generate electricity, few se-rious green house gas mitigation strategies do not include carbon capture and storage as part of the solution. The technological barrier to large scale CCS arises from high energetic penalty to scrubbing CO_2 with current methods. Although P/TSA systems are amongst the most energy efficient CO_2 scrubbing technologies, better sorbent materials are still needed. In this work, IISERP-MOF2 was found to have the lowest PE reported for post-combustion CO_2 capture, out-performing even Mg-MOF-74 (655 vs. 695 kJ/kg CO_2). IISERP-MOF2 has a modest CO_2 uptake at 0.15 bar and 313 K, an exceptional CO_2:N_2 selectivity of 1853 and low heat of adsorption. IISERP-MOF2 was found to have the lowest compression energy component of the PE of all materials surveyed. In addition to the record low PE, IISERP-MOF2 has remarkable hydrolytic stability, smooth separation kinetics as evidences from the dry and humid breakthrough measurements, easy scalability, and is made from readily available and inexpensive precursors, making it a highly promising candidate for large scale post-combustion CO_2 capture even under humid conditions. This work further shows that ultra-microporous MOFs can be excellent materials for gas separation applications and should be studied in more depth.

3.4. References:

1. CO_2 Emissions from Fuel Combustion Highlights (**2015** Edition) © OECD/IEA, 2015.
2. Singha, D.; Croiseta, E.; Douglasa, P. L.; Douglas, M. A. *Energy Conversion and Management* **2003**, *44*, 3073.
3. (a) Huck, J. M.; Lin, L. -C.; Berger, A. H.; Shahrak, M. N.; Martin, R. L.; Bhown, A. S.; Haranczyk, M.; Reuterb, K.; Smit, B. *Energy Environ. Sci*. **2014**, *7*, 4132. (b) Lin, L. -C.; Berger, A. H.; Martin, R. L.; Kim, J.; Swisher, J. A.; Jariwala, K.; Rycroft, C. H.; Bhown, A. S.; Deem, M. W.; Haranczyk, M.; Smit, B. *Nat. Mater*. **2012**, *11*, 633. (c) CO_2 Capture from Existing Coal-Fired Power Plants (US DOE): South Park Township, **2007**.

4. Ciferno, J. P.; Fout, T. E.; Jones, A. P.; Murphy, J. T. *Chem. Eng. Prog*. **2009**, *105*, 33.

5. Ko, D.; Siriwardane, R.; Biegler, L. T. *Ind. Eng. Chem. Res*. **2003**, *42*, 339.

6. (a) Pirngruber, G. D.; Carlier, V.; Leinekugel-le-Cocq, D. *Oil & Gas Science and Technology – Rev*. **2014**, *69*, 989. (b) Joos, L.; Swisher, J. A.; Smit, B. *Langmuir* **2013**, *29*, 15936.

7. (a) Li, J. -R.; Ma, Y.; McCarthy, M. C.; Sculley, J.; Yu, J.; Jeong, H. -K.; Balbuena, P. B.; Zhou, H. -C. *Coord. Chem. Rev*. **2011**, *255*, 1791. (b) Nguyen, N. T. T.; Furukawa, H.; Gndara, F.; Nguyen, H. T.; Cordova, K. E.; Yaghi, O. M. *Angew. Chem. Int. Ed.* **2014**, *53*, 10645. (c) Fracaroli, A. M.; Furukawa, H.; Suzuki, M.; Dodd, M.; Okajima, S.; Gándara, F.; Reimer, J. A.; Yaghi, O. M. *J. Am. Chem. Soc.* **2014**, *136*, 8863. (d) Zhou, H. -C. J.; Kitagawa, S. *Chem. Soc. Rev.* **2014**, *43*, 5415. (e) Xiang, S.; He, Y.; Zhang, Z.; Wu, H.; Zhou, W.; Krishna, R.; Chen, B. *Nat. Comm.* **2012**, *3*, 954. (f) Benson, O.; da Silva, I.; Argent, S. P.; Cabot, R.; Savage, M.; Godfrey, H. G. W.; Yan, Y.; Parker, S. F.; Manuel, P.; Lennox, M. J.; Mitra, T.; Easun, T. L.; Lewis,W.; Blake, A. J.; Besley, E.; Yang, S.; Schröder, M. *J. Am. Chem. Soc*. **2016**, *138*, 14828.

8. (a) Bhatt, P. M.; Belmabkhout, Y.; Cadiau, A.; Adil, K.; Shekhah, O.; Shkurenko, A.; Barbour, L. J.; Eddaoudi, M. *J. Am. Chem. Soc*. **2016**, *138*, 9301. (b) Liao, P. -Q.; Chen, X. -W.; Liu, S. -Y.; Li, X. -Y.; Xu, Y. -T.; Tang, M. -N.; Rui, Z. -B.; Ji, H. -B.; Zhang, J. -P.; Chen, X. -M. *Chem. Sci*. **2016**, *7*, 6528. (c) Zhou, H. C. J.; Long, J. R.; Yaghi, O. M. *Chem. Rev*. **2012**, *112*, 673. (d) Bae, Y. -S.; Farha, O. K.; Hupp, J. T.; Snurr. R. Q. *J. Mater. Chem*. **2009**, *19*, 2131. (e) Zhang, Z.; Yao, Z. -Z.; Xiang, S.; Chen, B. *Energy Environ. Sci*. **2014**, *7*, 2868. (f) Vaidhyanathan, R.; Iremonger, S. S.; Shimizu, G. K. H.; Boyd, P. G.; Alavi, S.; Woo, T. K. *Science* **2010**, *330*, 650. (g) An, J.; Geib, S. J.; Rosi, N. L. *J. Am. Chem. Soc.* **2010**, *132*, 38. (h) Dzubak1, A. L.; Lin, L. -C.; Kim, J.; Swisher, J. A.; Poloni, R.; Maximoff, S. N.; Smit, B.; Gagliardi, L. *Nat. Chem*. **2012**, *4*, 810. (i) Kumar, A.; Madden, D. G.; Lusi, M.; Chen, K. -J.; Daniels, E. A.; Curtin, T.; Perry IV, J. J.; Zaworotko, M. J. *Angew. Chem. Int. Ed*. **2015**, *54*, 14372.

9. (a) Mason, J. A.; Sumida, K.; Herm, Z. R.; Krishna, R.; Long, J. R. *Energy Environ. Sci.* **2011**, *4*, 3030. (b) Furukawa, H.; Cordova, K. E.; O'Keeffe, M.; Yaghi, O. M. *Science* **2013**, *341*, 974.

10. (a) Nandi, S.; De Luna, P.; Daff, T. D.; Rother, J.; Liu, M.; Buchanan, W.; Hawari, A. I.; Woo, T. K.; Vaidhyanathan, R. *Sci. Adv*. **2015**, *1*, e1500421. (b) Nandi, S.; Haldar, S.; Chakraborty, D.; Vaidhyanathan, R. *J. Mater. Chem. A*, **2017**, *5*, 535.
11. (a) Nugent, P.; Belmabkhout, Y.; Burd, S. D.; Cairns, A. J.; Luebke, R.; Forrest, K.; Pham, T.; Ma, S.; Space, B.; Wojtas, L.; Eddaoudi, M.; Zaworotko, M. J. *Nature*. **2013**, *495*, 80. (b) Mason, J. A.; McDonald, T. M.; Bae, T. H.; Bachman, J. E.; Sumida, K.; Dutton, J. J.; Kaye, S. S.; Long, J. R. *J. Am. Chem. Soc*. **2015**, *137*, 4787.
12. Kemmer, G.; Keller, S. *Nat. Protoc.* **2010**, *5*, 267–81.
13. Richter, E.; Schuetz, W.; Myers, A. L. *Chem. Eng. Sci.* **1989**, *44*, 1609–1616.
14. Myers, A. L.; Prausnitz, J. M. *AIChE J.* **1965**, *11*, 121–127.
15. (a)Malek, K.; Coppensa, M.-O. *J. Chem. Phys.* **2003**, *119*, 2801. (b) Adsorption analysis and equilibria and kinetics, D. D. Do, Imperial College Press, Ed. **2008**.
16. Freeman, S. A.; Dugas, R.; Wagener, D. V.; Nguyen, T.; Rochelle, G. T. *Energy Procedia*, **2010**, *1*, 119-124
17. Swisher, J. A.; Lin, L. -C.; Kim, J.; Smit, B. *AIChE*, **2013**, 59, 3054.
18. (a) Kizzie, A. C.; Wong-Foy, A. G.; Matzger, A. J. *Langmuir* **2011**, *27*, 6368. (b) Yu, J.; Balbuena, P. B. *J. Phys. Chem. C* **2013**, *117*, 3383.
19. (a) Saha, D.; Bao, Z.; Jia, F.; Deng, S. *Environ. Sci. Technol*. **2010**, *44*, 1820. (b) Zhao, Z.; Li, Z.; Lin, Y. S. Ind. *Eng. Chem. Res*. **2009**, *48*, 10015.
20. Silva, J. A. C.; Schumann, K.; Rodrigues, A. E. *Micro. Meso. Mater*. **2012**, *158*, 219.
21. Elsaidi, S. K.; Mohamed, M. H.; Schaef, H. T.; Kumar, A.; Lusi, M.; Pham, T.; Forrest, K. A.; Space, B.; Xu, W.; Halder, G. J.; Liu, J.; Zaworotko, M. J.; Thallapally, P. K. *Chem. Commun*. **2015**, *51*, 15530.
22. (a) Ye, Y.; Xiong, S.; Wu, X.; Zhang, L; Li, Z.; Wang, L.; Ma,X.; Chen, Q,. H.; Zhang, Z.; Xiang, S. *Inorg. Chem*. **2016**, *55*, 292; (b) Yao, Z.; Chen, Y.; Liu, L.; Wu, X.; Xiong, S.; Zhang, Z., Xiang, S. *ChemPlusChem* **2016**, *81*, 850 – 856.

3.A. Appendix for Chapter 3:

Single Crystal Structure Analysis: *Remarks on the Building Units Involved in the Structure of IISERP-MOF2:*

There are about 10 structures with Ni and isonicotinic acid or 4-pyridine carboxylic acid (PyC), some of these frameworks involve more than 1 ligand [A1] There are few structures with only PyC as linker. In all cases, the coordination around Ni is octahedral. In some cases tri nuclear hydroxo cluster or di nuclear hydroxo cluster is present.[A1b A2] Also there is one structure based on di nuclear water bridged unit, which we have published recently [10a]. In general, the hydroxo cluster based MOFs are less stable to water and steam compared to the ones built from water bridged clusters. To the best of our knowledge, structures built entirely from mononuclear octahedral Ni are very little known[A2] and they have not been investigated for CO_2 capture properties. However, in our experience, they seem to exhibit much higher hydrolytic and water stability than the other two.

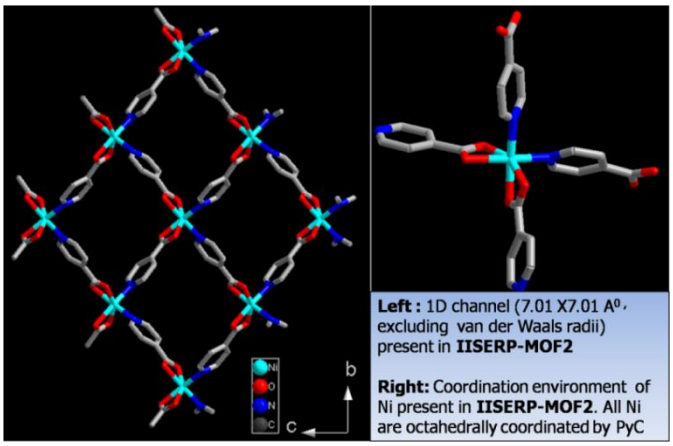

Figure 3.A.1. Left: one dimensional channels lined by Pyc linker present in IISERP-MOF2; Right: Octahedral coordination around Ni centers of IISERP-MOF2.

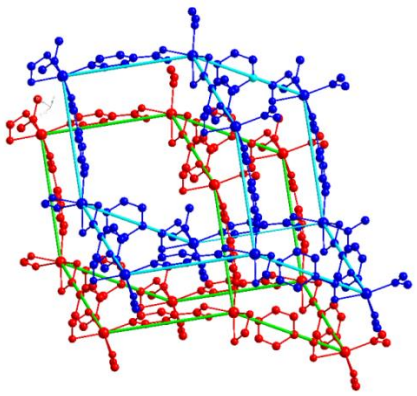

Figure 3.A.2. The Single crystal X-ray structure of IISERP-MOF2 showing the two-fold interpenetrated diamondoid net.

Analytical Characterizations:

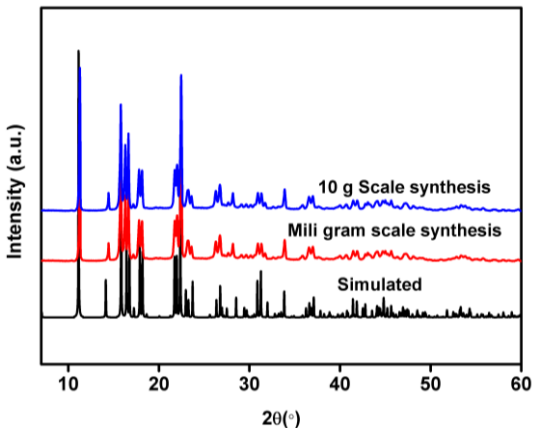

Figure 3.A.3. Comparison of the powder X-ray diffraction patterns of IISERP-MOF2 with the ones simulated from single crystal data.

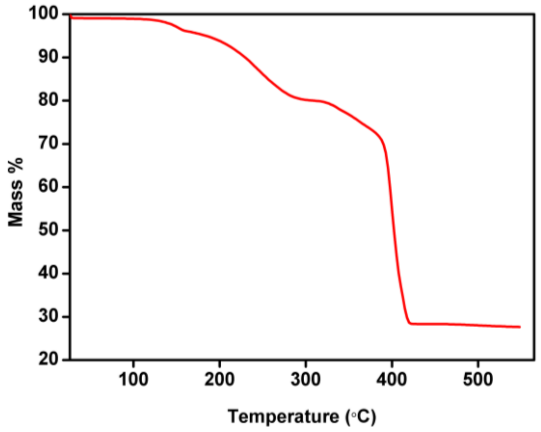

Figure 3.A.4. TGA plots of the as-made sample of IISERP-MOF2.

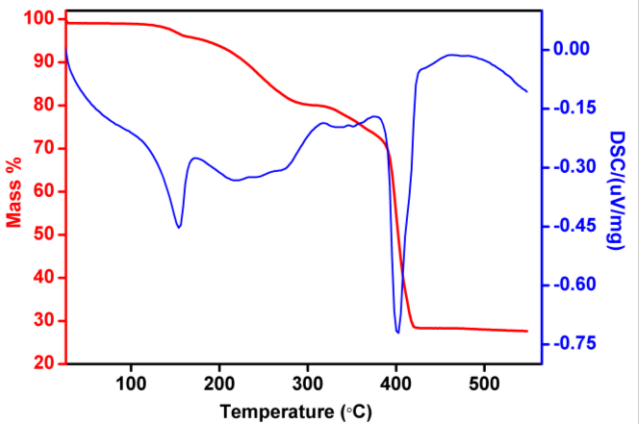

Figure 3.A.5. TGA carried out on the as synthesized sample of IISERP-MOF2. It was found that material has no weight loss up to 130ºC and from 130ºC to 280ºC there is a gradual weight loss which is due to the loss of DMF molecules trapped inside the pore (Wt. loss calc: 19.49%; obsd: 20.01%).

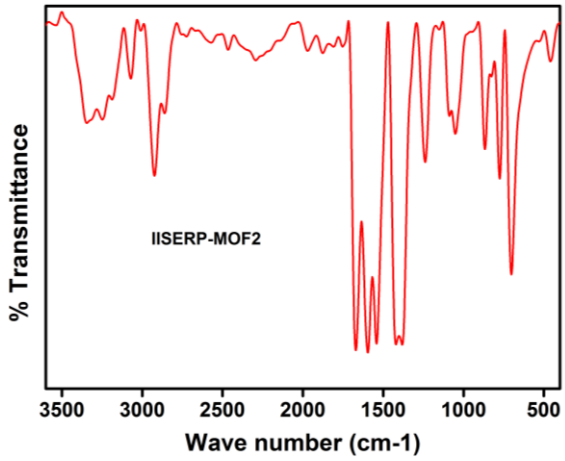

Figure 3.A.6. IRspectra of IISERP-MOF2, showing the various stretching and bending modes present. Selected peaks: IR (KBr pellet, cm^{-1}): v(O-H) surface solvent: 3472cm^{-1}; v(COO): 1664 cm^{-1} and 1596 cm^{-1}, v(CN)s 1429 cm^{-1}, 1369 cm^{-1}; v(C=C): 1200 to 900 cm^{-1}.

Adsorption Studies:

Table 3.A.1. Adsorption and desorption data for 195 K CO_2 for IISERP-MOF2

adsorption		Desorption	
Pa(bar)	Q(mmol/g)	Pd(bar)	Q(mmol/g)
4.24E-04	2.920294	0.924858	7.098458
0.001304	4.784641	0.915596	7.102443
0.002184	5.230547	0.877426	7.095304
0.003656	5.537741	0.836302	7.084414
0.004876	5.671918	0.79695	7.076555
0.006102	5.76327	0.756502	7.065809
0.010243	5.943663	0.714479	7.050956
0.017118	6.087744	0.675397	7.038297
0.019844	6.127495	0.633114	7.027226
0.022859	6.163919	0.592825	7.012317
0.028699	6.218341	0.553242	6.979797
0.038162	6.28426	0.512353	6.959636
0.04756	6.334696	0.472164	6.93937
0.063328	6.397578	0.431923	6.91809
0.078927	6.448419	0.39069	6.894234
0.092421	6.482398	0.350616	6.868323
0.105303	6.510718	0.309677	6.837974
0.118731	6.53897	0.269238	6.80469
0.132005	6.563125	0.249155	6.784634
0.150647	6.594456	0.22868	6.763826
0.16958	6.622408	0.188579	6.717469
0.179066	6.635181	0.14735	6.659823
0.188864	6.64833	0.107267	6.588262

0.20711	6.671488	0.086769	6.539328
0.22576	6.694539	0.066664	6.478491
0.245515	6.714444	0.046562	6.398419
0.263989	6.73245	0.026042	6.262213
0.282478	6.749759	0.015801	6.134899
0.302461	6.767949	0.010983	6.031847
0.320666	6.782726	0.005897	5.820646
0.358593	6.812432	0.003598	5.603634
0.395854	6.841849	0.001326	4.902018
0.432428	6.868651		
0.452923	6.884107		
0.471345	6.897317		
0.50938	6.916327		
0.547364	6.938246		
0.584815	6.958219		
0.620378	6.975005		
0.658328	6.990667		
0.698069	7.008971		
0.734833	7.028536		
0.771976	7.041449		
0.810406	7.057042		
0.849589	7.070817		
0.887676	7.082443		
0.924858	7.098458		

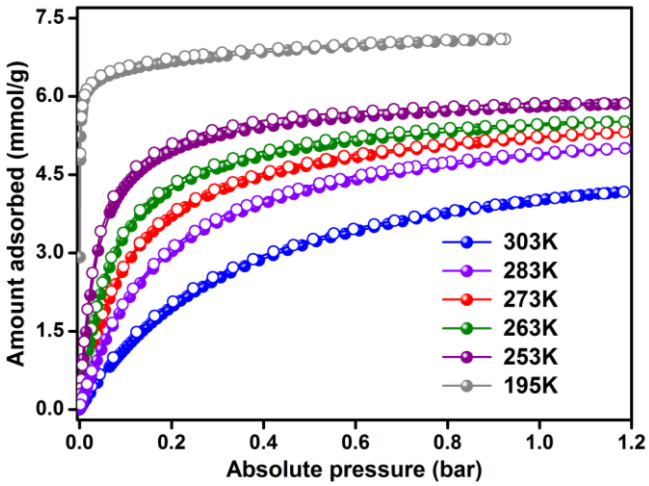

Figure 3.A.7. CO_2 isotherms of IISERP-MOF2 collected at 303, 283, 273, 263, 253 and 195 K temperature.

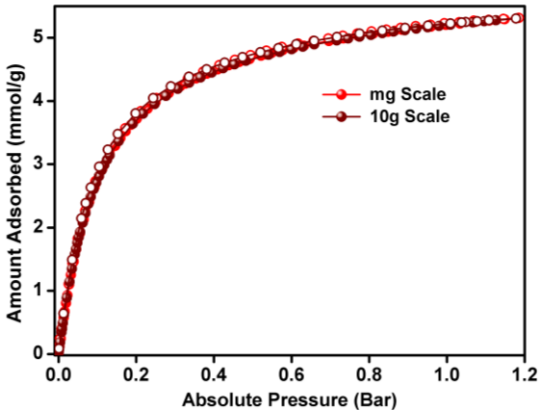

Figure 3.A.8. Comparison of the 273 K CO_2 adsorption isotherms of the mg and gm scale syntheses of IISERP-MOF2 .

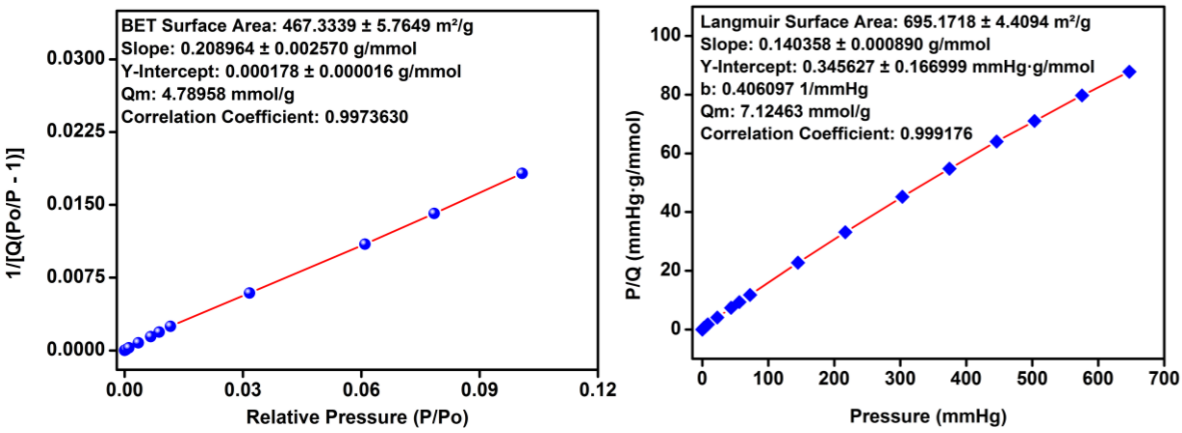

Figure 3.A.9. BET and Langmuir fits of IISERP-MOF2 from the 77 K N_2 data.

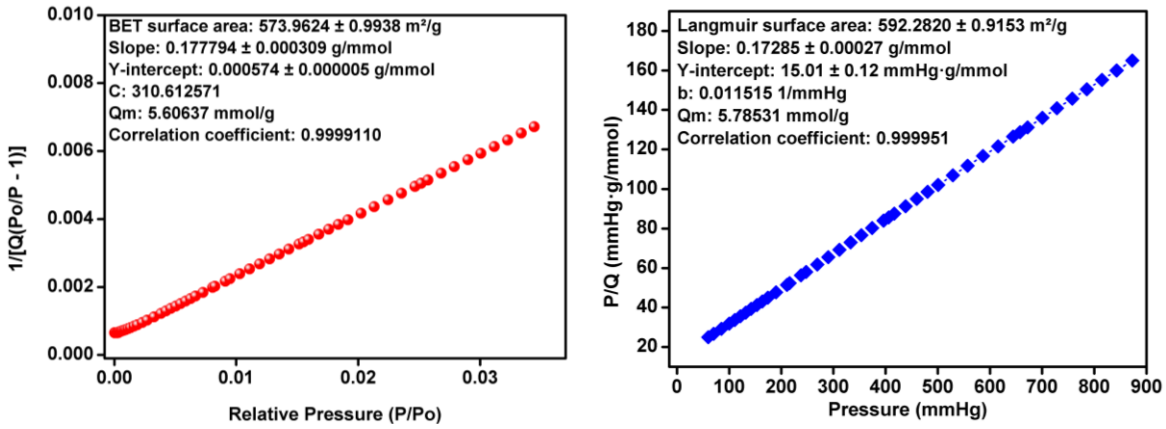

Figure 3.A.10. BET and Langmuir fits of IISERP-MOF2 from the 273 K CO_2 isotherm data.

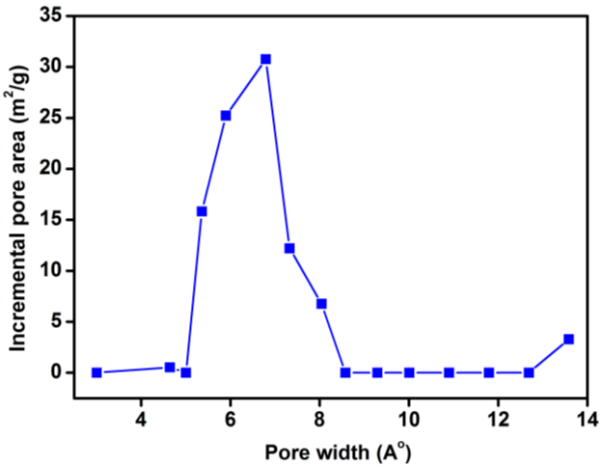

Figure 3.A.11. Pore size distribution in IISERP-MOF2 obtained by fitting the NLDFT model to the 77 K N_2 adsorption branch. Pore diameter ~6.0 Å.

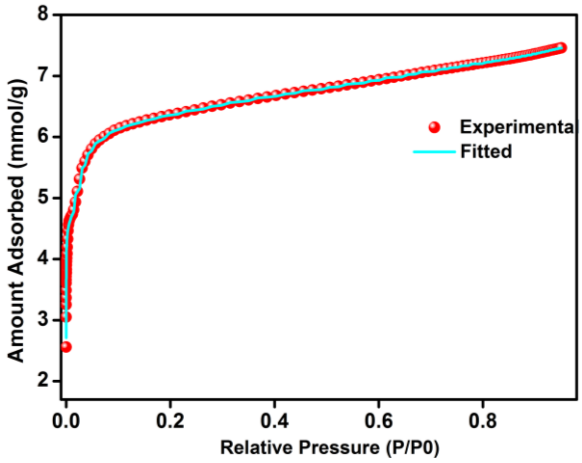

Figure 3.A.12. NLDFT fit of 77 K N_2 adsorption branch for IISERP-MOF2.

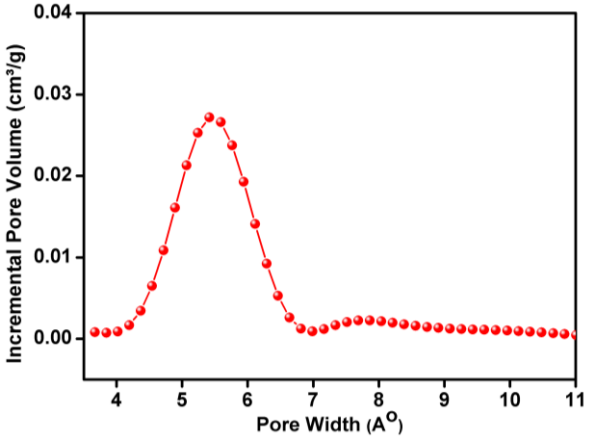

Figure 3.A.13. Pore size distribution in IISERP-MOF2 obtained by fitting the NLDFT model to the 273K CO_2 adsorption branch. Note the presence of pores with dimension ~5.5 Å agrees well with the ultra-microspores observed in the single crystal structure.

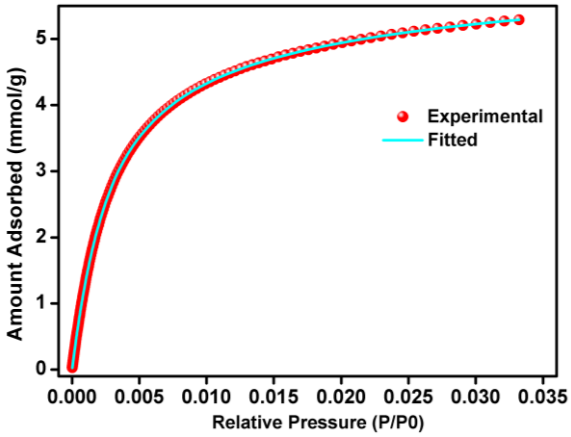

Figure 3.A.14. NLDFT fit of 273 K CO_2 adsorption branch for IISERP-MOF2.

Heat of Adsorption for CO_2 from Virial and NLDFT Models:

CO_2 adsorption was measured at 263, 273, 283, 303 K and were fitted by the virial equation.

$$ln(P) = ln(Va)+(A0+A1*Va +A2*Va^2 \ldots + A6*Va^6)/T+(B0+B1*Va) \quad (1)$$

Where P is pressure, Va is amount adsorbed, T is temperature, and A0, A1, A2 … , A4 and B0, B1 are temperature independent empirical parameters

Table 3.A.2: Summary of the fitted Virial parameters**.**

A0	-3943.633942	B0	17.49155951
A1	-489.529194	B1	1.51345055
A2	437.9397115	B2	-1.200111671
A3	-92.8872708		
A4	3.18204289		

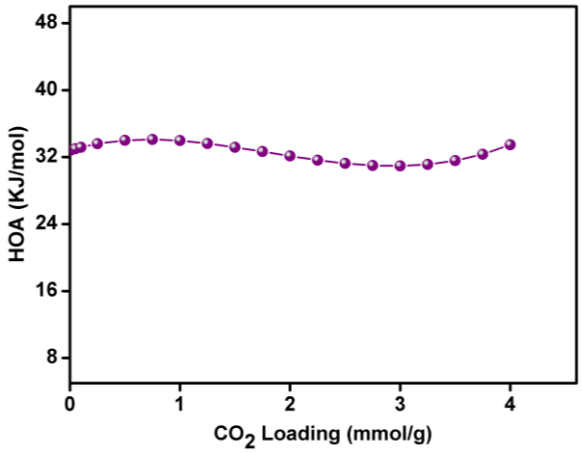

Figure 3.A.15. HOA calculated from Virial modeling done using the CO_2 isotherms carried out at -10°C, 0°C, +10°C and +30°C.

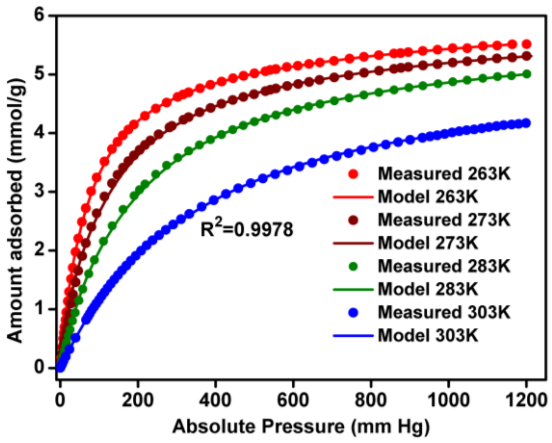

Figure 3.A.16. Comparison of experimental isotherms to the ones obtained from Virial modeling carried out using CO_2 isotherms collected at -10°C, 0°C, +10°C and +30°C.

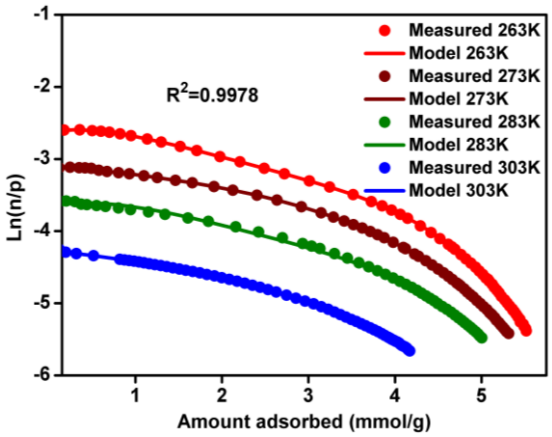

Figure 3.A.17. Virial plots carried out using CO_2 isotherms collected at -10°C, 0°C, +10°C and +30°C.

Dual Site Langmuir Model Fits:

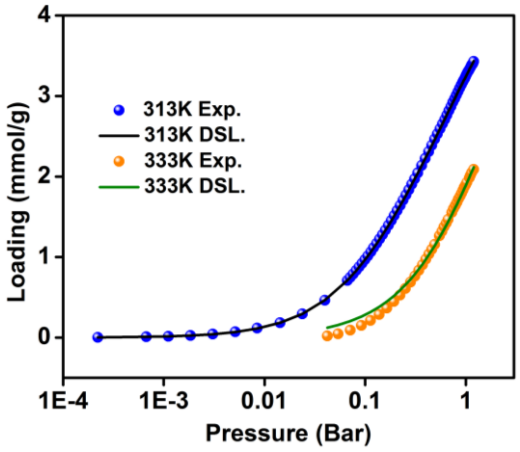

Figure 3.A.18. The log plot showing the fit between the experiment and the model obtained from a dual site equation using 313 and 333 K CO_2 isotherms.

Dual site model fit parameters

313 K 333 K

qsatA	1.891956	qsatA	1.895425
qsatB	3.298484	qsatB	3.301824
b_a	5.526728	b_a	0.575497
b_b	0.992234	b_b	0.575497

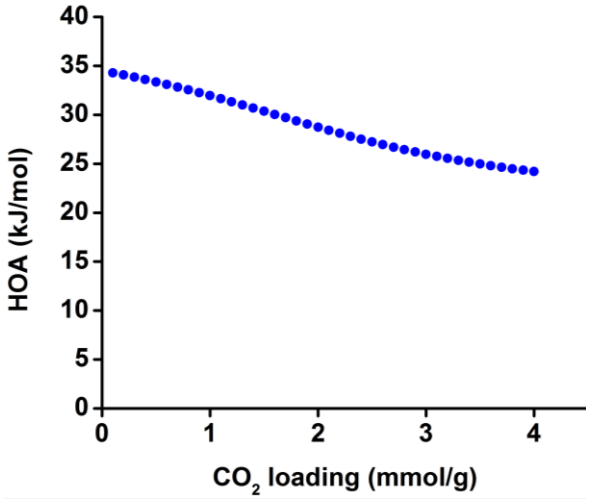

Figure 3.A.19. The CO_2 adsorption isotherms changed from dual-site to single site when the temperature was increased from 313 to 333 K and had different saturation capacities.

High Temperature CO_2 and N_2 Isotherms:

For Parasitic energy calculation high temperature isotherms were collected at 313 K and 333K temperature. It shows significant CO_2 uptake even at 333 K but unusually low N_2 uptake was observed in both cases.

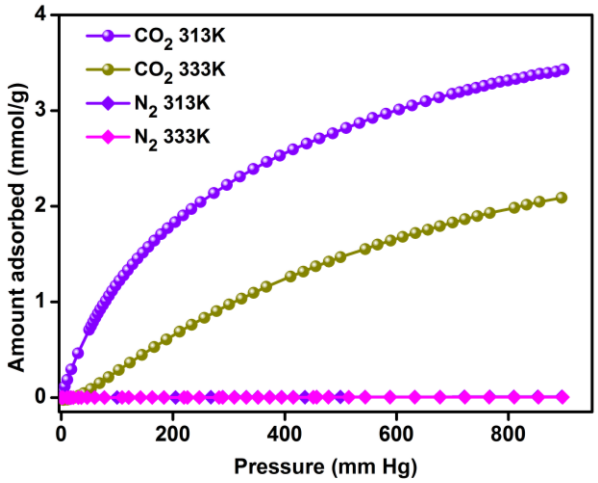

Figure 3.A.20. CO_2 and N_2 isotherms at 313 and 333 K showing the apparent selectivity.

IAST Selectivities:

CO_2/N_2 selectivity was calculated for IISERP-MOF2 using the experimental single component CO_2 and N_2 isotherms and ideal adsorbed solution theory (IAST) with a nominal composition of $14CO_2$:$86N_2$. At 1 bar total pressure, and 313 K, conditions of relevance to post-combustion CO_2 capture, IISERP-MOF2 has an exceptional CO_2/N_2 selectivity of 1853 which is remarkable. This unusually high selectivity is due to very low nitrogen uptake for the MOF at that temperature.

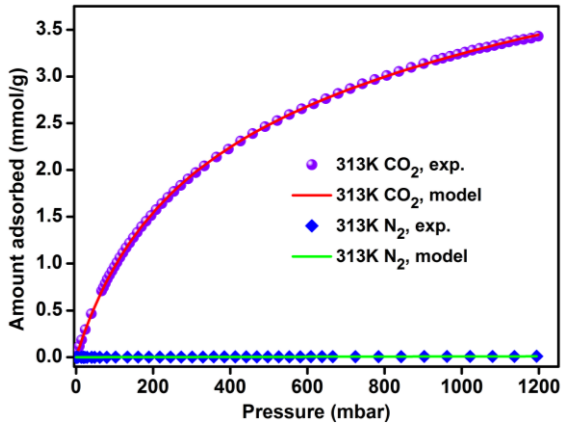

Figure 3.A.21. IAST fitting of 313 K CO_2 and N_2 isotherms.

Rate of Adsorption Studies- Self-Diffusion Coefficients Calculations and Analysis:

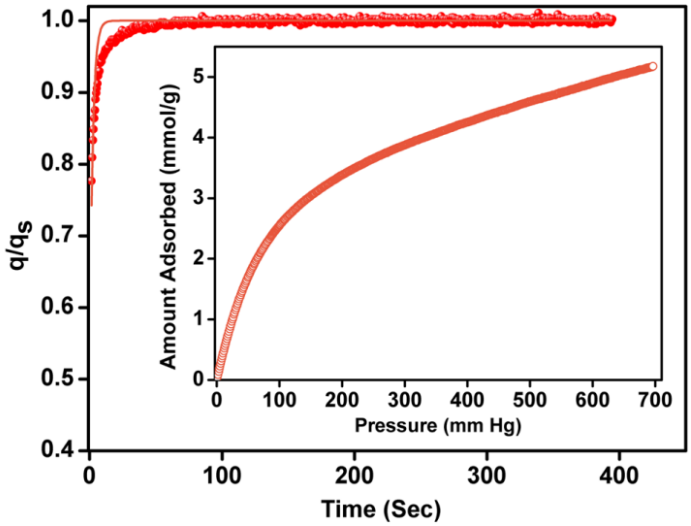

Figure 3.A.22. Representative plot of the adsorbate fractional filling vs time showing the fit between the spherical model (line) and the collected data (spheres) obtained from the single component CO_2 isotherm of IISERP-MOF2. Inset shows the high resolution 273 K (consisting 600 data points) adsorption isotherm used in this diffusion modeling. Note eight such fittings were considered to obtain the average diffusion coefficient.

Breakthrough Measurement: Comparitive Studies and Cycle Data:

Considering the results from typical laboratory based breakthrough instrument could vary from a number of experimental factors such as material loading and packing, accurate calculation of the sample weight, leak-free system etc. To validate the repeatability of the studies and the stability of the material under the breakthrough conditions, the breakthrough runs were repeated for two cycles on the same sample. The results indicated that there was not much difference between the two cyles (see Figs. 3.4e and 3.A.23). Apart from this, we evaluated benchmark NiMOF-74 (also known as NiDOBDC or MOF-74-Ni) for comparison. For this, the breakthrough run was carried out under the same experimental condition that was used for the IISERP-MOF2. As expected, NiMOF-74 showed efficient CO_2/N_2 separation (Fig. 3.A.24), and the uptake matches closely with those reported from the single component isotherm [A3].

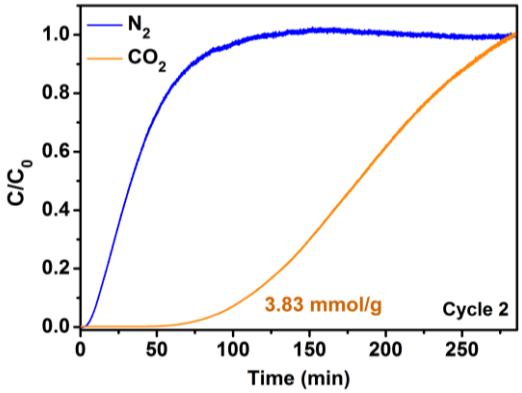

Figure 3.A.23. Breakthrough measurements on IISERP-MOF2 carried out for two consecutive cycles. In both cycles a nominal composition of 85:15 of N_2:CO_2 was used and the runs were carried out at RT and 1 bar pressure with a 1ml/min flow rate). The data corresponding to the first cycle is presented in figure 3.4e. This shows the cyclic stability of the material.

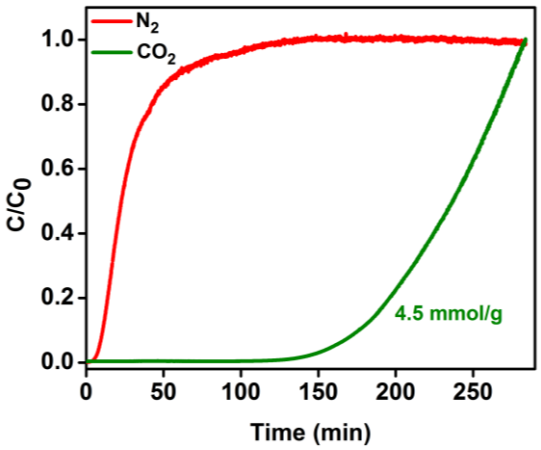

Figure 3.A.24. Breakthrough measurements on Ni-MOF74 carried out under the same conditions as reported in figure 3.A.23.

Additional Discussion on the Breakthrough Results:

The equilibrium CO_2 capacity for NiMOF under dynamic condition was found to be 4.5 mmol/g, matching well with the experimental pure component isotherm at that partial pressure (0.15 bar of CO_2,) [A3]. The CO_2 capacity of the IISERP-MOF2 under a flow rate of 1 ml/min was 3.97 mmol/g, which is lower than NiMOF-74 and higher than most of the SIFSIX analogues under identical conditions[A4]. For example, SIFSIX-3-Zn (1.9 mol/kg), SIFSIX-3-Cu (2.32 mol/kg), SIFSIX-3-Co (2.56 mol/kg), SIFSIX-3-Ni (2.54 mol/kg) all have lower capacities than IISERP-MOF2.

Stability Studies:

These ultra and microporous MOFs are quite interesting owing to their good stability to solvent removal as compare to the large pore MOFs which in many cases require highly demanding moisture free handling and in spite of that tend to show partial to complete loss of long range order.

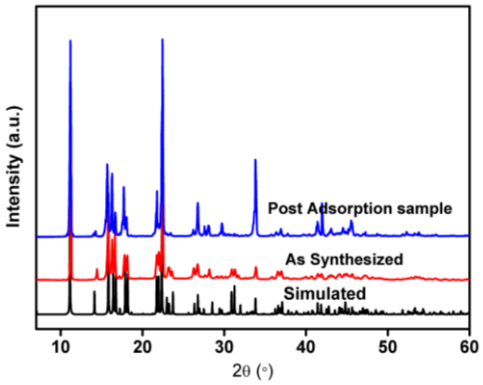

Figure 3.A.25. PXRD comparisons indicating the retention of crystallinity by IISERP-MOF2 following repeated heating and cooling during multiple gas adsorption studies.

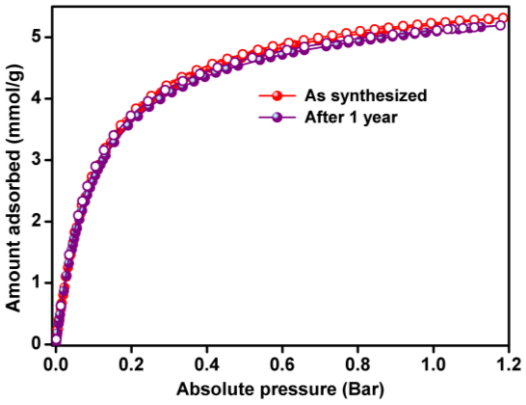

Figure 3.A.26. The comparison of the CO_2 adsorption (273 K) between a freshly prepared phase and one that has been sitting in a bottle for a year.

Computational Section:

Parasitic Energy Calculation:

Table 3.A.3. Isotherm fit parameters for IISERP-MOF2.

	CO_2				N_2		
Parameter	σ_1 (mmol/g)	k_{H1} (bar^{-1})	σ_2 (mmol/g)	k_{H2} (bar^{-1})	σ (mmol/g)	k_H (bar^{-1})	n
Adsorption	1.8920	5.5267	3.2984	0.9922	5.0081	0.001244	0.9617
Desorption	5.8116	0.4902	0	0	0.003802	5.0080	0.9600

Table 3.A.4. CO_2 adsorption properties and parasitic energy for IISERP-MOF2 compared to Mg-MOF-74 and SIFSIX-3-Zn.

Material	**IISERP-MOF2**	Mg-MOF-74[a]	SIFSIX-3-Zn[a]
Uptake (mmol/g)	1.2	4.91	2.34
Working capacity (mmol/g)	0.69	1.78	0.47
CO_2 HOA (kJ/mol)	33.6	37.4	41.5
Selectivity (CO_2/N_2)	1853	232	629
Parasitic energy (kJ/kg CO_2)	655	693	792

[a] calculated using data given in Huck *et al.*[3a]

Table 3.A.5. Comparison of the Parasitic Energy for some of the selected solid sorbents.

Materials Code	**Compression (kJ/kg CO_2)**	**Thermal (kJ/ kg CO_2)**	**Parasitic energy (kJ/kg CO_2)**
IISERP-MOF2	471.76403	183.1985	654.96253
Mme-Cubttri	472.59036	256.16331	728.75367
PPN-6-CH_2TETA	515.22034	197.14711	712.36745
Nax	537.581	200.82488	738.40588
ZIF-36-frl	539.65834	250.94585	790.60419
Caa-313	540.66248	220.54725	761.20973
SIFSIX-3-Zn	542.49593	249.71499	792.21092
Naa	546.15046	183.30366	729.45412
Mgx	546.82696	181.61114	728.4381
Mg-mof-74	548.47803	145.4653	693.94333
Mga	570.12779	183.92709	754.05488
Cax-313	573.25116	174.39228	747.64344
PPN-6-SO3Li	586.21952	227.35497	813.57449
Zn-mof-74	657.15166	148.26415	805.41581
Co-MOF-74-313	676.11514	174.55457	850.66971
SIFSIX-3-cu	676.86505	214.4156	891.28065
ZIF-36-cag	681.78625	241.43365	923.2199
Ni-mof-74	715.99217	224.42675	940.41892
ZIF-116-cag	877.7602	183.57314	1061.33334
ZIF-82	894.87169	261.72127	1156.59296
Ps-mfi	921.06694	291.40728	1212.47422
Zif-79	980.62322	403.88866	1384.51188

Cu-bttri	1065.73555	246.45942	1312.19497
ZIF-115-mer	1162.385	323.31865	1485.70365

We note that the PE calculation of Huck et al. that was followed does not include the energy needed to place the adsorbent under vacuum during the desorption cycle since the compression and decompression can occur in parallel. If the energy required to place the system under vacuum is included in the total PE, IISERP-MOF2 not only remains the best material in this respect but the difference in the PE to the next closest material increases from 39 to 86 kJ/kg CO_2 (Fig. 3.A.27).

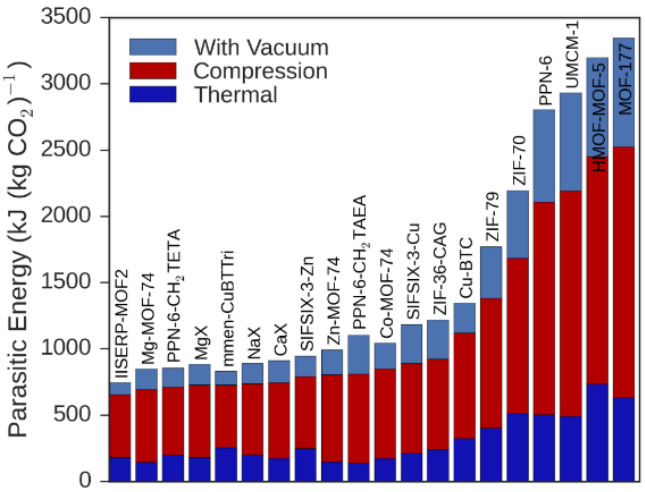

Figure 3.A.27. Optimized PEs of selected materials calculated with data taken from Huck *et al.* compared to that of IISERP-MOF2 wherein the energy required placing the system under vacuum is included in the total PE. The vacuum (light blue), thermal (dark blue) and compression (red) components of the PE are shown.

References for Appendix Section:

A1. (a) Yang *et al. Inorg. Chem. Commun.* **2011**, *14*, 1588. (b) Zhang *et al. Nat. Commun.* **2012**, *3*, 642. (c) Jiang *et al. Cryst. Growth Des*. **2011**, *11*, 3713.

A2. Cortijo *et al. Eur. J. Inorg. Chem*. **2013**, 2580–2590

A3. Yazaydın *et al. J. Am. Chem. Soc.* **2009**, *131*, 18198.

A4. Elsaidi *et al.* Chem. Commun. **2015**, *51*, 15530.

Chapter 4

Triazolyl, Imidazolyl and Benzimidazole Functionalized MOFs for Post-combustion CO_2 Capture.

Chapter 4-I

Azolyl-Carboxylate MOFs for Potential Humid CO_2 Capture.

4-I.1. Introduction:

Carbon dioxide (CO_2) is the most abundant greenhouse gas responsible for global warming.[1-4] Several industrial effluent streams contribute significantly to anthropogenic CO_2 emissions. Of which, a largest single-source contributor is the flue gas emitted from coal power plants. Removal of carbon from such sources require capturing CO_2 present in low-partial pressures and mixed with large amount of N_2 and significant quantities of moisture.[5-10] The humidity content in such streams can vary from 5-15% depending on the composition of the carbonaceous fuel. Pressure/vacuum swing adsorption using solid sorbents such as zeolites has been identified as the most energy efficient method for this large scale CO_2 capture.[9,11-13] CO_2 interacts very well with many sorbents compared to many other gases owing to its large quadrupole moment and easy polarizability. Metal organic frameworks built from metal nodes and π-electron rich aromatic groups linked by carboxylate or pyridyl or azolate or phosphonate or phosphate type (dispersive, electrostatic) linkers generally contain micropores with polarizing walls.[14-24] Some of them posses exceptional CO_2 capacity and their electrostatic/dispersive/quadrupole type interactions have been tuned to provide high CO_2 selectivities. However, the inherent higher polarizability of water makes it interact even stronger with the same sites. For this same reason, the zeolite-13x used for industrial CO_2 capture operates with high efficiency only when the gas feed stream is maintained dry.

In a typical post-combustion CO_2 capture using a solid adsorbent, the effluent or the flue gas at 90-100^oC is cooled down to 30-50^oC and stripped of water vapors. This relatively drier stream (85%N_2:15%CO_2) is then fed to the CO_2 recovery/adsorption unit.[25-27] The extent to which the flue gas stream is dried has a direct impact on the cost and design complexity involved in the capture process itself. Recently, Lin *et al.*[28] have shown that the liquid amine-based CO_2 capture technology gives energy penalty amounting to ~30% of the energy generated by the power plant itself, which is not economic. Instead, if a solid sorbent with a facile CO_2 regeneration is used it can be more cost-effective. Developing solid sorbents with good CO_2 uptake (> 3 mmol/g) at room temperature and 1 bar and high CO_2/N_2 selectivity (> 200) under humid conditions could minimize or take away the step involving stripping of humidity and thereby could bring down the parasitic load on the process. To capture CO_2 under the humid flue gas conditions, the pore wall needs to be functionalized in such a way that it interacts with CO_2 and at the same time it repels water,[29] which is a challenging task. Also, it is being increasingly realized that the stability of MOF towards water and steam are critical requirements to qualify them as suitable capture candidates.[30-35]

We and others have demonstrated the use of having protective functional groups such as -OCH_3 or -CH_2CH_3 strategically positioned next to the metal-binding oxygen rich functional groups as a means to improve hydrolytic stabilities in MOFs.[36,37] Meanwhile, Zaworotko and co-workers[38] showed that a smart combination of fluorinated ligands with basic pyridyl groups can provide optimal adsorption pockets that favour selective CO_2 capture under humid conditions. But, in general, fluorinated linkers due to their depleted e- clouds are not the best ligands, thus leaving few choices. Ultra-microporous MOFs[39-43] are found to be most suited for the low pressure CO_2 capture because of their inherent molecular sieving character, high CO_2/N_2 selectivity, good stability, shelf-life and facile scalability.[39] In some of them very good working capacity and facile CO_2 kinetics and cyclability have also been demonstrated.[38,39,41] Yet their small pore size makes it difficult to functionalize them to have CO_2 selective pore walls without losing the overall capacity. Here, by exploiting the modular tunability of MOF, we have designed a family of ultra-microporous MOFs with pores lined by basic azolyl functional groups capable of interacting with CO_2 and by strategically lacing the -OCH_3 groups from acetate moieties along the pore walls a water-repelling character is imparted to the pores. We report the superior CO_2 capture characteristics: high CO_2/N_2 selectivity, working capacity for a pressure swing of 1.2 to 0.1bar, optimal HOA for facile regeneration of CO_2 and ability for humid CO_2 capture in these six iso-structural MOFs. Furthermore, we identify the most-favourable CO_2 adsorption sites via simulated annealing methods. Simulations indicate the presence of polarized CO_2 molecules located adjacent to the π-electron rich pore walls. Importantly, these polarized molecules form T-shaped configurations among themselves via $C(\delta^+)...O(\delta^-)$ interactions resembling those found in solid CO_2, a cooperative feature that is not observed in the other CO_2 molecules in the structure, which are not proximal to the polarizing walls.

4-I.2. Materials and Methods:

All the chemicals were bought from Sigma Aldrich and used without further purification. 4-(1H-Imidazol-1-yl) benzoic acid and 4-(1H-1, 2, 4-triazol-1-yl) benzoic acid were synthesized according to the reported procedure with slight modification.

4-I.2.1. Synthesis of Linkers:

Synthesis of 4-(1H-Imidazol-1-yl) benzoic acid: Imidazole (4.1 g, 0.06 mol), 4-Fluorobenzonitrile (7.26 g, 0.06 mol) and potassium carbonate (16.6 g, 0.12 mol) were taken in 100 ml of DMF. The reaction mixture was heated at 130°C for 48 hours with constant

stirring under N_2 atmosphere. The mixture was cooled to room temperature and poured into 200 ml of ice-cold water. The white precipitate was then filtered resulting in a yield of 8.48 g of 4-(1H-Imidazol-1-yl) benzonitrile**.** In the second step 5 g of 4-(1H-Imidazol-1-yl) benzonitrile was dissolved in 100 ml of Ethanol followed by addition of 100 ml of 6M KOH solution. The mixture was then refluxed for 12 hrs. After cooling the mixture to room temperature it was acidified with 3N HCl until the p^H of the solution become 6. The White precipitate was filtered, washed with water and finally dried in hot air oven resulting in 5.2 g of Synthesis of 4-(1H-Imidazol-1-yl) benzoic acid.

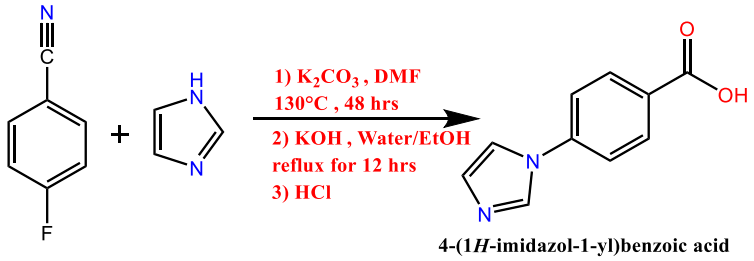

Scheme 4-I.1: Synthesis procedure of 4-(1H-Imidazol-1-yl) benzoic acid.

Synthesis of 4-(1H-1,2,4-triazol-1-yl)benzoic acid: 1, 2, 4-Triazole (4.15 g, 0.06 mol), 4-Fluorobenzonitrile (7.26 g, 0.06 mol) and potassium carbonate (16.6 g, 0.12 mol) were taken in 100 ml of DMF. The reaction mixture was heated at 130°C for 48 hours with constant stirring under N_2 atmosphere. The mixture was cooled to room temperature and poured into 200 ml of ice-cold water. The white precipitate was then filtered resulting in a yield of 8.54 g of 4-(1H-1,2,4-triazol-1-yl)benzonitrile**.** In the second step 5 g of 4-(1H-1,2,4-triazol-1-yl)benzonitrile was dissolved in 100 ml of Ethanol followed by addition of 100 ml of 6M KOH solution. The mixture was then refluxed for 12 hrs. After cooling the mixture to room temperature it was acidified with 3N HCl until the p^H of the solution become 6. The White precipitate was filtered, washed with water and finally dried in hot air oven resulting in 5.32 g of Synthesis of 4-(1H-1,2,4-triazol-1-yl) benzoic acid.

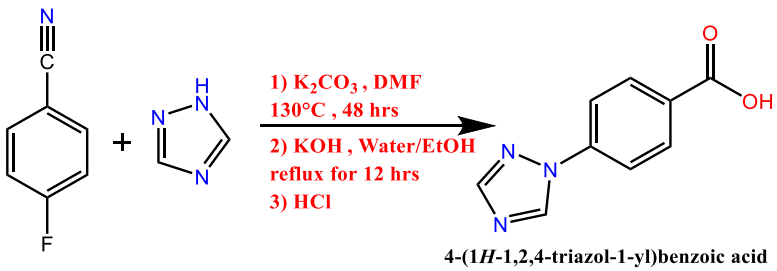

Scheme 4-I.2: Synthesis procedure of 4-(1H-1, 2, 4-triazol-1-yl) benzoic acid.

4-I.2.2. Synthesis of MOFs:

Synthesis of Mg(Tz-Bz) (CH_3COO).solvent;IISERP-MOF4: A solvothermal reaction between Magnesium$^{(II)}$ acetate tetra hydrate (0.107 g; 0.5 mmol), 4-(1H-1,2,4-triazol-1-yl) benzoic acid (0.142 g; 0.75 mmol) in a solution containing 4 ml of Dimethylformamide (DMF) and 3 ml of Acetonitrile (ACN) was carried out at 120°C for 48 hours. Colourless needle shaped crystals were isolated by filtration and was washed with plenty of methanol. The air-dried sample yielded ~71% (based on Mg). The PXRD pattern indicated this to be a pure phase of IISERP-MOF4. CHN analysis (calculated values within parentheses): C, 48.15% (48.51%); H, 4.89% (5.23%); N, 16.39% (16.16%).

Synthesis of Mn(Tz-Bz) (CH_3COO).solvent; IISERP-MOF5 : A solvothermal reaction between Manganese$^{(II)}$ acetate tetra hydrate (0.123 g; 0.5 mmol), 4-(1H-1,2,4-triazol-1-yl) benzoic acid (0.142 g; 0.75 mmol) in a solution containing 4 ml of Dimethylformamide (DMF) and 3 ml of Acetonitrile (ACN) was carried out at 120°C for 48 hours. Colourless needle shaped crystals were isolated by filtration and was washed with plenty of methanol. The air-dried sample yielded ~76% (based on Mn). The PXRD pattern indicated this to be a pure phase of IISERP-MOF5. CHN analysis (calculated values within parentheses): C, 44.95% (44.57%); H, 4.42% (4.81%); N, 14.32% (14.85%).

Synthesis of Co(Tz-Bz) (CH_3COO).solvent; IISERP-MOF6 : A solvothermal reaction between Cobalt$^{(II)}$ acetate tetra hydrate (0.125 g; 0.5 mmol), 4-(1H-1,2,4-triazol-1-yl) benzoic acid (0.142 g; 0.75 mmol) in a solution containing 4 ml of Dimethylformamide (DMF) and 3 ml of Acetonitrile (ACN) was carried out at 130°C for 72 hours. Colourless needle shaped crystals were isolated by filtration and was washed with plenty of methanol. The air-dried sample yielded ~71% (based on Co). The PXRD pattern indicated this to be a pure phase of IISERP-MOF6. CHN analysis (calculated values within parentheses): C, 43.85% (44.10%); H, 4.62% (4.76%); N, 14.12% (14.70%).

Synthesis of Mg(Im-Bz) (CH_3COO).solvent; IISERP-MOF7: A solvothermal reaction between Magnesium$^{(II)}$ acetate tetra hydrate (0.107 g; 0.5 mmol), 4-(1H-Imidazol-1-yl) benzoic acid (0.141 g; 0.75 mmol) in a solution containing 4 ml of Dimethylformamide (DMF) and 3 ml of Acetonitrile (ACN) was carried out at 120°C for 72 hours. Colourless needle shaped crystals were isolated by filtration and was washed with plenty of methanol. The air-dried sample yielded ~73% (based on Mg). The PXRD pattern indicated this to be a

pure phase of IISERP-MOF7. CHN analysis (calculated values within parentheses): C, 51.85% (52.28%); H, 5.12% (5.26%); N, 12.68% (12.19%).

Synthesis of Mn(Im-Bz) (CH_3COO).solvent; IISERP-MOF8: A solvothermal reaction between Manganese$^{(II)}$ acetate tetra hydrate (0.123 g; 0.5 mmol), 4-(1H-Imidazol-1-yl) benzoic acid (0.141 g; 0.75 mmol) in a solution containing 4 ml of Dimethylformamide (DMF) and 3 ml of Acetonitrile (ACN) was carried out at 120°C for 48 hours. Colourless needle shaped crystals were isolated by filtration and was washed with plenty of methanol. The air-dried sample yielded ~70% (based on Mn). The PXRD pattern indicated this to be a pure phase of IISERP-MOF8. CHN analysis (calculated values within parentheses): C, 48.45% (48.01%); H, 5.22% (4.83%); N, 11.62% (11.20%).

Synthesis of Co(Im-Bz) (CH_3COO).solvent; IISERP-MOF9: A solvothermal reaction between Cobalt$^{(II)}$ acetate tetra hydrate (0.125 g; 0.5 mmol), 4-(1H-Imidazol-1-yl) benzoic acid (0.141 g; 0.75 mmol) in a solution containing 4 ml of Dimethylformamide (DMF) and 3 ml of Acetonitrile (ACN) was carried out at 120°C for 48 hours. Colourless needle shaped crystals were isolated by filtration and was washed with plenty of methanol. The air-dried sample yielded ~77% (based on Co). The PXRD pattern indicated this to be a pure phase of IISERP-MOF9. CHN analysis (calculated values within parentheses): C, 47.87% (47.50%); H, 4.12% (4.78%); N, 11.58% (11.08%).

4-I.2.3. Analytical Characterization:

Single Crystal Structure Determination:

Single-crystals data were collected on a Bruker SMART APEX four-circle diffractometer equipped with a CMOS photon 100 detector (Bruker Systems Inc.) and with a Cu Kα radiation (1.5418 Å). The incident X-ray beam was focused and monochromated using Micro focus (IμS). Crystal of all the compounds were mounted on nylon Cryo loops with Paratone-N oil. Data was collected at 153(2) K. Data was integrated using Bruker SAINT Software and was corrected for absorption using SADABS. Structure was solved by Intrinsic Phasing module of the direct methods and refined using the SHELXTL 97 software suite. All non-hydrogen atoms were located from iterative examination of difference F-maps following which the structure was refined using least-squares method. Hydrogen atoms were placed geometrically and placed in a riding model.

Powder X-ray Diffraction:

Powder XRDs were carried out using a Rigaku Miniflex-600 instrument and processed using PDXL software.

Thermo Gravimetric Analysis:

Thermogravimetry was carried out on NETSZCH TGA-DSC system. The routine TGAs were done under N_2 gas flow (20 ml/min) (purge + protective) and samples were heated from 25ºC to 550ºC at 2 K/min.

IR Spectroscopy:

IR spectra were obtained using a Nicolet ID5 attenuated total reflectance IR spectrometer operating at ambient temperature. The KBr pellets were used for IR data collection.

4-I.2.4. Adsorption Analyses:

All gas sorption isotherms were measured on a Micromeritics ASAP 2020HD instrument using ultra-high purity gases (≥ 4.8 grade). Samples were first soaked in DCM and MeOH mixture for 4 days with replenishing the solvent in every 12 hrs. Then the solvent exchanged and dried sample (about 100 mg) was transferred to a glass tube for analysis, with one step activation: evacuation at 120ºC on the degas port for 24 hrs (10^{-6} mbar), at which point the outgas rate was ≤ 2 μbar/min.

Langmuir Fits:

In most cases the isotherms were fit to the Single-Site Langmuir (SSL) equation. Also modified Langmuir equations were utilized to account for significant errors in the Langmuir model. It is widely known that even small fitting errors will have a devastating impact on selectivity calculations.The isotherms were fit by solving the Langmuir equation using the Microsoft Excel following a similar protocol to Keller *et al.*[44] Utilizing this routine circumvents some of the problems associated with favouring either high or low pressure regions when linearizing the Langmuir equation[45] offers a balanced approach.

Single-Site Langmuir (SSL):

$$q_i = q_m \frac{K_i P}{1 + K_i P}$$

Dual-Site Langmuir (DSL):

$$q_i = q_{m,1} \frac{K_1 P}{1 + K_1 P} + q_{m,2} \frac{K_2 P}{1 + K_2 P}$$

Ideal Adsorbed Solution Theory (IAST):

IAST calculations were undertaken as described by Prausnitz *et al.*[46] The selectivity equation is provided below.

Selectivity:

$$S_{1,2} = \frac{q_1/q_2}{P_1/P_2}$$

Self-diffusion Coefficient CO_2 in the Material:

Diffusion coefficient was determined from Rate of Adsorption (ROA) measurements. For this, an extremely high resolution adsorption isotherm was collected using the rate of adsorption routine available with the Micromeritics instrument (ASAP2020HD), in the pressure range of 0-1bar. The diffusion coefficient was calculated as a function of CO_2 loading using 10 different loading points and each of the ROA data was fitted to a spherical pore model[47, 48]. The fittings were done using the solver method of the Microsoft Excel following our earlier procedure.

$$F = 1 - \frac{6}{\pi^2} \sum_{n=1}^{\infty} \frac{1}{n^2} \text{Exp}\left(-n^2 \pi^2 \tau\right)$$

F = fractional uptake; τ = non-dimensional time given by $\tau = D_t/R^2$, where R= particle size; t= time (secs); D = apparent diffusivity.

The spherical pore model gives the best fit compared to slit or slab models.

The single-component diffusion coefficient was estimated to be 1.025 x 10^{-8} m^2s^{-1} taking the average of these 10 points.

Steam Conditioning Experiments:

In this experiment the activated samples were exposed to a flow of humid N_2 (100 ml/min over a 75% RH, saturated NaCl solution maintained at 60^{o}C) for a period of 24 hrs. This steam conditioned materials were loaded on to the adsorption cell and without any further activation, a CO_2 adsorption was carried out on these materials.

4-I.3. Results and Discussion:

All the six MOFs presented here, were synthesized using solvothermal techniques. A reaction between the ligand (4-(1H-Imidazol-1-yl) benzoic acid/4-(1H-1,2,4-triazol-1-yl)

benzoic acid) and metal acetate in a solution containing 4 ml Dimethylformamide (DMF) and 4 ml Acetonitrile (ACN) at 120ºC was carried out for 48 to 72 hrs followed by a slow cooling to room temperature. The crystalline products were isolated by filtration and was washed with dimethyl formamide (DMF) (10 ml), tetrahydrofuran (THF) (10 ml), water (20 ml) and finally with methanol and acetone. A detailed synthesis procedure has been presented in the materials and method section. All MOFs were pure in bulk scale as observed from the Powder X-ray Diffraction (PXRD) (Figs. 4-I.A.3- 4-I.A.8).

4-I.3.1 Single Crystal Structure Analysis:

All six MOFs (IISERP-MOF4 to IISERP-MOF9) with a general formula M(Tz-Bz)(CH_3COO).solvent or M(Im-Bz)(CH_3COO).solvent (where Tz-Bz = 4-(1H-1,2,4-triazol-1-yl) benzoic acid and Im-Bz = (4-(1H-Imidazol-1-yl) benzoic acid and M = Mg or Mn or Co) are iso-structural. Hence, we have discussed the structure of only IISERP-MOF4 (Mg(Tz-Bz)(CH_3COO).solvent) as a representative. The structure of IISERP-MOF4 is built up from Mg acetate chains which are further connected in all three-directions by the ligand. The acetates play a crucial role in the construction of these chains and thereby the 3-D structure. There are two different octahedral metal centres in the metal acetate chain (Fig. 4-I.1A). There are two different acetate units; one is μ^{-3} bridging between three metal centres, while the other is bidentately chelating to only one metal centre. The other coordinations around the metal centres are from the ligand. The ligand is made by coupling imidazolyl or triazolyl unit to a benzoic acid unit. Thus the triazolyl or imidazolyl nitrogens coordinate through the apex of the metal octahedra and run cross-linking the Mg-acetate chains through the carboxylate end of the ligand. The carboxylate ends of the ligand connects two metal centres via a μ^{-2} chelating mode resembling typical paddle-wheel units found in classical metal carboxylate MOFs such as in HKUST. The cross-linking of the metal-acetate chains happen both in a- and b-direction (Fig. 4-I.1B) giving rise to a true 3-D structure with channels running along all the three orthogonal directions (Fig. 4-I.1). The largest channel is circular shaped (dia. 7.74 Å, the dimensions do not factor the Vander Waal radii of atoms, Fig. 4-I.1B) and runs along the c-axis. While the relatively smaller channels run along the a-axis (6.21 Å X 6.80 Å) and b-axis, (6.21 Å X 6.80 Å). These orthogonally running channels are inter-connected giving rise to a three-dimensionally porous framework, whose Connolly representation generated using a probe radius of 1.40Å is shown in figure 4-I.1B. The pore walls of the channel are simultaneously lined by nitrogens from the azolyl groups and the methyl group from the acetate units.

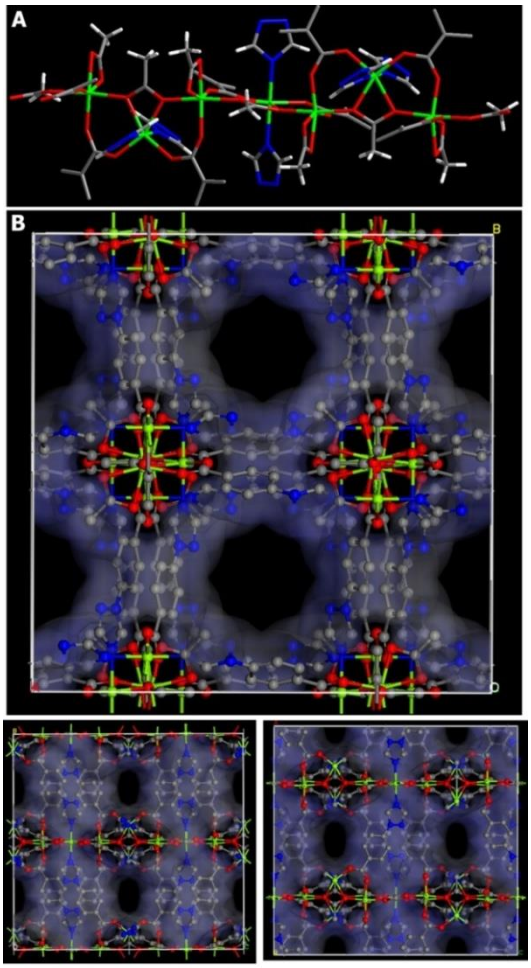

Figure 4-I.1. (A) Mg acetate chain, basic building unit of IISERP-MOF4 (B) Top: Connolly surface representation of IISERP-MOF4 along c axis (probe radius of 1.4 Å); Bottom: Connolly representation along a-axis (left) and b axis (right). Mg : green; O : red; N : blue; C : grey; Surface: greyish blue.

In ideal case, the basic nitrogens should favour CO_2 interactions, while the methyl groups should provide a water-repelling lining. This could make the framework selective to CO_2 over water, making it a contender for humid CO_2 capture.

All the MOFs showed good thermal stability as observed from the TGA (Fig. 4-I.A.9). They all show an initial loss of about 15-20% in the RT to 200°C corresponding to the solvents. While the Mg analogues start to decompose at 280°C, the other phases (Co, Mn) are stable upto 300°C. The solvents could not be located in the single crystal XRD (SXRD) structures, however, when a SQUEEZE routine was carried out using the PLATON suite,[49] the refinement parameters improved significantly (up to 8%), which supports the presence of extra-framework solvents. In fact, it revealed the presence of significant solvent accessible voids (~ 38% for IISERP-MOF4, 5 and 6; ~ 33% for IISERP-MOF7, 8 and 9) and the

electron counts observed matched well with the solvent amounts estimated from the TGA studies.

4-I.3.2. Porosity Analysis:

The permanent porosity of the MOFs has been established by N_2 adsorption isotherms at 77 K. All show characteristic type I isotherm, indicating microporous structure (Fig. 4-I.2). The Brunauer–Emmett–Teller (BET) surface areas of these IISERP-MOFs were determined

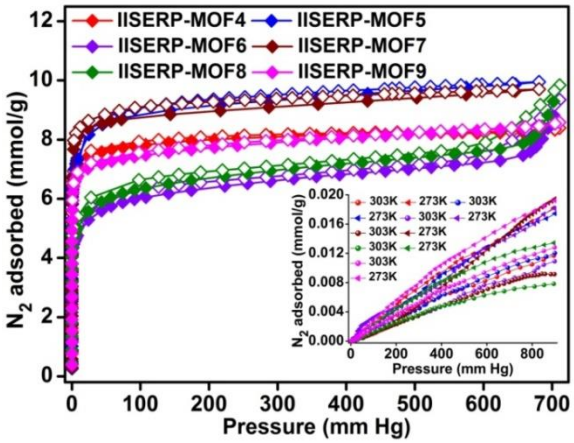

Figure 4-I.2. N_2 adsorption isotherms of IISERP-MOF4, IISERP-MOF5, IISERP-MOF6, IISERP-MOF7, IISERP-MOF8 and IISERP-MOF9 collected at 77 K. Inset shows the N_2 isotherms at 303 K and 273 K for the MOFs.

from the N_2 isotherms to be 560-900 m^2/g, while the Langmuir surface areas were 700-1000 m^2/g (Figs.4-I.A.11-4-I.A.16). From Non Localized Density Functional Theory (NLDFT) model the pore sizes where found to be distributed between 6 to 8 Å (Figs. 4-I.A.17-4-I.A.22). Complete porosity details of IISERP-MOF4 to -MOF9 are presented in Table 4-I.1.

Table 4-I.1. Porosity characteristics of IISERP-MOFs.

Code IISERP-	BET (m^2/g)	Langmuir (m^2/g)	Pore vol. (cc/g)	Pore dia. (Å)	CO_2 @ RT (mmol/g)	$S(CO_2/N_2)$ @ 303 K
MOF4	692	807	0.32	8.0	3.02	410
MOF5	722	920	0.33	7.0	2.97	417
MOF6	703	978	0.34	7.1	2.99	449
MOF7	645	913	0.32	7.3	2.98	355
MOF8	559	807	0.28	6.1	3.00	496
MOF9	548	761	0.33	7.2	2.96	348

The saturation CO_2 uptake (from 195 K CO_2) for these materials varies from 8.5 to 9.6 mmol/g (Fig. 4-I.3), which is quite remarkable. In all cases a type I isotherm was obtained for 195 K CO_2 except for IISERP-MOF4. IISERP-MOF4 shows a two step isotherm, which most probably is due to some gating phenomenon accessible only at 195 K.[50] However,

against our anticipation, all of them showed only a moderate CO_2 uptake of ~3.0 mmol/g at 303K. But advantageously, they did not show any noticeable N_2 uptake at 303 K. Encouraged by this, CO_2 and N_2 sorption isotherms at different temperatures (303 K, 283 K, 273 K, 263 K and 248 K) were collected. The CO_2 capacity for each of these MOFs systematically increases with decrease in temperature.

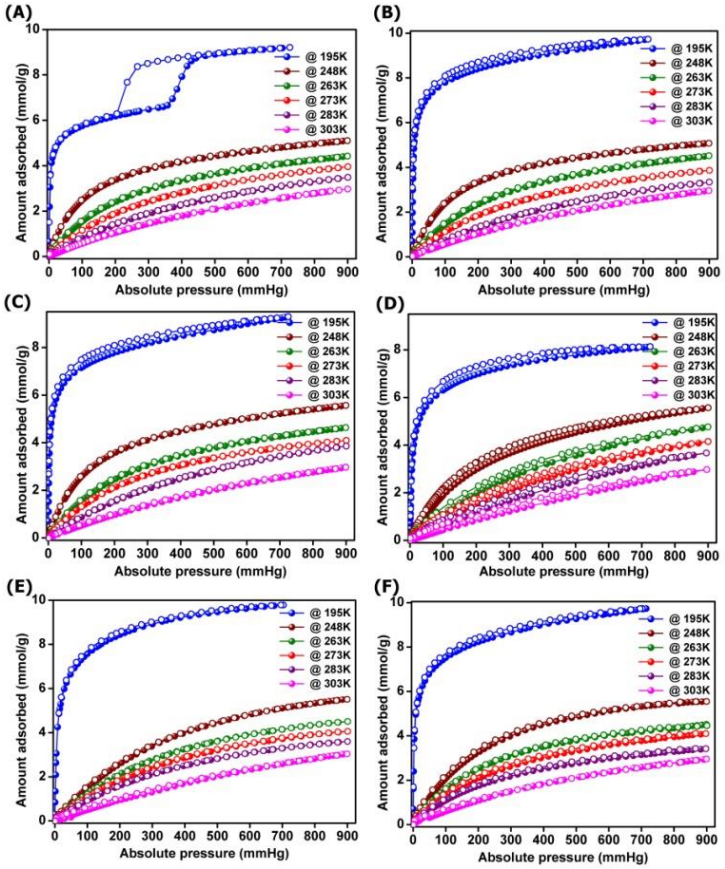

Figure 4-I.3. CO_2 sorption isotherms at different temperature for (A) IISERP-MOF4, (B) IISERP-MOF5, (C) IISERP-MOF6, (D) IISERP-MOF7, (E) IISERP-MOF8 and (F) IISERP-MOF9. Note that in all cases the saturation capacity (@ 195 K) is similar.

The CO_2/N_2 selectivity of all the MOFs was calculated using Ideal Adsorption Solution Theory (IAST) model. A typical flue gas composition, $15CO_2$:$85N_2$ was employed. The selectivity was calculated using 273 and 303 K CO_2 and N_2 isotherms. In the *IAST* calculation we excluded 195 K isotherms as it is close to the phase change temperature of CO_2. For all these MOFs very high CO_2/N_2 selectivities (> 400 @ low partial pressure and > 350 @ 1 bar) were observed (Fig. 4-I.4).

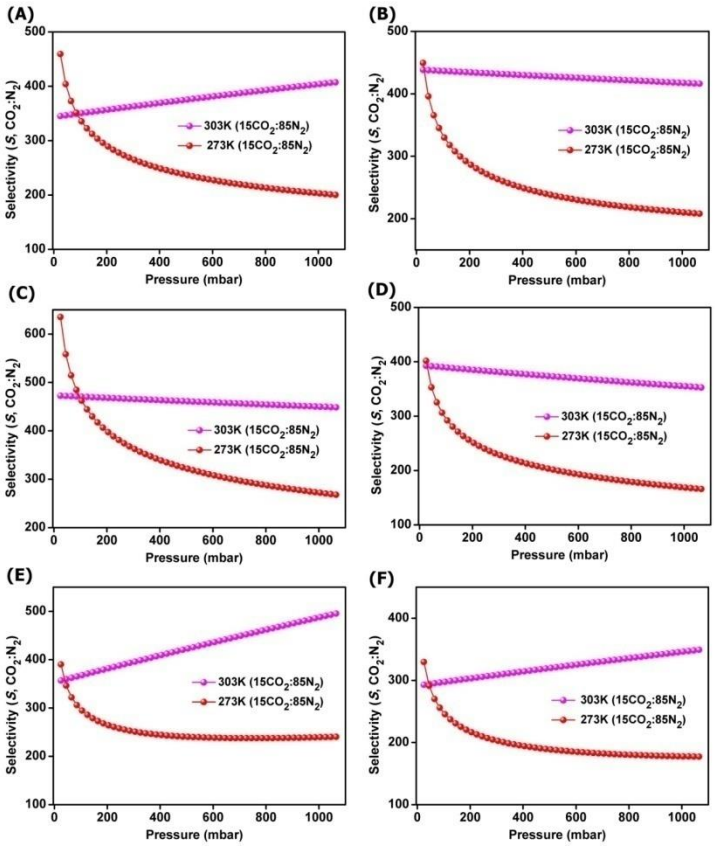

Figure 4-I.4. CO_2/N_2 selectivity for (A) IISERP-MOF4, (B) IISERP-MOF5, (C) IISERP-MOF6, (D) IISERP-MOF7, (E) IISERP-MOF8 and (F) IISERP-MOF9 calculated using *IAST* model. All the selectivity was calculated using typical flue gas composition ($15CO_2:85N_2$).

Even the IISERP-MOF9 which posed the lowest selectivity among all, had a selectivity of 348, which is quite high among MOFs.[38,39] From the IAST calculations using 273 K data it was seen that the selectivity values decreased with increasing pressure. On the contrary, at 303 K CO_2/N_2 selectivity increases with increasing pressure, this is quite rare.[51] This can be explained from the higher rate of increase in CO_2 uptake compared to the N_2 with increasing pressure (Figs. 4-I.A.27-4-I.A.30). Despite the structures being similar, we do see that there is noticeable difference in CO_2/N_2 selectivity. From the CO_2 and N_2 uptakes presented in figure 4-I.2 and 4-I.3, it can be seen that the CO_2 uptake between the samples vary from 3.04 mmol/g to 2.96 mmol/g which is about 2.6%, while the N_2 varies from 0.012 mmol/g to 0.008 mmol/g, which is about 35%. This clearly indicates that the N_2 uptake contributes significantly to the observed differences in selectivities between the phases. However it is harder to attribute this to any specific structural feature of the framework. The CO_2/N_2 selectivity observed in these MOFs are quite remarkable and higher than most of the highest-performing MOFs such as Mg(DOBDC): 49; Cu-TDPAT: 79; BioMOF-12: 52; ZIF-78: 50; en-Cu-BTTri: 44, all at 298 K.[39] It is worth mentioning that the recently reported

ultra-microporous MOFs do present selectivities > 500.[38] The working capacity defined as the amount of CO_2 recovered per gram of material for a specified pressure swing or temperature swing cycle. For these MOFs, the working capacity calculated from the pure component isotherms is found to be ~ 2.6 mmol/g for a typical 1 bar to 0.1 bar pressure swing, which is more than significant.[33, 38, 39] From figure 4-I.A.31 it can be seen that the amount of CO_2 recovered is about 90% of the total capacity. This is noteworthy and can be explained by the near-linear profile of the room temperature isotherms, which gives the largest slope, therefore large Henry's constant.

Facile removal of the adsorbed CO_2 contributes directly to the energy-efficiency of the capture process.[39] A zero-loading heat of adsorption for CO_2 in the range of [25-35] kJ/mol is indicative of a facile CO_2 regeneration.[9] In this case all the six MOF's had HOA values in the range of 22-30 kJ/mol (Fig. 4-I.5A) as observed from the virial modelling of the CO_2

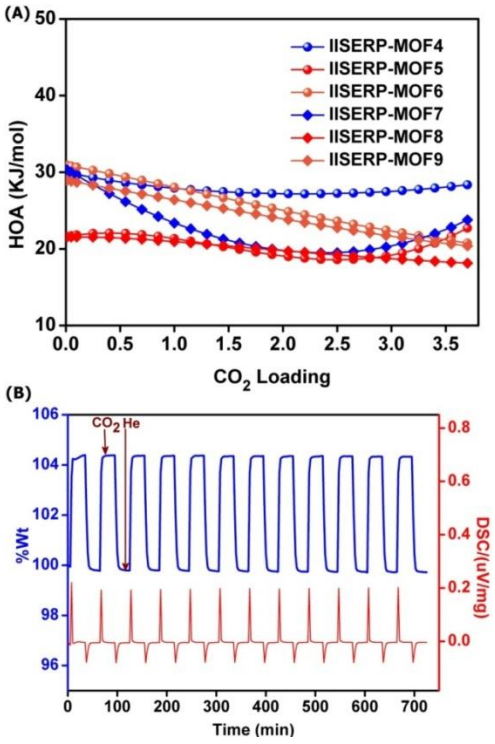

Figure 4-I.5. (A) CO_2 heat of adsorption for all the MOFs calculated using virial model. In all cases, HOA was calculated using 303 K, 283 K, 273 K and 263 K CO_2 isotherms. (B) Isothermal TGA cycling experiment showing the facile regeneration of CO_2 by a helium flow at 303 K. Note , we have carried the cycling experiment using IISERP-MOF4, having zero loading HOA of 30 kJ/mol. All the other MOFs presented in this manuscript have HOA values less than 30 kJ/mol.

isotherms at 303, 283, 273 and 263 K. The highest HOA was obtained for IISERP-MOF4 (29 kJ/mol) and lowest for IISERP-MOF9 (23 kJ/mol). To demonstrate the facile regeneration of CO_2, we carried out TGA cycling experiment on IISERP-MOF4 (Fig. 4-I.5B). In this

experiment, the activated IISERP-MOF4 was subjected to an isothermal cycling experiment with CO_2 and He flow in each alternate cycle. Almost 100% recovery of adsorbed CO_2 was obtained on the TGA by a He sweep at 303 K and fifteen such adsorption/desorption cycles have been carried out without any loss in capacity. We monitored the heat evolved during this adsorption-desorption processes by following the DSC trace during these cycles. The characteristics exothermic peaks were observed during adsorption of CO_2 and their intensities remained almost constant across the cycles suggesting a very homogenous process.

4-I.3.3. Solvent Sorption and Steam Conditioning Study:

As mentioned earlier, from the saturation uptakes (195 K) and the fact that the pores were designed to have azolyl based basic sites, we anticipated significantly larger CO_2 uptakes under ambient conditions, but it was not the case. Searching for an explanation, when we examined the structures where it could be seen that the pendant methyl groups from the acetate units were protruding right into the nano space present in the channels (Fig. 4-I.A.2). Typically at temperatures close to ambient, these groups would certainly have larger kinetic energy and can be expected to have higher degree of rotational freedom. However, such movements get arrested to a large extent at 195 K giving rise to much higher saturation uptake. Though this was disadvantageous, on hind sight, we realized that these methyl groups could provide a hydrophobic character to the pores and there by repel the water molecules giving a protective cover for the highly polar metal sites in the framework. Such features has been already demonstrated in a phosphonate ester based MOF.[36]

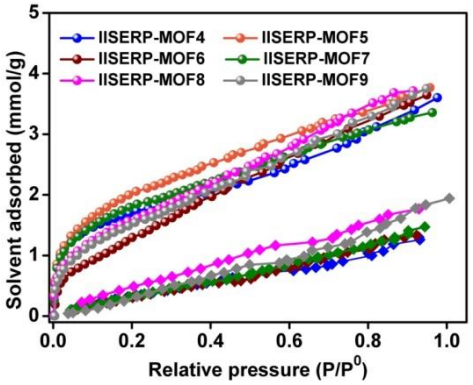

Figure 4-I.6. Benzene (spheres) and water (squares) vapour sorption isotherms of IISERP-MOFs at 298 K. In all cases benzene shows a type-I behaviour while water shows a near-linear water isotherms.

To evaluate this feature, we carried out solvent sorption using H_2O and benzene as hydrophilic and hydrophobic probes, respectively. It could be seen from figure 4-I.6 that in

all cases water sorption isotherms had a type III behaviour indicating very weak adsorbate-adsorbent interactions. On the other hand, benzene sorption isotherms had a type I behaviour suggestive of strong interaction between benzene and the framework. This could be due to the hydrophobic lining provided by the carbon rich backbone of the linkers and the hydrophobic methyl groups from the acetates.

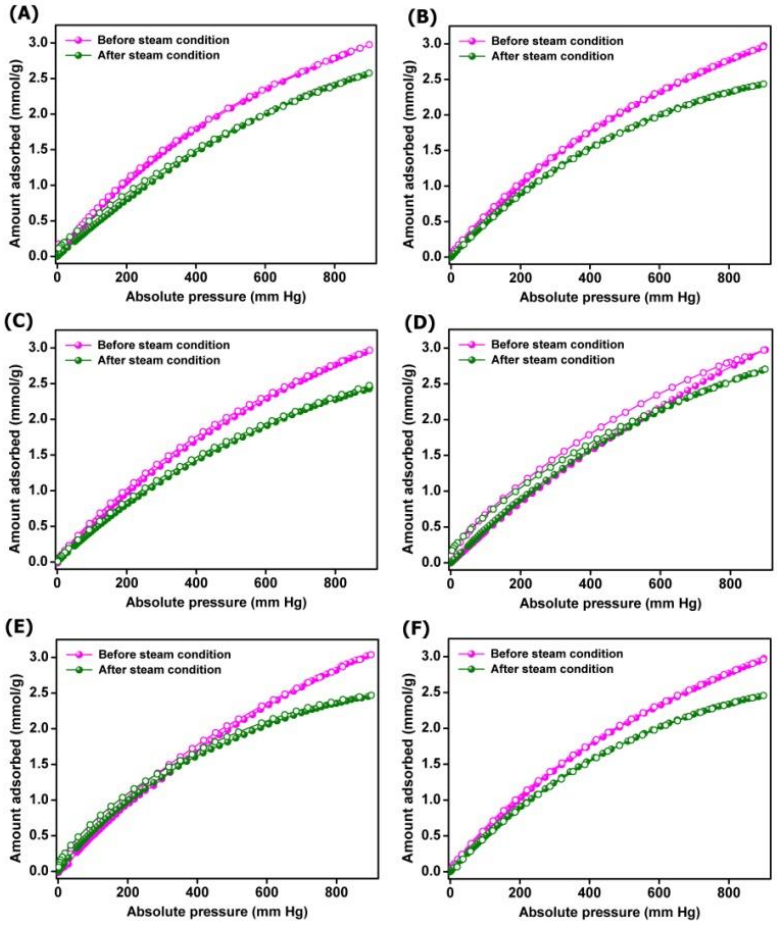

Figure 4-I.7. Comparison of the effect of humidity on the CO_2 adsorption behaviour of (A) IISERP-MOF4, (B) IISERP-MOF5, (C) IISERP-MOF6, (D) IISERP-MOF7, (E) IISERP-MOF8 and (F) IISERP-MOF9. All isotherms were carried out at 303 K. Note that the decrease in uptake upon steam-conditioning is ≤ 25%. Important: After the steam conditioning the material was not subjected to any further activation or pre-treatment.

Thus, all the MOFs presented here have stronger interaction with benzene than water. In our earlier work involving a porous hydrophobic polar framework, we had noticed the ability of such materials to retain most of its CO_2 capture capabilities despite being exposed to high humidity.[52] Here, the IISERP-MOFs under discussion, in fact, have a comparable framework with fine hydrophilic-hydrophobic balance. So, anticipating a similar behaviour, we tested the ability of these MOFs to retaining its CO_2 adsorption capacities under steam

conditioning treatments. The title materials were activated (120°C, 10^{-3} bar, 12 hrs) and then were exposed to a flow of humid N_2 (80 ml/min over a 75% RH generated from a saturated NaCl solution maintained at 60ºC) over a period of 12 hrs. These wet materials were tested for CO_2 adsorption without any further activation or pre-treatment. As can be seen from figure 4-I.7, these MOFs lose less than 25% of their original capacity. Where as in our previous study,[52] we have shown some of the highly polar framework materials such as HKUST and Y-Zeolite losing more than 80% of their original capacity while some of the hydrophobic standards such as CMS, Silica-Alumina lose less than 30% of their original capacity. Thus, in comparison, the MOFs reported here seems to be behaving more like the hydrophobic sieves. Importantly, this suggests that the ultra-microporous MOFs with water-repelling pore walls have highest promise as humid CO_2 capture sorbents.

4-I.3.4. Stability Study:

For being an apt candidate for industrial CO_2 capture the porous material needs to meet several stability requirements.[29, 53, 54] To investigate the stability of IISERP-MOFs, we subjected all six MOFs to steam treatment studies. Wherein the samples were exposed to 80% RH for 24 hrs and their post-treatment crystallinity was screened using PXRD measurements. No major loss of crystallinity was observed. To further substantiate their hydrolytic stability, the 195 K CO_2 isotherms were done using the steam treated samples and no considerable drop in capacity was observed (Figs. 4-I.A.34-4-I.A.37), which is quite remarkable.

4-I.3.5. CO_2 Diffusion Kinetics Study:

The solid sorbent, when used is PSA process, should have smooth and fast CO_2 diffusion kinetics for faster cycling times. As the MOFs presented here are made of very small pores, they might pose significant resistance to diffusion of CO_2 within them. To gain insights on the CO_2 diffusion, we carried out kinetics analysis on IISERP-MOF4. A high resolution Rate of Adsorption (ROA) data was procured on the sample using ASAP 2020HD instrument at 273 K in low pressure region. The equilibration kinetics associated with 10 different pressure points were extracted and the data was fitted to a spherical pore model[47] (See material methods section for more details). From this, an average diffusion coefficient of 10.20×10^{-9} m^2/s for CO_2 was obtained (Fig. 4-I.8). This diffusivity is comparable to those observed in some of the microporous MOFs: IISERP-MOF1, 3.38 x 10^{-9}; ZIF-8, 8 x 10^{-10}; MIL-53(Cr), ~5 x 10^{-8} ; MOF-5, 1.17 x 10^{-9} ; and MOF-177, 2.3 x 10^{-9} m^2/s at 298 K.[55-58] The diffusion

coefficient of IISERP-MOF4 is also two orders of magnitude higher than that of zeolite 13X, which is currently used in PSA scrubbers for natural gas purification.[59]

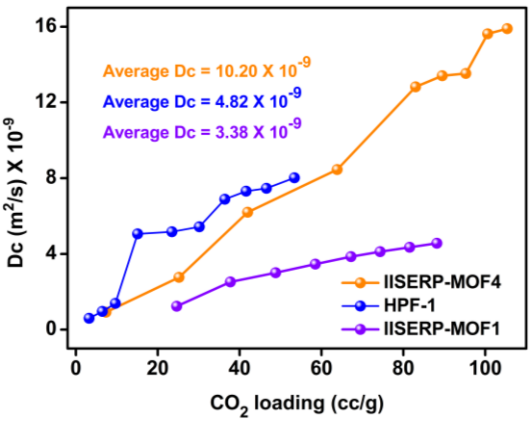

Figure 4-I.8. The Self-diffusion coefficient for CO_2 in IISERP-MOF4, HPF-1 and IISERP-MOF1 calculated using a spherical pore model. Diffusion coefficient data for HPF-1 and IISERP-MOF1 has been taken from literature[39, 52]

4-I.3.6. Theoretical Inputs:

Earlier, we had shown that for high CO_2 selectivities the presence of site-specific framework...CO_2 interactions and the importance of co-operative CO_2...CO_2 interactions under the nano confinement provided by the ultra-micropores are crucial.[24,39,40] To gain similar insights on these family of ultra-microporous MOFs under discussion, we modeled the most-favorable CO_2 adsorption sites via GCMC and simulated annealing. For this we calculated the CO_2 uptakes using GCMC simulations (Materials Studio V6). From which the number of CO_2 molecules per FU was evaluated to be ~29, which was in agreement with those calculated from experimental uptakes. Now placing this number of CO_2 molecules within the unit cell, a simulated annealing routine was carried out, which yielded a model displaying the most probable CO_2 adsorption sites (Fig. 4-I.A.38). Two strategies were adopted, one wherein the framework was frozen and the CO_2 molecules were allowed to settle into the lowest possible configurations. This yielded a final configuration with a relative energy of -153 kcal/mol and an average HOA of ~28 kJ/mol. As an alternate strategy, the framework atoms were allowed to geometry optimize, however, this did not yield a configuration far from the one obtained from the former strategy, both in terms of framework atom's and CO_2's positions. The final configuration in the latter case had a relative energy of -155 kcal/mol and an average HOA of ~27 kJ/mol. For the present discussions, this lowest energy configuration is being used. The different CO_2 locations within the framework has been presented in the figure 4-I.9. The CO_2 molecules proximal to the pore walls are denoted

in yellow, while the rest in cyan. Now, a lateral view of this pore shows the undulating nature of the pore giving rise to three important regions (Fig. 4-I.9B); (i) the channel with walls lined by azolyl and the phenyl group of the ligand, (ii) middle of the pore formed at the junction of the three cross-connected channels along a-, b- and c-axis, and (iii) the constricted area which does not support CO_2 residence.

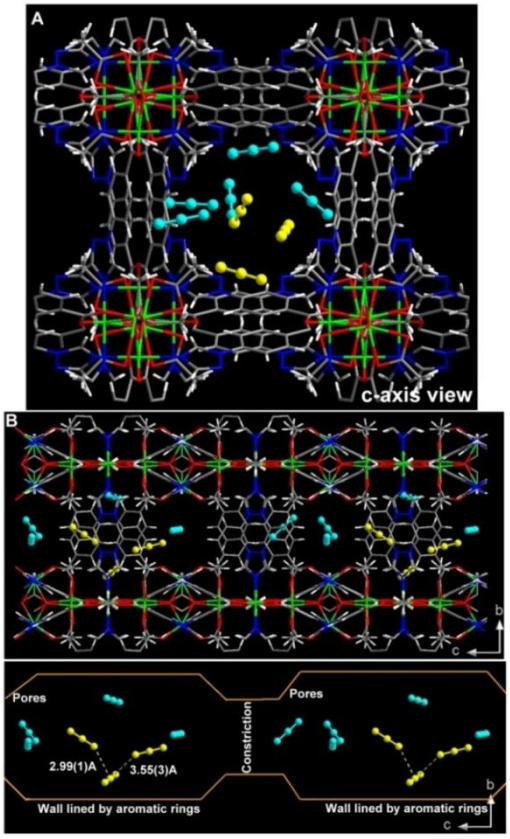

Figure 4-I.9. (A) Structure of IISERP-MOF4 showing the CO_2 locations within their pores obtained using Simulated Annealing. The CO_2 molecules shown in yellow are closer to the pore walls relative to the ones shown in cyan. (B) Top: A side-view showing the distribution of CO_2 within the channels. Bottom: A simplified schematic representation of the shape of the channel, running along the c-axis, showing the polarized CO_2 molecules (yellow) with T-shaped arrangements favouring strong $C(\delta^{+ve})...O(\delta^{-ve})$ interactions.

Most importantly, it can be seen that the CO_2 molecules adjacent to the π-carbon and azolyl rich pore walls are polarized. This is evident from their ability to form T-shaped $CO_2...CO_2$ configurations assisted by strong $C(\delta^{+ve})...O(\delta^{-ve})$ interactions (distance: 2.99 and 3.55 Å, Fig. 4-I.9B). Such short distances are typically associated with the T-shaped dimers present in solid phases of CO_2.[60] Interestingly, the other CO_2 molecules (shown in cyan) which are not proximal to the polarizing walls did not show any such cooperativity as their inter-molecular distances are much longer.

4-I.4. Conclusions:

Mg, Mn and Co based six isostructural metal organic frameworks have been developed using 4-(1H-1,2,4-triazol-1-yl) benzoic acid and 4-(1H-Imidazol-1-yl) benzoic acid as linkers. These MOFs show high selectivity towards CO_2 over N_2, which coupled with their near-linear CO_2 isotherms in the low pressure range helps realizing significantly large working capacities (~2.6 mmol/g) for a 1.2-0.1 bar pressure swing. They pose optimal HOA for CO_2 (25-30 kJ/mol), which gets reflected in the facile recovery of the CO_2 during the TGA cycling experiments. This is further substantiated by the high CO_2 self-diffusion coefficients registered by these MOFs. The IISERP-MOFs show good hydrolytic stability and recyclability as a sorbent. Importantly, they retain majority of their CO_2 adsorption capacity even upon exposure to high humidity as evidenced from the steam conditioning experiments. Simulations reveal the CO_2 molecules adjacent to the π-carbon and azolyl rich pore walls to be polarized. Such polarized CO_2 molecules form T-shaped CO_2...CO_2 configurations assisted by strong $C(\delta^{+ve})...O(\delta^{-ve})$ interactions. The ability of ultra-microporous MOF to provide a confined environment supporting such interactions is important to realizing high CO_2 selectivity in solid sorbents. These insights can be crucial to the future design of MOFs for humid CO_2 capture.

4-I.5. References:

1. Keith, D. W. *Science* **2009**, *325*, 1654-1655.
2. Rochelle, G. T. *Science*, 2009, 325, 1652-1654.
3. Quadrelli, R.; Peterson, S. *Energ. Policy* **2007**, *35*, 5938-5952.
4. Haszeldine, R. S. *Science* **2009**, *325*, 1647-1652.
5. Huck, J. M.; Lin, L. -C.; Berger, A. H.; Shahrak, M. N.; Martin, R. L.; Bhown, A. S.; Haranczyk, M.; Reuterb, K.; Smit, B. *Energy Environ. Sci.* **2014**, *7*, 4132.
6. Wang, Q.; Bai, J.; Lu, Z.; Pan, Y.; You, X. *Chem. Commun*. **2016**, *52*, 443.
7. Liu, Y.; Wang, Z. U.; Zhou, H.-C. *Greenhouse gases science and technology* **2012**, *2*, 239-259.
8. Sumida, K.; Rogow, D. L.; Mason, J. A.; McDonald, T. M.; Bloch, E. D.; Herm, Z. R.; Bae, T.-H.; Long, J. R. *Chem. Rev*. **2012**, *112*, 724-781.
9. Simmons, J. M.; Wu, H.; Zhou, W.; Yildirim, T.; *Energy Environ. Sci.* **2011**, *4*, 2177–2185.
10. Mason, J. A.; Sumida, K.; Herm, Z. R.; Krishna, R.; Long, J. R. *Energy Environ. Sci*. **2011**, *4*, 3030-3040.

11. Liu, J.; Tallapally, P. K.; McGrail, B. P.; Brown, D. R.; Liu, J.; *Chem. Soc. Rev*. **2012**, *41*, 2308-2322.
12. Ruthven, D. M.; Farooq, S; Knaebel, K. S. *Pressure Swing Adsorption* (VCH Publishers,**1994**).
13. Zhang, Z.; Yao, Z. -Z.; Xiang, S.; Chen, B. *Energy Environ. Sci*. **2014**, *7*, 2868. 2899.
14. Zhou, H. C.; Long, J. R.; Yaghi, O. M. *Chem. Rev*. **2012**, *112*, 673-674.
15. Zhou, H.-C. J.; Kitagawa, S. *Chem. Soc. Rev*. **2014**, *43*, 5415- 418.
16. Kumar, A.; Madden, D. G.; Lusi, M.; Chen, K.-J.; Daniels, E. A.; Curtin, T.; Perry IV, J. J.; Zaworotko, M. J. *Angew. Chem. Int. Ed*. **2015**, *54*, 14372-14377.
17. Noro, S.-I.; Mizutani, J.; Hijikata, Y.; Matsuda, R.; Sato, H.; Kitagawa, S.; Sugimoto, K.; Inubushi, Y.; Kubo, K; Nakamura, T. *Nat. Commun*. **2015**, *6*, 6851.
18. Mohamed, M. H; Elsaidi, S. K.; Pham, T.; Forrest, K. A.; Tudor, B.; Wojtas, L.; Space, B.; Zaworotko, M. J. *Chem. Commun*. **2013**, *49*, 9809-9811.
19. Li, J.-R.; Yu, J.; Lu, W.; Sun, L.-B.; Sculley, J.; Balbuena, P. B.; Zhou, H.-C. *Nat. Commun*. **2013**, *4*, 1538.
20. Yang, S.; Lin, X.; Lewis, W.; Suyetin, M.; Bichoutskaia, E.; Parker, J. E.; Tang, C. C.; Allan, D. R.; Rizkallah, P. J.; Hubberstey, P; Champness, N. R.; Thomas, K. M.; Blake, A. J.; Schröder, M. *Nat. Mater*. **2012**, *11*, 710-716.
21. Zhou, D.-D.; He, C.-T.; Liao, P.-Q.; Xue, W.; Zhang, W.-X.; Zhou, H.-L.; Zhang, J.-P.; Chen, X.-M. *Chem. Commun*. **2013**, *49*, 11728.
22. Banerjee, A.; Nandi, S.; Nasa, P.; Vaidhyanathan, R. *Chem. Commun*. **2016**, *52*, 1851-1854.
23. Mah, R. K.; Gelfand, B. S.; Taylor, J. M.; Shimizu, G. K. H. *Inorg. Chem. Front*. **2015**, *2*, 273-277.
24. Vaidhyanathan, R.; Iremonger, S. S.; Shimizu, G. K. H.; Boyd, P. G.; Alavi, S.; Woo, T. K. *Angew. Chem. Int. Ed*. **2012**, *51*, 1826.
25. Boot-Handford, M. E.; Abanades, J. C.; Anthony, E. J.; Blunt, M. J.; Brandani, S.; Dowell, N. M.; Fernández, J. R.; Ferrari, M.-C.; Gross, R.; Hallett, J. P.; Haszeldine, R. S.; Heptonstall, P; Lyngfelt, A.; Makuch, Z.; Mangano, E.; Porter, R. T. J.; Pourkashanian, M.; Rochelle, G. T.; Shah, N.; Yaoa, J. G.; Fennell, P. S. *Energy Environ. Sci*. **2014**, *7*, 130.
26. Wang, Q.; Luo, J.; Zhong, Z.; Borgna, A. *Energy Environ. Sci*. **2011**, *4*, 42.

27. Markewitz, P.; Kuckshinrichs, W; Leitner, W.; Linssen, J.; Zapp, P.; Bongartz, R.; Schreibera, A.; Muller, T. E. *Energy Environ. Sci*. **2012**, *5*, 7281.
28. Lin, L. -C.; Berger, A. H.; Martin, R. L.; Kim, J.; Swisher, J. A.; Jariwala, K.; Rycroft, C. H.; Bhown, A. S.; Deem, M. W.; Haranczyk, M.; Smit, B. *Nat. Mater*. **2012**, *11*, 633.
29. Fracaroli, A. M.; Furukawa, H.; Suzuki, M.; Dodd, M.; Okajima, S.; Gándara, F.; Reimer, J. A.; Yaghi, O. M. *J. Am. Chem. Soc*. **2014**, *136*, 8863-8866.
30. Burtch, N. C.; Jasuja, H.; Walton, K. S. *Chem. Rev*. **2014**, *114*, 10575-10612.
31. Canivet, J.; Fateeva, A.; Guo, Y.; Coasnecd, B.; Farrusseng, D. *Chem. Soc. Rev*. **2014**, *43*, 5594-5617.
32. Yu, J.; Balbuena, P. B. *J. Phys. Chem. C* **2013**, *117*, 3383-3388.
33. Datta, S. J.; Khumnoon, C.; Lee, Z. H.; Moon, W. K.; Docao, S.; Nguyen, T. H.; Hwang, I. C.; Moon, D.; Oleynikov, P.; Terasaki, O.; Yoon, K. B. *Science* **2015**, *350*, 302.
34. Yang, Q.; Vaesen, S.; Ragon, F.; Wiersum, A. D.; Wu, D.; Lago, A.; Devic, T.; Martineau, C; Taulelle, F.; Llewellyn, P. L.; Jobic, H.; Zhong, C.; Serre, C.; Weireld, G. D.; Maurin, G. *Angew. Chem. Int. Ed*. **2013**, *52*, 10316-10320.
35. Zuluaga, S.; Fuentes-Fernandez, E. M. A.; Tan, K.; Xu, F.; Li, J.; Chabal, Y. J.; Thonhauser, T. *J. Mater. Chem. A* **2016**, *4*, 5176-5183.
36. Taylor, J. M.; Vaidhyanathan, R.; Iremonger, S. S.; Shimizu, G. K. H. *J. Am. Chem. Soc*. **2012**, *134*, 14338-14340.
37. He, C.-T.; Jiang, L.; Ye, Z.-M.; Krishna, R.; Zhong, Z.-S.; Liao, P.-Q.; Xu, J.; Ouyang, G.; Zhang, J.-P.; Chen, X.-M. *J. Am. Chem. Soc*. **2015**, *137*, 7217-7223.
38. Nugent, P.; Belmabkhout, Y.; Burd, S. D.; Cairns, A. J.; Luebke, R.; Forrest, K.; Pham, T.; Ma, S.; Space, B.; Wojtas, L.; Eddaoudi, M.; Zaworotko, M. J. *Nature* **2013**, *495*, 80-84.
39. Nandi, S.; De Luna, P.; Daff, T. D.; Rother, J.; Liu, M.; Buchanan, W.; Hawari, A. I.; Woo, T. K.; Vaidhyanathan, R.; *Sci. Adv*. **2015**, *1*, e1500421.
40. Vaidhyanathan, R.; Iremonger, S. S.; Shimizu, G. K. H.; Boyd, P. G.; Alavi, S.; Woo, T. K. *Science* **2010**, *330*, 650-653.
41. Xiang, S.; He, Y.; Zhang, Z.; Wu, H.; Zhou, W.; Krishna, R.; Chen, B. *Nat. Commun*. **2012**, *3*, 954.

42. Shekhah, O.; Belmabkhout, Y.; Chen, Z.; Guillerm, V.; Cairns, A.; Adil, K.; Eddaoudi, M. *Nat. Commun*. **2014**, *5*, 5228.
43. Bhatt, P. M.; Belmabkhout, Y.; Cadiau, A.; Adil, K.; Shekhah, O.; Shkurenko, A.; Barbour, L. J.; Eddaoudi, M. *J. Am. Chem. Soc*. **2016**, *138*, 9301–9307.
44. Kemmer, G.; Keller, S. *Nat. Protoc*. **2010**, *5*, 267–81.
45. Richter, E.; Schuetz, W.; Myers, A. L. *Chem. Eng. Sci*. **1989**, *44*, 1609–1616.
46. Myers, A. L.; Prausnitz, J. M. *AIChE J*. **1965**, *11*, 121–127.
47. Malek, K; Coppensa, M.-O. *J. Chem. Phys*. **2003**, *119*, 2801.
48. Do, D. D. Adsorption analysis and equilibria and kinetics, *Imperial College Press*, Ed. **2008**.
49. Spek, A. L. *Acta Cryst*. **2009**, *D65*, 148-155.
50. Yang, W.; Davies, A. J.; Lin, X.; Suyetin, M.; Matsuda, R.; Blake, A. J.; Wilson, C; Lewis, W.; Parker, J. E.; Tang, C. C; George, M. W.; Hubberstey, P.; Kitagawa, S.; Sakamoto, H.; Bichoutskaia, E.; Champness, N. R.; Yang, S.; Schroder, M. *Chem. Sci*. **2012**, *3*, 2993.
51. Patel, H. A.; Je, S. H.; Park, J.; Chen, D. P.; Jung, Y.; Yavuz, C. T.; Coskun, A. *Nat. Commun*. **2013**, *4*, 1357.
52. Nandi, S.; Werner-Zwanziger, U; Vaidhyanathan, R. *J. Mater. Chem. A* **2015**, *3*, 21116-21122
53. Kizzie, A. C.; Wong Foy, A. G.; Matzger, A. J. *Langmuir* **2011**, *27*, 6368-6373.
54. Gelfand, B. S.; Shimizu, G. K. H. *Dalton Trans.* **2016**,*45*, 3668-3678
55. Zhang, L.; Wu, G.; Jiang, J. *J. Phys. Chem. C* **2014**, *118*, 8788-8794.
56. Salles, F.; Jobic, H.; Ghoufi, A.; Llewellyn, P. L.; Serre, C.; Bourrelly, S.; Férey, G.; Maurin, G. *Angew. Chem. Int. Ed*. **2009**, *48*, 8335–8339.
57. Zhao, Z.; Li, Z.; Lin, Y. S. *Ind. Eng. Chem. Res*. **2009**, *48*, 10015-10020.
58. Saha, D.; Bao, Z.; Jia, F.; Deng, S. *Environ. Sci. Technol*. **2010**, *44*, 1820-1826.
59. Silva, J. A. C.; Schumann, K.; Rodrigues, A. E. *Microporous Mesoporous Mater.* **2012**, *158*, 219-228.
60. Iota, V.; Yoo, C.-S. *Phys. Rev. Lett*. **2001**, *86*, 5922.

4-I.A. Appendix for Chapter 4-I:

Crystal Structure Analysis:

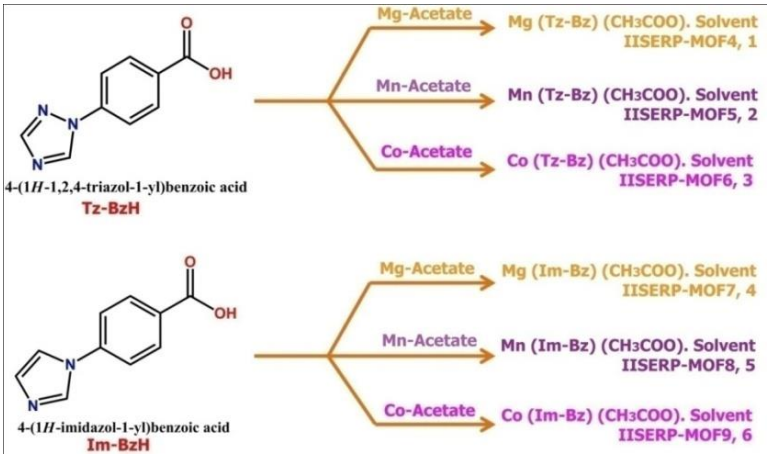

Figure 4-I.A.1. Schematic representation of the six MOFs that have been developed using metals (Mg, Mn and Co) of different Lewis acidity.

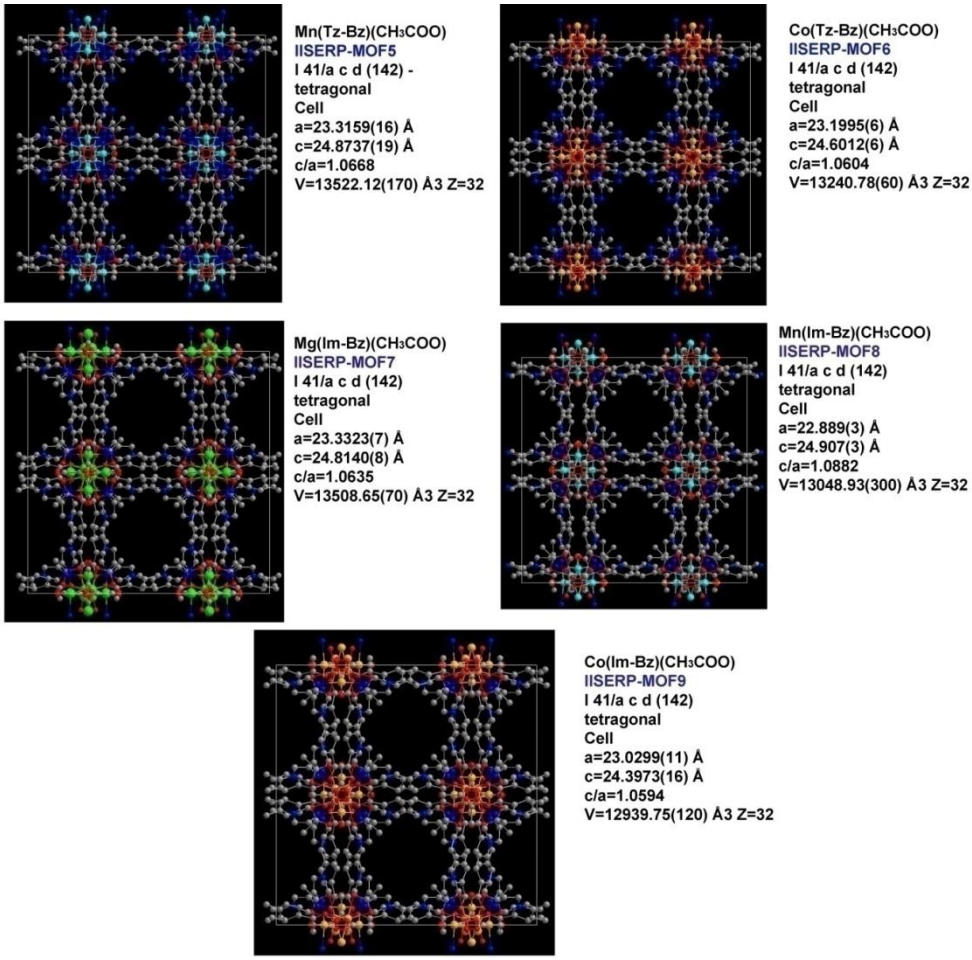

Figure 4-I.A.2. C-axis view of the IISERP-MOFs showing their isostructural frameworks. There are only subtle differences in their lattice parameters.

Analytical Characterization:

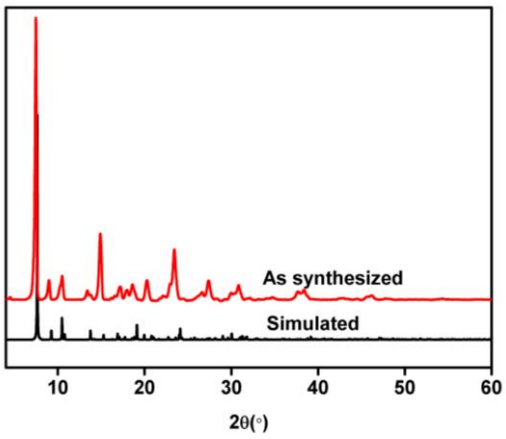

Figure 4-I.A.3. A comparative PXRD plot showing the bulk purity of IISERP-MOF4.

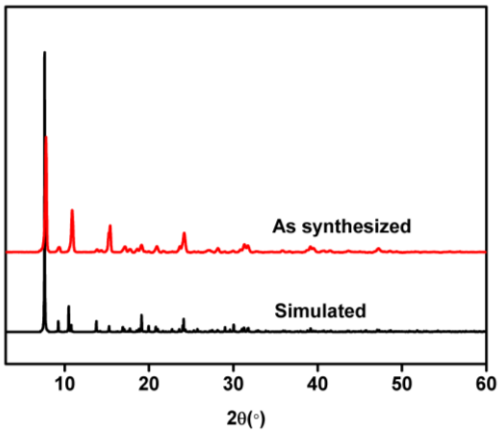

Figure 4-I.A.4. A comparative PXRD plot showing the bulk purity of IISERP-MOF5.

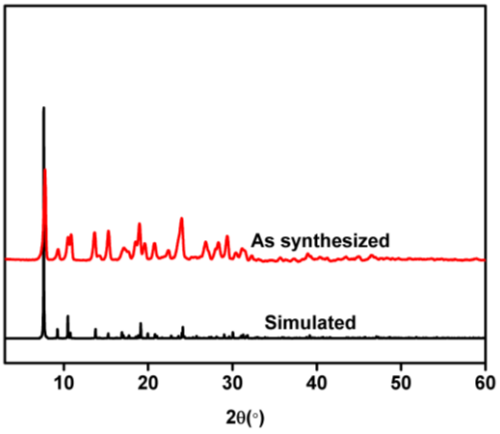

Figure 4-I.A.5. A comparative PXRD plot showing the bulk purity of IISERP-MOF6.

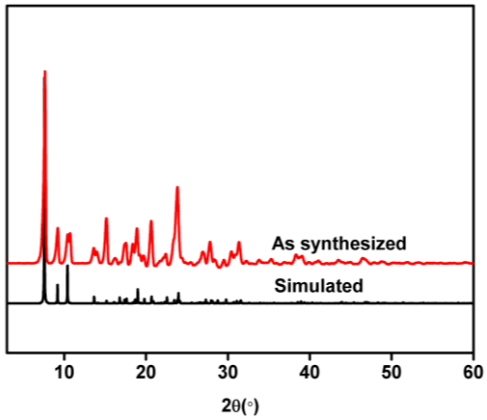

Figure 4-I.A.6. A comparative PXRD plot showing the bulk purity of IISERP-MOF7.

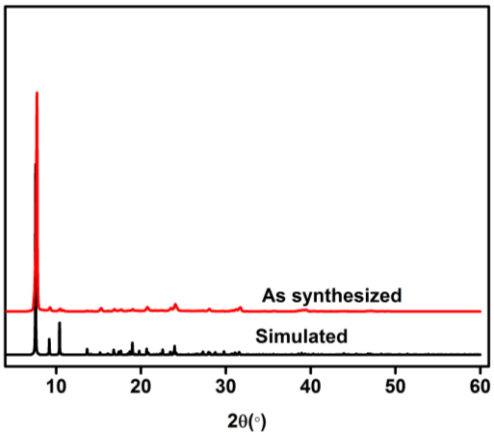

Figure 4-I.A.7. A comparative PXRD plot showing the bulk purity of IISERP-MOF8.

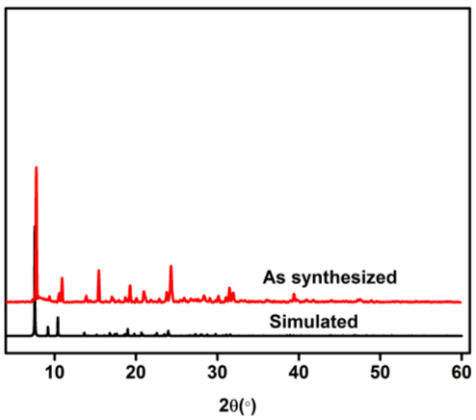

Figure 4-I.A.8. A comparative PXRD plot showing the bulk purity of IISERP-MOF9.

Note: In all cases, there are some differences between the simulated and the experimental PXRDs, particularly in their relative intensities. These differences are arising due to preferred orientation, which is expected considering that these MOFs grow as thin-needle shaped crystals and even

thorough grinding of the sample could not correct this mis-match in relative intensities. Of course, some contribution could be coming from the solvent variations.

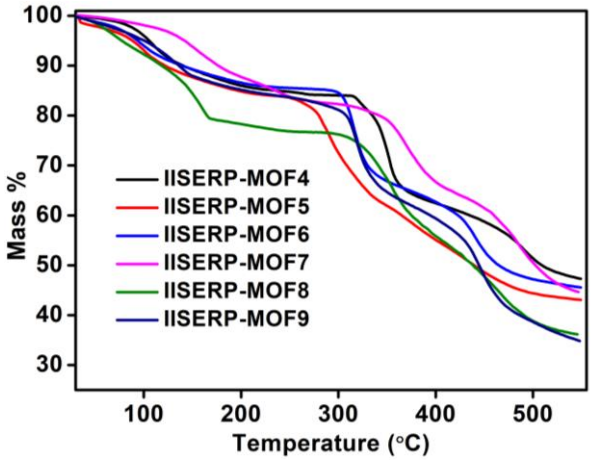

Figure 4-I.A.9. TGA plot for the as synthesized sample of IISERP-MOF4-MOF9. The initial weight loss in temperature range 30 to 250°C is due to the solvent molecules.

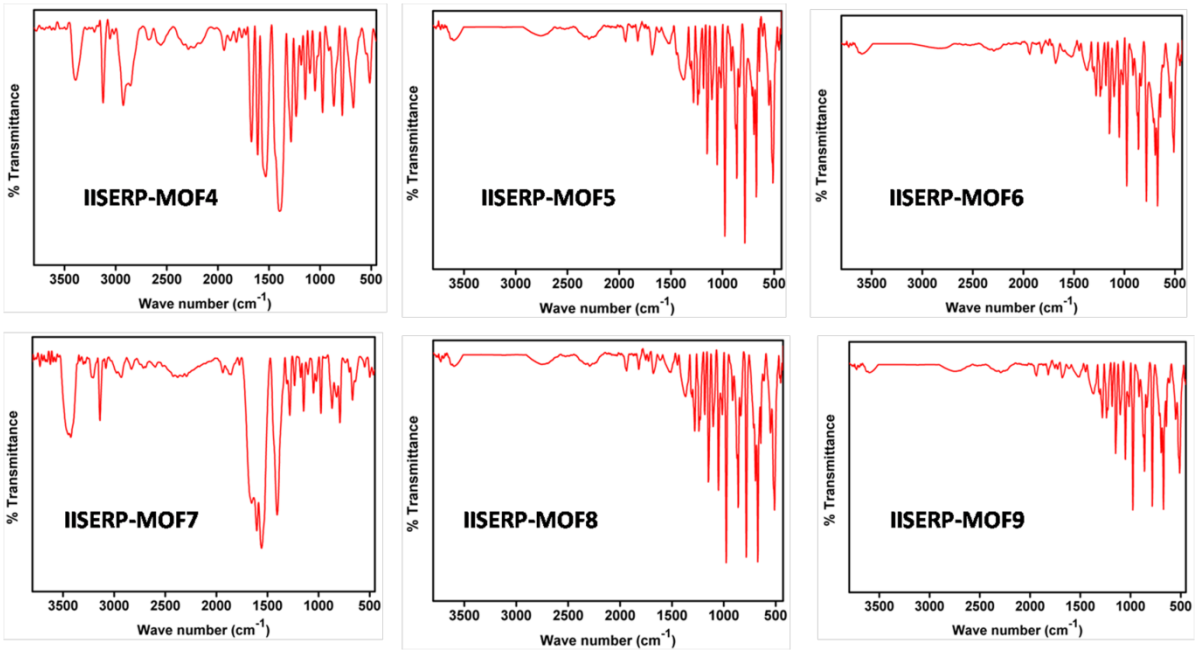

Figure 4-I.A.10. IR spectra of IISERP-MOF4 to MOF9 showing the characteristic stretching frequencies.

Gas Sorption Analysis:

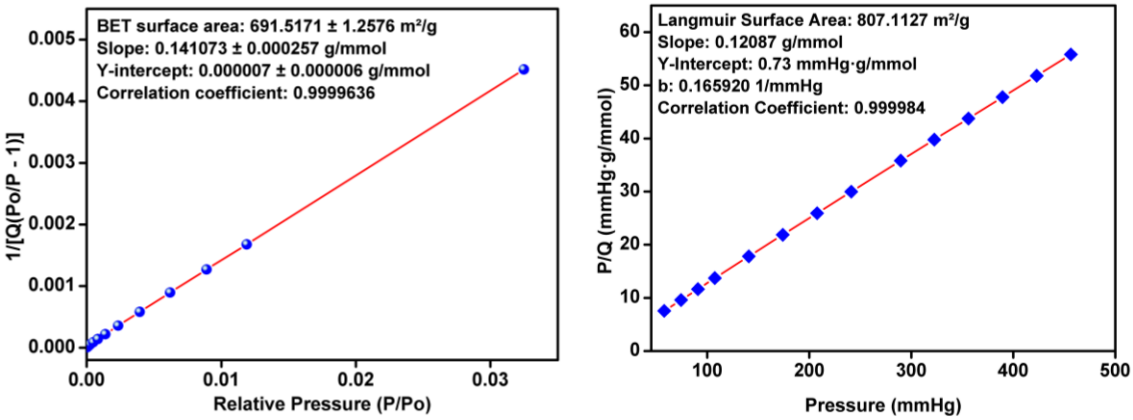

Figure 4-I.A.11. (Left): BET fit for IISERP-MOF4 from the 77 K N_2 data. (Right): Langmuir fit for IISERP-MOF4 from the 77 K N_2 data.

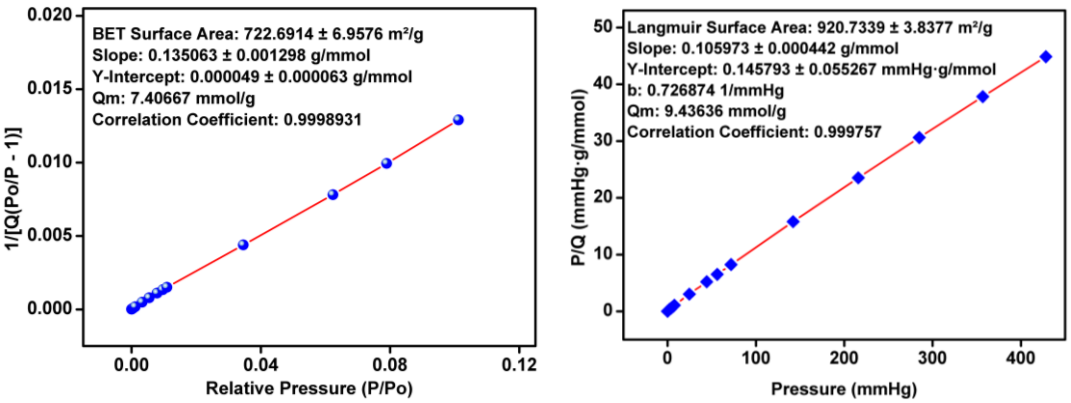

Figure 4-I.A.12. (Left): BET fit for IISERP-MOF5 from the 77 K N_2 data.(Right): Langmuir fit for IISERP-MOF5 from the 77 K N_2 data.

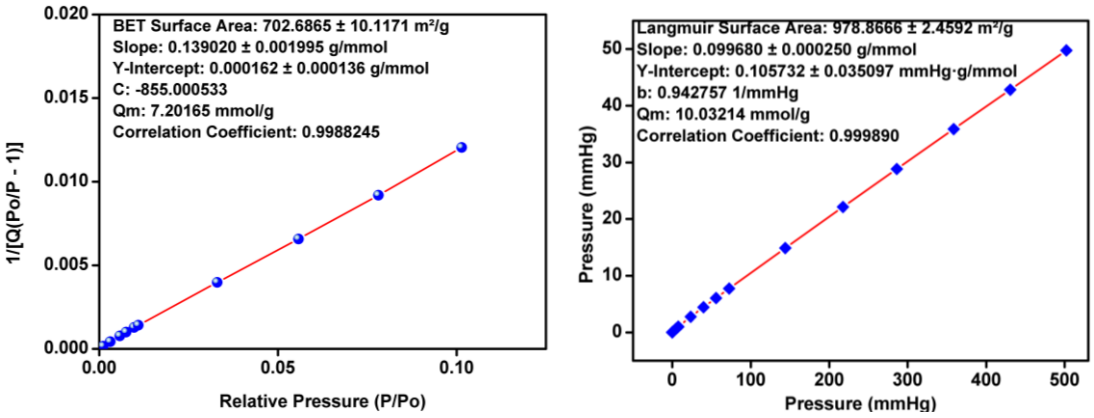

Figure 4-I.A.13. (Left): BET fit for IISERP-MOF6 from the 77 K N_2 data. (Right): Langmuir fit for IISERP-MOF6 from the 77 K N_2 data.

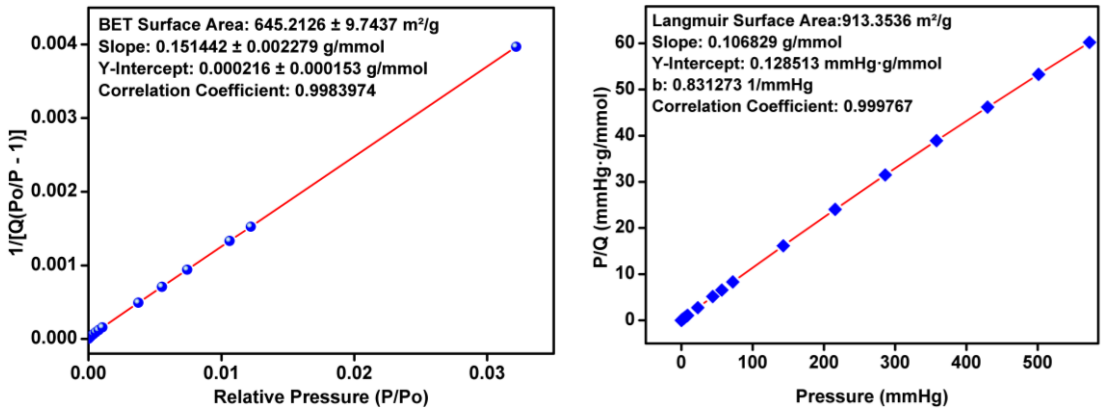

Figure 4-I.A.14. (Left): BET fit for IISERP-MOF7 from the 77 K N_2 data. (Right): Langmuir fit for IISERP-MOF7 from the 77 K N_2 data.

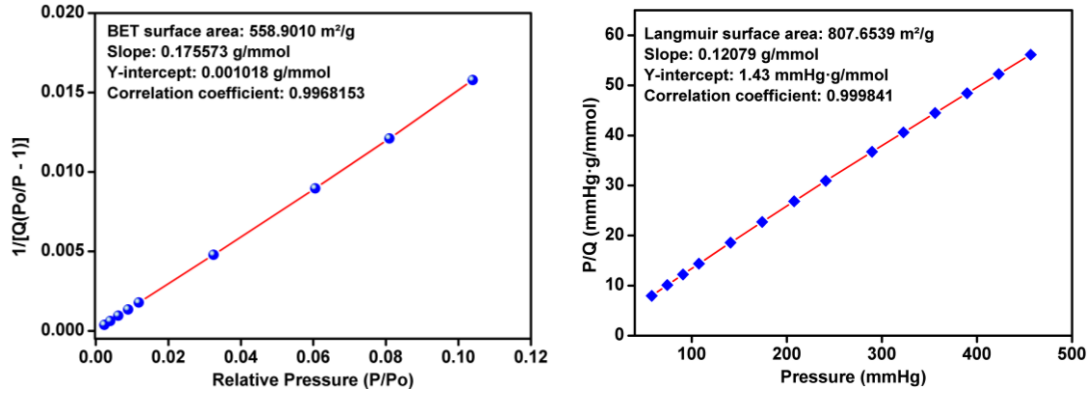

Figure 4-I.A.15. (Left): BET fit for IISERP-MOF8 from the 77 K N_2 data. (Right): Langmuir fit for IISERP-MOF8 from the 77 K N_2 data.

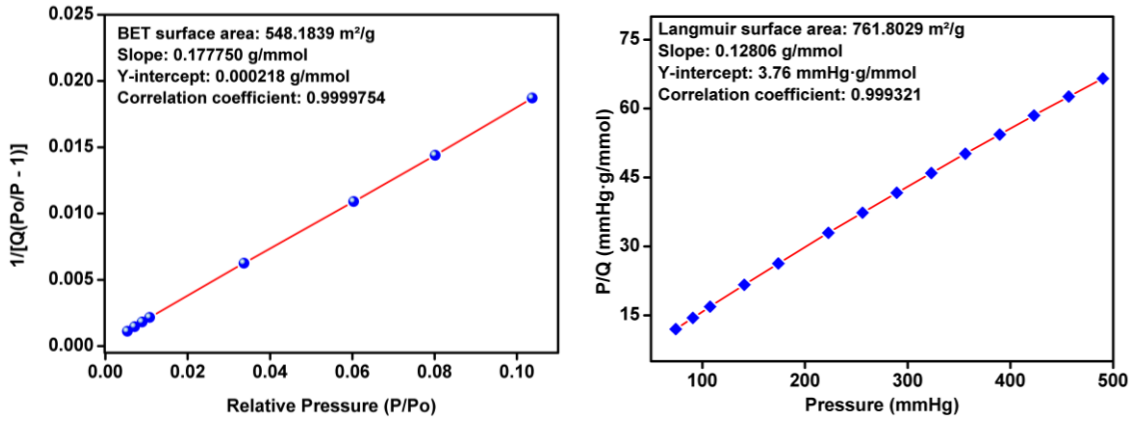

Figure 4-I.A.16. (Left): BET fit for IISERP-MOF9 from the 77 K N_2 data. (Right): Langmuir fit for IISERP-MOF9 from the 77 K N_2 data.

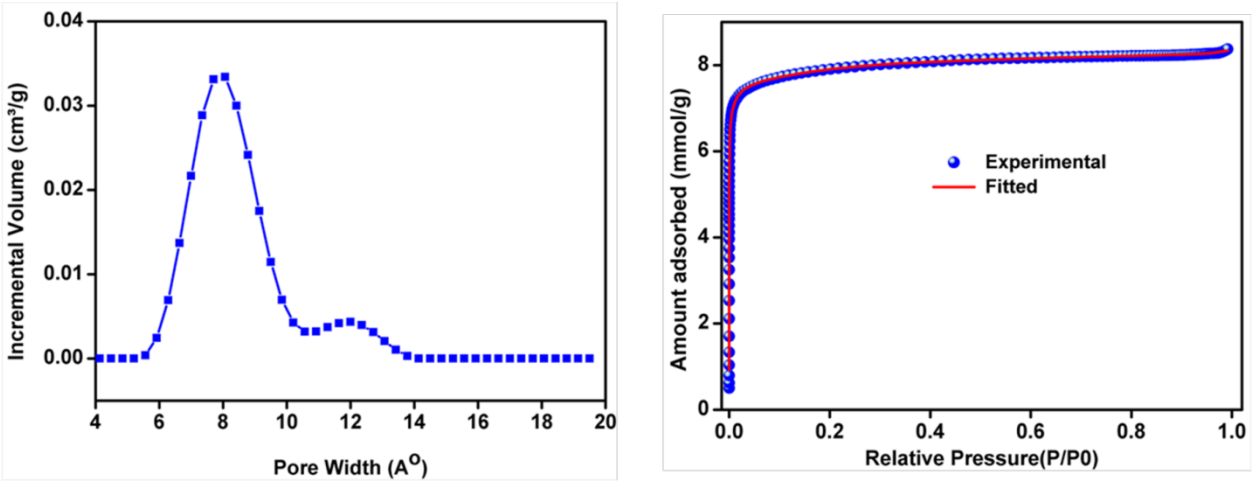

Figure 4-I.A.17. Left: Pore size distribution in IISERP-MOF4 obtained by fitting NLDFT model to the 77 K N_2 adsorption branch. Note the average pore diameter of 8.0 Å was obtained from the fit. This agrees well with the pore dimension observed in the single crystal structure. **Right**: Shows the fitting comparison for IISERP-MOF4 obtained for the NLDFT fit done using the adsorption branch of the 77 K N_2 adsorption data.

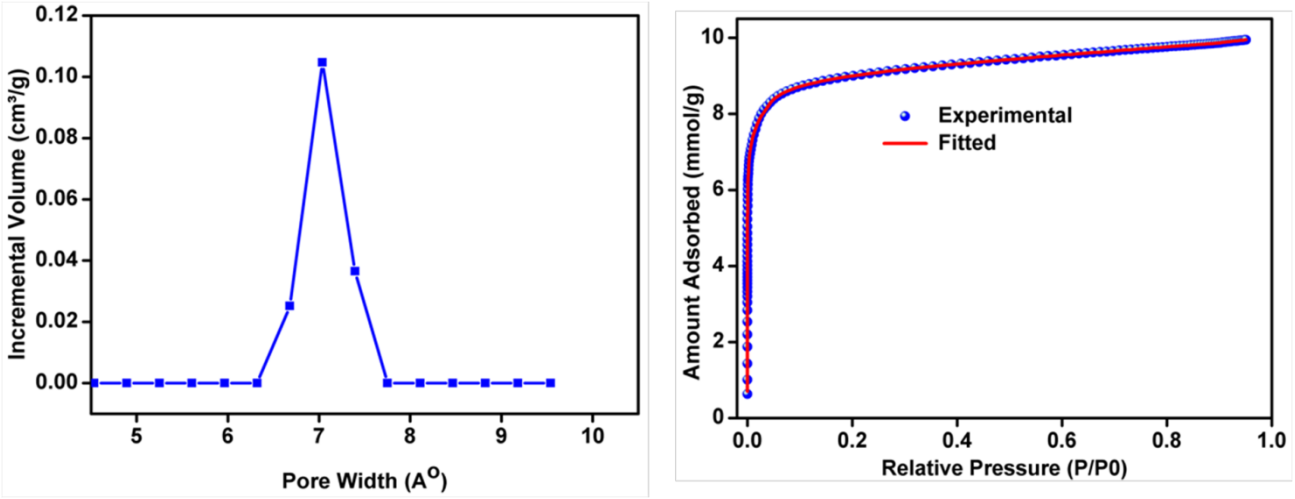

Figure 4-I.A.18. Left: Pore size distribution in IISERP-MOF5 obtained by fitting the NLDFT model to the 77 K N_2 adsorption branch. Note the average pore diameter of 7.0 Å was estimated from the fit. **Right:** Shows the fitting comparison for IISERP-MOF5 obtained for the NLDFT fit done using the adsorption branch of the 77 K N_2 adsorption data.

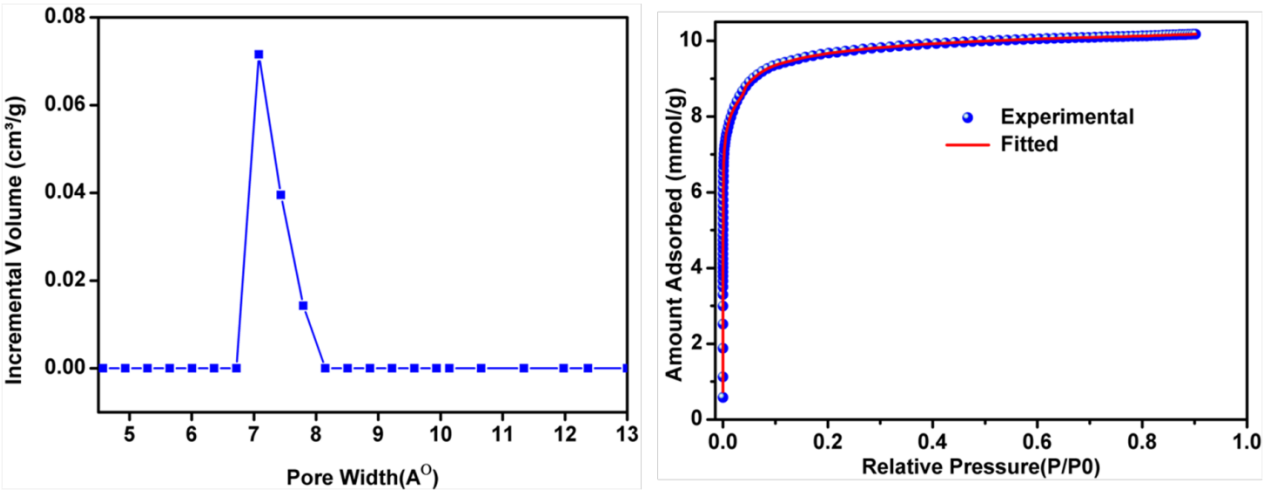

Figure 4-I.A.19. Left: Pore size distribution in IISERP-MOF6 obtained by fitting the NLDFT model to the 77 K N_2 adsorption branch. Note the average pore diameter of 7.1 Å was obtained from the fit. This agrees well with the pore dimension observed in the single crystal structure. **Right**: Shows the fitting comparison for IISERP-MOF6 obtained for the NLDFT fit carried out using the adsorption branch of the 77 K N_2 adsorption data.

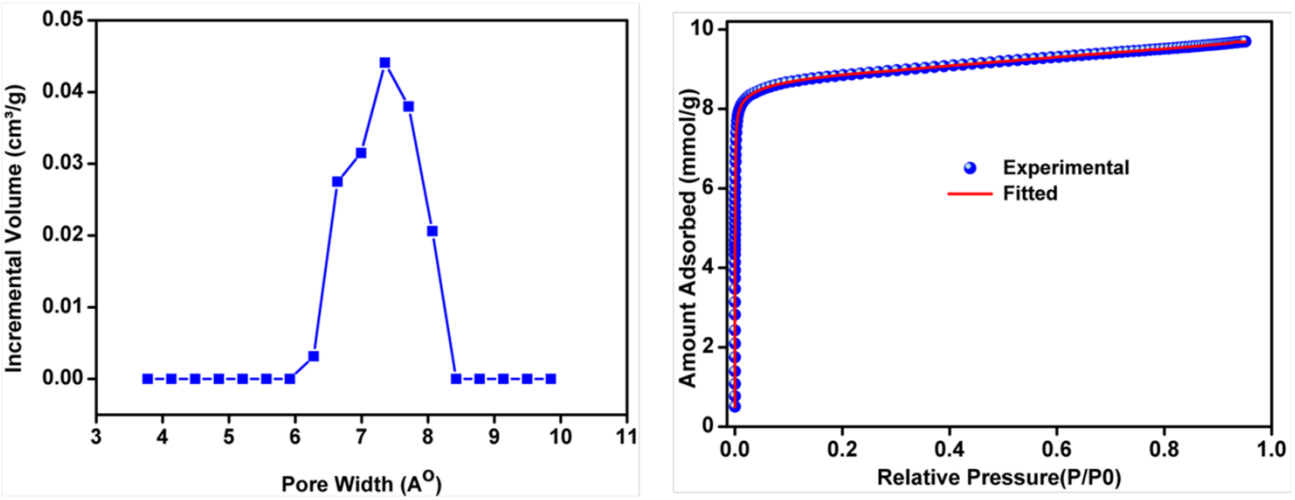

Figure 4-I.A.20. Left: Pore size distribution in IISERP-MOF7 obtained by fitting the NLDFT model to the 77 K N_2 adsorption branch. Note the average pore diameter of 7.3 Å was obtained from the fit. **Right**: Shows the fitting comparison for IISERP-MOF7 obtained for the NLDFT fit form the adsorption branch of the 77 K N_2 adsorption data.

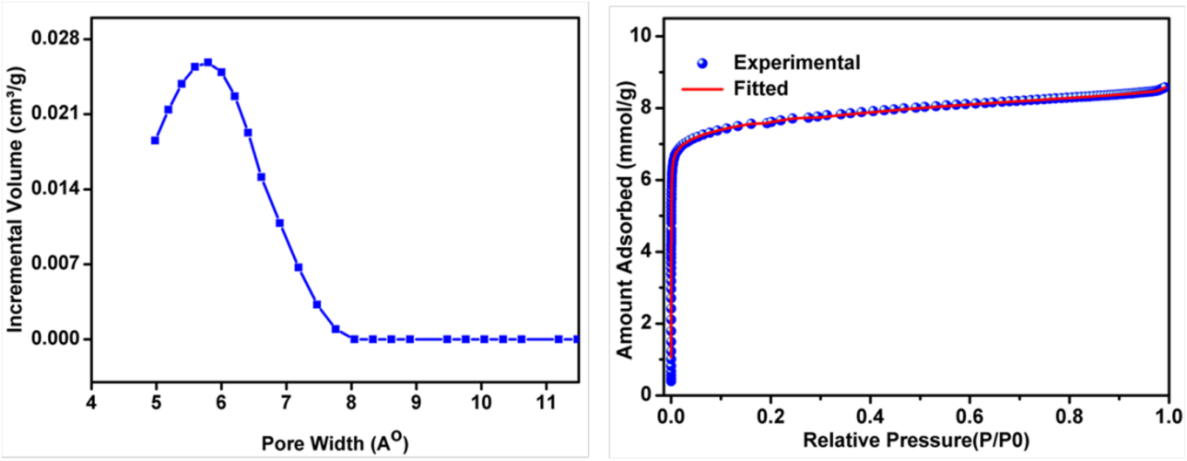

Figure 4-I.A.21. Left: Pore size distribution in IISERP-MOF8 obtained by fitting the NLDFT model to the 77 K N_2 adsorption branch. Note the average pore diameter of 6.0 Å . This agrees well with the pore dimension observed in the single crystal structure.**Right**: Shows the fitting comparison for IISERP-MOF8 obtained for the NLDFT fit done using the adsorption branch of the 77 K N_2 adsorption data.

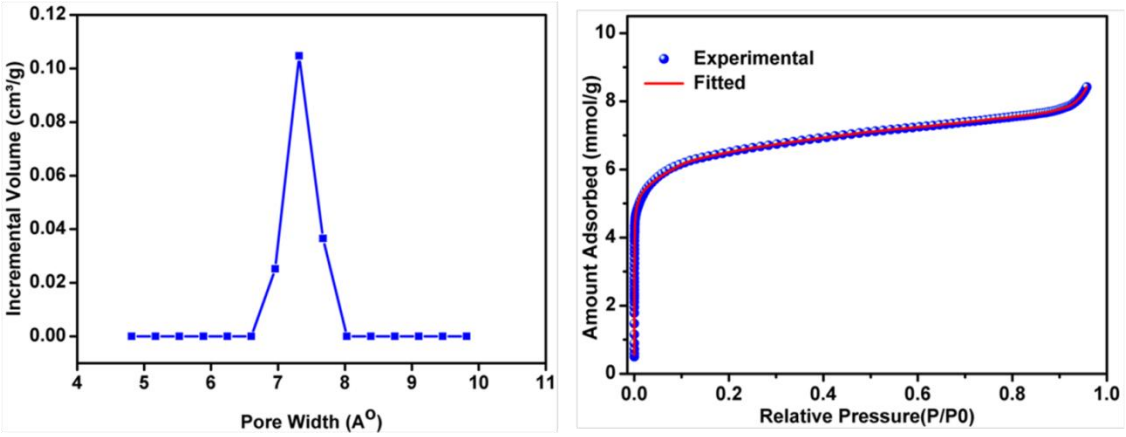

Figure 4-I.A.22. Left: Pore size distribution in IISERP-MOF9 obtained by fitting the NLDFT model to the 77 K N_2 adsorption branch. Note the average pore diameter of 7.2 Å was obtained from the fit. Right: Shows the fitting comparison for IISERP-MOF9 obtained for the NLDFT fit done using the adsorption branch of the 77 K N_2 adsorption data.

Virial Analysis:

The CO_2 adsorption data were measured from 0- 1bar at 303, 283, 273, 263, 248 and 195 K. For virial fitting the 303, 283, 273 and 263 K isotherms were taken and fitted by the virial equation (1).

$$ln(P) = ln(Va)+(A0+A1*Va +A2*Va^2 \ldots + A6*Va^6)/T+(B0+B1*Va) \ldots\ldots\ldots (1)$$

Where P is pressure, Va is amount adsorbed, T is temperature, and A0, A1, A2 … , A4 and B0, B1 are temperature independent empirical parameters

The virial fit has been presented below for IISERP-MOF4 and IISERP-MOF7 as representative.

Table 4-I.A.1: Summary of the fitted Virial parameters for IISERP-MOF4

A0	-2722.621886	B0	14.46887252
A1	190.7436991	B1	-0.413493728
A2	-6.407377843	B2	-0.018961943
A3	-14.83487308		
A4	3.691722007		

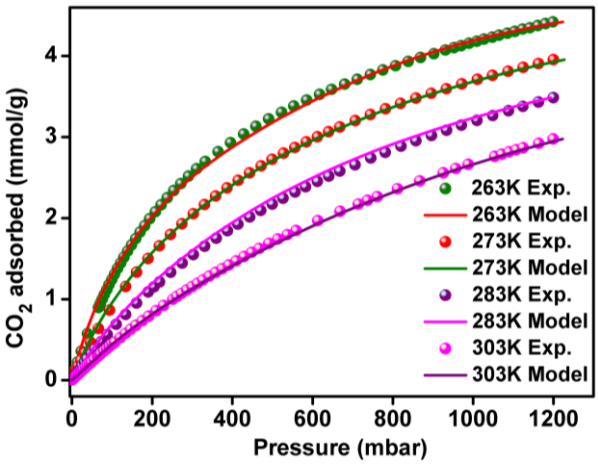

Figure 4-I.A.23. Comparison of experimental isotherms of IISERP-MOF4 to the ones obtained from virial modelling carried out using CO_2 isotherms collected at 303, 283, 273 and 263 K.

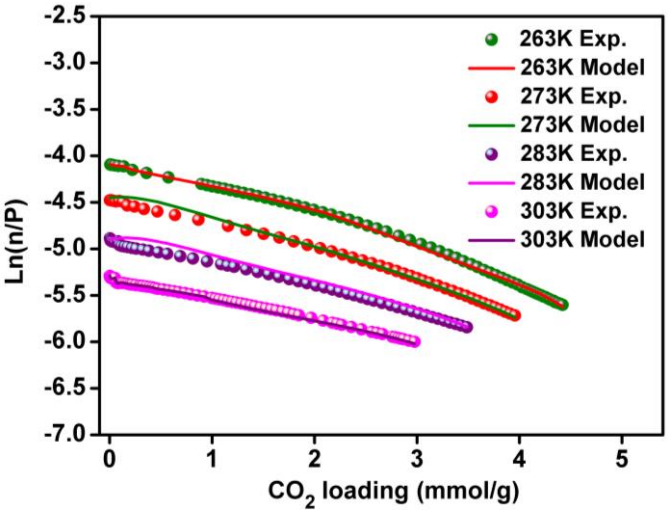

Figure 4-I.A.24. Virial plots of IISERP-MOF4 fitted using CO_2 isotherms collected at 303, 283, 273, 263 K.

Table 4-I.A.2: Summary of the fitted Virial parameters for IISERP-MOF7

A0	-2591.665002	B0	14.62093607
A1	-31.96990944	B1	-0.220428586
A2	160.0040647	B2	-0.095600681
A3	-68.68509774		
A4	14.36764174		
A5	-1.406571934		

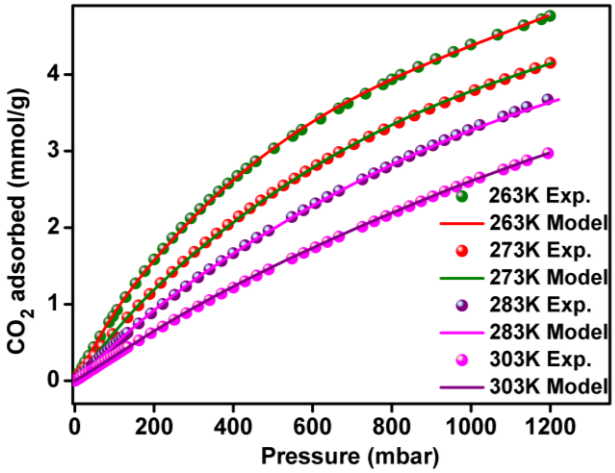

Figure 4-I.A.25. Comparison of experimental isotherms of IISERP-MOF7 to the ones obtained from virial modelling using CO_2 isotherms collected at 303, 283, 273 and 263 K.

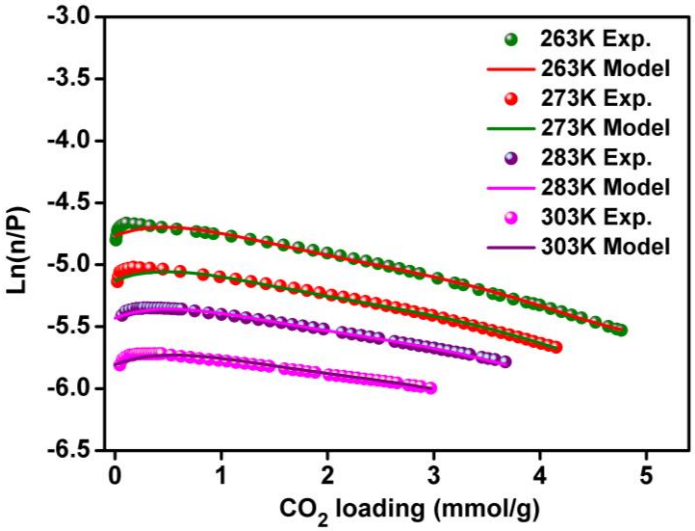

Figure 4-I.A.26. Virial plots of IISERP-MOF7 carried out using CO_2 isotherms collected at 303, 283, 273 and 263 K.

IAST Fitting Parameters for IISERP-MOF4 (CO_2/N_2):

273 K

Gas A =CO_2

Gas B = N_2

Gas Mixture			
YA =	0.15		
YB =	0.85		
Gas A Constants		Gas B Constants	
qA1 =	5.665099622	qA1 =	0.2166862
qA2 =	0	qA2 =	0
kA1 =	0.001869241	kA1 =	7.9759E-05
kA2 =	0	kA2 =	0
na1 =	0.784739867	na1 =	1.00001056
na2 =	0	na2 =	0
HA1 =	0.010589435	HB1 =	1.7283E-05
HA2 =	0	HB2 =	0

303 K

Gas Mixture			
YA =	0.15		
YB =	0.85		
Gas A Constants		Gas B Constants	
qA1 =	6.221401951	qA1 =	0.03773723
qA2 =	0	qA2 =	0
kA1 =	0.000757322	kA1 =	0.00036331
kA2 =	0	kA2 =	0
na1 =	1	na1 =	1.00006497
na2 =	0	na2 =	0
HA1 =	0.004291691	HB1 =	4.1083E-05
HA2 =	0	HB2 =	0

IAST Fitting Parameters for IISERP-MOF7 (CO_2/N_2):

273 K

Gas Mixture			
YA =	0.15		
YB =	0.85		
Gas A Constants		Gas B Constants	
qA1 =	8.180423116	qA1 =	0.49853529
qA2 =	0	qA2 =	0
kA1 =	0.000857778	kA1 =	2.1234E-05
kA2 =	0	kA2 =	0
na1 =	0.784739867	na1 =	1.00006282
na2 =	0	na2 =	0
HA1 =	0.007016987	HB1 =	1.0586E-05
HA2 =	0	HB2 =	0

303 K

Gas Mixture			
YA =	0.15		
YB =	0.85		
Gas A Constants		Gas B Constants	
qA1 =	11.09415015	qA1 =	0.42479508
qA2 =	0	qA2 =	0
kA1 =	0.000306675	kA1 =	2.0337E-05
kA2 =	0	kA2 =	0
na1 =	1	na1 =	1.00006497
na2 =	0	na2 =	0
HA1 =	0.003402301	HB1 =	8.6393E-06
HA2 =	0	HB2 =	0

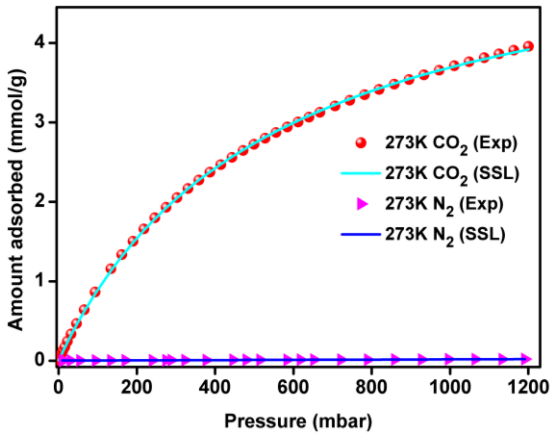

Figure 4-I.A.27. *IAST* fitting of CO_2 and N_2 isotherms for IISERP-MOF4 collected at 273 K.

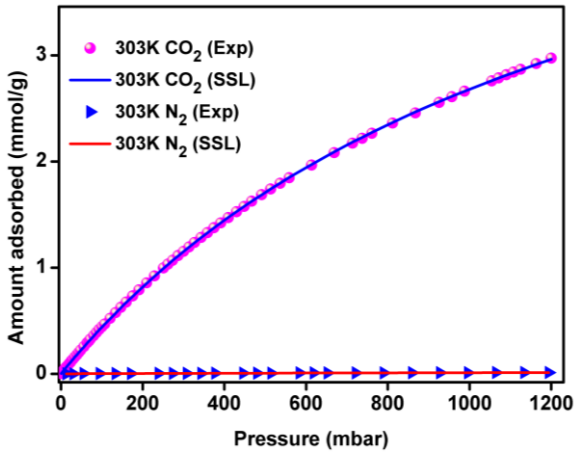

Figure 4-I.A.28. *IAST* fitting of CO_2 and N_2 isotherms for IISERP-MOF4 collected at 303 K.

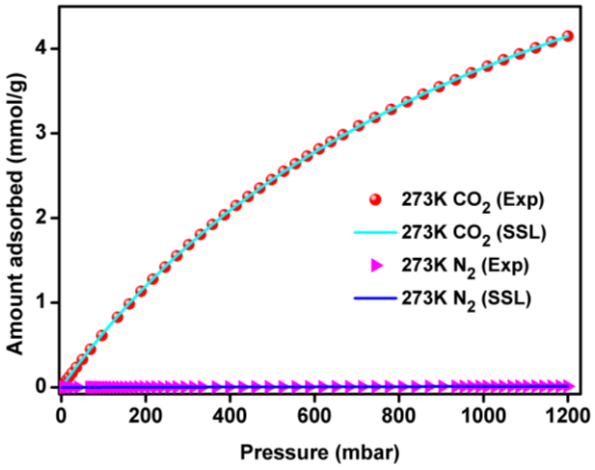

Figure 4-I.A.29. *IAST* fitting of CO_2 and N_2 isotherms for IISERP-MOF7 collected at 273 K.

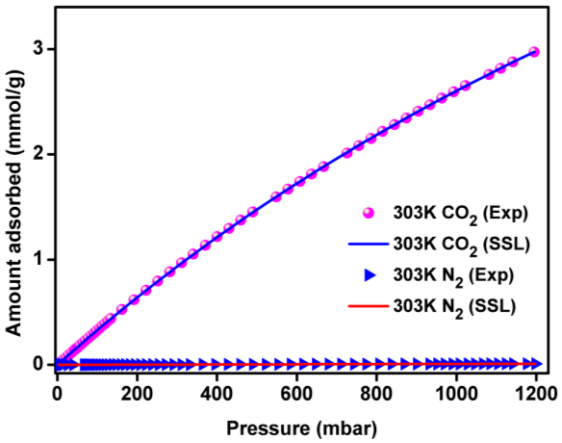

Figure 4-I.A.30. *IAST* fitting of CO_2 and N_2 isotherms for IISERP-MOF7 collected at 303 K.

Working Capacity:

Working capacity is defined as the amount of CO_2 recovered per gram of any material using a specific pressure swing. Here, working capacity of all the materials has been calculated for 1.2 bar to 0.1 bar pressure swing. The isotherms, involved in this calculation are all pure component isotherms at 303 K. Figure 4-I.A.31 shows the working capacity of all the material.

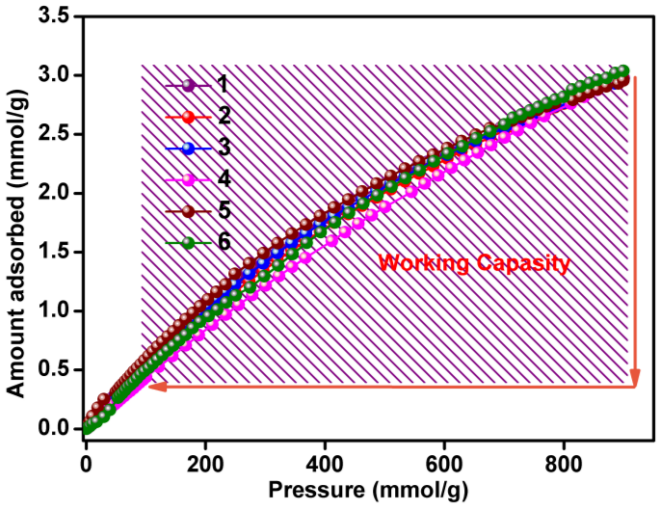

Figure 4-I.A.31. The working capacity of all the materials for a 1.2 to 0.1 bar pressure swing.

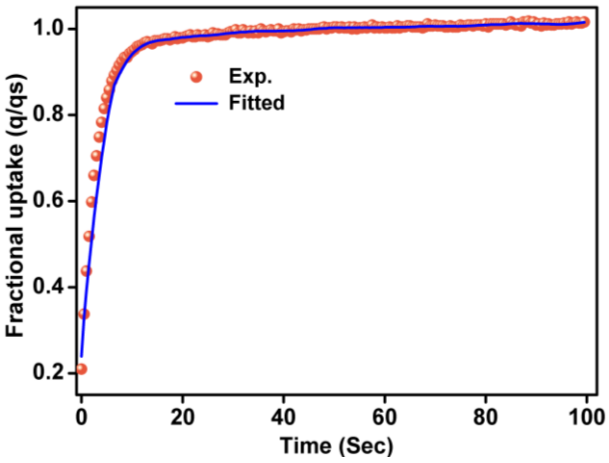

Figure 4-I.A.32. Representative plot of the adsorbate fractional filling vs time showing the fit between the spherical model (line) and the collected data (spheres) obtained from the single component CO_2 isotherm of IISERP-MOF4 (loading = 7 cc/g). Note 10 such fittings were considered to obtain the average diffusion coefficient.

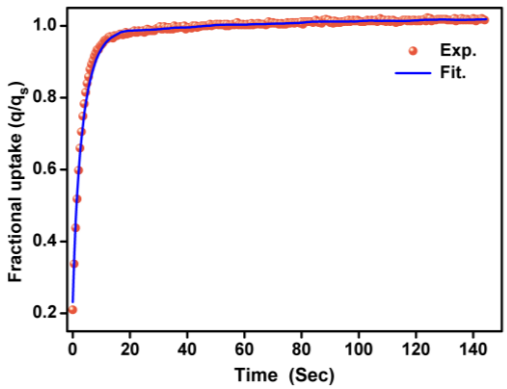

Figure 4-I.A.33. Representative plot of the adsorbate fractional filling vs time showing the fit between the spherical model (line) and the collected data (spheres) obtained from the single component CO_2 isotherm of IISERP-MOF4 (loading = 26 cc/g). Note 10 such fittings were considered to obtain the average diffusion coefficient.

Stability Studies:

Hydrolytic stability of the MOFs have been demonstrated using steam treatment experiments and the stability towards the repeated activation (heat + vacuum) and deactivation cycles (exposure to air + gases) during the gas sorption measurements. There were no major changes in crystallinity as observed from the PXRD of the steam-treated materials. We have carried out the 195 K CO_2 isotherms on all the steam treated phases. The saturation capacity in all the cases almost remains same. As representative we have shown the PXRD and CO_2 isotherms for MOF-4 and MOF-7.

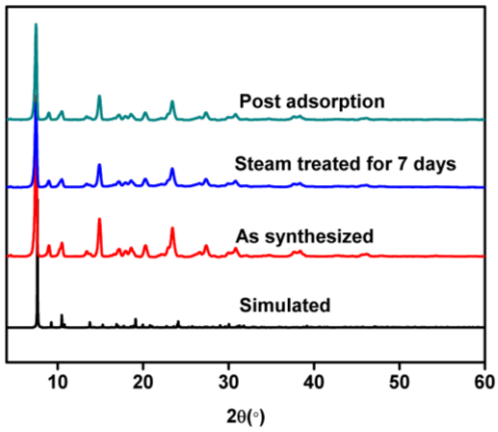

Figure 4-I.A.34. Pxrd comparison of the as-synthesized activated and steam treated sample of IISERP-MOF4 showing the stability of the sample.

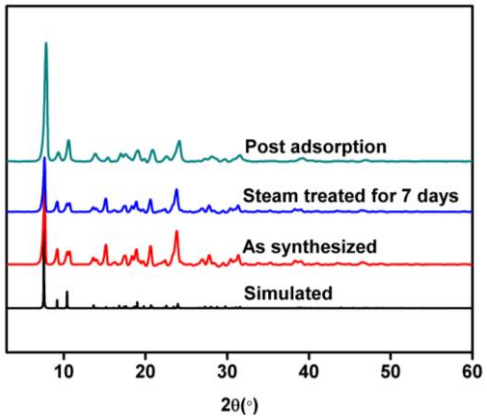

Figure 4-I.A.35. Pxrd comparison of the as-synthesized, activated and steam treated sample of IISERP-MOF7 showing the stability of the sample.

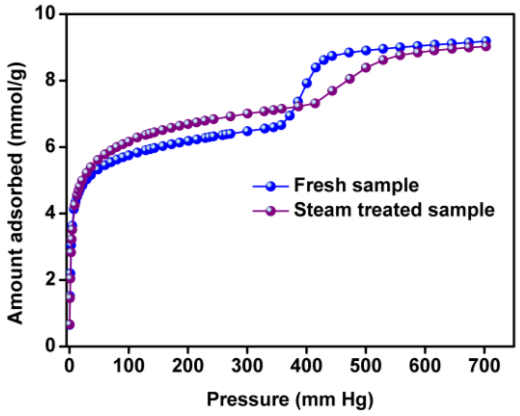

Figure 4-I.A.36. A comparison of 195 K CO_2 isotherms obtained from fresh sample vs steam treated sample of IISERP-MOF4.

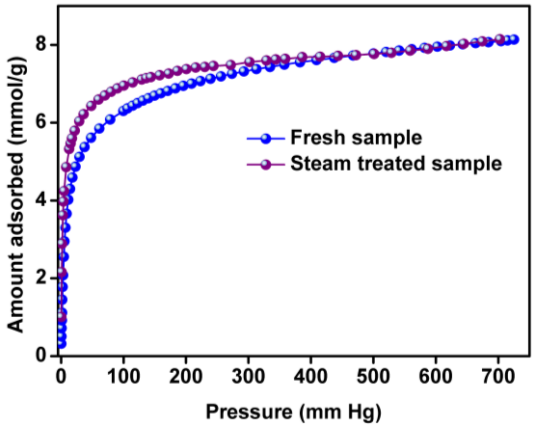

Figure 4-I.A.37. A comparison of 195 K CO_2 isotherms obtained from fresh sample vs steam treated sample of IISERP-MOF7.

Computational Details:

The CIF files from the single crystal structure were utilized as inputs. The most probable locations for CO_2 were obtained from a GCMC routine carried out using Materials Studio V. 6.0. For this routine the rotational and translational degrees of freedom were eased for the adsorbate molecules and a Metropolis Algorithm was employed. The resulting simulated model revealed a total of 29 CO_2 molecules per unit cell of Mg-triazolyl MOF. Following this, the direct positions of CO_2 were located by carrying out a geometry optimization using the Simulated Annealing routine of the Materials Studio. During this, the framework atoms were constrained and the CO_2 molecules were optimized with both rotational and translational freedom. The default force fields were employed.

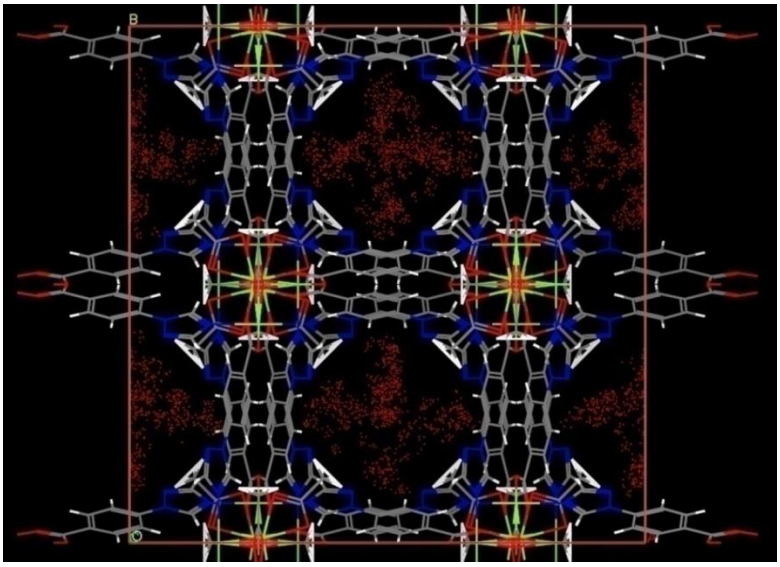

Figure 4-I.A.38. Shows the most probable positions for CO_2 molecules within the unit cell of IISERP-MOF4 obtained from the Simulated Annealing method.

Chapter 4-II

Investigating CO_2 Adsorption Behaviour of an Ultra-microporous MOF with Cavities Lined by Basic Groups and Open-metal Sites

4-II.1. Introduction:

Carbon dioxide (CO_2) is a key heat-trapping gas responsible for global warming through the greenhouse effect. Anthropogenic activities such as deforestation and burning fossil fuels generate substantial proportions of CO_2, in addition to the natural processes such as respiration and volcanic eruptions.[1] The recent report (2017) from NASA evidently reveals the atmospheric CO_2 concentration reaching alarming levels. In fact, the Mid-Tropospheric CO_2 levels have gone up from 365ppm to 475ppm in the last 15 years.[1a] Capturing CO_2 from industrial sources will have marked impact on the global CO_2 concentration.[2] Pre- and Post-combustion CO_2 capture are two efficient technologies for such large-scale capture.[3] Pressure and temperature swing adsorption (P/TSA)[4] based gas separation methods are recognized as the most energy efficient and thereby cost-effective capture technologies.[5,6]

Solid sorbents provide many benefits as industrial sorbents.[6] Current industrial scrubbers are zeolites with high molecular sieving capability.[7] In this regard, Metal Organic Frameworks (MOFs) have attracted significant attraction due to their high structural tunability, CO_2 capacity, selectivity and faster kinetics as well as low regeneration/parasitic energy.[8,9] For example, in addition to the molecular sieving effects of zeolites, MOFs can be chemically manipulated to selectively adsorb CO_2. Ultra-microporous MOFs (Um-MOFs) (pore size < 6 Å) built from rigid short linkers with basic character are suitable for selective CO_2 capture. The high selectivity arises from enhanced framework-CO_2 and co-operative CO_2...CO_2 interactions within the pore confinement.[8c] Such molecular level interactions express as optimal heat of adsorption, which goes on to define the ease of CO_2 regeneration.[9c] Enormous efforts are invested in identifying and optimizing the framework-CO_2 interaction in MOFs.[10] Some of the most energetic framework-CO_2 interactions are amine-CO_2 interaction,[8c,10a,10b] open-metal-CO_2 interaction,[10c,10d] aromatic π cloud-CO_2 interaction[9b,10e] and functional group-CO_2 interaction[10f,10g]. Understanding the adsorption sites of highperforming MOF is vital for the future design of superior sorbents.

Herein, we report a 2D Cu based ultra-microporous MOF (IISERP-MOF20) built from a single organic ligand, 2-(4- carboxyphenyl)-1 H-benzo[d]imidazole-5-carboxylate. It shows high CO_2 uptake as well as high CO_2/N_2 selectivity for flue gas compositions at room temperature. Also, this MOF poses an optimal Heat of Adsorption (HOA) for CO_2 which further ensures the low regeneration energy demand. Here, using Grand Canonical Monte Carlo (GCMC) methods, we have simulated the different binding sites present in this MOF.

Notably, some unique CO_2-metal interactions are identified, which deviate from the previously observed ones.

4-II.2. Material and Methods:

All the chemicals were bought from Sigma Aldrich and used without further purification.

4-II.2.1. Synthesis of 2-(4-carboxyphenyl)-1 H-benzo*[d]*imidazole-5-carboxylic acid:

In a 500 ml roundbottom-flask, a solution of 4-formyl benzoic acid (7.5 g, 0.05 mol) in ethanol (120 ml) was prepared by ultrasonication for 1 hr. After that, a suspension of 3, 4-diaminobenzoic acid (7.6 g, 0.05 mol) in EtOH (100 ml) was added and stirred at room temperature for 1 hour. Following this, 5 ml of aqueous acetic acid (6N) was added to the reaction mixture. The reaction mixture was heated at 60^{o}C for 12 hrs. After cooling down to room temperature, the orange yellow solid formed was filtered off, washed with cold EtOH, deionized water and acetone followed by drying under vacuum for 12 hrs at 100 °C to afford the desired compound as a yellowish off white powder (11.3 g, 80% yield). The ligand was further recrystallized from a DMF/water mixture and dried for 24 h at 100 °C. Then the desired ligand was characterized via ^{1}H and ^{13}C NMR.

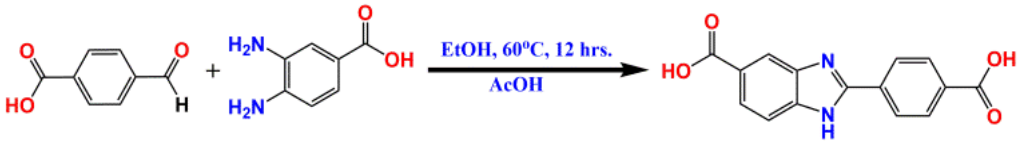

Scheme 4-II.1. Schematic representation of the synthesis of 2-(4-carboxyphenyl)-1 H-benzo[d]imidazole-5-carboxylic acid.

4-II.2.2. Synthesis of [Cu (L_1) H_2O.] 1.5DMF. 1.5 EtOH; IISERP-MOF20:

A solvothermal reaction between $Cu(NO_3)_2.3H_2O$ (0.121 g; 0.5 mmol) and 2-(4-carboxyphenyl)-1 H-benzo*[d]*imidazole-5-carboxylic acid (0.141 g; 0.5 mmol) in a solution containing 4 ml of Dimethylformamide, 3 ml of ethanol (EtOH) and 1 ml of water was carried out at 80°C for 36 hours. After cooling to room temperature, blue–colour thin square plate shaped crystals were isolated by filtration and was washed with EtOH and finally with acetone. The air-dried sample yielded ~74% (based on Cu). The PXRD pattern indicated this to be a pure phase of IISERP-MOF20. In a single synthesis up to 1g of the MOF was synthesized just by scaling up of the above synthesis.

Single Crystal Structure Determination:

Single-crystals data were collected on a Bruker SMART APEX four-circle diffractometer equipped with a CMOS photon 100 detector (Bruker Systems Inc.) and with a

Cu Kα radiation (1.5418 Å). The incident X-ray beam was focused and monochromated using Micro focus (IμS). Crystal was mounted on nylon Cryo loops with Paratone-N oil. Data was collected at 100(2) K. Data was integrated using Bruker SAINT Software and was corrected for absorption using SADABS. Structure was solved by Intrinsic Phasing module of the direct methods and refined using the SHELXTL 2014 software suite. All non-hydrogen atoms were located from iterative examination of difference F-maps following which the structure was refined using least-squares method. Hydrogen atoms were placed geometrically in a riding model.

4-II.2.3. Analytical Characterization:

Powder X-ray Diffraction:

Powder XRDs were carried out using a Rigaku Miniflex-600 instrument and processed using PDXL software.

Thermo Gravimetric Analysis:

Thermogravimetry was carried out on NETSZCH TGA-DSC system. The routine TGAs were done under N_2 gas flow (20 ml/min) (purge + protective) and samples were heated from 25ºC to 550ºC at 2 K/min.

IR Spectroscopy:

IR spectra were obtained using a Nicolet ID5 attenuated total reflectance IR spectrometer operating at ambient temperature. The KBr pellets were used for IR data collection.

4-II.2.4. Adsorption Analyses:

All gas sorption isotherms were measured on a Micromeritics ASAP 2020HD/ Autosorb IQ instrument using ultra-high purity gases (≥ 4.8 grade). Samples were first soaked in DCM for 24 hrs with replenishing the solvent in every 4 hrs. Then the solvent exchanged and dried sample (about 80 mg) was transferred to a glass tube for analysis, with one step activation: evacuation at 160ºC on the degas port for 24hrs (10^{-6} mbar), at which point the outgas rate was ≤ 2 μbar/min.

Langmuir Fits:

In most cases the isotherms were fit to the Single-Site Langmuir Freundlich (SSLF) equation. Also modified Langmuir equations were utilized to account for noteworthy errors

in the Langmuir model. It is widely known that even minute fitting errors will have a large impact on selectivity calculations.

The isotherms were fit by solving the Langmuir equation using the solver function in Microsoft Excel following a similar protocol to Keller *et al.*[11] Utilizing this routine circumvents some of the problems associated with favouring either high or low pressure regions when linearizing the Langmuir equation[12] and offers a balanced approach.

Single-Site Langmuir (SSL):

$$q_i = q_m \frac{K_i P}{1 + K_i P}$$

Dual-Site Langmuir (DSL):

$$q_i = q_{m,1} \frac{K_1 P}{1 + K_1 P} + q_{m,2} \frac{K_2 P}{1 + K_2 P}$$

Ideal Adsorbed Solution Theory (IAST):

IAST calculations were undertaken as described by by Prausnitz *et al.*[13] The selectivity equation is provided below.

Selectivity: $S_{1,2} = \frac{q_1/q_2}{P_1/P_2}$

Kinetics study:

Self-diffusion Coefficient CO_2 in IISERP-MOF20:

Diffusion coefficient determination from Rate of Adsorption (ROA) studies: For this purpose an extremely high resolution rate of adsorption measurement was performed using the ASAP2020HD instrument in the pressure range of 0-1 bar. The diffusion coefficient (Dc) was calculated as a function of CO_2 loading. 10 different adsorption points were used and each of the ROA data was fitted to spherical pore model [14, 15]. The fittings were done using Excel equipped with solver programme according to our previous report.

$$F = 1 - \frac{6}{\pi^2} \sum_{n=1}^{\infty} \frac{1}{n^2} \mathrm{Exp}\left(-n^2 \pi^2 \tau\right)$$

F = fractional uptake; τ = non-dimensional time given by $\tau = Dt/R^2$, where R= particle size; t= time (secs); D = apparent diffusivity.

The single-component diffusion coefficient was estimated to be ~2.25 x 10^{-9} m^2s^{-1} taking the average of these 10 points.

Cycling Experiment:

CO_2 regeneration from the MOF was evaluated from cycling experiments on the ASAP2020HD adsorption instrument. During this, the sample was subjected to a pressure swing from 1.18 bar to 0.02 bar. The amount of CO_2 adsorbed remains almost the same after 14 cycles and both the adsorption and desorption happen smoothly.

4-II.3. Result and Discussion:

The IISERP-MOF20 was synthesized via a solvothermal reaction between $Cu(NO_3)_2.3H_2O$ and 2-(4-carboxyphenyl)-1 Hbenzo[d]imidazole-5-carboxylic acid in a mixture of DMF, water and ethanol at 80^oC for 36 hrs. Following an ethanol wash and air-drying, a blue colored product was obtained in good yield (74% w.r.t. Cu) as clean crops of thin square-shaped platy crystals.

4-II.3.1. Single Crystal Structure Analysis:

Single crystal structure analysis reveals that IISERP-MOF20 crystallized in orthorhombic system (a= 20.8093(11); b= 9.7634(5); c= 25.2583(11) Å; Sp. Gr. C m c a). The structure consists of typical Cu_2 paddle-wheel unit where the Cu-Cu dimers are connected by four different 2-(4- carboxyphenyl)-1 H-benzo[d]imidazole-5-carboxylate units (Fig. 4-II.A.3). Each Cu is penta-coordinated. Among the five coordinations, four are satisfied by oxygen atoms of the carboxylate unit and the fifth one is satisfied by a water molecule. These Cu_2 paddle-wheel nodes are extended by four ligand units into a 2D-layer along the ac-plane with large near square-shaped apertures (16.21 x 16.21 Å, shown with green lines in figure 4-II.1 and 4-II.A.5). The adjacent layers are shifted exactly by half-a-unit cell along the a- and c- directions and are rotated by 90° giving a staggered ABAB... arrangement (Fig. 4-II.A.6). This positions the five-membered heteroatomic rings of the benzimidazole unit from the adjacent layer right at the edges of the square aperture and the Cu_2 paddle-wheel from the adjacent layers above and below the centre of the square aperture in the middle layer. Now, for each square shown (in green) in figure 4-II.1, there are four N-containing 5-membered rings at the edges which hydrogen bond above and below the plane, thus forming a column of N-H...N hydrogen bonds (N...H-N = 2.0137 Å). These are vital in holding the 2D layers together into a stable 3D framework. Also, the Cu_2 paddlewheels from alternate layers run as a column along the b direction.

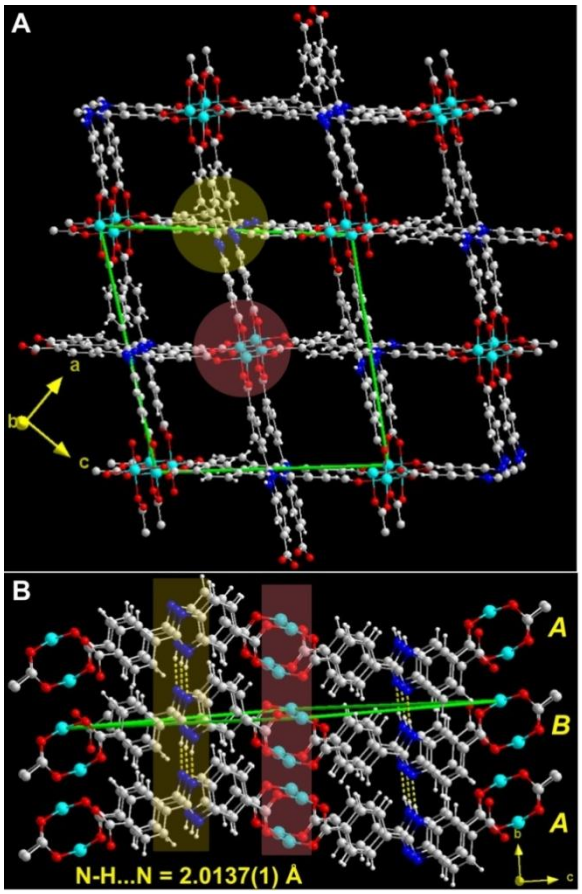

Figure 4-II.1. A) Three-dimensional structure of the IISERP-MOF20 formed by the ABAB... stacking of the Cu_2 paddle-wheel based layers. The green line is a guide for the eye to see the large square shaped aperture formed in each layer. Yellow and Maroon circles show the nodes present in the structure. B) The column of inter-layer N-H....N hydrogen bonds between the nitrogens of the 5-membered rings of the benzimidazole units and the column of Cu_2 paddle-wheels is shown (Cu..Cu = ~7.36 Å).

The half-unit cell shift in the adjacent layers thus compartmentalizes the large aperture in each paddle-wheel derived layer into four smaller pores creating a rhombic channel of dimension 7.63 X 7.63 Å (not factoring the Van der Waals radii, Fig. 4-II.1 and Fig. 4-II.A.5). In fact, the overall 3D structure is held together by the covalent bonds between metal and the ligand in the ac-plane and by the hydrogen bond interactions running along the perpendicular b- direction. Removal of the co-ordinated water molecules generates two open-metal sites at each paddle-wheel units and the open-metal sites from the adjacent A-A layers in the ABAB stacking line up at a distance of 7.36(3) Å. A PLATON analysis suggests a 48% solvent accessible void present in the structure. A squeeze refinement drastically improves the R factor indicating presence of disordered solvent molecules which could not be modelled properly. However, the electron count from the squeeze analysis could be assigned to 1.5

DMF and 1.5 EtOH molecules per unit cell which matches well with the TGA analysis of the IISERP-MOF20.

4-II.3.2. Bulk Characterization and Porosity Analysis:

For a practical large-scale industrial CO_2 capture process, the sorbents are required in tonnes. Hence, even in a laboratoryscale, it makes it imperative to demonstrate the MOF synthesis in grams. In this regard, the MOF was synthesized in gram scale by merely scaling up the constituents from the mg scale synthesis and the purity was confirmed via Powder X-ray Diffraction (PXRD) analysis as presented in figure 4-II.2A and 4-II.A.7. From TGA, the MOF was found to be stable up to 260◦C (Fig. 4-II.A.8).

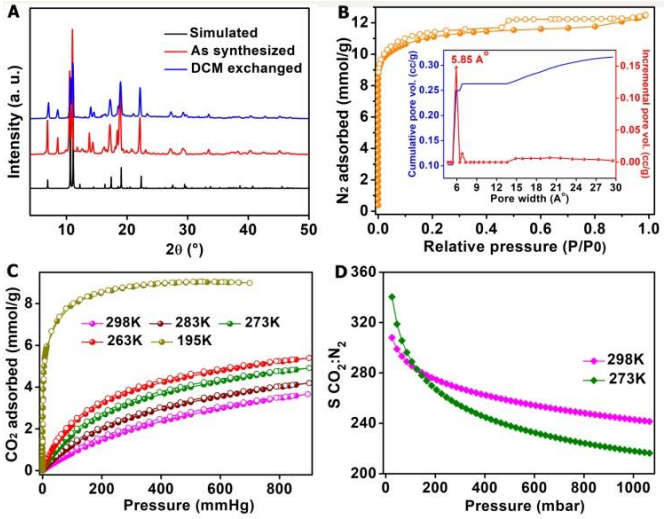

Figure 4-II.2. (A) A comparative PXRD of as synthesized, Simulated and DCM exchanged IISERP-MOF20 showing the bulk purity. (B) The 77 K N_2 isotherm of IISERP-MOF20. Inset shows the pore size distribution. C) CO_2 sorption isotherms at different temperature on IISERP-MOF20. D) CO_2/N_2 selectivity of IISERP-MOF20 calculated using *IAST* model employing a nominal composition of $15CO_2$:$85N_2$.

The N_2 adsorption at 77 K confirms the permanent porosity of the MOF (Fig. 4-II.2B). A Brunauer-Emmet-Teller (BET) fit to the adsorption branch of the 77 K N_2 isotherm yields a surface area of 945 m^2/g (Fig. 4-II.A.10), which is quite high for an ultra-microporous MOF.[8c, 8f, 9a] Nonlocalized Density Functional Theory (NLDFT) fit yields a pore diameter of 5.85 Å, which matches extremely well with the pore size (Inset Fig. 4-II.2B and 4-II.A.11). Notably, this ultramicroporous MOF adsorbs good amount of CO_2 (3.5 mmol/g) at 1 bar and 298 K (Fig. 4-II.2C) and has a saturation CO_2 capacity of 9.0 mmol/g (195 K CO_2 isotherm). However, it shows less N_2 uptake at room temperature. The Ideal Adsorption Solution Theory (IAST) calculation at 273 and 298 K using a nominal composition of

$15CO_2$:$85N_2$ yields a CO_2/N_2 selectivity of 220 and 250, respectively (Figs. 4-II.2D and 4-II.A.12). Although the selectivity values are not as high as the recently reported UMMOFs,[8f, 9a] these are sufficient to achieve the benchmarked 99% purity during separation.[16]

The HOA calculated using both virial and DFT model employing the 298, 283, 273 and 263K CO_2 isotherms was 26 kJ/mol at zero loading. At higher loadings the HOA reaches values of 20-22 kJ/mol (Figs. 4-II.3A and 4-II.A.13). Such moderate HOA (25-30 kJ/mol) is optimal for facile regeneration.[9] This was further confirmed by an iso-cycling experiment.As can be seen from the figure 4-II.3B, the CO_2 uptake remains almost the same even after 14 cycles.

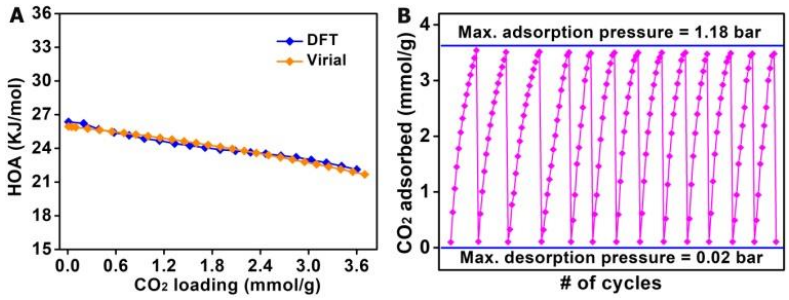

Figure 4-II.3. (A) HOA as a function of CO_2 loading in IISERP-MOF20 calculated using DFT and virial model. (B) CO_2 adsorption-desorption cycles at room temperature.

Also, the CO_2 sorption is very smooth, suggesting smooth diffusion of CO_2 in the MOF. Diffusion kinetics was confirmed from a Rate of Adsorption (ROA) analysis at 273 K. The average diffusion coefficient (Dc) for CO_2 within the pores of IISERP-MOF20 was calculated to be 2.25 x 10^{-9} m^2/s over a range of CO_2 loadings (Fig. 4-II.A.15). This diffusion coefficient is comparable to a recently reported 1D porous Ni-PyC MOF[9a] and much higher than that observed in other MOFs with similar or larger pores such as MOF-5 (1.17 x 10^{-9} m^2/s) or MOF-177 (1.17 x 10^{-9} m^2/s).[17] It is worth mentioning that, the Dc observed for IISERP-MOF20 is at least 2 orders of magnitude higher than zeolite-13X,[17c] the current industrial CO_2 scrubber.

4-II.3.3. Theoretical Consideration:

Considering that the activated MOF consists of appropriately oriented open-metal sites and basic secondary amine groups, the observed moderate HOA's were puzzling. We have used simulations to probe this. For this, the number of CO_2 molecules (saturation capacity from 195 K adsorption) for a 2 x 2 x 2 cell was calculated to be 200. These many

CO_2 molecules were allowed to diffuse into the cell freely. From which, the most probable positions for CO_2 inside the structure were identified using the simulated annealing method embedded in the Materials Studio programme (see Appendix section). The observed CO_2 positions provide some useful information. As shown in figure 4-II.4A, even in the lowest energy configurations, the majority of the CO_2 molecules preferred the middle of the pore despite having open metal sites and secondary amine groups lining the channels. Also, the adjacent CO_2 molecules were separated by distances in the range of 3.4 to 4.7 Å (Figs. 4-II.4B and 4-II.A.17). Weak intermolecular dispersive interactions operate at such distances.[8c] Some of the CO_2 molecules arrange themselves into a typical T-shaped configuration where the δ- oxygen of one CO_2 interacts with the δ+ carbon of another CO_2 molecule (Figs. 4-II.4B and 4-II.A.17). This T-shaped configuration among CO_2 molecules is quite common in solid phase CO_2.[18] All these results are consistent with our previous reports.[8c] But the surprising result comes from the orientation of the CO_2 molecules that reside proximal to the open metal sites (Fig. 4-II.4C). Typically, the CO_2 molecules interact with the open-metal sites via M.....O(δ-)=C(δ+)=O(δ-) (head-on interaction, M...O distance = ~2.4 Å).[19]In contrast, in our case, the CO_2 molecules align parallel to the open-metal sites and gets sandwiched between two openmetal sites from the alternate layers. This enables the CO_2 oxygens to interact weakly but equally with both the metal sites (Fig. 4-II.4C) and simultaneously with the other proximal CO_2 molecules in the pore.

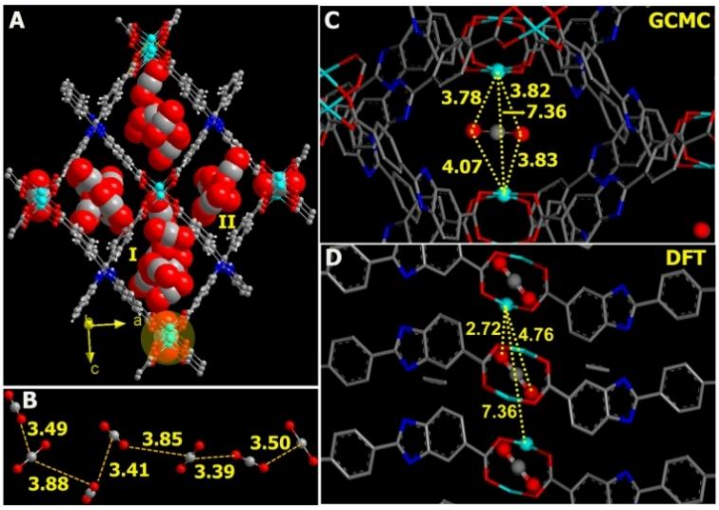

Figure 4-II.4. (A) CO_2 positions from GCMC simulations. (B) Interactions and distances between CO_2 molecules in the pore labelled as I. (C) A specific CO_2 sandwiched between the open-metal sites. Note: The other CO_2 molecules in the pore have not been shown for clarity. (D) Lowest energy configuration from periodic DFT for a sandwiched/pillaring CO_2, calculated without including any other CO_2 molecules in the pore.

To emphasize the role of CO_2...CO_2 cooperative interactions and to evaluate the feasibility of a pillaring CO_2 to get activated at these open-metal sites separation we carried out further DFT simulations. For this, as an initial model, we positioned a CO_2 molecule to pillar the Cu_2 paddle-wheels with the oxygens of the CO_2 interacting in a head-on fashion with the metal (Cu...O=C=O = 2.46; O=C = 1.22 Å). The 2.46 Å is as per the value available in the literature for the strongest headon interaction with the open-metal site.[19] No other CO_2 molecules were included. We optimized the geometry using a periodic DFT (CASTEP program), with a constraint on the metal-organic layers (to retain the coordinates from the single crystal XRD, Cu-Cu distance = 7.36 Å).

At this separation, this CO_2 molecule does not remain perpendicular, instead, tilts by an angle of ~53° (about the mean plane) and the Cu...O=C=O distance equilibrates to 2.72Å and the O=C to 1.18 Å (Fig. 4-II.4D). This explains that for the CO_2 to be strongly activated the inter-layer distance needs to be even shorter. But the N-H...N hydrogen bonds keeps the layers away at a distance of 7.36 Å, thus decreasing the polarization of the CO_2 molecules by the open-metal sites. It is noteworthy that this distance (Cu...O=C=O = 2.72 Å) is different from the distance observed from GCMC routine as in this case the cooperative effects from the other CO_2 molecules in the pores were not included. In fact, considering the mere moderate HOA (22-26 kJ/mol), the parallel to mean-plane orientation observed from the GCMC simulations seems to be the most probable. Also, this orientation most probably gets stabilized by the co-operative interactions between the CO_2 molecules in the pore. For a CO_2 to act as a pillar between two open-metal sites and to get activated, the metalmetal separation needs to be < 7.3 Å or there has to be cooperative interactions from other directions within a pore to place the trapped CO_2 molecule in a perfectly linear pillaring position.

4-II.4. Conclusions:

We have developed a new H-boned Um-MOF with good CO_2 capacity, Decent CO_2/N_2 selectivity and smooth CO_2 diffusion kinetics. The HOA observed for this material is quiet low compared to what was anticipated from the functionalization (benzimidazole and open metal site) present in it. This was further examined from a periodic DFT calculation.

4-II.5. References:

1. (a) https://climate.nasa.gov/vital-signs/carbon-dioxide/. (b) Inventory of U.S. Greenhouse Gas Emissions and Sinks: **1990–2015**. (c) Keith, D. W.; *Science* **2009**, *325*, 1654.
2. Rochelle, G. T.; *Science* **2009**, *325*, 1652.
3. (a) Herm, Z. R.; Swisher, J. A.; Smit, B.; Krishna R.; Long, J. R. *J. Am. Chem. Soc*. **2011**, *133*, 5664. (b) Samanta, A.; Zhao, A.; Shimizu, G. K. H.; Sarkar, P.; Gupta, R. *Ind. Eng. Chem. Res*. **2012**, *51*, 1438.
4. (a) Sircar, S.; Golden, T. C. *Sep. Sci. Technol*. **2000**, *35*, 667. (b) Ciferno, J. P.; Fout, T. E.; Jones, A. P.; Murphy, J. T. *Chem. Eng. Prog*. **2009**, *105*, 33.
5. Raksajati, A.; Ho, M. T.; Wiley, D. E. *Ind. Eng. Chem. Res*. **2013**, *52*, 16887.
6. Lin, L. -C.; Berger, A. H.; Martin, R. L.; Kim, J.; Swisher, J. A.; Jariwala, K.; Rycroft, C. H.; Bhown, A. S.; Deem, M. W.; Haranczyk, M.; Smit, B. *Nat. Mater*. **2012**, *11*, 633.
7. Ko, D.; Siriwardane, R.; Biegler, L. T.; *Ind. Eng. Chem. Res*. **2003**, *42*, 339.
8. (a) Huck, J. M.; Lin, L. -C.; Berger, A. H.; Shahrak, M. N.; Martin, R. L.; Bhown, A. S.; Haranczyk, M.; Reuterb, K.; Smit, B. *Energy Environ. Sci*. **2014**, *7*, 4132. (b) Mason, J. A.; Sumida, K.; Herm, Z. R.; Krishna, R.; Long, J. R. *Energy Environ. Sci*. **2011**, *4*, 3030, (c) Vaidhyanathan, R.; Iremonger, S. S.; Shimizu, G. K. H.; Boyd, P. G.; Alavi, S.; Woo, T. K. *Science* **2010**, *330*, 650. (d) Zhang, Z.; Yao, Z. -Z.; Xiang, S.; Chen, B. *Energy Environ. Sci*. **2014**, *7*, 2868. (e) Liao, P. -Q.; Chen, X. W.; Liu, S. -Y.; Li, X. -Y.; Xu, Y. -T.; Tang, M. -N.; Rui, Z. B.; Ji, H. -B.; Zhang, J. -P.; Chen, X. -M. *Chem. Sci*. **2016**, *7*, 6528. (f) Nugent, P.; Belmabkhout, Y.; Burd, S. D.; Cairns, A. J.; Luebke, R.; Forrest, K.; Pham, T.; Ma, S.; Space, B.; Wojtas, L.; Eddaoudi, M.; Zaworotko, M. J. *Nature* **2013**, *495*, 80. (g) Xiang, S.; He, Y.; Zhang, Z.; Wu, H.; Zhou, W.; Krishna, R.; Chen, B. *Nat. Commun*. **2012**, *3*, 954. (h) Fracaroli, A. M.; Furukawa, H.; Suzuki, M.; Dodd, M.; Okajima, S.; Gándara, F.; Reimer, J. A.; Yaghi, O. M. *J. Am. Chem. Soc*. **2014**, *136*, 8863. (i) Bhatt, P. M.; Belmabkhout, Y.; Cadiau, A.; Adil, K.; Shekhah, O.; Shkurenko, A.; Barbour, L. J.; Eddaoudi, M. *J. Am. Chem. Soc.* **2016**, *138*, 9301–9307. (j) Liu, J.; Tian, J.; Thallapally, P. K.; McGrail, B. P. *J. Phys. Chem. C* **2012**, *116*, 9575. (k) Kumar, A.; Hua, C.; Madden, D. G.; O'Nolan, D.; Chen, K. –J.; Keane, L. –A. J.; Perry IV, J. J.; Zaworotko, M. J. *Chem. Commun*.

2017, *53*, 5946. (l) Adil, K.; Belmabkhout, Y; Pillai, R. S.; Cadiau, A.; Bhatt, P. M.; Assen, A. H.; Maurin, G.; Eddaoudi, M. *Chem. Soc. Rev*. **2017**, *46*, 3402-3430.

9. (a) Nandi, S.; Collins, S.; Chakraborty, D.; Banerjee, D.; Thallapally, P. K.; Woo, T. K.; Vaidhyanathan, R. *J. Am. Chem. Soc*. **2017**, *139*, 1734–1737. (b) Nandi, S.; De Luna, P.; Daff, T. D.; Rother, J.; Liu, M.; Buchanan, W.; Hawari, A. I.; Woo, T. K.; Vaidhyanathan, R.; *Sci. Adv*. **2015**, *1*, e1500421. (c) Simmons, J. M.; Wu, H.; Zhou, W.; Yildirim, T.; *Energy Environ. Sci*. **2011**, *4*, 2177–2185.
10. (a) Lin, J. B.; Zhang, J.-P.; Chen, X. M. *J. Am. Chem. Soc*. **2010**, *132*, 6654. (b) Demessence, A.; Alessandro, D. M. D.; Foo, M. L.; Long, J. R. *J. Am. Chem. Soc*. **2009**, *131*, 8784–8786. (c) Poloni, R.; Lee, K.; Berger, R. F.; Smit, B.; Neaton, J. B. *J. Phys. Chem. Lett*. **2014**, *5*, 861. (d) Das, M. C.; Xiang, S.; Zhang, Z.; Chen, B. *Angew. Chem., Int. Ed*. **2011**, *50*, 10510. (e) Yang, L.; Chang, G.; Wang, D. *ACS Appl. Mater. Interfaces* **2017**, *9*, 15213. (f) Lee, H. M.; Youn, I. S.; Saleh, M.; Lee, J. W.; Kim, K. S. *Phys. Chem. Chem. Phys*. **2015**, *17*, 10925 (g) Collins, S. P.; Daff, T. D.; Piotrkowski, S. S.; Woo, T. K. *Sci. Adv*. **2016**, *2*, e1600954.
11. Kemmer, G.; Keller, S. *Nat. Protoc*. **2010**, *5*, 267–81.
12. Richter, E.; Schuetz, W.; Myers, A. L. *Chem. Eng. Sci.* **1989**, *44*, 1609–1616.
13. Myers, A. L.; Prausnitz, J. M. *AIChE J.* **1965**, *11*, 121–127.
14. Malek, K; Coppensa, M.-O. *J. Chem. Phys*. **2003**, *119*, 2801.
15. Do, D. D. Adsorption analysis and equilibria and kinetics, Imperial College Press, Ed. **2008**.
16. Chung, Y. G.; Gómez-Gualdrón, D. A.; Li, P.; Leperi, K. T.; Deria, P.; Zhang, H.; Vermeulen, N. A.; Stoddart, J. F.; You, F.; Hupp, J. T.; Farha, O. K.; Snurr, R. Q. *Sci. Adv.* **2016**, *2*, e1600909.
17. (a) Saha, D.; Bao, Z.; Jia, F.; Deng, S. *Environ. Sci. Technol*. **2010**, *44*, 1820. (b) Zhao, Z.; Li, Z.; Lin, Y. S. *Ind. Eng. Chem. Res*. **2009**, *48*, 10015. (c) Silva, J. A. C; Schumann, K.; Rodrigues, A. E. *Micro. Meso. Mater*. **2012**, *158*, 219.
18. Iota, V.; Yoo, C.-S. *Phys. Rev. Lett*. **2001**, *86*, 5922.
19. Valenzano, L.; Civalleri, B.; Chavan, S.; Palomino, G. T.; Areán, C. O.; Bordiga, S. *J. Phys. Chem. C* **2010**, *114*,11185.

4-II.A. Appendix for Chapter 4-II

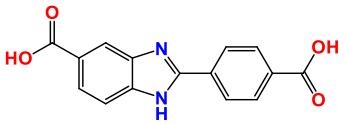

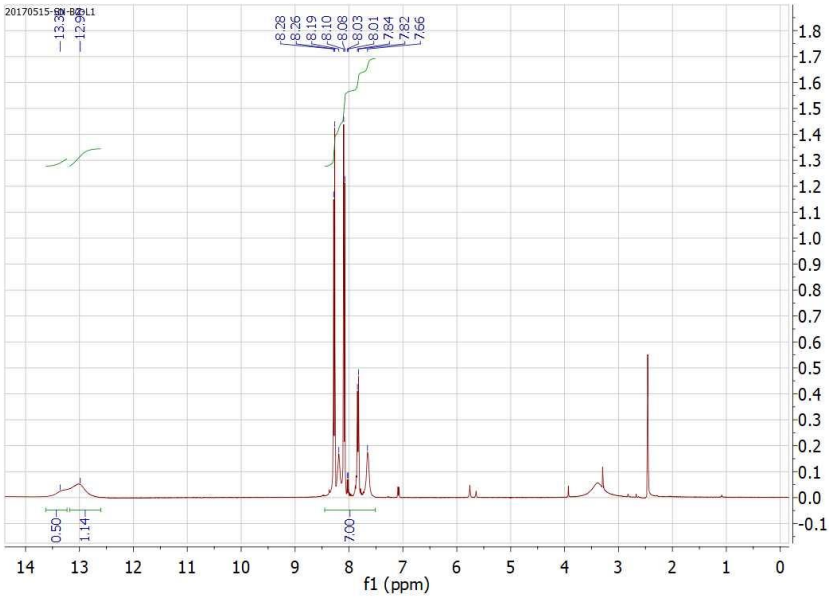

Figure 4-II.A.1. ^{1}H NMR of ligand showing the characteristics signals. The signal around 2.5 and 3.5 ppm is due to d6-DMSO and H_2O.

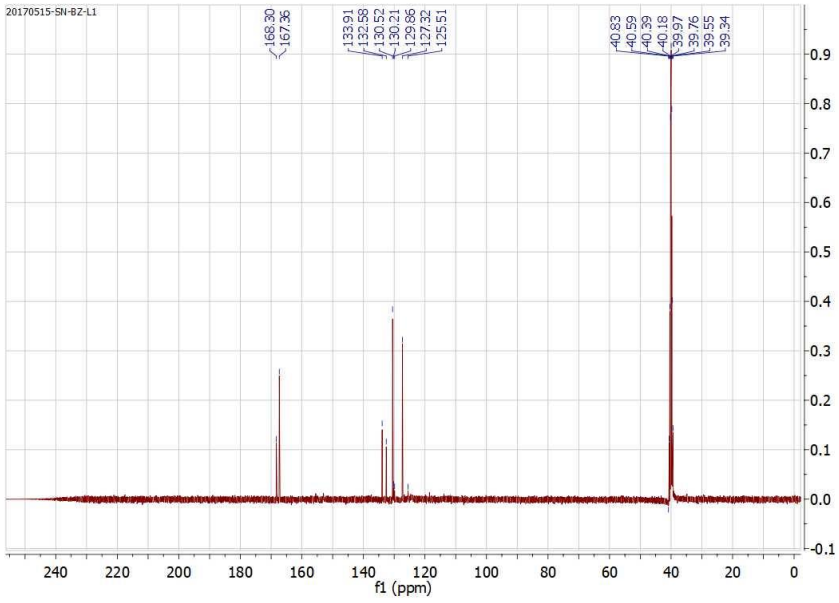

Figure 4-II.A.2. ^{13}C NMR of ligand showing the characteristics signals. Signal around 40 ppm is due to d6-DMSO.

Single Crystal Structure Analysis:

Cell parameters: Orthorhombic; a= 20.8093(11); b= 9.7634(5); c= 25.2583(11) Å; Sp. Gr. Cmca.

Crystallographic Structure of IISERP-MOF20:

The asymmetric unit consists of a $Cu^{(II)}$ centre coordinated by the carboxylate oxygens of the ligand and a terminal water molecule. Each layer is built from the linking of the Cu_2 dimers by the ligands. Now, the two $Cu^{(II)}$ centres in a dimer are related by a reflection produced by a c-glide. Further, a combination of this c-glide and a a-glide perpendicular to it shifts the Cu_2 dimers from the adjacent layers by 1/2 unit cell along the a- and c-direction. This gives rise to a mirror 'm' perpendicular to both a and c-glide planes. These three major symmetry elements constituting the 'Cmca' space group arrange the dimers between the adjacent layers, while their linking by the ligands related by the same symmetry operations, result in the rhombic-shaped channels along the b-direction (7.63 x 7.63 Å). In fact, if the layers had adopted a perfectly eclipsed configuration in a higher symmetry, the pore apertures would have dimensions 4 times this. However, a framework with such large aperture may not be stable.

From the electron counts per unit cell obtained for the unassigned electron density in the pore using the squeeze routine the formula was determined to be $Cu(C_{15}H_8N_2O_5).(DMF)_{1.5}(EtOH)_{1.5}$. This matches well with the composition expected based on the weight losses from the TGA.

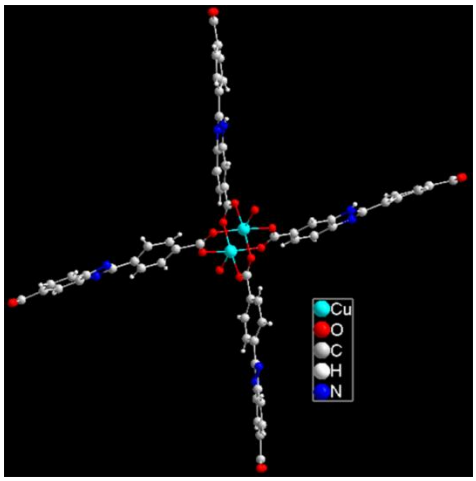

Figure 4-II.A.3. Basic building unit (Cu_2 paddel wheel) present in IISERP-MOF20. Each Cu is penta-coordinated. Out of the five coordinations, four are satisfied by oxygen atoms of the carboxylate unit and the fifth one is satisfied by a water molecule.

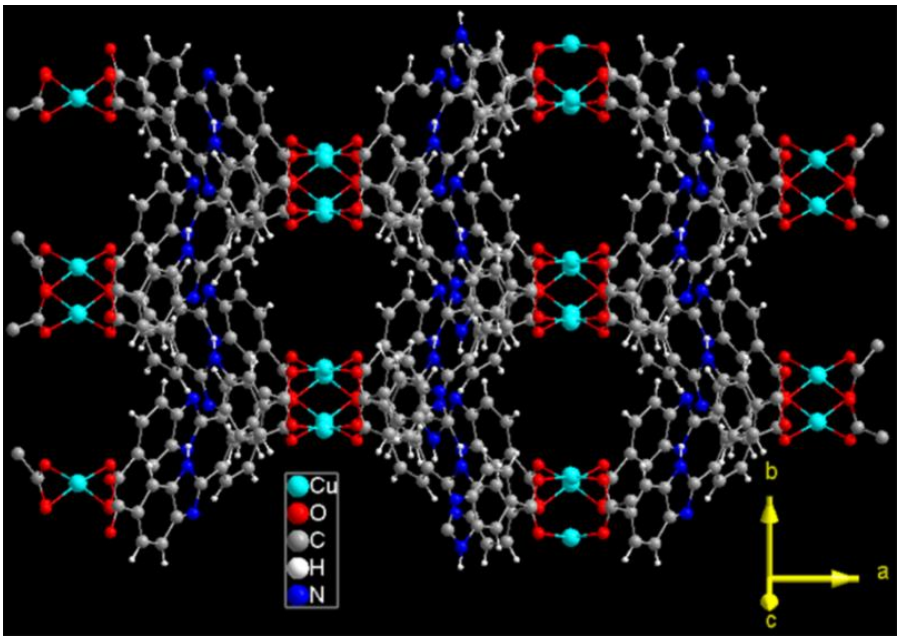

Figure 4-II.A.4. Three dimensional view of the crystal structure along 011 plane.

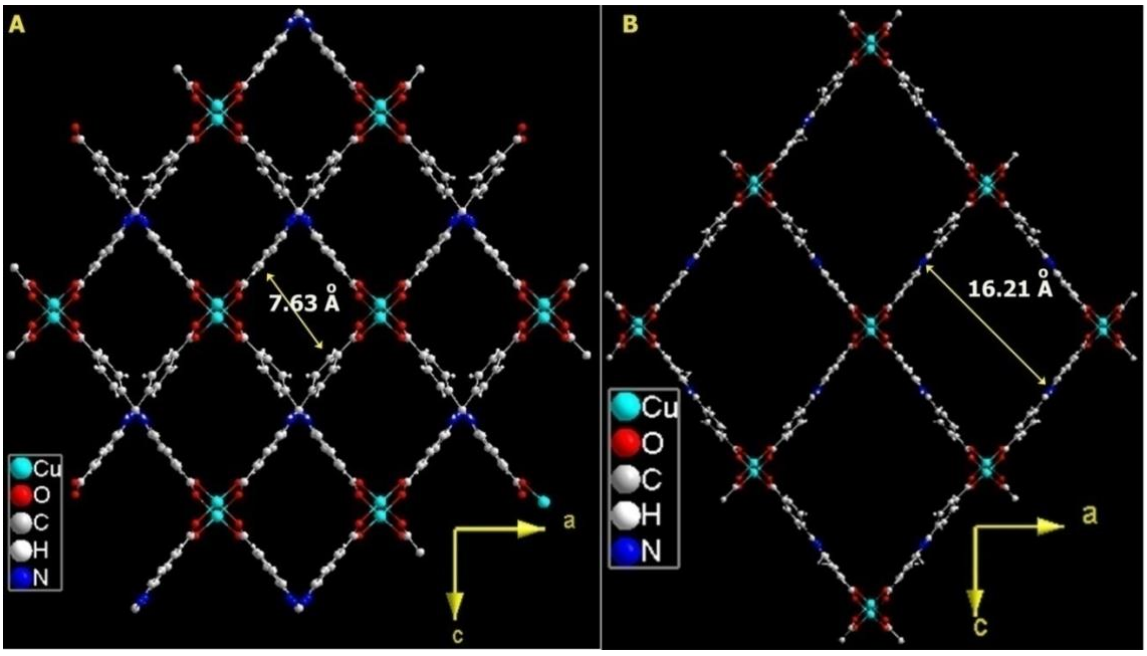

Figure 4-II.A.5. (A)Three dimensional view of the crystal structure along b- axis. There is a half-a-unit cell shit along a- and c- directions and a 90° rotation between the adjacent layers- ABAB... stacking. This generates one dimensional channel along b-axis. (B) Three dimensional view of a single layer along the same crystallographic axis.

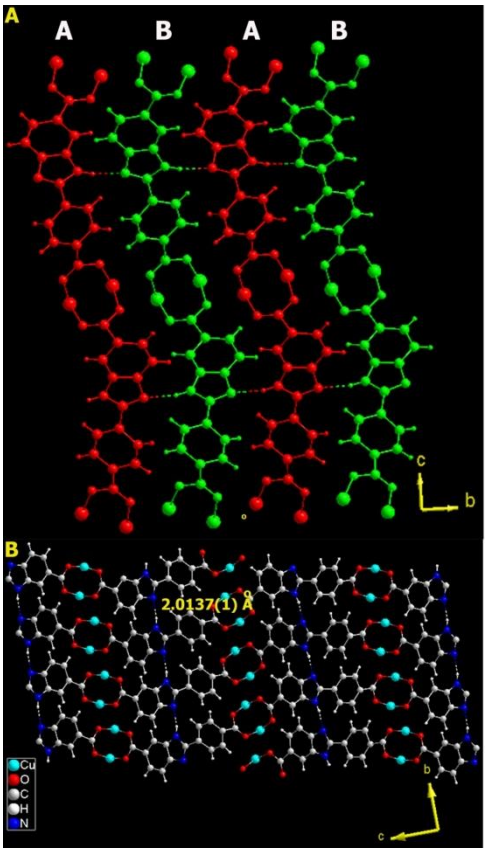

Figure 4-II.A.6. (A) Different layers of IISERP-MOF20 stacked in a ABAB... arrangement. (B) Adjacent layers are held together by strong N-H.....N type hydrogen bonds (distance is 2.0137 Å).

Analytical Characterization:

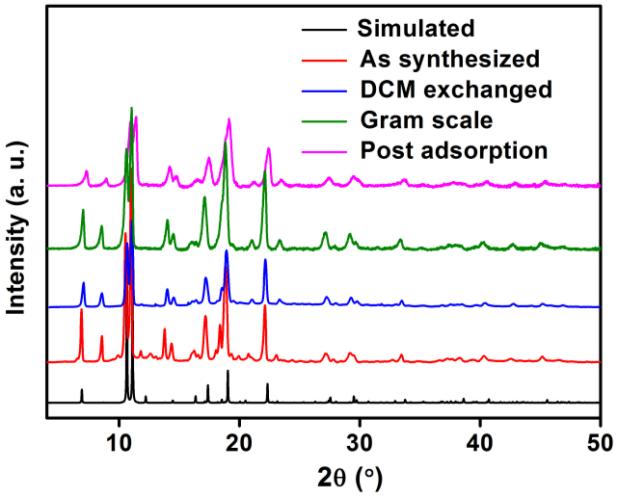

Figure 4-II.A.7. A comparative PXRD plot showing the bulk purity and stability of IISERP-MOF20. Note: This material can be scale up to 1 gram in a single synthesis.

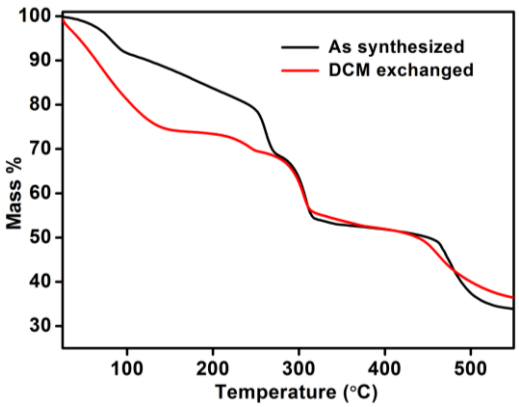

Figure 4-II.A.8. TGA plot carried out using the as synthesized and DCM exchanged IISERP-MOF20.

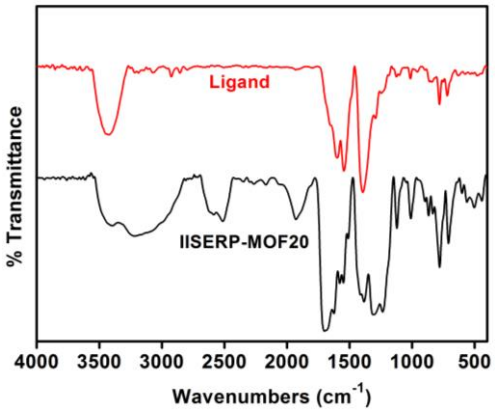

Figure 4-II.A.9. (A) IR spectra of IISERP-MOF-20 and the ligand showing different stretching frequencies.

Gas Sorption Analysis:

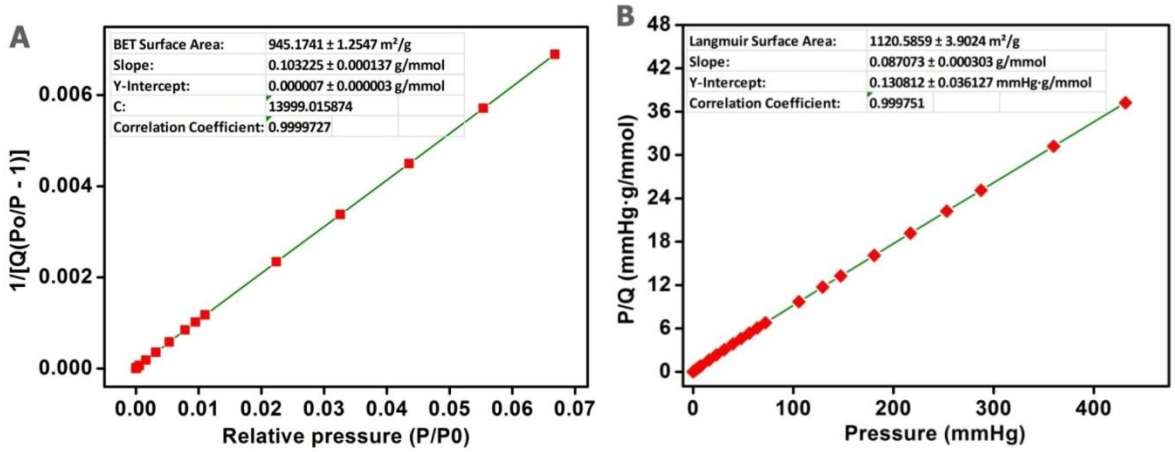

Figure 4-II.A.10. (A) BET fits of IISERP-MOF-20 from the 77 K N_2. (B) Langmuir fits for IISERP-MOF-20 from the 77 K N_2.

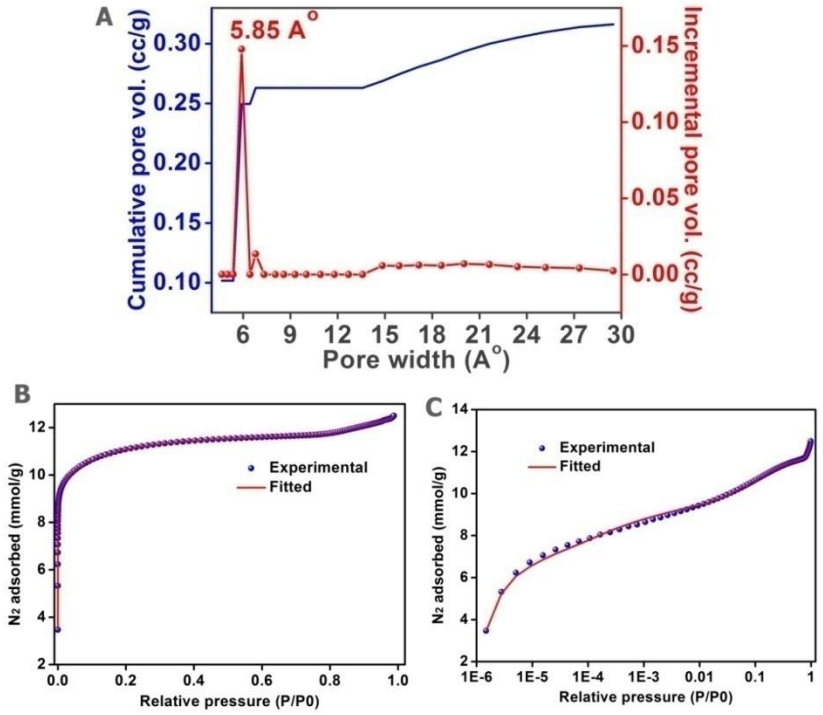

Figure 4-II.A.11. (A) Pore size distribution in IISERP-MOF20 obtained by fitting the NLDFT model to the 77 K N_2 adsorption branch. Note the average pore diameter of 5.85 Å was obtained from the fit. This agrees well with the pore dimension observed from the single crystal structure. (B) Shows the fitting comparison for IISERP-MOF20 obtained for the NLDFT fit done to the adsorption branch of the 77 K N_2 adsorption data. (C) Log plot of the NLDFT fit obtained from N_2 77 K isotherm.

IAST Fitting Parameters for* IISERP-MOF20 *(CO_2/N_2):

273 K

Gas A =CO_2

Gas B = N_2

Gas Mixture			
YA =	0.15		
YB =	0.85		
Gas Constants	A	Gas B Constants	
qA1 =	7.033817008	qA1 =	0.22183339
qA2 =	0	qA2 =	0
kA1 =	0.003978057	kA1 =	0.00032006
kA2 =	0	kA2 =	0
na1 =	0.893837211	na1 =	1
na2 =	0	na2 =	0
HA1 =	0.027980922	HB1 =	7.0999E-05
HA2 =	0	HB2 =	0

298 K

Gas Mixture			
YA =	0.15		
YB =	0.85		
Gas A Constants		Gas B Constants	
qA1 =	7.017176072	qA1 =	0.2829213
qA2 =	0	qA2 =	0
kA1 =	0.0012786	kA1 =	9.6344E-05
kA2 =	0	kA2 =	0
na1 =	0.95174041	na1 =	1
na2 =	0	na2 =	0
HA1 =	0.008972158	HB1 =	2.7258E-05
HA2 =	0	HB2 =	0

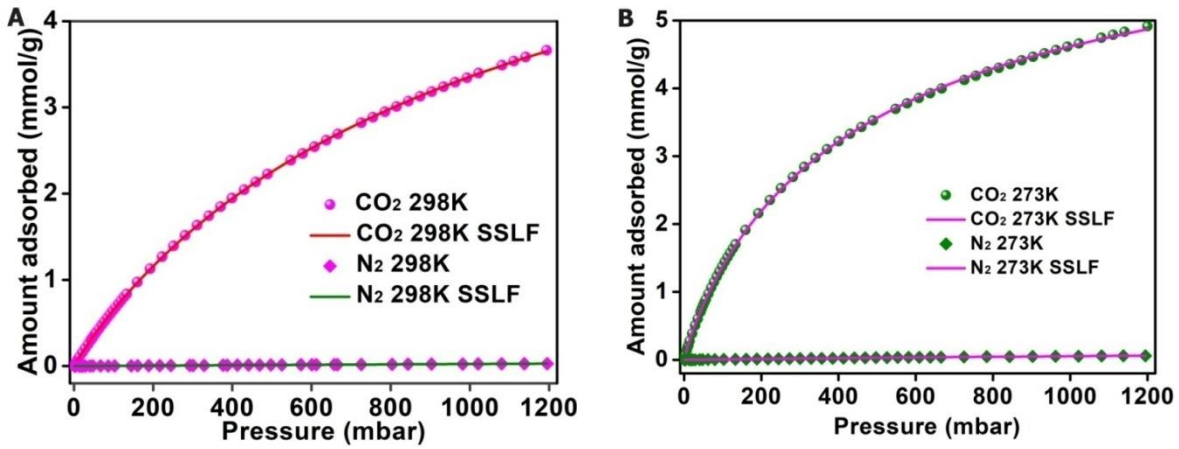

Figure 4-II.A.12. *IAST* fitting of CO_2, and N_2 isotherms for IISERP-MOF20 collected at 298 K (A) and 273 K (B).

Virial Analysis:

The CO_2 adsorption data were measured from 0- 1bar at 298, 283, 273, 263 K and 195K. For virial fitting the 298, 283, 273 and 263 K isotherms were chosen and fitted by the virial equation as follows.

$$ln(P) = ln(Va)+(A0+A1*Va +A2*Va^2 \ldots + A6*Va^6)/T+(B0+B1*Va) \quad (1)$$

Where P is pressure, Va is amount adsorbed, T is temperature, and A0, A1, A2 … , A4 and B0, B1are temperature independent empirical parameters.

Table 4-II.A.1: Summary of the fitted Virial parameters for IISERP-MOF20**.**

A0	-3121.307438	B0	15.36861015
A1	92.02889325	B1	-0.114778127
A2	11.80220901	B2	-0.027625476
A3	0.225989127		

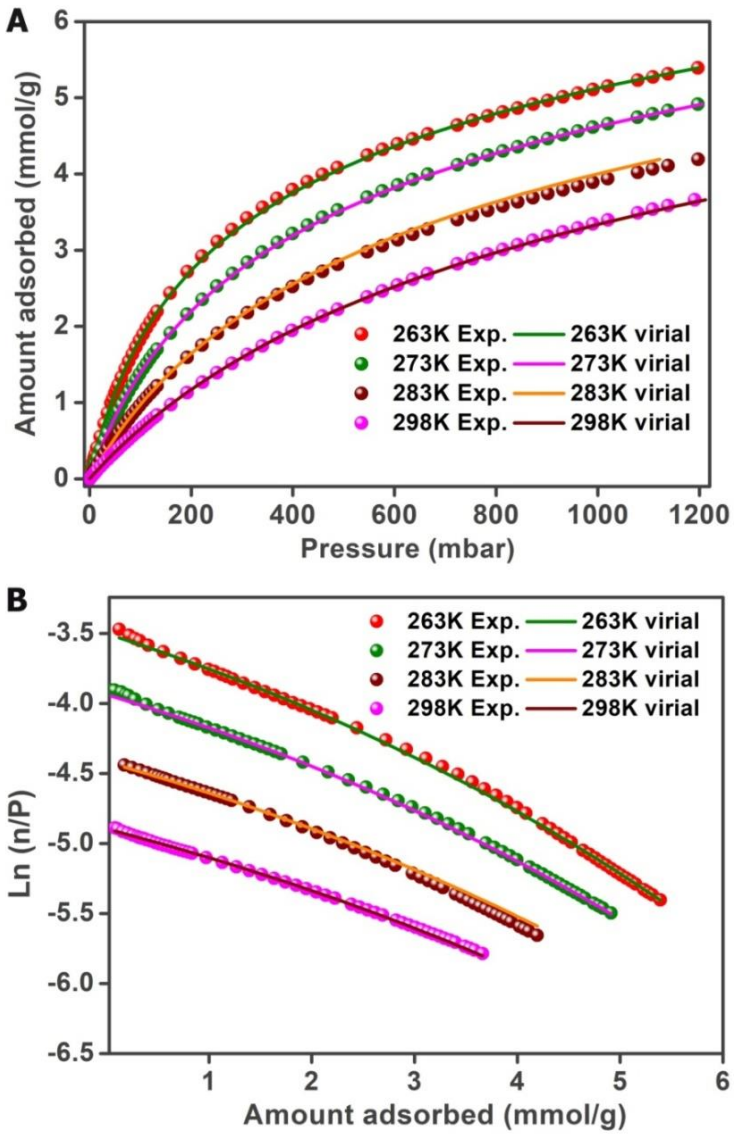

Figure 4-II.A.13. (A) Comparison of experimental isotherms of IISERP-MOF20 to the ones obtained from virial modelling carried out using CO_2 isotherms collected at 298, 283, 273 and 263 K. (B) Virial plots of IISERP-MOF20 carried out using CO_2 isotherms collected at 298, 283, 273 and 263 K.

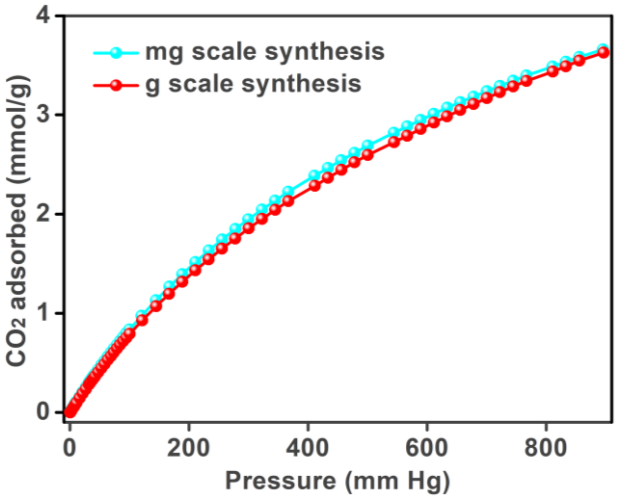

Figure 4-II.A.14. CO_2 adsorption isotherm (at room temperature) of mg scale and g scale synthesis.

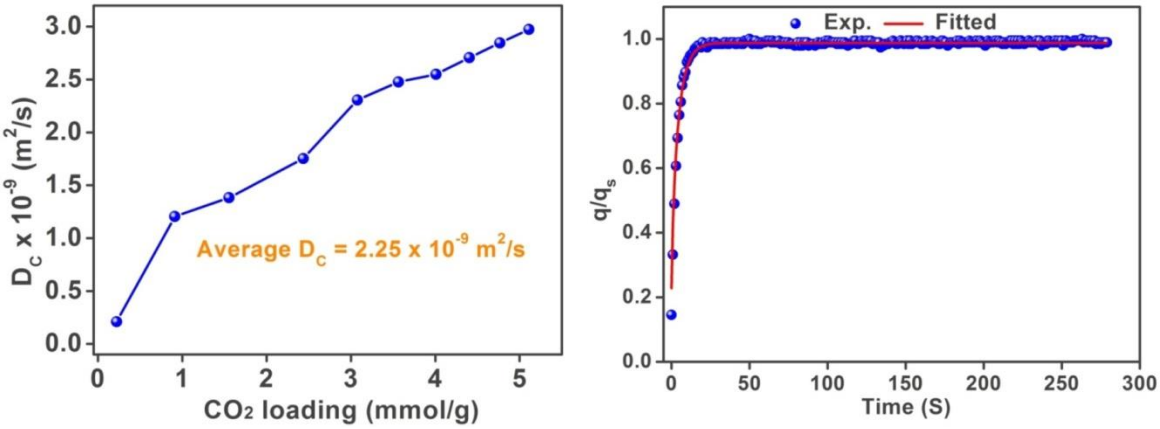

Figure 4-II.A.15. (**Left**) CO_2 self diffusion coefficient in IISERP-MOF20 calculated from kinetics measurement. (**Right**) Representative plot of the adsorbate fractional filling vs. time showing the fit between the spherical model (line) and the collected data (spheres) obtained from the single component CO_2 isotherm of IISERP-MOF20 (loading = 10 cc/g). Note 10 such fittings were considered to obtain the average diffusion coefficient.

Computational Calculation:

The computational calculations have been carried out using Material Studio program V.6.0. The calculations were done employing a 2x2x2 super cell. The number of CO_2 molecules for this 2x2x2 unit cell has been calculated from the experimental saturation capacity (195 K CO_2 isotherm) to be 200. For the binding site location, the framework was frozen and the CO_2 molecules were allowed to find the most-probable positions using the Simulated Annealing program based on the Grand Canonical Monte-Carlo routine. An automated temperature control and Universal force field were used with about 100000 steps

per cycle. Energy distribution, density and energy field were all optimized. The CO_2 positions were obtained from the lowest energy configuration have been shown in figure 4-II.A.16.

The periodic DFT calculation was carried out using the unit cell using the CASTEP programme. For these, the Ultrasoft pseudopotentials with a plane wave basis cut-off of 400eV was employed and the LDA-CA-PZ functional was used. All calculations were performed on the unit cell. During this calculation the metal organic layers were constrained to make the inter-layer Cu_2 paddlewheel dimers to be spaced exactly at the same distance as obtained from the single crystal X-ray structure (7.36 Å). Importantly, no other CO_2 molecules (from the GCMC) were introduced other than the CO_2 molecules proximal to the open metal site.

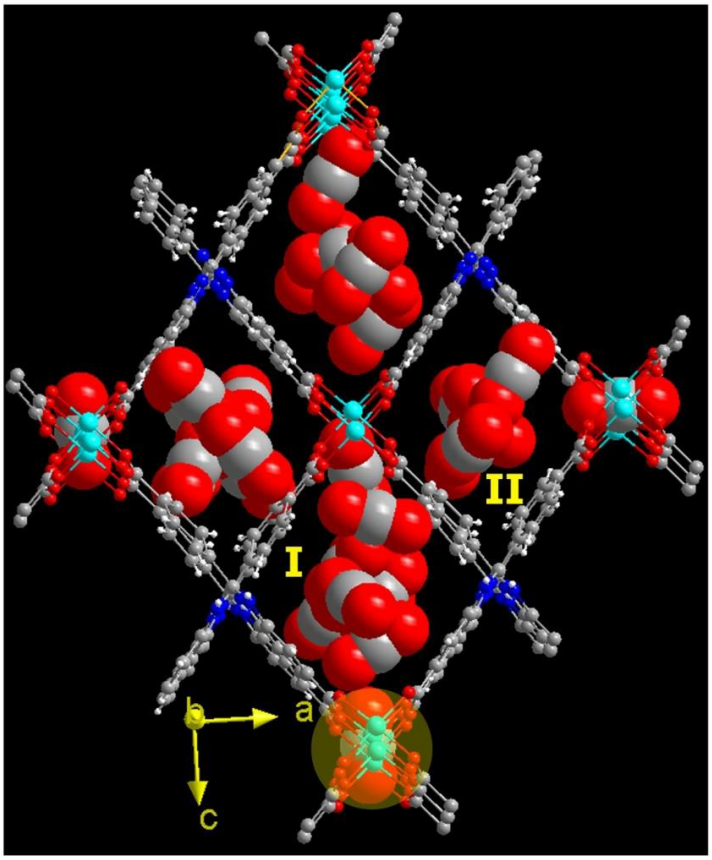

Figure 4-II.A.16. The most-probable positions for CO_2 in IISERP-MOF20 obtained from the simulated annealing routine. The two different channels with different orientations of CO_2 have been labelled as I and II.

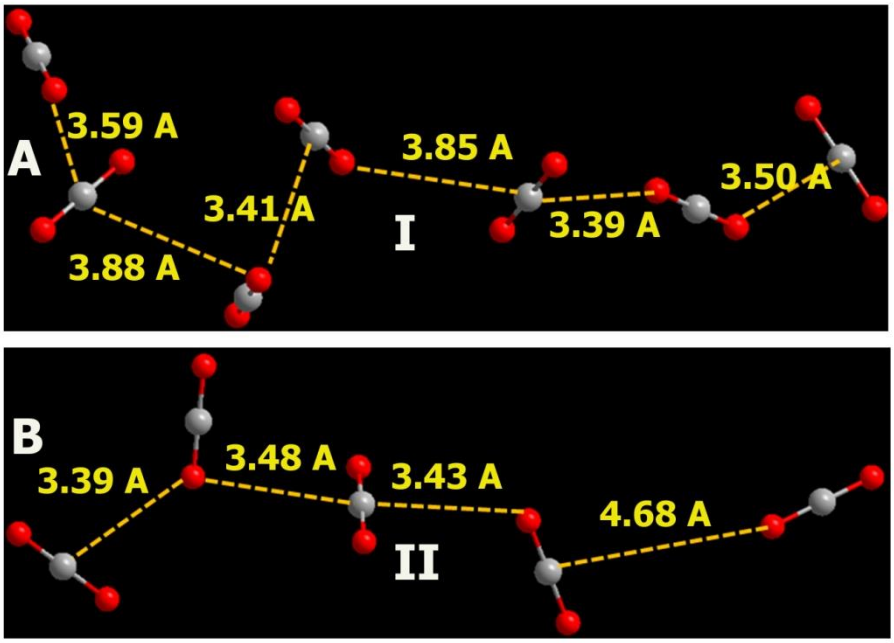

Figure 4-II.A.17. Orientation and distances between cooperatively interacting CO_2 molecules inside the pore (labelled as I and II in the Fig. 4-II.A.16.) of IISERP-MOF20.

Chapter 5

Gas and Pressure Dependent Porosity into a Non-porous Solid via Coordination Flexibility

5.1. Introduction:

Solids with metal-organic links provide an excellent platform to play around with the coordination, electronic, magnetic properties of the metal and at the same time provides means to access more by functional tuning of the organic ligands.[1-3] Stability and rigidity in a framework go in concert while the dynamic character in most cases is associated with flexible organic linkers.[4] This flexibility of organic linkers has rendered some metal organic frameworks as soft porous materials.[5-10] Such dynamic frameworks in an extended solid has been placed as an important feature for guest encapsulation favoring separation,[11-22] storage,[23-24] sensing[25-26] and biomedical application.[27-29]

Generally, the interactions of gases with organic or metal-organic frameworks are of the order of 20 to 50 kJ/mol, which is lower in comparison to those exhibited by solvents, for example, water (45-65 kJ/mol). However, such interactions can co-operatively posses sufficient energy, even at extremely low partial pressures, to cause significant modifications on the structure by manipulating specific sites of the ligand. A good example of such a structural change includes the gate-opening or breathing phenomenon observed in microporous metal organic frameworks.[4, 6, 11, 19, 20, 30-32] This has been witnessed both at low and high pressure adsorptions. Such pressure-controlled opening up of porosity makes these materials operate like a switch or a transducer to detect specific gases present above or below certain partial pressures. When they occur at larger pressures, the very phenomenon could provide good stimuli responsive smart separation membranes. Usually, such gate openings are associated with soft-porous frameworks built up from relatively long and/or flexible linkers. [3, 4, 14, 16, 22, 23, 33-34] Large structural change is observed in the x-ray and neutron diffractions upon gate opening via breathing mechanisms. Most importantly, the flipping of the carboxylate bonds of the BDC units in MIL-53 series happens only at elevated temperatures making it a thermo-mechanical process.[35] The breathing in metal (hydroxy) carboxylate framework, MIL-53 is due to the strong CO_2 interactions with corner-sharing μ^2-OH groups, which has a significant electrostatic part to it.[30] A thorough look into the literature would reveal there are many structures with μ^2 or μ^4-oxo anions compared to those with bridging hydroxyl groups; this means the introduction of such hydroxyl groups, capable of creating breathing behavior, by design is a challenge. The oxo anion based clusters do not seem to favor the CO_2 assisted breathing.[36-41]

Another type of gate opening is the molecular-rotating gate [4] where the rotation of the aryl rings acts as a gate; only a limited number of such examples exist. Kitagawa and co-workers [42] reported a layered-pillared structure where the aryl ring could rotate as a function of hydration. Unfortunately, in this particular case, the dehydration and the concurrent gate opening results in a decrease of porosity. More recently, Schroder and co-workers on the basis of grand canonical Monte Carlo simulations, powder XRD (PXRD), and IR experiments, concluded that the pyridyl rings in their linkers rotate in the presence of CO_2 to open the channels.[18]

In most cases, the breathing behavior is triggered by solvents. [9, 16, 17, 20, 33, 35, 43-45] Few cases are reported wherein just a gas is able to do it. [11, 19, 22, 46] Except for the Schroder's case,[18] all these breathing behaviors under a purist's argument are lattice changes and not necessarily a molecular motion causing a gate opening. Also, they all have made a porous framework into a more open or less open framework. However, accessing the porosity of a completely dense MOF build from very small linkers via gate opening is highly challenging and extremely rare. Though the gate-opening or breathing in such systems has been investigated, [47] a systematic tuning of coordination flexibility in a family of MOF and the resulting gating is not known, particularly in ultra-microporous MOFs.

Ultra-microporous networks constructed from small ligands tend to be rigid, while flexible porous networks, typically built from longer linkers, tend to be 'soft porous material'. So having a porous system that is flexible or dynamic and rigid is rare. Herein we report three MOFs, $M(4\text{-}PyC)_2$ (where M= Mg/Mn/Cu; 4-PyC = 4-pyridylcarboxylate aka isonicotinate) out of which the former two shows CO_2 specific gate opening and the later does not show any such features. Importantly, the non-porous framework of the Mg and Mn phases open-up into an ultra-microporous one at a low partial pressure of CO_2. In fact, we have exploited the concept of hard-soft acid-base (HSAB) theory by utilizing the metal as a hard Lewis acid and the organic ligand serving as a borderline hard base to aptly tune their coordination strengths. This introduces coordination flexibility assisted CO_2-specific gate-opening that converts an otherwise non-porous material into an ultra-microporous material with a nominal surface area (~400 m^2/g) along with exceptional CO_2 selectivity. The CO_2 adsorption data suggests there are two gate opening events that occur with minimal changes in the crystal lattice of the material. An isomorphous metal replacements study has been carried out to gain insights into

the contribution coming from the hard-soft character of the metal and ligand towards the gate opening.

5.2. Material and Methods:

All the chemicals were bought from Sigma Aldrich and used without further purification.

5.2.1. Milligram Scale Synthesis:

Synthesis of Mg 4-PyC (IISERP-MOF21):

A solvothermal reaction between magnesium acetate tetra hydrate (0.215 g; 1 mmol) and pyridine-4-carboxylic acid (0.244 g; 2 mmol) in a solution containing 5 ml dimethylformamide (DMF) + 3 ml acetonitrile was carried out at 120^{o}C for 72 hrs. Colorless cube shape crystals were isolated by filtration and were washed with plenty of methanol and acetone. The air dried sample gave a yield of ~ 85% (based on Mg). The PXRD pattern indicated this to be a pure phase of IISERP-MOF21. We have also prepared 10-25 gms of this sample with an easy scale-up procedure. CHN analysis (calculated values within brackets): C: 53.41 (53.15); H: 4.03 (3.80); N: 11.20 (11.48) %. Though it was made in DMF medium, it could be exchanged in a post-synthetic manner with DCM, or it can be directly activated at 160ºC under vacuum. Also, the use of dimethylacetamide (DMA) instead of DMF led to the same phase.

Synthesis of Mn 4-PyC (IISERP-MOF22):

A solvothermal reaction between manganese acetate tetra hydrate (0.245 g; 1 mmol) and pyridine-4-carboxylic acid (0.244 g; 2 mmol) in a solution containing 5 ml DMF + 3 ml acetonitrile was carried out at 120^{o}C for 72 hrs. Colorless rod shape crystals were isolated by filtration and were washed with plenty of methanol and acetone. The air dried sample gave a yield of ~ 85% (based on Mn). The PXRD pattern indicated this to be a pure phase of IISERP-MOF22. We have also prepared 10-25gms of this sample with an easy scale-up procedure. CHN analysis (calculated values within brackets): C: 48.58 (48.30); H: 3.66 (3.45); N: 10.26 (10.43) %. Though it was made in DMF medium, it could be exchanged in a post-synthetic manner with DCM, or it can be directly activated at 160ºC under vacuum. Also, the use of DMA instead of DMF led to the same phase.

Synthesis of Cu 4-PyC (IISERP-MOF23):

A solvothermal reaction between copper acetate mono hydrate (0.200 g; 1 mmol) and pyridine-4-carboxylic acid (0.244 g; 2 mmol) in a solution containing 2 ml DMF + 2 ml ethanol + 3 ml tetrahydrofuran was carried out at 110^{o}C for 72 hrs. Blue color cube shape crystals were isolated by filtration and were washed with plenty of methanol and acetone. The air dried sample gave a yield of ~ 80% (based on Cu). The PXRD pattern indicated this to be a pure phase of IISERP-MOF23. CHN analysis (calculated values within brackets): C: 49.22 (48.91); H: 3.21 (3.52); N: 7.90 (8.15) %. Though it was made in DMF medium, it could be exchanged in a post-synthetic manner with DCM, or it can be directly activated at 140^{o}C under vacuum. Also, the use of DMA instead of DMF led to the same phase.

10gm scale synthesis:

Synthesis of Mg 4-PyC:

About5.33 g of magnesium acetate anhydrous was added to 6.08 g of 4-PyC in a solution containing 40 ml DMF + 30 ml acetonitrile; contents were stirred for 2.5 hrs at room temperature. Contents were placed in a 123 ml Teflon-lined Parr stainless steel autoclave and heated at 130^{o}C for 72 hrs. Colorless polycrystalline product identical in appearance to the small scale preparation was obtained. The air dried sample gave a yield of ~81% (based on Mg).

Synthesis of Mn 4-PyC:

About 6.10 g of magnesium acetate anhydrous was added to 6.08 g of 4-PyC in a solution containing 40 ml DMF + 30 ml acetonitrile; contents were stirred for 2.5 hrs at room temperature. Contents were placed in a 123 ml Teflon-lined Parr stainless steel autoclave and heated at 130^{o}C for 72 hrs. Colorless polycrystalline product identical in appearance to the small scale preparation was obtained. The air dried sample gave a yield of ~80% (based on Mn).

5.2.2. Single Crystal Structure Determination:

Single-crystal data was collected on a Bruker SMART APEX four-circle diffractometer equipped with a CMOS photon 100 detector (Bruker Systems Inc.) and with a Cu Kα radiation (1.5418 Å). The incident X-ray beam was focused and monochromated using Microfocus (IμS). Crystals were mounted on nylon Cryo loops with Paratone-N oil. Data were collected at 100(2) K. Data was integrated using Bruker SAINT software and was corrected for absorption using SADABS. The structure was solved by Intrinsic Phasing

module of the direct methods and refined using the SHELXTL 97 software suite. All non-hydrogen atoms were located from an iterative examination of difference F-maps following which the structure was refined using the least-squares method. Hydrogen atoms were placed geometrically and placed in a riding model.

5.2.3. Analytical characterizations

Powder X-ray Diffraction:

Powder XRDs were carried out using a Rigaku Miniflex-600 instrument and processed using PDXL software.

Thermo Gravimetric Analysis:

Thermogravimetry was carried out on NETSZCH TGA-DSC system. The routine TGAs were done under N_2 gas flow (20 ml/min) (purge + protective) and samples were heated from RT to 550°C at 2 K/min.

For the cycling experiments, no protective gas was used, and the gas flows were systematically switched between CO_2 and N_2 on the purge lines. The DCM exchanged and activated (160°C, 15 hrs) sample of IISERP-MOF21 was loaded on to the Pt pans and evacuated for 5 hrs prior to the runs. TGA and DSC calibration and base-line corrections runs were done before carrying out the cycling experiments.

Infrared (IR) Spectroscopy:

IR spectra were obtained using a Nicolet ID5 attenuated total reflectance IR spectrometer operating at ambient temperature. The KBr pellets were used as background blanks.

5.2.4. Adsorption Analysis:

All gas sorption isotherms were measured on a Micromeritics ASAP 2020HD or 3-FLEX instrument using ultra-high purity gases (≥ 4.8 grade). Samples were transferred to a glass tube for analysis, with dual stage activation: The as-made samples were solvent exchanged by soaking 200 mg in 7 ml DCM (reagent grade) for 24 hours, with the solvent being replenished every 6hrs. Following this, about 100 mg of the solvent exchanged sample was transferred to an analysis glass vial and evacuated at 180ºC on the degas port for 36 hrs (10^{-6} mbar), at which point the outgas rate was ≤ 2 μbar/min.

The rate of adsorption experiments were carried out on the Micromeritics ASAP2020HD instrument equipped with a ROA software capabilities. Numerous equilibrium points and associated kinetic data were recorded at 273 K. For data analysis, regularly spaced 10 CO_2 loading points were picked in the interval of 0 to 1000 mbar.

Self-diffusion Coefficient CO_2 in IISERP-MOF21:

Diffusion coefficient determination from Rate of Adsorption (ROA) studies: For this purpose, a high-resolution rate of adsorption measurement was performed using the ASAP 2020HD instrument in the pressure range of 0-1 bar. The diffusion coefficient (Dc) was calculated as a function of CO_2 loading. 10 different adsorption points were used and each of the ROA data was fitted to spherical pore model [48, 49]. The fittings were done using Excel equipped with solver programme.

$$F = 1 - \frac{6}{\pi^2} \sum_{n=1}^{\infty} \frac{1}{n^2} \text{Exp}\left(-n^2 \pi^2 \tau\right)$$

F = fractional uptake; τ = non-dimensional time given by $\tau = D_t/R^2$, where R= particle size; t= time (secs); D = apparent diffusivity.

5.3. Results:

5.3.1. Single Crystal Structure Analysis:

Materials were synthesized via a solvothermal reaction between $M(acetate)_2$ (M= Mg/Mn/Cu) and 4-pyridine carboxylic acid (4-PyC) in a DMF/Acetonitrile or DMF/EtOH/THF mixture by heating at 110-120°C for 72 hrs (*See synthesis section*). The $Mg(4\text{-PyC})_2$, IISERP-MOF21 and $Mn(4\text{-PyC})_2$, IISERP-MOF22 were scaled up to 10 g in our laboratory synthesis. Also, they are isostructural. Whereas $Cu(4\text{-PyC})_2$, IISERP-MOF23 is slightly different from the other two. Hence, we are explaining the structure of IISERP-MOF21 as a representative. Structure of IISERP-MOF21, is a cubic three-dimensional lattice (α- Po type) built up from the linking of Mg centers by 4-PyC aka isonicotinate (Fig. 5.1). There are two crystallographically unique Mg centers which are connected by the μ^{-2} bridging carboxylate units to form chains, where the Mg(1) and Mg(2) alternate within the chain. Four such chains running along the a-axis and placed on the bc-plane in a square lattice disposition are further connected by 4-PyC units to form a 3-D cubic topology. Alternate 4-PyC rings are rotated by ~90° with respect to each other which only leaves an ultra-microporous 1-D channel along the a-axis (5.5 x 6.5 Å, not factoring the van der Waals radii, Figs. 5.1 and

5.A.1). The c- and b-axes do not contain any pores or channels. These 1-D channels are occupied by DMF guest molecules.

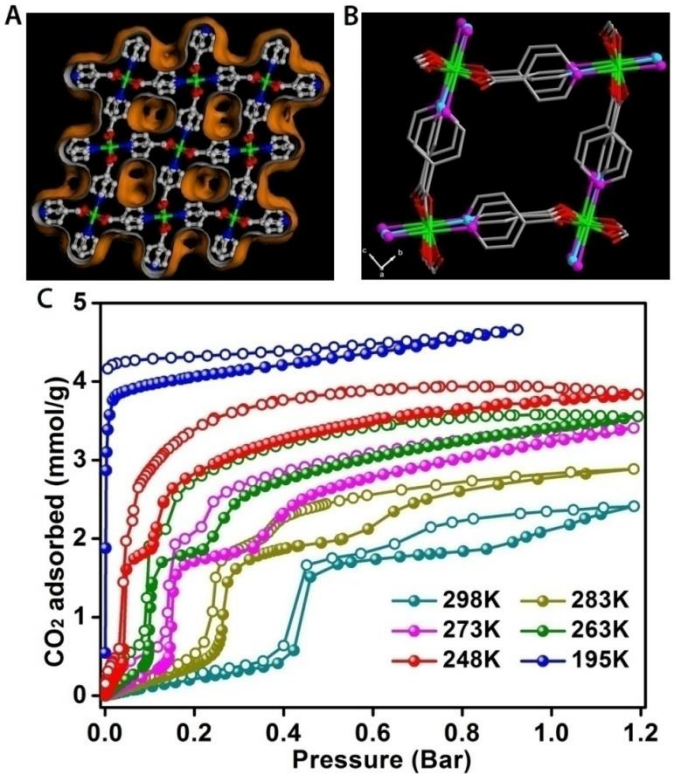

Figure 5.1. (A) Experimentally determined single crystal structure of Mg 4-PyC with its Connolly surface represented. The Mg centers are linked by 4-PyC units that form a cubic three-dimensional lattice. Color scheme: Green-Mg; Grey-C; Blue-N; Red-O. Hydrogens are omitted for clarity. (B) A single channel has been shown, and the pyridyl nitrogens have been color coded to indicate the presence of two different Mg-N distances within the lattice. The purple ones have Mg(1)-N distance = 2.22 Å, and the cyan ones have the Mg(2)-N bond distance = 2.20 Å. Both Mg(1) and Mg(2) bind to carboxylate oxygens strongly (av. Mg-O distance = 2.05 Å). (C) CO_2 adsorption-desorption isotherms (closed and open symbols, respectively) collected at different temperatures.

5.3.2. Bulk Characterization and Gas Adsorption Studies:

Considering the presence of just an ultra-microporous 1-D channel (Fig. 5.1A), we expected this material to be non-porous or to have negligible porosity. Accordingly, the 77 K and 298 K N_2 adsorption showed no gas uptake; however, the 195 K and 298 K CO_2 adsorption showed saturation uptakes of 4.7 mmol/g and 2.42 mmol/g, respectively. In this ultra-microporous framework of IISERP-MOF21, built from short linkers, CO_2 gas is capable of generating a stepped isotherm showing an abrupt increase in pore accesses (Fig. 5.1C). This increase in CO_2 uptake occurs at two different pressure points and is observed only for CO_2. In IISERP-MOF21, at 273 K, there is no significant porosity before the abrupt increase in CO_2 uptake at 0.1 bar. Typically, breathing MOFs have some initial porosity and the

desolvation (activation) causes the framework to adopt a more open structure with increased uptake.[11-24] However, in IISERP-MOF21, this is not the case. What we observe here is likely to be a gating phenomenon. [4, 18, 42] With this interpretation, at 273 K, with a CO_2 pressure of 0.1 bar the uptake jumps-up from 0.3 mmol/g to 1.7 mmol/g, indicating the first gate opening (Fig. 5.1C). As the CO_2 pressure is further increased to 0.3 bar, the uptake again jumps-up from 1.8 mmol/g to 2.6 mmol/g, indicating second gate opening (Fig. 5.1C). The gate opening is persistent across different temperatures (298, 283, 273, 263 and 248 K), however, the pressure at which both gate openings occur moves to lower values as the temperature decreases. Additionally, the pressure difference between the two gate opening points becomes smaller as the temperature decreases. At 195 K the trend suggests that the gate is already fully opened at very low pressures.

To ascertain if these gate openings are assisted by any temperature effects, variable temperature PXRD measurements were carried out in the temperature range of 303 to 548 K under 10^{-3} vacuum as shown in figure 5.2A. The PXRD plots indicated lack of any major structural changes. The (011) peak does shift from 2θ of 11.0 to 11.35° as the temperature reaches ~445 K indicates a slight structural contraction likely due to loss of DMF. The same peak then shifts back to lower angles as the temperature is raised beyond 445 K, likely due to lattice expansion. Above this temperature, the crystallinity remains intact even until 548 K. This is in agreement with the exceptional thermal stability (up to 450 °C) observed from the TGA (Fig. 5.A.11 and 5.A.12). This is quite unusual and, to the best of our knowledge, unreported for an Mg-pyridyl based compound. Furthermore, we have carried out a variable temperature single crystal X-ray diffraction studies. Figure 5.2B gives a plot of the unit cell parameters as a function of the temperature determined from single crystal diffraction study. The plot reveals that the a- and c-axes showed subtle changes, while b-axis showed no change as the temperature is varied from 100 K to 375 K. Within the same temperature range, the monoclinic beta angle only decreases from 101 to 98°. These small changes in the unit cell parameters suggest only minor structural changes, possibly due to solvent loss. This suggests the gate opening is not due to a major structural change. A linker rotation, which should not change the cell parameters significantly, may be responsible for this gate opening.

The bond distances analysis from the single crystal structure shows the carboxylate groups forming rigid bonds with the Mg (average Mg-O = 2.05 Å), while the pyridyl nitrogens form relatively weaker bonds. There are two types of Mg-pyridyl bonds; one with a

Mg-N bond length of 2.20 Å (Mg(1)-N) and the other with a 2.22 Å (Mg(2)-N) bond length. The rotation of the pyridyl ring along Mg-N bond is likely to be responsible for such gate opening.

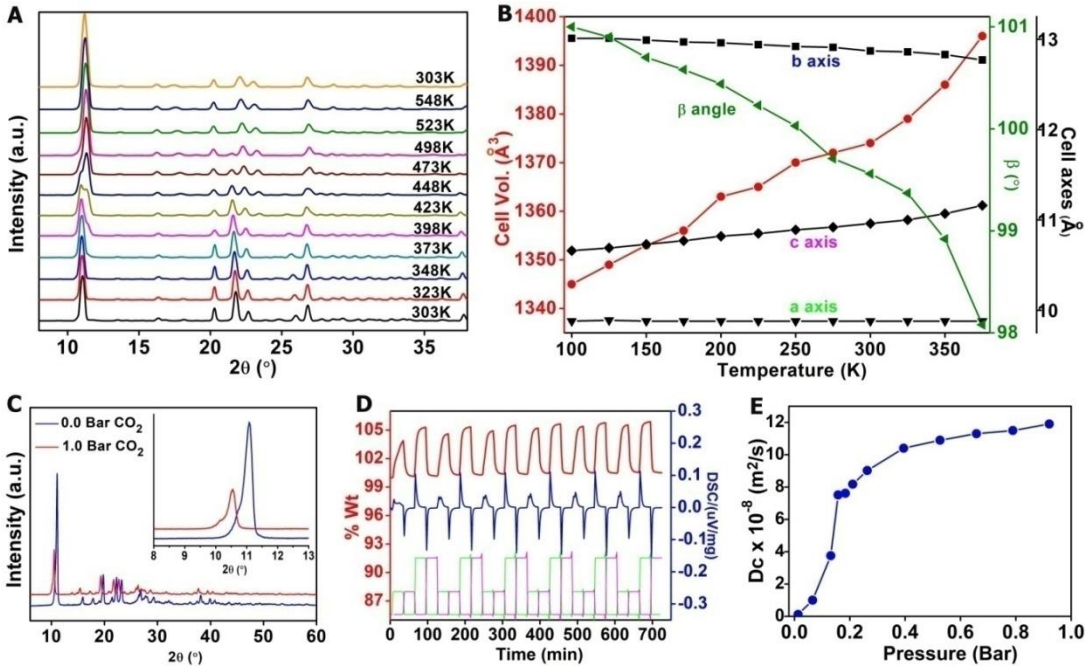

Figure 5.2. (A) Variable temperature PXRD plots of the as-synthesized form of IISERP-MOF21. The plots at 303 K (orange) shows the stability of sample heated at 548 K and cooled back to 303 K. (B) A plot of the change in single crystal unit cell parameters of IISERP-MOF21, obtained from single crystal diffraction, as a function of temperature. (C) A comparative PXRD study of activated and CO_2 loaded sample (under an environmental cell). The peak due to (011) reflection shifts to lower 2θ values when the sample was maintained at 1 bar of CO_2. This suggests expansions along the b and c-directions upon CO_2 sorption. (D) TGA cycling of IISERP-MOF21, with alternating flows of CO_2 and N_2. The cycle involves a flow of CO_2-20 ml/min, N_2-20 ml/min, CO_2-50 ml/min, N_2-50 ml/min, CO_2-20 ml/min, N_2-20 ml/min. (E) Plot of the self-diffusion coefficient of CO_2 in IISERP-MOF21 as a function of CO_2 pressure.

The gate opening behavior was further characterized via in situ PXRD measurements under the CO_2 environment (using an environmental cell). Figure 5.2C shows the comparative PXRD plot of activated vs. CO_2 (1.0 bar) loaded sample. The peak due to 011 reflection shifts (2θ =11-10.5°) to lower 2θ value upon loading with 1 bar CO_2. This indicates the subtle expansion of the lattice during the gate opening.

A TGA cycling experiment was carried out using IISERP-MOF21, where the CO_2 flow rate was set to low (20ml/min) and high (50 ml/min) values. It could be seen that there was a quantitative difference between the CO_2 uptakes when the CO_2 flow was varied between cycles (Fig. 5.2D). Each CO_2 cycle included a 20 ml/min CO_2 flow, followed by a 20 ml/min N_2 sweep and then by a 50 ml/min CO_2 flow which is swept with a 50 ml/min N_2

flow. A comparison of the DSC trace between the 20 and 50 ml/min CO_2 flow cycles shows the possibility of CO_2 accessing different sites at different flow rates. Considering that the 20 and 50 ml/min flows mimic the low and high pressure CO_2 adsorption equilibrium points, it is possible that there are distinct sites. Under 50 ml/min flow all the sites fill up immediately where as in case of 20 ml/min flow the distinct sites fill up gradually.[50] For the 20 ml/min flow, there are two exothermic DSC peaks as against just one for the 50 ml/min flow and this is consistent between the alternating flow and the single flow experiments. This could suggest the sites accessed during the different flows are different. Of course, there does exist an alternate interpretation involving the slow equilibration of the CO_2 uptake with the 20 ml/min flow compared to the 50 ml/min flow; however, it would not explain the presence of two DSC peaks in the lower flow cyclings nor its marked difference from the DSC profile observed for the 50 ml/min cycle. Also, a routine CO_2 on-off cycling on a TGA at a constant flow of (either 20 ml/min or 50 ml/min) confirmed facile adsorption-desorption of CO_2 (Figs. 5.A.15 and 5.A.16).

IISERP-MOF21 lies on the borderline of being non-porous or porous. Thus, any small structural change could produce a significant change in the accessibility of the porous spaces within the material and the associated CO_2 kinetics. This can be tracked from the changes in the CO_2 self-diffusion coefficients during the gate-opening processes. For this purpose, we carried out a rate of adsorption experiment on the ASAP 2020HD instrument at 273 K in the pressure range of 0-1 bar and 8 different pressure points were used to determine the diffusion coefficients by fitting them against a slit/spherical pore models (Appendix section). Interestingly, the self-diffusion coefficient showed appreciable jump (9.9×10^{-9} to 6.5×10^{-8} m^2s^{-1}) at the low pressure gate opening point (0.1 bar) and a relatively lower jump (7.5×10^{-8} to 9.1×10^{-8} m^2s^{-1}) at the higher pressure gate opening (0.3 bar) (Fig. 5.2E). Above this pressure, the diffusion steadily increases to a value of 12×10^{-8} m^2s^{-1} giving almost two orders of magnitude increase in diffusion as we go from lowest partial pressure to 1 bar. This is quite high compared to diffusion in zeolites and some of the other metal organic frameworks.[51-54]

The gate opening happens at a CO_2 pressure of 0.1 bar at 273 K giving a CO_2 uptake of 1.7 mmol/g (82% increase w.r.t the unopened form). When the CO_2 pressure is 0.3 bar, the total uptake reaches the highest capacity of 3.4 mmol/g (~ 31% increase w.r.t. the partially opened form at 0.1 bar pressure). The gate opening pressure shifts to lower pressures as we

go down in temperature, where at 195 K, a condition that mimics high pressure adsorption, the gate is fully open with a maximum saturation capacity of 4.7 mmol/g is observed (Fig. 5.1C). A NLDFT model of the 195 K isotherm shows the presence of uniform 3.58 Å pores (Figs. 5.A.24 and 5A.25). The surface area turns out to be ~400 m^2/g. Due to the complex gate-opening the 273 K CO_2 isotherm could not satisfactorily be modelled using NLDFT (Figs. 5.A.26 and 5.A.27).

A striking aspect of the gate-opening in IISERP-MOF21 includes the fact that only CO_2 is able to do this and neither N_2/CH_4 nor heat can impart any structural flexibility. The crux of the CO_2 adsorption in IISERP-MOF21 lies in the choice of the framework components which brings dynamic behavior to a rigid framework.

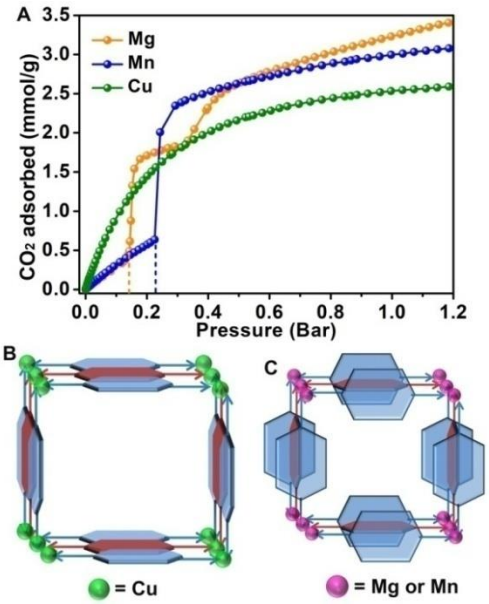

Figure 5.3. (A) A comparison of CO_2 isotherms for IISERP-MOF21, MOF-22 and MOF-23 at 273 K. (B) The initial configuration of Cu 4-PyC showing the existence at open pore configuration (C) The initial configuration of Mg/Mn 4-PyC showing the existence at closed pore configuration.

The gate opening mechanism is facilitated by the co-ordination flexibility of the Mg-N bonds. $Mg^{(II)}$ is a hard Lewis acid whereas the pyridyl is typically a borderline soft base. This mismatch provides sufficient coordination flexibility. Besides, any small distortion caused to the framework of IISERP-MOF21 by the rotation around the Mg-N bonds could produce a significant change in the accessibility of the ultra-microporous channels within the material.

To evaluate the applicability of the Hard Soft Acid Base (HSAB) principle to provide coordination-assisted rotational flexibility, we attempted to synthesize the isostructural

analogues of IISERP-MOF21 wherein Mg is replaced by Mn, Ni and Cu. We successfully, isolated Mn and Cu, however, we could not form the Ni phase. The CO_2 isotherm measurements on Mn and Cu phases brought out some observations that were consistent with HSAB rule. $Mn^{(II)}$, a softer Lewis acid compared to $Mg^{(II)}$, showed only a single gate-opening, but at a pressure higher (Fig. 5.3A). Meanwhile, Cu phase shows no gating phenomenon which can be explained by the lack of sufficient energy from CO_2 toward spinning the stronger Cu-N bonds. Although the gate opening was not observed in case of Cu 4-PyC, the CO_2 uptake at 273 K was comparable to that observed for Mg/Mn 4-PyC. This is because the Cu 4-PyC exists in open pore configuration even in its crystal structure (Fig. 5.3B). However, the Mg/Mn 4-PyC exists in closed pore configuration where the alternate 4-PyC linkers are rotated by 90◦ w.r.t. each other (Fig. 5.3C).

5.3.3. Discussion:

On an experimental observation note, the results from the variable temperature PXRD show that the mechanism for the porosity generation via bond rotation is much more subtle compared to the gate opening by breathing mechanisms, where a large structural change is observed in the x-ray and neutron diffractions. The molecular-rotating gate observed here is comparable to the rotation of the aryl rings acting as a gate. As reported by Kitagawa and co-workers, the rotation of aryl ring happens with the increase of hydration in a layered-pillared metal organic structure and this is known to decrease porosity upon dehydration. [42] This is markedly different from our case where simple rotation of pyridyl linkers drastically improves the porosity of an almost dense framework. This could be due to a lot of dispersive interactions exist between the framework and CO_2, and CO_2-CO_2. Also this is reflected in their self-diffusivity coefficients. Since the pore-dimensions of IISERP-MOF21is on the ultra-microporous regime, the molecular rotation's effect is so drastic that a discrete set of inaccessible nanospaces get connected into a gas-selective porous framework. Compared to other breathing phenomenon our hard-soft acid-base assisted coordination flexibility could be relatively easier to embed into a range of extended metal-organic structures to make them functioning or operating more selectively under milder triggering conditions.

Other interesting classes of systems where this chemistry or even the exact choice of metal and ligand are adoptable would be the metallo-cyclodextrins, [55] crystalline cavitands, [56] metal-organic nanotubular assemblies,[57] MOFs with large discrete cages,[58] crystalline molecular flasks,[59] and polycatenanes/pseudorotaxanes[60]. Most of these systems posses

massive nano-sized discrete cages accessible to guest solvent, but are locked for gases. This approach could expand their limits by unlocking these cages into gas-selective 1 or 2 or 3-D nano channels.

5.4. Conclusion:

In conclusion, we have shown how even a non-porous and rigid solid can be made into a dynamic porous solid with good CO_2 uptake and selectivity through 'coordination flexibility'. The CO_2-specific gate-opening in such a rigid framework is unprecedented. Considering the expansive library of ligands and metals available, it is evident that the approach can effectively be used in a variety of metal-organic systems to successfully impart guest-triggered porosity. The effect of the metal replacement on the framework has quantified the contributions from the hard-soft acid-base character of the framework towards the coordination flexibility. This presents a new perspective into introducing gas-selective porosity into a wide range of dense metal-organic solids.

5.5. References:

1. Zhou, H.-C.; Long, J. R.; Yaghi, O. M. *Chem. Rev*. **2012**, *112*, 673−674.
2. Ryan, J. K.; Timmons, D. J.; Fang, Q.-R.; Li, J.-R.; Makal, T. A.; Young, M. D.; Yuan, D.; Zhao, D.; Zhuang, W.; Zhou, H.-C. *Coord. Chem. Rev.* **2009**, *253*, 3042–3066.
3. Paz, F. A. A.; Klinowski, J.; Vilela, S. M. F.; Tome´, J. P. C.; Cavaleiro, J. A. S.; Rocha, J. *Chem. Soc. Rev*. **2012**, *41*, 1088–1110.
4. Henke, S.; Schneemann, A.; Wütscher, A.; Fischer, R. A. *J. Am. Chem. Soc.* **2012**, *134*, 9464−9474.
5. Kitagawa, S.; Uemura, K. *Chem. Soc. Rev*. **2005**, *34*, 109–119.
6. Ferey, G.; Serre, C.´ *Chem. Soc. Rev.* **2009**, *38*, 1380−1399.
7. Horike, S.; Shimomura, S.; Kitagawa, S. *Nat. Chem*. **2009**, *1*, 695−704.
8. Sato, H.; Kosaka, W.; Matsuda, R.; Hori, A.; Hijikata, Y.; Belosludov, R. V.; Sakaki, S.; Takata, M.; Kitagawa, S. *Science* **2014**, *343*, 167−170.
9. Schneemann, A; Bon, V.; Schwedler, I.; Senkovska, I.; Kaskel, S.; Fischer, R. A. *Chem. Soc. Rev*. **2014**, *43*, 6062-6096.
10. Sarkisov, L.; Martin, R. L.; Haranczyk, M.; Smit, B. *J. Am. Chem. Soc.* **2014**, *136*, 2228-223.

11. Thallapally, P. K.; Tian, J.; Radhakishan, M.; Fernandez, C. A.; Dalgarno, S. J.; McGrail, P. B.; Warren, J. E.; Atwood, J. L.*J. Am. Chem. Soc.* **2008**, *130*, 16842-16843.
12. Fletcher, A. J., Thomas, K. M.; Rosseinsky, M. J. *J. Solid State Chem.* **2005**, *178*, 2491–2510.
13. Chang, Z.; Yang, D.-H.; Xu, J.; Hu, T.-L.; Bu, Z.-H. *Adv. Mater.* **2015**, *27*, 5432-5441.
14. Lin, Z.-J.; Lu¨, J.; Hong, M.; Cao, R. *Chem. Soc. Rev*. **2014**, *43*, 5867-5895.
15. Li, L.; Lin, R.-B.; Krishna, R.; Wang, X.; Li, B.; Wu, H.; Li, J.; Zhou, W.; Chen, B. *J. Am. Chem. Soc.* **2017**, *139*, 7733-7736.
16. Motkuri, R. K.; Thallapally, P. K.; Annapureddy, H. V. R.; Dang, L. X.; Krishna, R.; Nune, S. K.; Fernandez, C. A.; Liu, L.; McGrail, B. P. *Chem. Commun*. **2015**, *51*, 8421.
17. Belosludov, R. V.;Sakaki, S.; Takata, M.; Kitagawa, S.; Mendes, P. A. P.; Horcajada, P.; Rives, S.; Ren, H.; Rodrigues, A. E.; Devic, T.; Magnier, E.; Trens, P.; Jobic, H.; Ollivier, J.; Maurin, G.; Serre, C.; Sil, J. A. C. *Adv. Funct. Mater*. **2014**, *24*, 7666-7673.
18. Yang, W.; Davies, A. J.; Lin, X.; Suyetin, M.; Matsuda, R.; Blake, A. J.; Wilson, C.; Lewis, W.; Parker, J. E.; Tang, C. C.; George, M. W.;Hubberstey, P.; Kitagawa, S.; Sakamoto, H.; Bichoutskaia, E.; Champness, N. R.; Yang, S.; Schroder, M. *Chem. Sci*. **2012**, *3*, 2993.
19. Bourrelly, S.; Llewellyn, P. L.; Serre, C.; Millange, F.; Loiseau, T.; Ferey, G. *J. Am. Chem. Soc*. **2005**, *127*, 13519-13521.
20. Carrington, E. J.; McAnally, C. A.; Fletcher, A. J.; Thompson, S. P; Warren, M.; Brammer, L. *Nat. Chem*. **2017**, *9*, 882-889.
21. Shimomura, S.; Higuchi, M.; Matsuda, R.; Yoneda, K.; Hijikata, Y.; Kubota, Y.; Mita, Y.; Kim, J.; Takata, M.; Kitagawa, S. *Nat. Chem.* **2010**, *2*, 633-637.
22. Yang, S.; Lin, X.; Lewis, W.; Suyetin, M.; Bichoutskaia, E.; Parker, J. E.; Tang, C. C.; Allan, D. R.; Rizkallah, P. J.; Hubberstey, P.; Champness, N. R.; Thomas, K. M.; Blake A. J.; Schröder, M. *Nat. Mater*. **2012**, *11*, 710-716.
23. Mason, J. A.; Oktawiec, J.; Taylor, M. K.; Hudson, M. R.; Rodriguez, J.; Bachman, J. E.; Gonzalez, M. I.; Cervellino, A.; Guagliardi, A.; Brown, C. M.; Llewellyn, P. L.; Masciocchi, N.; Long, J. R. *Nature*, **2015**, *527*, 357-361.

24. Li, B.; Wen, H.-M.; Zhou, W.; Chen, B. *J. Phys. Chem. Lett*. **2014**, *5*, 3468-3479.
25. Klein, N.; Herzog, C.; Sabo, M.; Senkovska, I.; Getzschmann, J.; Paasch, S.; Lohe, M. R.; Brunner, E.; Kaskel, S. *Phys. Chem. Chem. Phys*. **2010**, *12*, 11778-11784.
26. Chen, Q.; Chang, Z.; Song, W.-C.; Song, H.; Song, H.-B.; Hu, T.-L.; Bu, X. H. *Angew. Chem. Int. Ed*. **2013**, *52*, 11550 -11553.
27. Horcajada, P.; Gref, R.; Baati, T.; Allan, P. K.; Maurin, G.; Couvreur, P.; Ferey, G.; Morris, R. E.; Serre, C. *Chem. Rev*. **2012**, *112*, 1232-1268.
28. McKinlay, A. C.; Eubank, J. F.; Wuttke, S.; Xiao, B.; Wheatley, P. S.; Bazin, P.; Lavalley, J.-C.; Daturi, M.; Vimont, A.; Weireld, G. D.; Horcajada, P.; Serre, C.; Morris, R. E. *Chem. Mater*. **2013**, *25*, 1592-1599.
29. Horcajada, P.; Serre, C.; Maurin, G.; Ramsahye, N. A.; Balas, F.; Vallet-Regí, M.; Sebban, M.; Taulelle, F.; Férey, G. *J. Am. Chem. Soc*. **2008**, *130*, 6774-6780.
30. Serre, C.; Bourrelly, S.; Vimont, A.; Ramsahye, N. A.; Maurin, G.; Llewellyn, P. L.; Daturi, M.; Filinchuk, Y.; Leynaud, O.; Barnes, P.; Férey, G. *Adv. Mater*. **2007,** *19*, 2246-2251.
31. Xiao, J.; Wu, Y.; Li, M.; Liu, B.-Y.; Huang, X.-C.; Li, D. *Chem. Eur. J*. **2013**, *19*, 1891-1895.
32. Coudert, F.-X., Mellot-Draznieks, C., Fuchs, A. H.; Boutin, A. *J. Am. Chem. Soc*. **2009**, *131*, 11329-11331.
33. Maji, T. K.; Matsuda, R.; Kitagawa, S. *Nat. Mater*. **2007**, *6*, 142.
34. Fukuhara, K.; Noro, S.-I.; Sugimoto, K.; kutagawa, T.; Kubo, K.; Nakamura, T. *Inorg. Chem*. **2013**, *52*, 4229-4237.
35. Serre, C.; Millange, F.; Thouvenot, C.; Nogues, M.; Marsolier, G.; Louer, D.; Ferey, G. *J. Am. Chem. Soc*. **2002**, *124*, 13519-13526.
36. 36.Sumida, K.; Rogow, D. L.; Mason, J. A.; McDonald, T. M.; Bloch, E. D.; Herm, Z. R.; Bae, T.-H.; Long, J. R. *Chem. Rev.* **2012**, *112*, 724-781.
37. Eddaoudi, M.; Li, H.; Yaghi, O. M. *J. Am. Chem. Soc.* **2000**, *122*, 1391-1397.
38. Furukawa, H.; Ko, N.; Go, Y. B.; Aratani, N.; Choi, S. B.; Choi, E.; Yazaydin, A. O.; Snurr, R. Q.; O'Keeffe, M.; Kim, J.; Yaghi, O. M. *Science* **2010**, *329*, 424-428.
39. Millward, A. R.; Yaghi, O. M. *J. Am. Chem. Soc*. **2005**, *127*, 17998.
40. Yang, Q.; Vaesen, S.; Ragon, F.; Wiersum, A. D.; Wu, D.; Lago, A.; Devic, T.; Martineau, C.; Taulelle, F.; Llewellyn, P. L.; Jobic, H.; Zhong, C.; Serre, C.; Weireld, G. D.; Maurin, G. *Angew. Chem. Int. Ed.* **2013**, *52*, 10316 -10320.

41. Cmarik, G. E.; Kim, M.; Cohen, S. M.; Walton, K. S. *Langmuir* **2012**, *28*, 15606-15613.
42. Seo, J.; Matsuda, R.; Sakamoto, H.; Bonneau, C.; Kitagawa, S. *J. Am. Chem. Soc*. **2009**, *131*, 12792-12800.
43. Serre, C.; Mellot-Draznieks, C.; Surblé, S.; Audebrand, N.; Filinchuk, Y.; Férey, G. *Science*, **2007**, *315*, 1828.
44. Nijem, N.; Wu, H.; Canepa, P.; Marti, A.; Balkus, K. J.; Thonhauser, T.; Li, J.; Chabal, Y. J. *J. Am. Chem. Soc.* **2012**, *134*, 15201-15204.
45. Mellot-Draznieks, C.; Serre, C.; Surble, S.; Audebrand, N.; Ferey, G. *J. Am. Chem. Soc.* **2005**, *127*, 16273-16278.
46. Seo, J.; Bonneau, C.; Matsuda, R.; Takata, M.; Kitagawa, S. *J. Am. Chem. Soc.* **2011**, *133*, 9005-9013.
47. Banerjee, D.; Wang, H.; Plonka, A. M.; Emge, T. J.; Parise, J. B.; Li, J. *Chem. Eur. J.* **2016**, *22*, 11816-11825.
48. Malek, K; Coppensa, M.-O. *J. Chem. Phys.* **2003**, *119*, 2801.
49. Do, D. D. *Imperial College Press* Ed. **2008**.
50. Vaidhyanathan, R.; Iremonger, S. S.; Shimizu, G. K. H.; Boyd, P. G.; Alavi, S.; Woo T. K. *Science* **2010**, *330*, 650-653.
51. Saha, D.; Bao, Z.; Jia, F.; Deng, S. *Environ. Sci. Technol*. **2010**, *44*, 1820.
52. Zhao, Z.; Li, Z.; Lin, Y. S. *Ind. Eng. Chem. Res.* **2009**, *48*, 10015.
53. Kizzie, A. C.; Wong-Foy, A. G.; Matzger, A. J. *Langmuir* **2011**, *27*, 6368.
54. Nandi, S.; Collins, S.; Chakraborty, D.; Banerjee, D.; Thallapally, P. K.; Woo, T. K.; Vaidhyanathan, R. *J. Am. Chem. Soc.* **2017**, *139*, 1734-1737.
55. Hartlieb, K. J.; Holcroft, J. M.; Moghadam, P. Z.; Vermeulen, N. A.; Algaradah, M. M.; Nassar, M. S.; Botros, Y. Y.; Snurr, R. Q.; Stoddart, J. F. *J. Am. Chem. Soc.* **2016**, *138*, 2292-2301.
56. Holst, J. R.; Trewin, A.; Cooper, A. I. *Nat. Chem*. **2010**, *2*, 915.
57. Otsubo1, K.; Wakabayashi, Y.; Ohara, J.; Yamamoto, S.; Matsuzaki, H.; Okamoto, H.; Nitta, K.; Uruga, T.; Kitagawa, H. *Nat. Mater*. **2011**, *10*, 291.
58. Vaidhyanathan, R.; Bridges, C. A.; Bradshaw, D.; Rosseinsky, M. J. *Crystal Growth & Design* **2010**, *10*, 4348.
59. Inokuma, Y.; Kawano, M.; Fujita, M. *Nat. Chem*. **2011**, *3*, 349.
60. Jiang, L.; Ju, P.; Meng, X.-R.; Kuang, X.-J.; Lu, T.-B. *Sci. Rep*. **2012**, *2*, 668.

5.A. Appendix for Chapter 5:

Single Crystal Structure Analysis:

Table 5.A.1: Unit cell parameters for Mg 4-PyC, Mn 4-PyC and Cu 4-PyC.

Materials	a (Å)	b (Å)	c (Å)	α (◦)	β(◦)	γ(◦)	V (Å^3)	Sp.Gr
Mg 4-PyC	9.8793(6)	13.0109(8)	10.6809(7)	90.00	100.873(2)	90.00	1348.26(15)	P2(1)
Mn 4-PyC	9.9665(4)	13.2955(5)	10.6833(4)	90.00	103.110(2)	90.00	1378.74(9)	P2(1)
Cu 4-PyC	11.4487(8)	12.3600(8)	12.3919(8)	90.00	117.201(3)	90.00	1559.60(18)	P2(1)/c

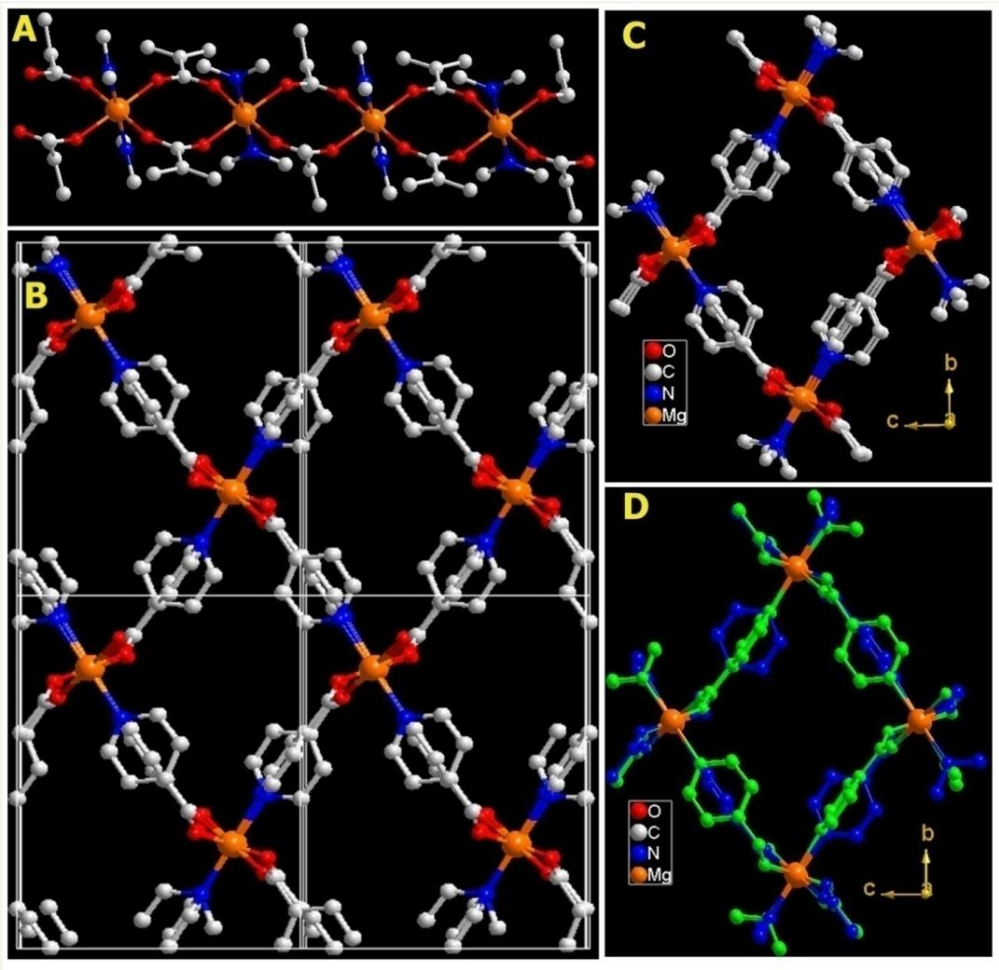

Figure 5.A.1. (A) Basic building unit of IISERP-MOF21. Each Mg is octahedrally coordinated. (B) The three-dimensional structure of IISERP-MOF21viewed along the a-axis. (C) Three-dimensional structure, showing a single channel. (D) The channel where two different orientation of the linker has been represented in different colors.

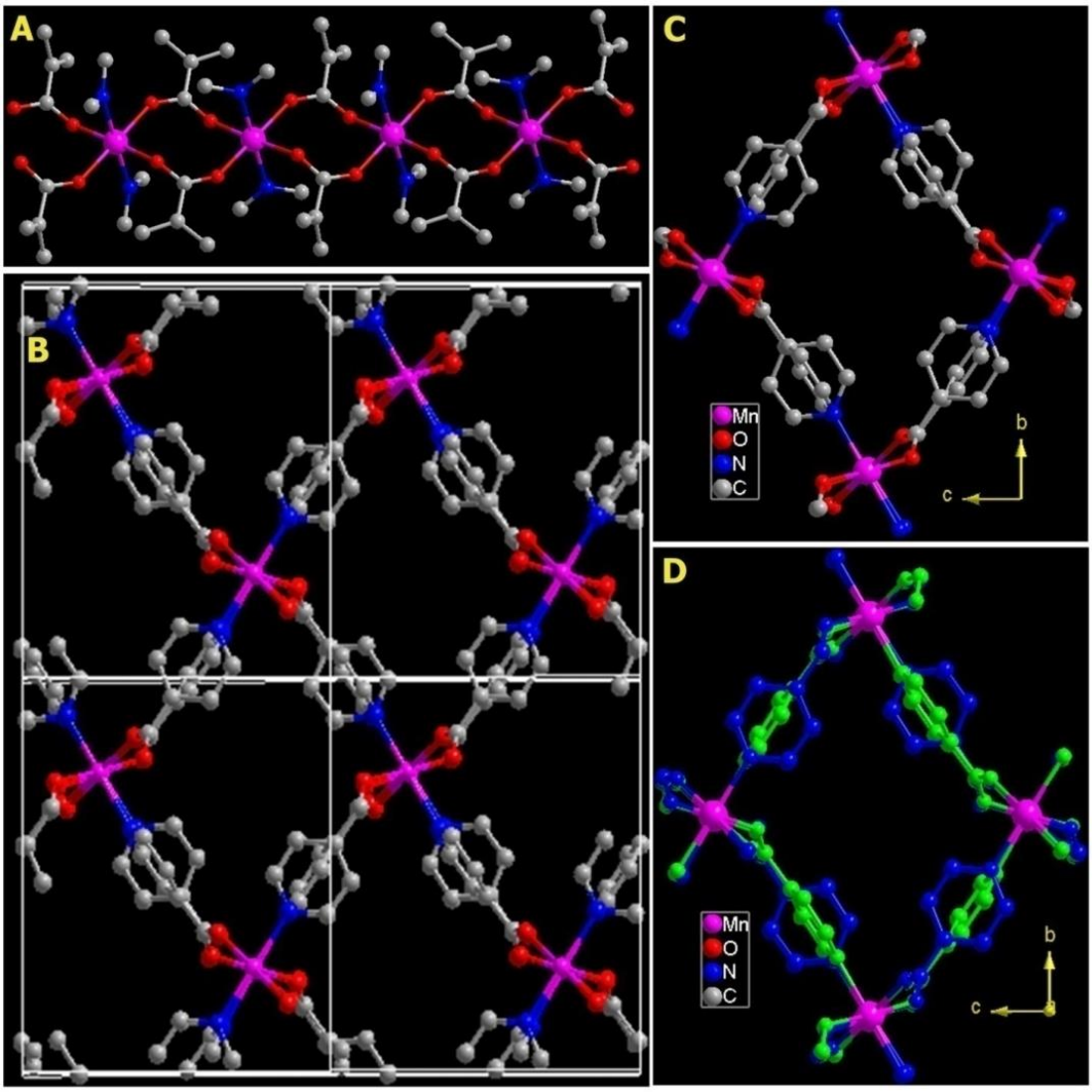

Figure 5.A.2. (A) Basic building unit of IISERP-MOF22. Each Mn is octahedrally coordinated. (B) The three-dimensional framework of IISERP-MOF22 viewed along the a-axis. (C) Structure of IISERP-MOF22 showing a single channel formed by the linking of isolated metal octahedral by the 4-PyC units. (D) The 1-D channel along the a-axis, where two different orientation of the linker has been presented with different colors.

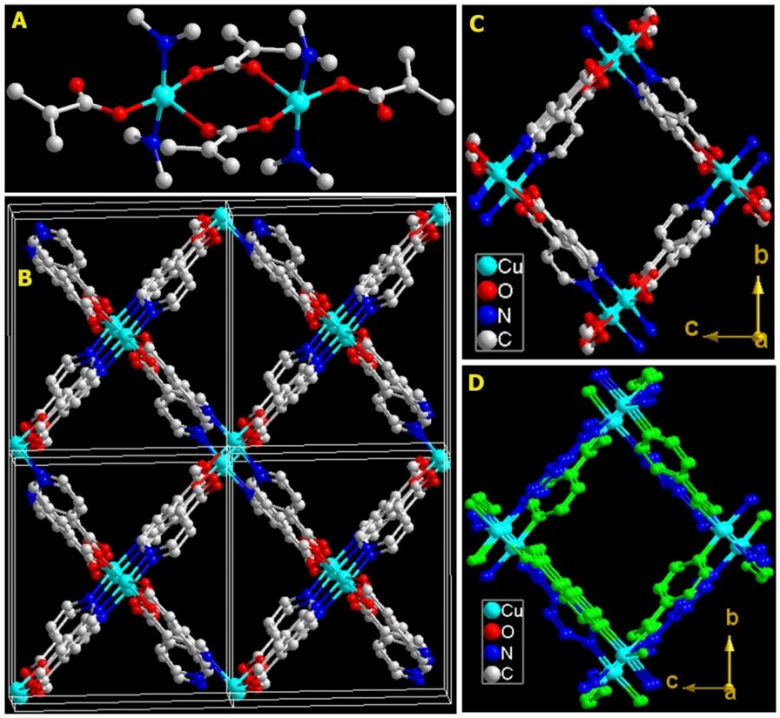

Figure 5.A.3. (A) Basic building unit present in IISERP-MOF23. Unlike other two cases, here the Cu adopts a pentagonal pyramidal coordination geometry.(B) The three-dimensional structure of **3** along the a-axis. (C) The 1-D channels, running along the a-axis in IISERP-MOF23. (D) The two different orientations of the linker 4-PyC have been presented with different colors. Here, two linkers are not oriented in 90° to each other; rather the orientation is almost the same for these crystallographically independent linker units.

Analytical Characterizations:

Powder X-ray Diffraction:

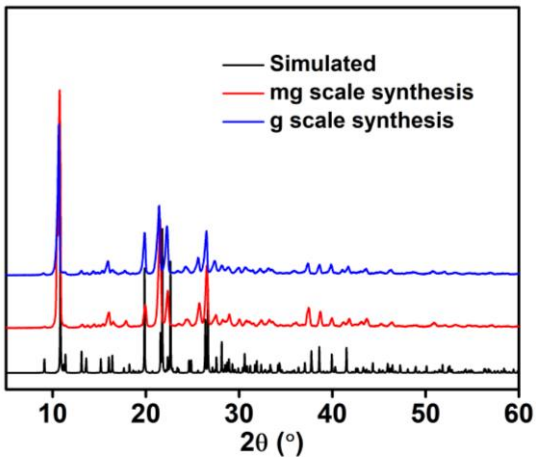

Figure 5.A.4. Comparison of the experimental powder X-ray diffraction (PXRD) patterns of IISERP-MOF21 (small scale and large scale) with the patterns simulated from the single crystal x-ray diffraction.

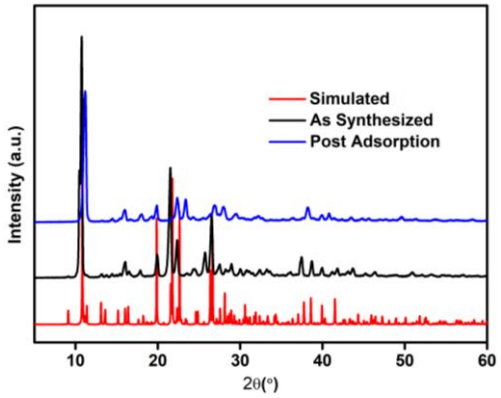

Figure 5.A.5. Comparative PXRD of IISERP-MOF21**:** Simulated vs. as-synthesized as well as the post-adsorption sample. Note that IISERP-MOF21 is exceptionally stable to heating under vacuum (activation during adsorption-desorption cycles).

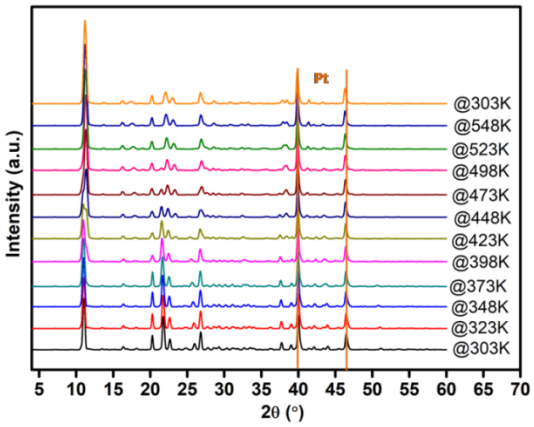

Figure 5.A.6. Variable temperature PXRD of IISERP-MOF21. The material possesses exceptional thermal stability**.** The peak around 2θ=40° and 47° is due to reflection from the platinum plate (from the sample holder).

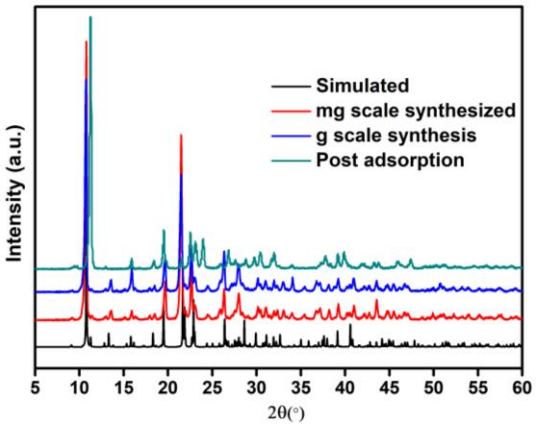

Figure 5.A.7. Comparison of the PXRD of IISERP-MOF22**:** Simulated vs. as-synthesized as well as the post-adsorption sample. Note that IISERP-MOF22 is exceptionally stable to heating under vacuum.

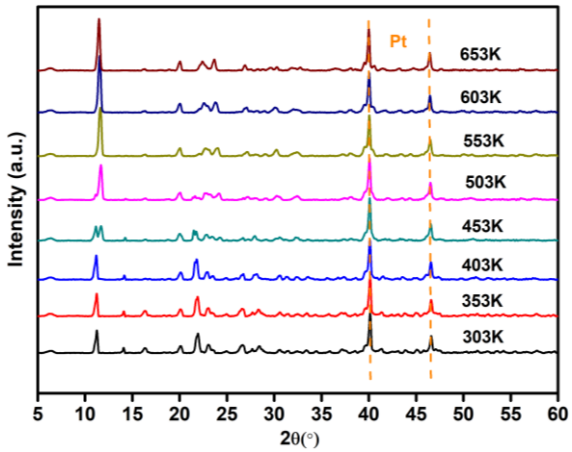

Figure 5.A.8. Variable temperature PXRD of IISERP-MOF22. The material shows exceptional thermal stability just like IISERP-MOF21**.** Platinum peaks are from the sample holder.

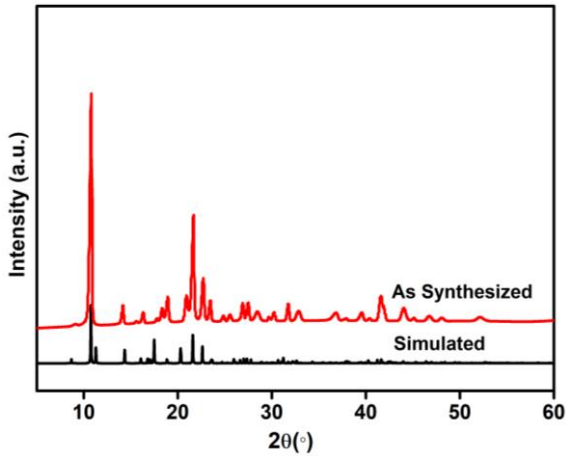

Figure 5.A.9. Comparative PXRD of IISERP-MOF23**:** Simulated vs. as-synthesized sample.

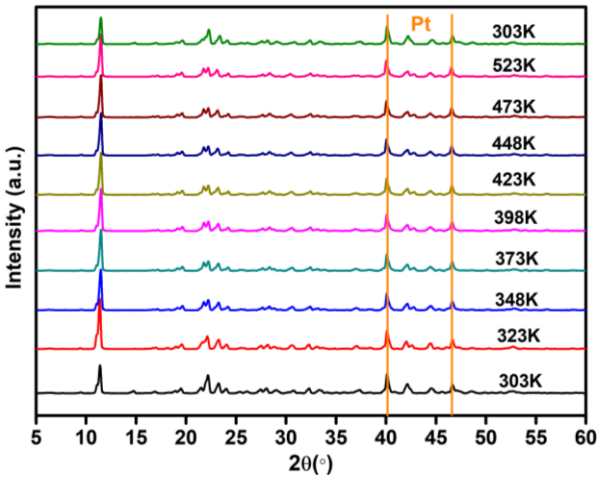

Figure 5.A.10. Variable temperature PXRD of IISERP-MOF23. Peaks due to the Pt plate (sample holder) are observed.

Thermo Gravimetric Analysis (TGA):

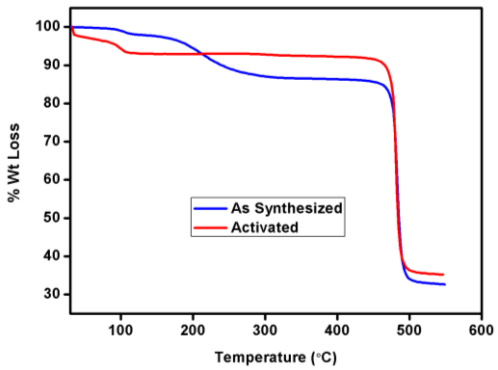

Figure 5.A.11. TGA plots of the as-made IISERP-MOF21 and the completely activated (solvent exchanged and heated at 150°C for 24 hrs under vacuum) sample.

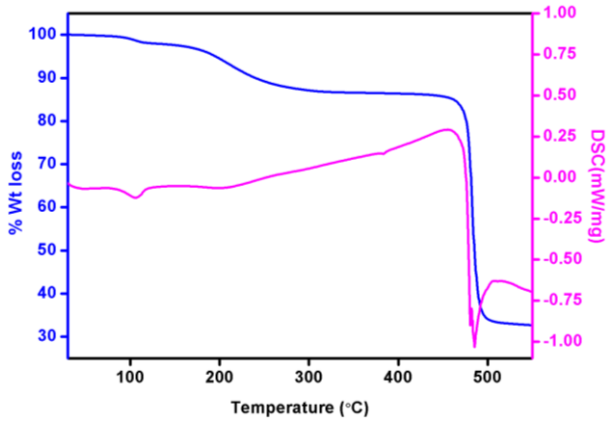

Figure 5.A.12. TGA carried out on the as-synthesized sample of IISERP-MOF21. The weight loss has been calculated using the formula $Mg_2(C_6NH_4O_2)_4(C_3H_7NO)$ (M. Wt. **610.11**). All the surface solvent molecules are removed by 100°C (loss ~2%), while most of the free DMF molecules come off at 180° to 230°C (calc.: 9.61%; obsd.: 11.19).

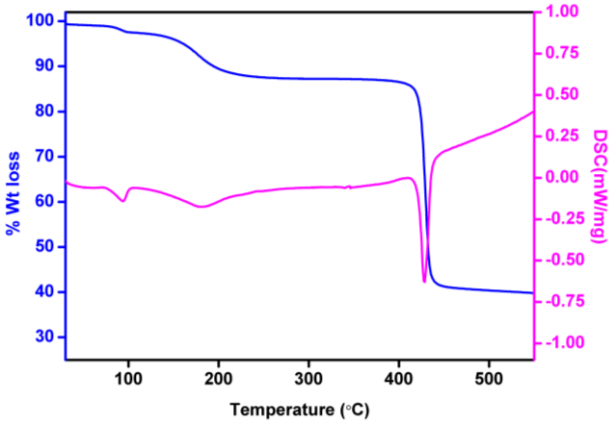

Figure 5.A.13. TGA carried out using the as-synthesized sample of IISERP-MOF22. The weight loss has been calculated using the formula Mn_2 $(C_6NH_4O_2)_4(C_3H_7NO)$ (M. Wt. **671.37**). All the surface solvent molecules are removed by 100°C (loss ~2%), while most of the free DMF come off at 180° to 230°C (calc.: 10.87 %; obsd.: 10.49).

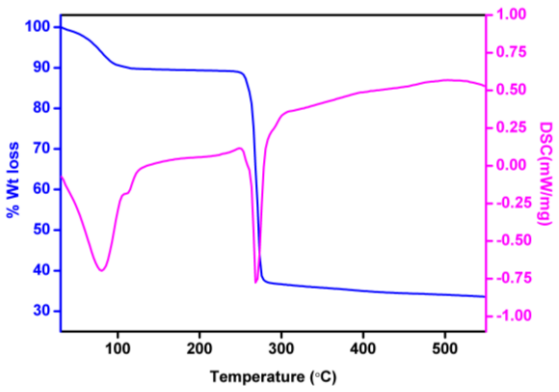

Figure 5.A.14. TGA carried out on the as synthesized sample of IISERP-MOF23. The weight loss has been calculated using the formula Cu_2 $(C_6NH_4O_2)_4(C_4H_8O)$ (M. Wt. **687.60**). All the solvent molecules, THF, are removed by 100°C (calc.: 10.61 %; obsd.: 10.91).

TGA Cycling Experiment:

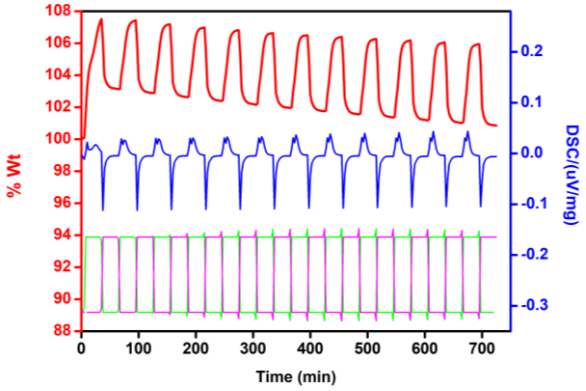

Figure 5.A.15. CO_2/N_2 cycling experiment using IISERP-MOF21. A flow rate of 20 ml/min was used. DSC traces show two different peak- could be due to the presence of two different but closely related adsorption sites.

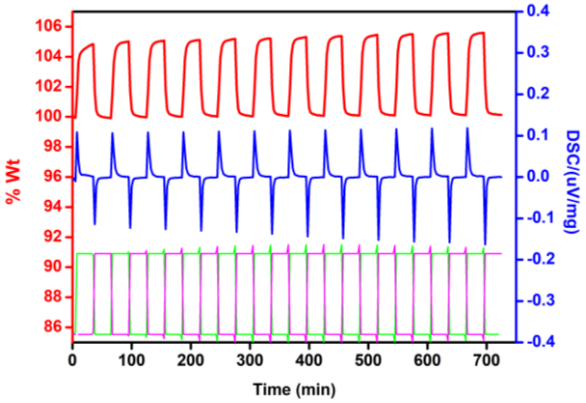

Figure 5.A.16. CO_2/N_2 cycling experiment using IISERP-MOF21. A flow rate of 50 ml/min was employed. DSC traces showing two different peak.

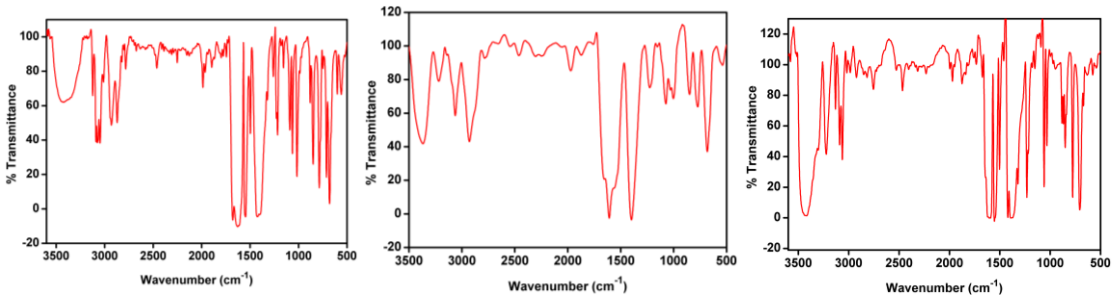

Figure 5.A.17. Infra-red spectra of IISERP-MOF21, MOF-22 and MOF-23 showing the various stretching and bending modes present.Selected peaks: IR (KBr pellet, cm^{-1}): v(O-H) solvent: 3465; v(C-H): 2992; v(COO): 1658 and 1598, v(C=C): 1208 to 800. (Source: Infrared and Raman Spectra of Inorganic and Coordination Compounds, Part B, Applications in Coordination, Organometallic, and Bioinorganic Chemistry, 6th Edition, Kazuo Nakamoto).

Adsorption Analysis:

Table 5.A.2. CO_2 adsorption and desorption data at 195 K for IISERP-MOF21

Absolute Pressure (mmHg)	Amount adsorbed (mmol/g)	Absolute Pressure (mmHg)	Amount adsorbed (mmol/g)
0.331270248	0.543809612	702.2460327	4.658147638
1.012192369	1.877483828	665.7689819	4.6280629
2.017788887	2.867530286	635.1241455	4.603871199
2.779516935	3.098605084	604.1782837	4.5783839
4.641766071	3.385548277	574.8915405	4.5567397
7.9339118	3.575026545	543.8469238	4.531805898
13.01223087	3.758892186	513.2229004	4.512110885
17.40641594	3.808977669	482.3674011	4.494519177
21.56363106	3.837914367	451.4325562	4.477380319
28.99429703	3.860039063	420.5057983	4.457237546
36.01469803	3.882058933	389.8466797	4.436293827
48.20235062	3.906672115	358.8648071	4.417482358
60.03760529	3.933636105	328.1066284	4.400371055
70.17875671	3.95223758	296.2582703	4.385290686
80.08010101	3.966506205	265.0784302	4.369985975
90.18074036	3.981945257	234.3279419	4.354046393
100.3346863	3.997525435	204.8252869	4.340208742
114.5876541	4.012275073	173.9718475	4.327308083
128.9645538	4.028766234	143.085556	4.313831494
136.2297668	4.039437249	112.2762375	4.301115955
143.3015289	4.049635405	81.51797485	4.289087003
157.621582	4.06718715	50.77935028	4.26836934
171.9382324	4.082963445	35.01835251	4.251142493
186.3448486	4.097537832	19.70196533	4.23186596
200.4986572	4.110125408	12.04301167	4.210029297
214.7712555	4.126552196	4.473938942	4.161871179
229.2537079	4.143534093		
243.7911987	4.158862037		
272.461853	4.181423175		
301.3612366	4.209319306		

329.68573	4.237730309		
343.9915771	4.255377354		
358.1341858	4.273777981		
386.572937	4.298031714		
415.5287781	4.325638888		
443.9020691	4.352484439		
472.4134827	4.380422859		
501.1263428	4.411545041		
530.0723877	4.445076977		
559.321106	4.481042125		
587.9716797	4.515962745		
616.5640869	4.551426555		
645.7827759	4.590157791		
674.7662354	4.624035342		
702.2460327	4.658147638		

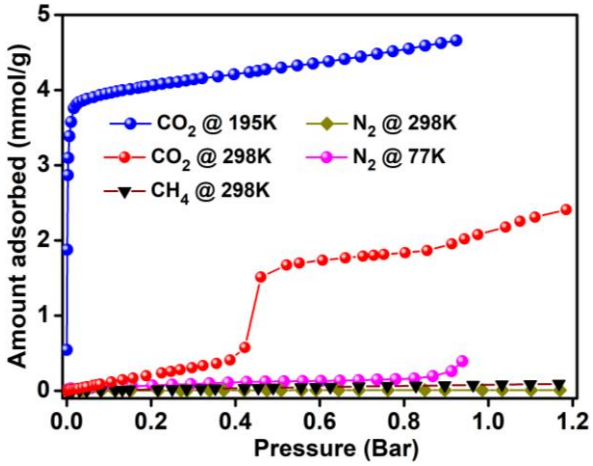

Figure 5.A.18. CO_2, N_2 and CH_4 adsorption isotherms of IISERP-MOF21**.** Note that only CO_2 is able to acces the nanospace through gate opening.

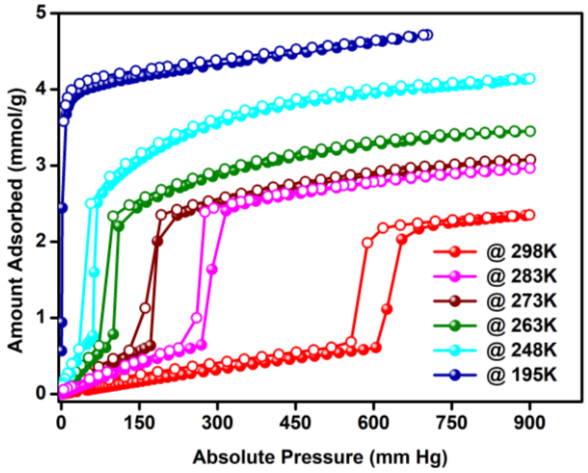

Figure 5.A.19. CO_2 adsorption/desorption isotherms of IISERP-MOF22 at different temperatures showing the gating at different pressures of CO_2.

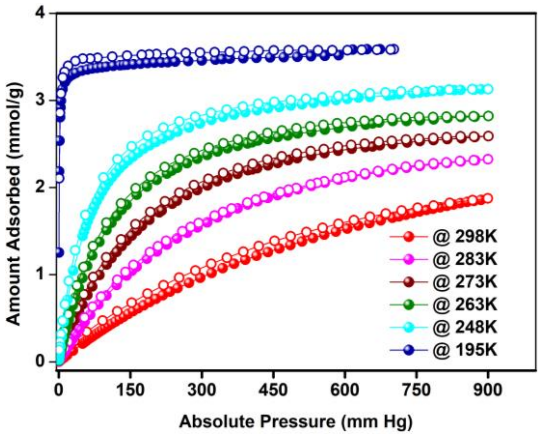

Figure 5.A.20. CO_2 adsorption/desorption isotherms of IISERP-MOF23 at different temperatures showing no gating. This is due to the fact that in this case material is already in *open pore* configuration. The stronger N-Cu bond needs more energy compared to other two cases and thats why CO_2 is not showing any gating phenomenon.

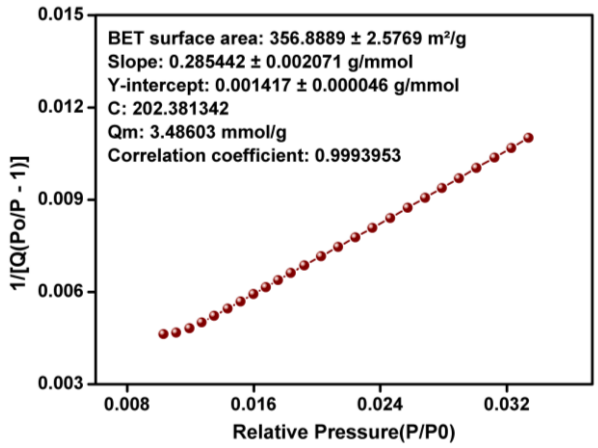

Figure 5.A.21. BET surface area fit for IISERP-MOF21 calculated using the 273 K CO_2 adsorption isotherm.

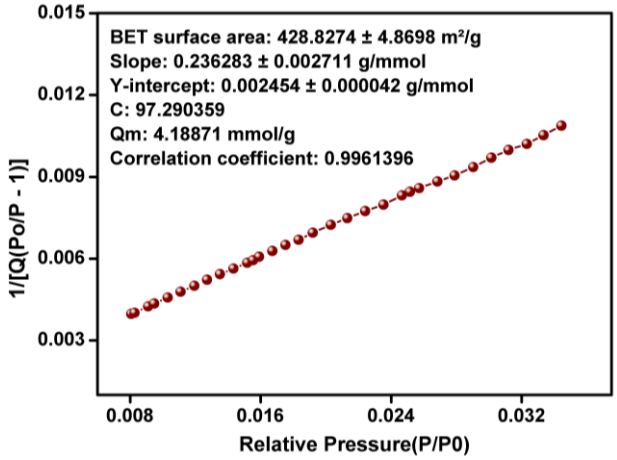

Figure 5.A.22. BET surface area fit for IISERP-MOF22 calculated using the 273 K CO_2 adsorption isotherm.

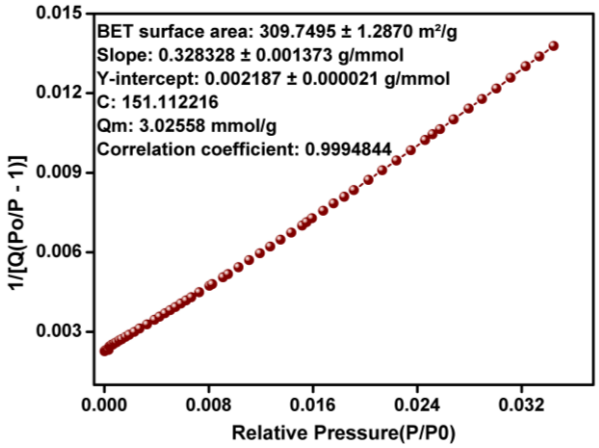

Figure 5.A.23. BET surface area fit for IISERP-MOF23 calculated using the 273 K CO_2 adsorption isotherm.

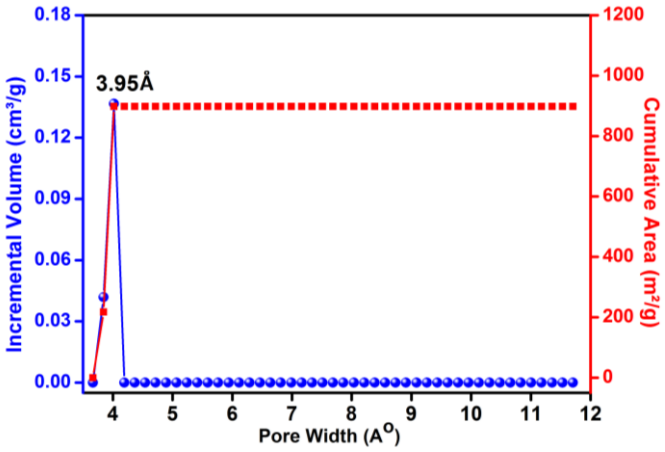

Figure 5.A.24. Pore size distribution (NLDFT, Slit pore model) of IISERP-MOF21 calculated using the 195 K CO_2 adsorption isotherm.

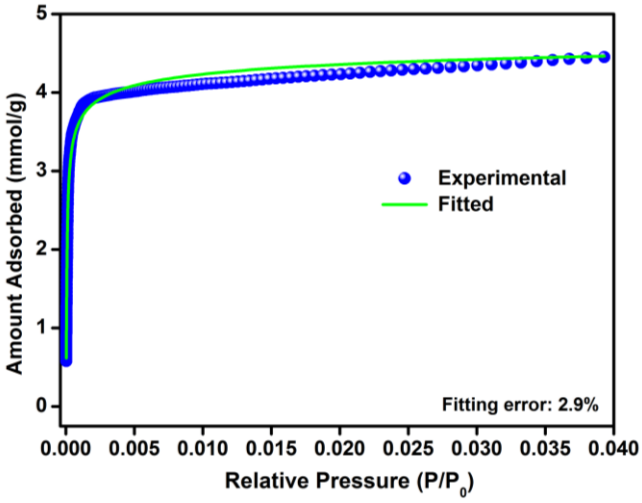

Figure 5.A.25. NLDFT fitting comparision for IISERP-MOF21. Note that an average fit was obtained using the entire range of data points of the 195 K CO_2 adsorption isotherm.

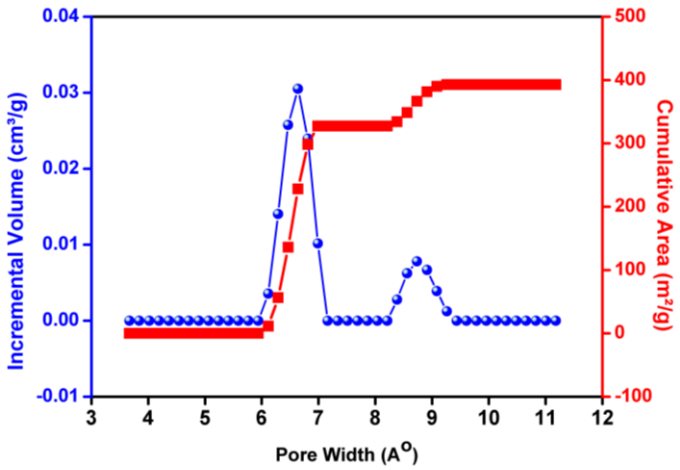

Figure 5.A.26. Pore size distribution (NLDFT Slit pore model) of IISERP-MOF21 calculated using the 273 K CO_2 adsorption isotherm.

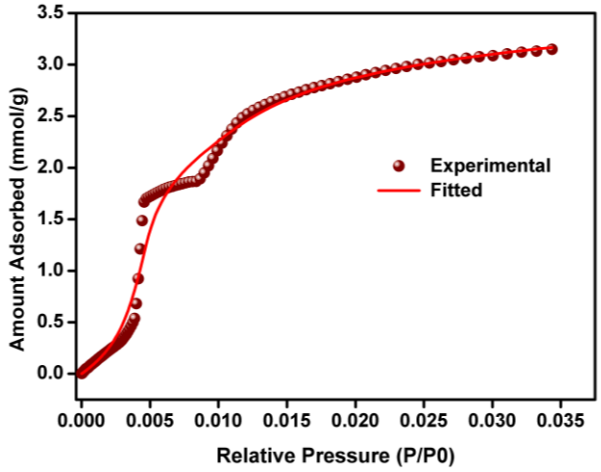

Figure 5.A.27. NLDFT fitting comparision for IISERP-MOF21. Note that an average fit was obtained using the entire range of data pointsof the 273 K CO_2 adsorption isotherm.

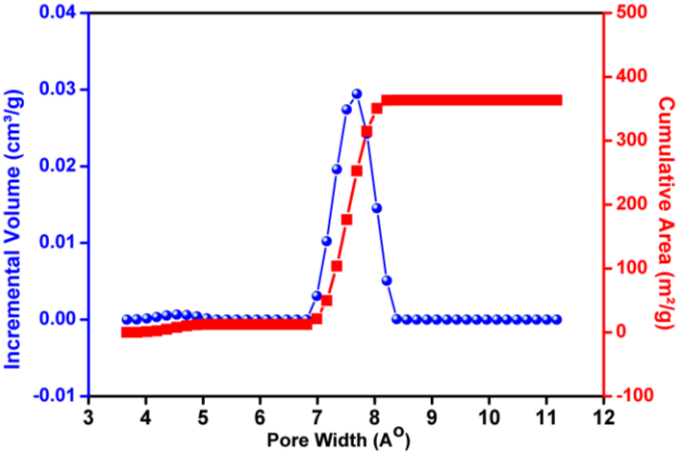

Figure 5.A.28. Pore size distribution (NLDFT Slit pore model) of IISERP-MOF22 calculated using the 273 K CO_2 adsorption isotherm.

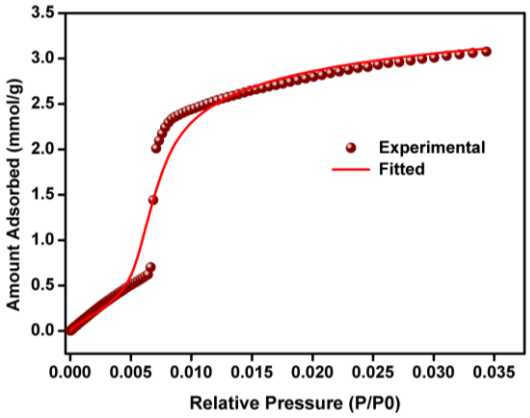

Figure 5.A.29. NLDFT fitting comparision for IISERP-MOF22. Note that an average fit was obtained using the whole range of data points of the 273 K CO_2 adsorption isotherm.

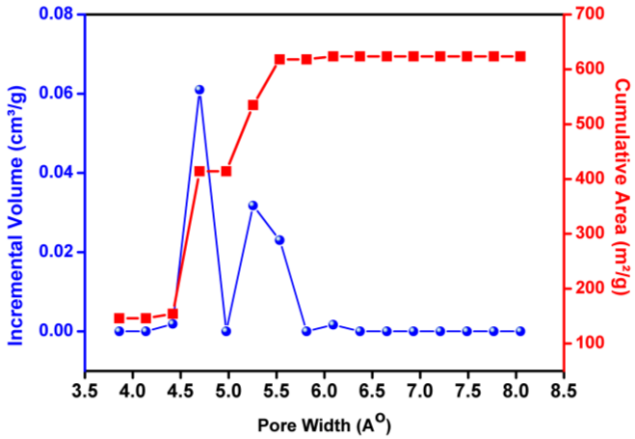

Figure 5.A.30. Pore size distribution (NLDFT Slit pore model) of IISERP-MOF23 calculated using the 273 K CO_2 adsorption isotherm.

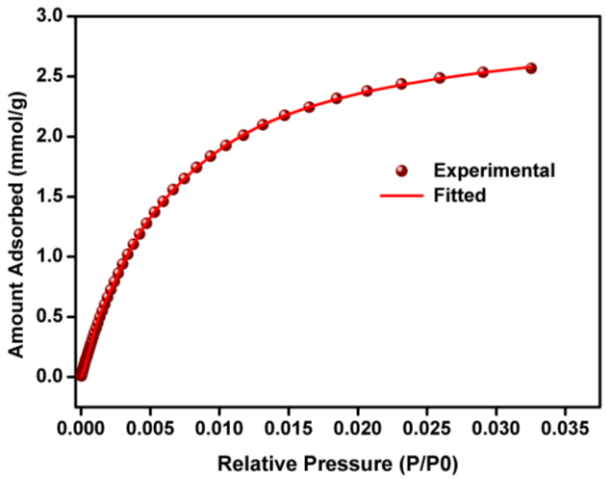

Figure 5.A.31. NLDFT fitting comparision for IISERP-MOF23. Note that an average fit was obtained using the entire range of data points of the 273 K CO_2 adsorption isotherm.